Transparent Conducting Oxide Based Devices

Marita Kay O'Sullivan

School of Physics

University of Dublin

A thesis submitted for the degree of

Doctor of Philosophy

29^{th} April 2011

DECLARATION

I declare that this thesis has not been submitted as an exercise for a degree at this or any other university and it is entirely my own work.

I agree to deposit this thesis in the Universitys open access institutional repository or allow the library to do so on my behalf, subject to Irish Copyright Legislation and Trinity College Library conditions of use and acknowledgement.

For Jon, who makes everything better.

Acknowledgements

Firstly, I would like to thank my supervisor, Prof. J. M. D. Coey for giving me the opportunity to carry out this research in Trinity College. I am grateful for all the support, both financial and academic, that I have received throughout the past few years, it will not easily be forgotten. A debt of gratitude is also owing to Prof. J. G. Lunney, who gave freely of his time and attention to advance this research. The use of his facilities, without which the results herein would not have been realised, was readily proffered and I appreciate it greatly.

Sincerest thanks are due to Dr. P. Stamenov whose wisdom, direction and friendship are unerring. This thesis would not have been possible without your dedication and willingness to work at all hours, and your very tolerant family, Maria and Stani, who generously share you with the School of Physics. Thanks are due to Dr. M. Venkatesan, for his supervision in the early days, and for the many SQUID measurements. I am grateful to Dr. C. McGuinness for the training and use of his XPS system. A number of measurements in this dissertation have been performed in the IPCMS in Strasbourg, and I would like to express my appreciation for the training in TEM sample preparation and measurements carried out by Dr. S. Colis and Dr. C. Ulhaq-Bouillet and for the AFM measurements performed by Mr. C. Leuvrey.

I would like to thank Dr. R. Gunning for teaching me the inner-workings and superstitions involved in PLD (we're still finding samples in the bottom of the chamber!), I received an excellent grounding for what was yet to come. Many thanks also to Dr. L. Dorneles for landing me with the XRD responsibility. For having met and shared a lab with Dr. P. Dunne, the unfailing gentleman, and Dr. Z. Diao, the muffin man, who with his usual delicacy and tact, in the initial week of my PhD, informed me that there was a minimum size of scientist, I am eternally grateful.

"It was the best of times, it was the worst of times,... "

To the members and summer students of Group D, past and present - Plamen, Venky, Zhu, Peter, Fiona, Robbie, Fowley, Greg, Lucio, Chris, Darragh, Cathy, Gen, Eoin, Damaris, Simone, Kaan, Warren, Niizeki, Huseyin, Huseyin, Fernando, Oscar, Franklyn, Karl, Lorena, Charles, Nicholas, Olé, Claudia, Paddy, Kwan, Marion, Ali, and many more, to Maria and Stani, to Roseanne and all the crowd in CRANN, to the plasma guys - Tony, Enrique, Brendan and Clelia, to the workshop guys - Mick, Pa and Gordon, to my close friends Maeve, Michelle, Sinead, Amy and Cormac, to my favourite brother, Kier, to my loving parents, and to my wonderful husband, Jon - thank you for sharing the best of times with me.

Abstract

Transparent conducting oxide (TCO) materials, formerly regarded as degenerate conductors of only one carrier type, can now be considered as transparent semiconductors possessing the potential for integration into more sophisticated transparent electronic settings. A general description of this class of materials is presented in the introductory chapter, setting the objectives of the dissertation as a natural progression from material preparation and characterisation towards device design and prototyping. After surveying the existing literature on transparent conducting oxides at the beginning of chapter 2, a concise introduction to the general theory of semiconductors is put forth. Later, attention is drawn to the theory of electronic transport in those materials with particular attention to magnetic field effects. Systematics of the most important physical properties of the TCO family follows, details are given on the design of their transparency by exploiting the feigned window between plasma reflection and direct bandgap absorption. Various important characteristics and figures of merit are summarised. A combinatorial chemistry approach to the TCO problem has been suggested, with an emphasis on the strategy of amalgamating an existing p-type semiconducting system, such as Cu_2O, with another $3d$ metal oxides thus widening the gap via hybridisation. Emphasis has been placed on a materials presenting a particular crystal structure - the delafossites. This family of compounds satisfy all of the requirements of the above combinatorial approach. The effects of off-stoichiometry and doping have also been considered.

McConnellite $CuCrO_2$, possessing the most favourable electrical characteristics of the delafossite family, is reviewed in chapter three, with particular attention to the electronic band structure, magnetic and electrical properties. Details of the preparation and characterisation of polycrystalline $CuCrO_2$, which have been synthesised with a view to fabricating source materials for laser ablation to achieve thin films, have been provided. The solubility limit of Mg in the $CuCrO_2$ lattice has been examined. Description of the optimisation of the layer growth, for which the solubility of the dopant ion has been investigated, follows. X-ray diffraction was used to assess the quality of the films, and the epitaxial relations between the film and the substrate. Surface morphology has been studied by atomic force microscopy in order to confirm the suitability of the films for stacking into multilayer (at least three layers with thicknesses relevant

to diffusive electronic transport length scales - on the order of tens of nanometres) electronic devices. A number of different techniques for studying composition and band structure have been employed: optical characterisation to study the bandgap; x-ray photoemission spectroscopy to verify Mg-dopant concentration; and low-temperature, high-field magnetotransport in order to study the positions of the impurity levels and the degeneracy of the valence band.

A similar preparation and characterisation algorithm has been followed for two different material systems. The first, bipolar delafossite TCO - $CuInO_2$, and the second, n-type wurtzite TCO - ZnO. In chapter four, two possible doping schemes, p-type doping with Ca ions, and n-type doping with Sn, of $CuInO_2$ have been studied. Both variations have been found to be excessively resistive, exhibiting low carrier mobilities despite their high structural qualities. The highly transparent films have been found to exhibit two distinct activation energies, both of the order of 0.3 eV. These large values, combined with the low carrier mobility exclude the possibility of incorporating these films into homojunction p-n diodes and transistors.

The remaining option, of constructing heterojunction-based devices utilising another family of n-type wide bandgap semiconductors, have thereafter been pursued. One of the most studied systems, namely Al-doped ZnO, has been chosen for optimisation. Measures have been taken to discover the conditions for stoichiometric growth of undoped zincite, prior to optimising the impurity-doped ZnO compound, to achieve a degree of control over the carrier concentration. The structural quality and electrical performance of the Al-doped ZnO layers have provided an appropriate n-type component for subsequent device structures.

The recipes developed in the previous three chapters have been manipulated in order to realise the magnetic analogs of two of the workhorses of conventional semiconductor electronics, the p-n junction diode and the bipolar transistor. After a brief survey of the conventional theory of operation of diffuse p-n junctions and heterojunctions, at the beginning of chapter 6, the steps taken towards the fabrication of the prototypical devices have been described. Apart from the characterisation sequence, already described in previous chapters for the individual active layers of the studied devices, additional efforts to realise the concept and operation of transparent oxide structures are discussed.

Contents

Nomenclature

Roman Symbols

α_0	common-base current gain
a_0	hydrogen Bohr radius
a_H^*	Bohr radius
β_0	common-emitter current gain
$\mathbf{B}$	magnetic field
C	Curie constant
c	speed of light
D	diffusion coefficient
d	thickness
$\mathcal{E}$	electric field
E_A	acceptor energy level
E_a	activation energy
E_D	donor energy level
E	energy
e	elementary charge
$f(E)$	Fermi-Dirac distribution function
$\mathbf{F}$	Lorentz force

γ	emitter efficiency
G	generation rate
$\hbar$	reduced Planck constant
h	Planck constant
I_B	base current
I_{Cn}	collector electron current
I_{Cp}	collector hole current
I_{En}	emitter electron current
I_{Ep}	emitter hole current
I	current
$\boldsymbol{J}_d$	drift current density
J_C	collector-base junction
J_{dif}	diffusion current density
J_E	emitter-base junction
J	total current density
k_B	Boltzmann constant
k	wave vector
L	grain size
m^*	effective mass
m_0	hydrogen free electron mass
n_0	thermal equilibrium electron concentration
N_C	density of states in the conduction band
n_c	Mott critical doping concentration

N_i	concentration of impurity centres
n_i	intrinsic electron concentration
N_V	density of states in the valence band
N	refractive index
n	carrier concentration
n(E)	electron density
p_0	thermal equilibrium hole concentration
p_i	intrinsic hole concentration
p(E)	hole density
q	charge
R_H	Hall coefficient
R_s	sheet resistance
R	recombination rate
R	resistance
S_{RT}	thermopower
T_N	Néel temperature
T	transparency
U	net recombination rate
u	fractional atomic position
v	average velocity
V	voltage
W	depletion layer width
x	doping concentration

Greek Symbols

α	absorption coefficient
χ	molar susceptibility
δn	excess carrier concentration
ϵ	relative permittivity
ϵ_0	permittivity of vacuum
ϵ_∞	high frequency permittivity limit
ϵ_s	dielectric permittivity
κ	dimensionless susceptibility
κ	extinction coefficient
κ_{TF}	Thomas-Fermi screening wave vector
λ	wavelength
λ_{mfp}	mean free path
μ	carrier mobility
μ_B	Bohr magneton
μ_{eff}	effective moment
$\boldsymbol{v}_d$	carrier drift velocity
ν	frequency
ω_c	cyclotron frequency
ω_p	plasma frequency
Φ_{gb}	grain boundary potential
$\hat{\rho}$	resistivity tensor
ρ	electrical resistivity

ρ_s space charge density

$\hat{\sigma}$ conductivity tensor

σ electrical conductivity

σ_0 Drude conductivity

τ_c relaxation time

θ_{CW} Curie-Weiss temperature

θ_H Hall deflection angle

Superscripts

E_g bandgap energy

Acronyms

CB conduction band

TCO transparent conducting oxide

VB valence band

Chapter 1

Introduction

Transparent Conducting Oxides (TCOs) are an unusual group of materials possessing both high optical transparency and high electrical conductivity, two properties that are generally considered to be mutually exclusive Hartnagel *et al.* (1995). This rare combination of physical properties can only be achieved if a material has a sufficiently large energy bandgap so that it does not absorb visible light, i.e. > 3 eV Chopra *et al.* (1983), and also possesses a high enough concentration of electrical carriers that the material can be considered a tolerable conductor of electricity. Such an electrical conductor requires a degenerate electron or hole concentration $\geq 10^{19}$ cm^{-3} Edwards *et al.* (2004), with a moderately large mobility, ≥ 1 cm^2 V^{-1}s^{-1}. The charge carriers are not inherent to the materials, they arise from chemical doping or non-stoichiometry Banerjee & Chattopadhyay (2005). The carrier concentration must be sufficient for the Fermi energy to exceed the mobility edge, yet insufficient to create significant plasma absorption in the visible range of the spectrum according to the Drude model for a free electron gas.

1.1 Transparent Conductors

Despite their limited numbers, research has led to the discovery of many transparent conductors which are increasingly used in commercial applications today Gordon (2000). Since the initial fabrication of TiN thin films by CVD in 1986 Kurtz & Gordon (1986), the nitrides have proven to be highly functional materials Khan *et al.* (1992) and investigation has led to the fabrication of GaN *p-n* homo-junctions Monroy *et al.* (1999) and eventually blue LEDs Nakamura *et al.* (1994). In recent years attention has turned to the development of transparent conducting polymers as a result of the discovery of conducting polymers which received the Nobel prize for chemistry in 2000 Chiang *et al.* (1978). Very recently carbon nanotubes have been used to fabricate solar cells

Contreras *et al.* (2007), and a transparent thin film transistor (TFT) Kim *et al.* (2010). Graphene has been the focus of a number of studies into transparent conductors in recent publications Wang *et al.* (2008). Lately, however, a number of *p*-type transparent conducting chalcogenides, BaCuS:F and BaCuSe:F Yanagi *et al.* (2003b), and oxy-chalcogenides, $(La_{1-x}Sr_xO)CuS$ Hiramatsu *et al.* (2002) and $LaCuOS_{1-x}Se_x$ $0 < x < 1$ Ueda & Hosono (2002), have been reported. These materials enjoy increased covalency over oxides due to reduced electronegativity on the chalcogenide ion.

Many of these transparent conducting non-oxide materials have highly attractive electrical and optical qualities, however they also have other less appealing properties. They are not as thermodynamically stable in air as oxide transparent conductors, the preparation of selenides can be hazardous Minami (2000). Fabrication costs of GaN, for example, can be excessive since sophisticated techniques such as MBE must be employed, and these kinds of techniques cannot provide the large area thin films required in industry. The most attractive class of transparent conductors has been the transparent conducting oxides (TCOs), which is the focus of our study, will be detailed in the following section.

1.2 Transparent Conducting Oxides

Wide bandgap oxides have historically been considered strict electrical insulators, with utility limited to dielectric functions and optical applications Kawazoe *et al.* (2000). There is, however, a subset of these materials that exhibit unexpectedly high, almost metallic, conductivity. This class of materials, the transparent conducting oxides is central to this thesis. The properties of these materials will be discussed in detail in the ensuing chapters.

Baedekar grew cadmium oxide (CdO) thin films by the thermal oxidation of sputtered cadmium in 1907. This was the first report of TCO growth Baedekar (1907). Since then a large number of TCO materials have been investigated over the years, the most common being indium oxide In_2O_3, tin oxide SnO_2, zinc oxide ZnO and their doped oxides. Of all the TCO films, indium tin oxide (ITO) is the most widely used for optoelectronic device applications, most notably flat panel displays Lewis & Paine (2000). SnO_2 films, with F substitution, are used for architectural glass applications Ginley & Bright (2000). Al and Ga-doped ZnO films have also attracted much attention as the transparent electrode in many device applications, such as solar cells Minami (2000), because they are nontoxic and inexpensive and have comparable electrical and optical properties to ITO Gordon (2000). The original TCO, CdO, has more recently been reported to exhibit a very high electron mobility when doped with In or Sn Yan *et al.* (2001). The historical

approach to developing new TCO materials has been to combine the aforementioned binary basis TCOs to form new ternary and multicomponent oxide phase systems, such as cadmium stannate Cd_2SnO_4 Nozik (1972), $CdIn_2O_4$ Freeman *et al.* (2000), and Zn_2SnO_4 Palmer *et al.* (1997).

Material	Bandgap (eV)	T (%)	ρ (Ωcm)	n (cm^{-3})	μ (cm^2/Vs)	Fabrication	Ref.
In_2O_3	3.56	> 90	2×10^{-4}	4×10^{20}	70	Thermal evap.	[1]
SnO_2:F	4.41	> 80	5×10^{-4}	4.6×10^{20}	28	Spray	[2]
In_2O_3:Sn	4.0	> 85	8.45×10^{-5}	1.38×10^{21}	53.5	PLD	[3]
ZnO:Al	3.4	> 80	8.5×10^{-5}	1.5×10^{21}	47.6	PLD	[4]
Cd_2SnO_4		> 80	5×10^{-4}	5×10^{20}	40	Sputtering	[5]

Table 1.1: Electrical properties of common transparent conducting oxides. T = transparency, ρ = resistivity, n = carrier concentration, μ = carrier mobility. Reference [1] = Pan & Ma (1981), [2] = Shanthi *et al.* (1982), [3] = Suzuki *et al.* (2002), [4] = Agura *et al.* (2003), [5] = Schiller *et al.* (1982).

TCOs have formerly been used in a passive electrical manner, as conductors or resistors Minami (2005). Typically, these types of applications require the TCO conductivity to be as large as possible for optimal performance. Thus, a great deal of research has been undertaken to maximise the TCO conductivity. The electrical resistivity, ρ, of TCO films depends on the carrier concentration, n, and carrier mobility, μ, as follows:

$$\rho = \frac{1}{ne\mu} = \frac{1}{\sigma} \tag{1.1}$$

where e is the electron charge and σ is electrical conductivity. Limitations of TCOs become more critical as passive and active devices based on these materials become more sophisticated. Simply increasing the thickness to obtain increased conductivity is not acceptable since the optical absorption will increase. To achieve lower resistivity of the films, the carrier concentration n and the carrier mobility μ should be simultaneously optimised, without increasing their optical absorption.

Although the above listed TCOs are considered to be passable conductors from the perspective of a semiconductor, they are actually very poor conductors compared to metals. Calculations of the electrical performance limits of TCOs have been carried out, taking account of the ionised impurity scattering of carriers due to degenerate doping concentrations Bellingham *et al.* (1992) Chen *et al.* (2000), however it appears that advances in TCO materials development are converging on these increasingly achievable limitations Edwards *et al.* (2004).

1.3 Transparent Electronics

Transparent conducting oxides (TCOs) have potential applications in transparent electronics because they have the unique features of optical transparency in the visible region and controllable electrical conductivity, from almost insulating to degenerate semiconducting ($\sim 10^4$ Scm^{-1}) behaviour. Despite this abundantly wide and controllable range of conductivity, until recent years, the applications of TCOs have been limited to transparent electrodes. The origin of this limited application seems to be the lack of p-type conducting transparent oxide materials. All of the well-known and commercially relevant TCOs are n-type. p-Type TCOs are a relatively new phenomenon and their conductivity performance is quite poor compared to that of n-type TCOs. To a large extent, this is due to the very low mobility of these materials, typically less than ~ 1 $cm^2V^{-1}s^{-1}$, compared to mobilities in the range of $\sim 10 - 40$ $cm^2V^{-1}s^{-1}$ and above for n-type TCOs.

1.3.1 p-Type TCOs

With a view to diverse device applications, it is now of the utmost importance to prepare various new types of p-TCOs with superior optical and electrical characteristics, at least comparable to the existing, widely used n-TCOs, which have a transparency above 80% in the visible region and a conductivity of about 1000 Scm^{-1} or more Minami (2005). Intense works have been carried out in recent years to conceive of new material design strategies Kawazoe *et al.* (2000), and to fabricate new p-TCOs by various deposition techniques, such as $CuAlO_2$ Kawazoe *et al.* (1997), $CuGaO_2$ Yanagi *et al.* (2000a), $SrCu_2O_2$ Kudo *et al.* (1998), and Ga and N-codoped ZnO Guo *et al.* (2001); Joseph *et al.* (1999). Consequently, transparent, p-type semiconducting crystalline thin films have gained considerable interest in the field of active devices. All-transparent junctional devices have begun a new generation in optoelectronics technology called "Invisible Electronics" Thomas (1997). Nonstoichiometric and doped versions of various new types of p-type transparent conducting oxides (p-TCO) with improved optical and electrical properties have been synthesised in the last few years for use in this field.

1.4 Thesis Outline and Objectives

This research endeavour has broadly been motivated by the prospect of advancing TCO materials development, and bridging the gap between passive and active transparent device applications. In response to recent interest in the p-type delafossite TCOs, two promising members of this family

have been selected for investigation, namely $CuCrO_2$ and $CuInO_2$. The principal attractions of cuprous chromate can be summarily ascribed to its high conductivity p-type semiconducting nature and simultaneous transparency in the visible range of the electromagnetic spectrum, added to its antiferromagnetic ordering below ~ 25 K. The bipolar semiconducting properties of impurity-doped $CuInO_2$, on the other hand, suggest the potential to fabricate transparent homojunction devices. The properties of the transparent conducting oxides will be examined in detail in chapter 2. The engaging qualities of the two selected materials, $CuCrO_2$ and $CuInO_2$, are manifold and will be comprehensively discussed in chapters 3 and 4 respectively. The well-studied n-type TCO Al-doped ZnO forms an integral part of this work and is utilised for its concurrent high conductivity n-type semiconducting character and transparency. Al-doped ZnO will be analysed in chapter 5.

The aims of this project were threefold. Firstly, there was the technical aspect, the goal of which was to synthesise and grow high crystallinity, phase-pure p-type delafossite and n-type transparent conducting oxides and to characterise them structurally, optically, morphologically, electrically and magnetically. This involved powder synthesis studies and optimisation of the thin film fabrication of these complex multication oxides by pulsed laser deposition, which will be discussed in chapters 3, 4 and 5, and more thoroughly detailed in appendix A. The second objective, on a more fundamental level, was to gain an insight into the conduction mechanism at work in the delafossite materials, to understand the origin of the charge carriers and the factors that influence the wide variation in their conductivity, including doping. This will be discussed in chapters 3 and 4. In the case of $CuCrO_2$, an investigation of the curious interplay between the magnetic and the electrical properties was carried out, this will also be discussed in chapter 3. The third aim was to integrate these p-type TCO materials in an operational transparent device. To this end, an n-type transparent oxide counterpart was required in order to realise an all-oxide bipolar electronic device, and ZnO, whose property optimisation will be discussed in chapter 5, was the chosen candidate. Implementing high quality materials and gaining an understanding of their properties was crucial for the final aim. A number of junction device configurations were fabricated with the various components for the different layers, the deposition and operation of these devices will be examined in chapter 6. Firstly, a heterojunction device composed of p-type $CuCrO_2$ and n-type ZnO layers was characterised. Secondly, a homojunction structure composed of p and n-type layers of the bipolar TCO $CuInO_2$ was constructed and studied. And lastly, a p-n-p heterojunction bipolar transistor was fabricated using p-$CuCrO_2$ for the collector and the emitter, and n-ZnO for the base component, the performance of this device will be discussed in

chapter 6. Such junction devices, fabricated by both n and p-type TCO thin films, are a key structure for "Invisible Electronics" Thomas (1997).

Chapter 2

Transparent Conducting Oxides

2.1 Literature Review

At the turn of the century, it was recognised that the rate of advance of new transparent conducting oxide materials was surpassed only by the increased applications-driven demand for improved properties. The swift advancements in TCO-incorporated technology have prompted more sophisticated applications concepts demanding greater performance from this class of materials and pushing them to their limits. The demands for optimal operation require TCO conductivity to be as large as possible while transparency is maintained. The limitations of TCOs become more critical with increasing demand for larger-area displays and hence faster graphics writing speeds, for example Ginley & Bright (2000). The modern requirements of resilience to harsh environments Gordon (2000), such as radiation hardness and high temperature performance, non-toxicity, smooth surface morphology for improved interfacial compatibility, and the prospect of all-oxide electronics place further demands on the industry Ginley & Bright (2000). Increasingly cost effective deposition techniques are also required, and source materials that are more abundantly available than semiprecious indium metal and hence have greater price stability Lewis & Paine (2000), but which maintain the high performance properties of the current leading TCOs.

The majority of research designed to decrease the resistivity of the TCO materials has focused on increasing the free carrier concentration through substitutional doping, creation of oxygen vacancies or implantation of interstitials Minami (2000). According to the electrical resistivity equation in the introduction, the conductivity can also theoretically be enhanced with increased mobility. The mobility, however, is dependent on intrinsic scattering mechanisms, which will be discussed later in this chapter, and cannot be controlled directly. By introducing donor or

acceptor doping, it is possible to control the conductivity. Depending upon the valence of dopants or vacant sites, acceptor or donor states will induce p- or n-type conductivity. At very high doping concentration the semiconductor becomes degenerate, however, at some point, increasing the carrier density via doping or oxygen vacancies is self-limiting because the excess free carriers have the effect of decreasing the mobility due to carrier-carrier scattering due to the non-parabolicity of the bands, which will be detailed in section 2.2.5. Furthermore, the optical properties are affected by the doping concentration. Hence, there is a trade-off between the carrier density and the carrier mobility for achieving low resistivity.

In order to progress, it is important to understand the character of the conductivity, where the carriers derive from, the impact of doping, and the scattering mechanisms in operation that are limiting the TCO mobility and also those intrinsic limits on TCO performance, to arrive at the optimum balance between mobility and carrier concentration. This mobility-carrier concentration compromise corresponds to that which preserves the requisite conductivity and transparency without giving rise to mid-gap states that would interfere with the transparency Ginley & Bright (2000). Before discussing the more explicit electrical and optical properties of transparent conducting oxides, a brief digression into carrier transport regimes within the band model theory of semiconductors would be instructive.

2.2 Band Model of Solids

In order to gain a more complete understanding of both the electrical and optical properties of transparent semiconductors and how they coexist, it is necessary to explore carrier transport theory and optical processes in terms of semiconductor band theory.

Solid-state materials are commonly classed in terms of their electrical properties as insulators, semiconductors or conductors (metals). A rudimentary definition of a semiconductor is as a material whose conductivity lies between that of an insulator and that of a metal, and which has a characteristic resistivity increase with decreasing temperature. In 1931, Wilson identified the reason for the sharp distinction between metals and non-metals in terms of energy band theory Wilson (1931a), Wilson (1931b). Since the energies of the electron states in crystalline materials lie in bands, he recognised a non-metal as a material in which all bands are either completely full or completely empty, while a metal has one or more bands that are only partly full.

Although the behaviour of conduction electrons (charge carriers) in some metals can easily and quite accurately be described by the Free Electron Model of Drude's Theory of Metallic Conduction

Drude (1900a) Drude (1900b), which neglects the interaction between the electrons, this model is insufficient to describe the behaviour of charges constrained by various potentials such as that imposed by the crystal lattice. The waves propagating in such periodic structures are not perfectly free but constrained to form Bloch waves. An electron in a crystalline solid will experience a periodic potential whose wave function, in accordance with the Bloch theorem Bloch (1928), will differ from that at another point in the perfectly periodic crystal lattice only by a phase factor. A profound consequence of the periodicity is that there are some ranges of energy within which wave propagation is forbidden.

Energy band theory, which was crucial to Wilson's classification of solid materials, applies the quantum mechanical concept of discrete quantised energy states for a single-electron atom, along with Pauli's exclusion principle, to describe the behaviour of the electrons in an extended single-crystal solid. The formation of allowed and forbidden energy bands results from the overlap of wave functions of the many closely-packed atoms comprising a crystal. With decreasing interatomic distance, the electronic states of the atoms increasingly interact and overlap. The discrete quantised energy levels split into bands of discrete energy levels, and at the equilibrium interatomic distance some states are in the lower or valence band (VB) of the atoms and some are in the upper or conduction band (CB), as illustrated in fig. 2.1. At absolute zero all electrons are in the lowest energy states available to them. The energy separation between the top of the VB and the bottom of the CB is the width of the forbidden energy band known as the bandgap energy, E_g. The probability of an electron near one atom passing to the next depends on the height and width of the interatomic potential barrier relative to the energy of the electron. Thus electrons in the higher bands (CB) are free to move throughout the lattice, whereas those in the lower bands (VB) are more closely associated with particular atoms.

2.2.1 Metals, Insulators and Semiconductors

A metal can exhibit very high electrical conductivity, and this can be attributed to one of two possible scenarios. The first is a partially filled CB, as indicated in fig. 2.1 (a), and the second is a CB that overlaps with the VB, where either the uppermost electrons in the CB or the electrons at the VB maximum can move to higher energy levels upon application of an electric field. This small contribution of energy is sufficient to promote conduction in metals because there are many unoccupied states close to the occupied energy states, hence their characteristic low resistivity.

The band model describes a material as an insulator if its energy bands are either completely empty or completely full, as illustrated by fig. 2.1 (b). The bandgap energy of such a material

is typically very large. This band configuration precludes charge carriers from contributing to a current under an applied electric field, even at room temperature, where the CB is virtually empty and the VB is completely full, and hence the resistivity of an insulator is very large.

A material with a band scheme similar to that of an insulator, but with a much smaller bandgap energy, and with bands that are either almost full or almost empty is a semiconductor, as indicated in fig. 2.1 (c). At absolute zero degrees all valence electrons in a semiconductor are in the VB in the lowest available states, and the CB is empty. As thermal, optical or any form of energy is supplied a few VB electrons will increasingly gain enough energy to break their bonds and jump into the CB. The semiconductor is necessarily neutrally charged, therefore a charge-compensating "hole" is created in the original bonding position in the VB. Both of these charge carriers contribute to electrical current in an intrinsic semiconductor in the presence of an externally applied force. The conductivity of a semiconductor may be poor in comparison with a metal, it can, however, be controlled and varied widely making it very conducive to electronic applications. The focus will lie primarily on semiconductors in this section since they are central to the dissertation.

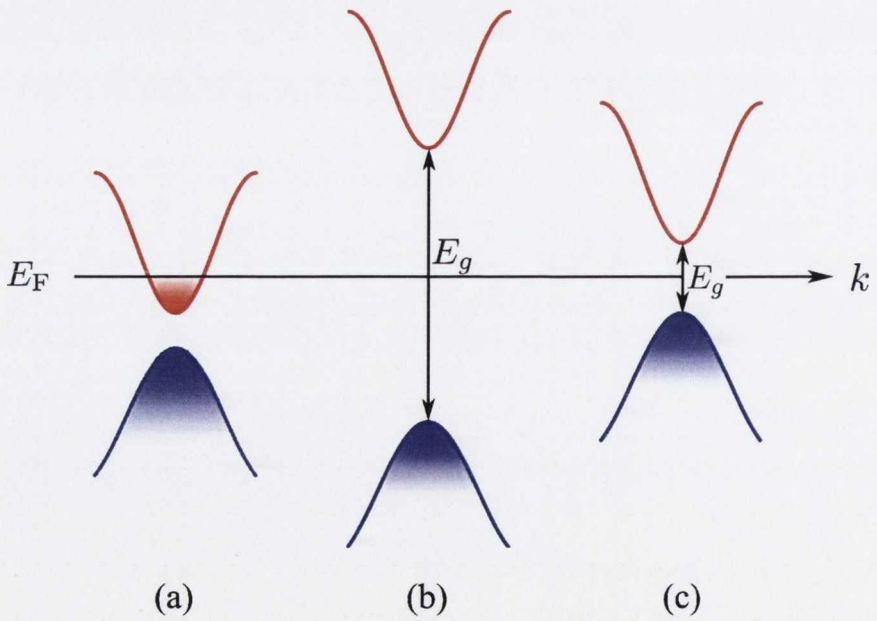

Figure 2.1: Energy band diagram of (a) a metal, (b) an insulator, and (c) a semiconductor.

2.2.2 Energy Band Diagrams and Effective Mass

Many electrical and optical properties of materials can be explained with the aid of energy-momentum or energy band diagrams. The energy bands of a semiconductor crystal are constrained by a periodic potential due to the crystal lattice. The energy of an electron in the CB can be related to an effective carrier mass parameter, in a similar manner to the free electron model Drude (1900a) Drude (1900b), as follows:

$$E = \frac{\hbar^2 k^2}{2m^*} \tag{2.1}$$

where m^* is the effective mass of the charge carrier, and $\hbar k$ is the crystal momentum. Both the effective mass and the crystal momentum take account of the internal forces acting on the particle. A plot of the energy against the momentum of the band gives a parabolic dispersion in accordance with the above equation, however in real three dimensional crystals the band structure is far more complicated. In the approximation of the parabolic band, the effective carrier mass is inversely proportional to the curvature of the band:

$$\frac{1}{m^*} = \frac{1}{\hbar^2}\frac{d^2E}{dk^2} \tag{2.2}$$

A narrow parabola corresponds to a small effective mass, while a broad curve corresponds to a large effective mass. It is customary to plot the energy E as a function of k, the wave vector, in band diagrams as shown in fig. 2.2. In real semiconductors, the minimum of the CB and the maximum of the VB may be parabolic in shape, however they do not always coincide at the same k-value. This allows us to distinguish between direct and indirect semiconductors which will be discussed later in this section.

The Hole An earlier paragraph, describing basic conduction in a semiconductor, alluded to a second charge carrier usually referred to as a "hole". This positively-charged "empty state" remains in the original position of a valence electron that has been thermally (or otherwise) elevated from the VB into the CB. The vacant state can contribute to current in the material in the event that a small but sufficient amount of energy is supplied to a neighbouring valence electron to allow it to hop into the empty state. Thus, a new empty state is created in the original position of that valence electron. In this way, the net motion of electrons in a nearly-full band can be equally described by the motion of the positively-charged vacant states.

The effective mass of the hole can again be related to the curvature of the VB maximum according to the equation above. However, the curvature is typically broader for the VB maximum than for the CB minimum. This infers that the effective mass of the hole is larger than that of

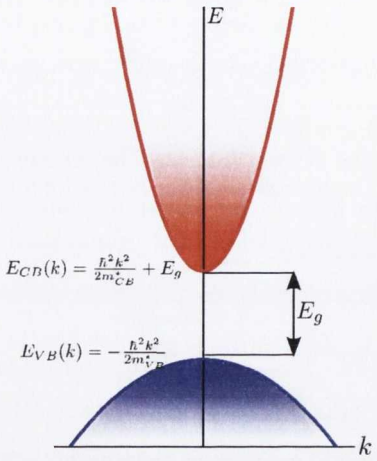

Figure 2.2: Energy band diagram of a wide bandgap semiconductor.

the electron. The valence bands tend to be degenerate near the band edge owing to the presence of heavy hole (hh) and light hole (lh) bands, and also a band due to splitting from the spin-orbit interaction, this typically arises in the *III-V* semiconductors. This complicates the energy surfaces in the VB, particularly for indirect-gap semiconductors, which will be defined presently, and so it is difficult to characterise the hole effective masses.

2.2.3 Direct and Indirect Gap Semiconductors

The relative k-space alignments of the conduction band minimum and valence band maximum in the band structure of materials can be related to the nature of the transitions occurring between the bands in the absorption region. The fundamental bandgap in a material is identified as the minimum energy difference between the uppermost point in the valence bands and the lowest point in the conduction bands. These two points do not necessarily occur at the same symmetry point in the band structure, and when they do not coincide the material is referred to as an indirect bandgap semiconductor, otherwise band-to-band transitions occur directly between the same point in k-space and the material is a direct bandgap semiconductor. The difference between these two classes of semiconductor, shown in fig. 2.3, is that transitions in indirect gap semiconductors require the absorption or emission of a phonon which provides the appropriate momentum to correct for the k-vector misalignment between the band extrema, which significantly reduces the statistics of absorption and recombination processes occurring. Direct gap semiconductors require no such momentum adjustments, and are therefore more suitable for LED and laser diode applications.

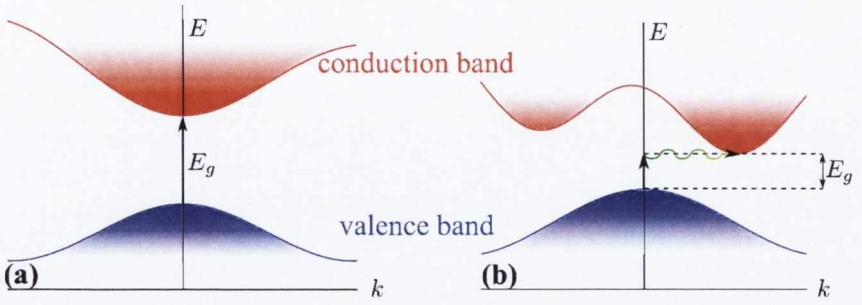

Figure 2.3: Semiconductors with (a) a direct bandgap and (b) an indirect bandgap.

2.2.4 Semiconductor Fundamentals

In the early days of materials exploration, semiconductors did not receive the acclaim they do today. In 1851, Johann Wilhelm Hittorf observed a linear relation between $log\sigma$ and T^{-1}in Cu_2S and Ag_2S Hittorf (1851). Without knowing what kind of charge carriers were responsible for the conduction, he had unwittingly made the first measurement of the conductivity of a semiconductor. In 1879, Edwin Herbert Hall, and his supervisor, H. A. Rowland, observed a transverse potential difference that was proportional to both the current and to the magnetic field in a thin gold leaf mounted on a plate of glass Hall (1879) Rowland (1880). Koenigsberger classified electronically conducting solids into metals, insulators and "variable conductors" according to their dissociation energy Koenigsberger (1914), and in 1910 his student, Weiss, published a paper referring to a "Halbleiter", or semiconductor, for the first time Koenigsberger & Weiss (1911). In 1907, as previously mentioned, Baedekar tried a new technique with a view to improving the reproducibility of his samples Baedekar (1907). He sputtered thin metallic layers on glass or mica sheets and then exposed the films to oxygen or other gases to produce compounds with the metals. He observed the semiconducting properties of CuI to vary depending on the stoichiometric composition. During World War I semiconductor research abated significantly, it was commonly thought that semiconductors were useless due to their unpredictable behaviour and their irreproducibility, and later, even in 1931 Pauli shared this view Busch (1989). Gudden reasoned semiconduction to be the result of impurities and imperfections in solids Gudden (1930). And in the early 1930s, Wagner and Schottky developed their theories of lattice defects (Fehlordnungs-Erscheinungen) Wagner & Schottky (1931). In 1931 Alan Wilson explained the difference between metals and insulators, and produced his classic papers on semiconductors which distinguished between "intrinsic" and "ex-

trinsic" semiconductors based on the band theory of solids Wilson (1931a) Wilson (1931b). Also in 1931, Heisenberg showed that the empty states in a nearly full band, the holes, are equivalent to positively charged carriers Heisenberg (1931). Since this time, the semiconductor has become recognised as one of the most important materials for electronic applications. The following sections will elucidate some of the concepts that puzzled the early researchers.

2.2.4.1 Intrinsic Semiconductors

In an ideal intrinsic semiconductor crystal there would be no impurity atoms or lattice defects. However, this is never the case, therefore a real intrinsic semiconductor crystal is identified as having a relatively low density of impurity atoms compared with the density of thermally generated current carriers.

Thermal equilibrium conditions assume the temperature of the semiconductor is constant and that there are no external forces, such as applied voltage, magnetic or electric fields or temperature gradients, acting on the material. The electron and hole carrier densities in this regime can be defined as follows:

$$n(E) = \int_{E_C} N_C(E) f(E) dE \tag{2.3}$$

or

$$p(E) = \int_{E_V} N_V(E) f(E) dE \tag{2.4}$$

where $N_C(E)$ is the density of states in the CB,

$$N_C(E) = \frac{4\pi(2m_n^*)^{\frac{3}{2}}}{\hbar^3}\sqrt{E - E_C} \tag{2.5}$$

where m_n^* is the electron effective mass, E_C is the energy of the bottom edge of the CB. $N_V(E)$ is the density of states in the VB,

$$N_V(E) = \frac{4\pi(2m_p^*)^{\frac{3}{2}}}{\hbar^3}\sqrt{E_V - E} \tag{2.6}$$

where m_p^* is the hole effective mass, and E_V is the energy of the top edge of the VB. The Fermi-Dirac distribution function, $f(E)$, gives the probability for an electron to occupy the energy state E

$$f(E) = \frac{1}{1 + exp\left(\frac{E - E_F}{k_B T}\right)} \tag{2.7}$$

where k_B is the Boltzmann constant, T is the absolute temperature, and E_F is the Fermi level.

The concentration of electrons in the CB in thermal equilibrium, n_0 is expressed as

$$n_0 = N_C exp\left(\frac{-(E_C - E_F)}{k_B T}\right) \tag{2.8}$$

where

$$N_C = 2\left(\frac{2\pi m_n^* k_B T}{\hbar^2}\right)^{\frac{3}{2}} \tag{2.9}$$

while the thermal equilibrium concentration of holes in the VB is

$$p_0 = N_V exp\left(\frac{-(E_F - E_V)}{k_B T}\right) \tag{2.10}$$

where

$$N_V = 2\left(\frac{2\pi m_p^* k_B T}{\hbar^2}\right)^{\frac{3}{2}} \tag{2.11}$$

For an intrinsic semiconductor, the concentration of electrons in the CB, n_i, is equal to the concentration of holes in the VB, p_i. We can write the product of the intrinsic electron concentration and the intrinsic hole concentration

$$n_i = n_0 = N_C exp\left(\frac{-(E_C - E_{Fi})}{k_B T}\right) \tag{2.12}$$

$$p_i = p_0 = n_i = N_V exp\left(\frac{-(E_{Fi} - E_V)}{k_B T}\right) \tag{2.13}$$

so that

$$n_i^2 = N_C N_V exp\left(\frac{-(E_C - E_V)}{k_B T}\right) = N_C N_V exp\left(\frac{-E_g}{k_B T}\right) \tag{2.14}$$

where N_C and N_V are as above, and E_g is the familiar bandgap energy. This relation illustrates that n_i is constant in thermal equilibrium conditions, but varies appreciably with temperature. It also indicates that the intrinsic carrier density will be smaller for a larger bandgap.

For an intrinsic semiconductor the Fermi level, E_{Fi}, lies in the centre of the bandgap if the electron effective mass is equal to the hole effective mass. However, this is not the usual case. If $m_p^* > m_n^*$, the intrinsic Fermi level is slightly above the centre, and if $m_p^* < m_n^*$, it is slightly below the centre of the bandgap.

2.2.4.2 Extrinsic Semiconductors

A far more potent and adaptable class of materials are the extrinsic semiconductors. Substitution of predetermined concentrations of impurity atoms into the lattice of such crystals can dramatically alter their electrical and optical properties. In this way, their properties can be tuned to fit an arbitrary purpose in a commercial semiconductor-based device, for example. This process, which is central to this thesis, is called doping.

Donor Conduction: n-Type A substitutional impurity, with a valence of 1 greater than that of the lattice element it is to replace, is added to the semiconductor crystal in controlled concentrations to achieve certain desired electrical properties in the semiconductor. The excess electron, which is not required in the bonding, is called a donor electron. At very low temperatures the donor electron is bound to the donor atom, however the energy required to elevate the donor electron to the CB is considerably less than that for the electrons involved in the bonding, since a permitted donor energy level, E_D, is introduced in the forbidden energy gap close to the CB minimum. These impurity levels are localised, and do not interact with each other appreciably, since the spacing between impurity centres is much greater than the normal interatomic distance for all but the most impure semiconductors. The donor electron requires only a small contribution of thermal energy to induce it into the CB. A positively charged ion is left behind in the original position of the donor impurity atom. The amount of energy needed to promote the donor electron into the CB is termed the ionisation energy of the material. In contrast to intrinsic semiconductors, donor impurities in extrinsic semiconductors provide conduction electrons without any hole byproducts in the VB. This donor-doped material is an n-type semiconductor, the current is carried by electrons, and it has impurity levels which are normally occupied at low temperatures.

Acceptor Conduction: p-Type Now consider a substitutional impurity with a valence of 1 less than that of the lattice element it is to replace. Upon dissolution into the lattice one bonding position is left vacant and the acceptor dopant atom has a negative charge state. A small amount of thermal energy is sufficient for the valence electrons to move about in the crystal filling the holes, but not sufficient to promote them to the CB.

The presence of the impurity introduces an acceptor energy level, E_A, in the forbidden energy gap close to the VB maximum. A small amount of energy is sufficient to promote a valence electron to the acceptor impurity level just above the VB maximum, leaving a vacant state behind in its place.

Hole current is thus generated in the opposite direction to the motion of the valence electrons into the electron holes, and the negatively charged acceptor atom is fixed in the crystal. This p-type conduction is characterised by the generation of holes in the VB without introducing electrons in the CB. The acceptor impurity levels are unoccupied at absolute zero. As a result, the thermal-equilibrium electron and hole concentrations differ from the intrinsic carrier concentration in the semiconductor.

Compensated Semiconductors Due to processing, semiconductor materials frequently contain a combination of donor and acceptor impurities, usually in unequal concentrations. Such a material is called a compensated semiconductor. The various energy levels and charges in such a material are shown schematically in fig. 2.4. The predominant charge carrier decides whether the material is n-type or p-type. If the donor and acceptor concentrations are identical, the material is fully compensated and behaves like an intrinsic semiconductor.

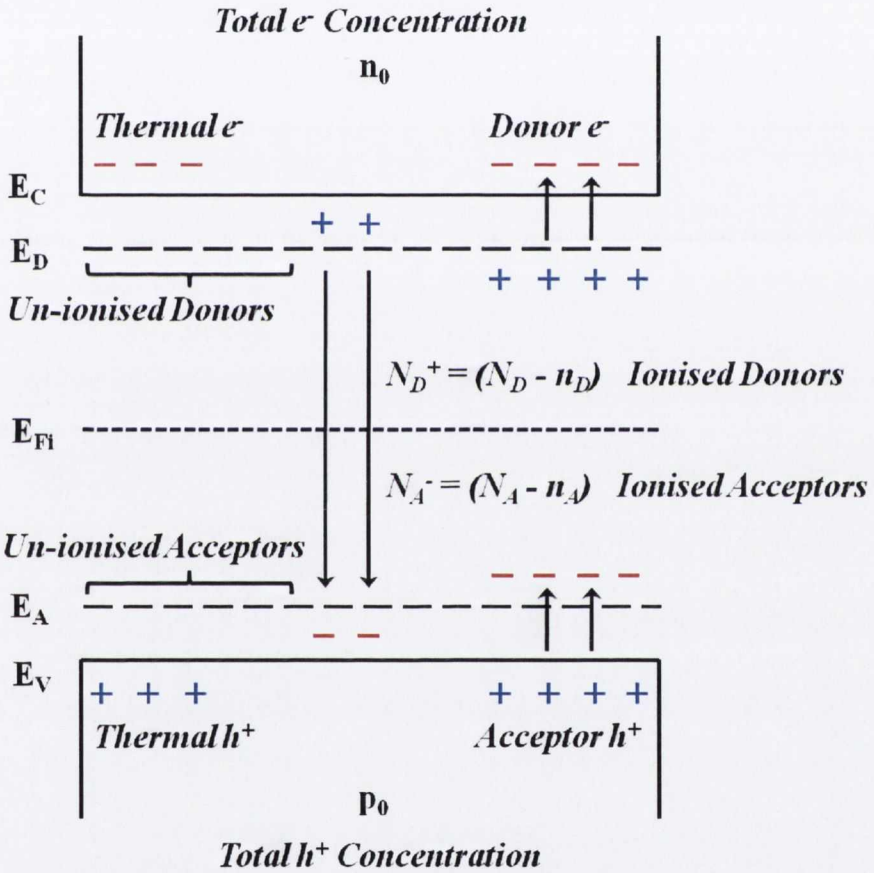

Figure 2.4: Energy band diagram of compensated semiconductor.

In an n-type semiconductor, the electrons are the majority charge carrier, while the holes are the minority carrier. As the concentrations of electrons and holes change with doping, the Fermi level, E_F, will shift accordingly. The thermal-equilibrium concentrations of electrons, n_0, and holes, p_0, respectively, in extrinsic semiconductors can be redefined as

$$n_0 = n_i exp\left(\frac{(E_F - E_{Fi})}{k_B T}\right) \tag{2.15}$$

and

$$p_0 = n_i exp\left(\frac{-(E_F - E_{Fi})}{k_B T}\right) \tag{2.16}$$

where, as defined in the previous section,

$$n_i = N_C exp\left(\frac{-(E_C - E_{Fi})}{k_B T}\right) \tag{2.17}$$

A significant property of an extrinsic semiconductor in thermal equilibrium conditions is that the product of the electron and hole concentrations is a constant

$$n_0 p_0 = n_i^2 = N_C N_V exp\left(\frac{-E_g}{k_B T}\right) \tag{2.18}$$

Charge Neutrality Under thermal equilibrium conditions, a semiconductor is necessarily neutrally charged in order to circumvent the alternative high Coulombic energy cost. Regardless of the distribution of electrons in the various energy states, the overall charge of the material is null. As a consequence of the charge neutrality criterion, the densities of positive and negative charges must be equal and, assuming complete ionisation, the majority electron and minority hole concentrations in an n-type compensated semiconductor can be determined from the following relations

$$n_0 + N_A = p_0 + N_D \tag{2.19}$$

$$n_0 = \frac{(N_D - N_A)}{2} + \sqrt{\left(\frac{N_D - N_A}{2}\right)^2 + n_i^2} \tag{2.20}$$

where

$$p_n = \frac{n_i^2}{n_n} \tag{2.21}$$

This expression is also valid for an n-type semiconductor where there are no acceptor states, i.e. $N_A = 0$.

Degenerate Semiconductors An interesting case arises when the impurity concentration introduced into an extrinsic semiconductor becomes large enough for the charge carriers to interact with each other. For the n-type semiconductors electron interaction leads to further energy level splitting, this time in the donor energy level. Eventually the donor energy band will overlap the bottom of the CB. The concentration of electrons in the CB will exceed the density of states, N_C, and the Fermi level will lie within the CB. The acceptor energy levels split in a similar fashion in a highly-doped p-type semiconductor, and the acceptor band will overlap the top of the VB with increased hole concentration. Once the density of states in the VB is surpassed, the Fermi level will lie within the VB. An important consequence of this high doping concentration is the

narrowing of the bandgap. These materials are termed degenerate n- and p-type semiconductors, and schematics of their respective energy band diagrams are presented in fig. 2.5.

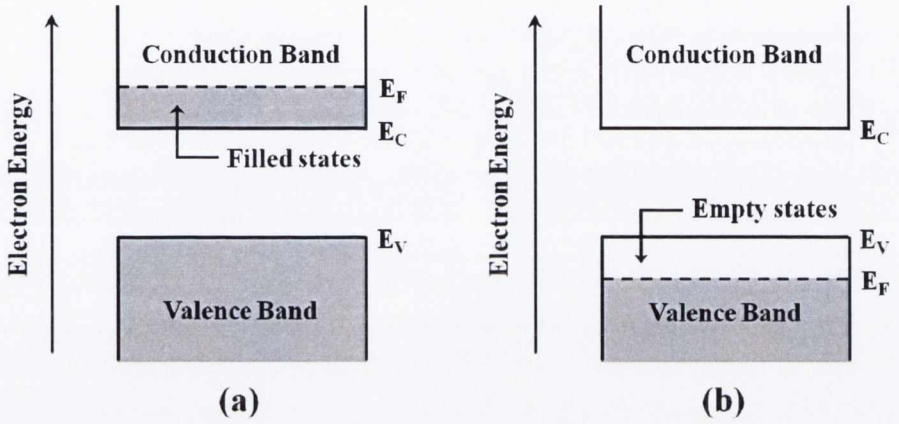

Figure 2.5: Energy band diagrams of degenerately doped (a) n-type and (b) p-type semiconductor.

2.2.4.3 Temperature-Dependent Semiconductor Regimes

Given an n-type semiconductor, at typical doping concentrations the donor states are completely ionised at room temperature. Similarly, in a p-type semiconductor, the probability of finding holes in the acceptor states is zero since each acceptor atom has received a VB electron. At the other extremum, all of the donor states must contain an electron, since no donor electrons have been promoted to the CB, while all of the acceptor states must be devoid of electrons, since no VB electrons have jumped into the acceptor states at absolute zero temperature. For the n-type semiconductor the Fermi level lies between the CB minimum and the donor energy level, while for the p-type material the Fermi level is midway between the acceptor energy level and the VB maximum. This regime is known as freeze-out.

In the intervening temperature region, commonly referred to as the extrinsic region, the donor or acceptor atoms are partially ionised to varying extents. Above room temperature, increased donor dopant concentration expands the electron concentration in the CB above the intrinsic carrier concentration. Within this extrinsic regime, the electrons are reshuffled among the energy states and, as a result, the minority carrier hole concentration decreases below n_i. Amid this redistribution, some donor electrons will drop into some empty states in the VB nullifying the intrinsic holes, and further decreasing the minority carrier concentration. As the temperature increases farther above room temperature, however, ancillary electron-hole pairs are produced and

the intrinsic carrier concentration becomes more significant, eventually dominating the extrinsic behaviour. This is the intrinsic regime. The behaviour of the carrier concentration in each of these temperature regimes is shown in fig. 2.6.

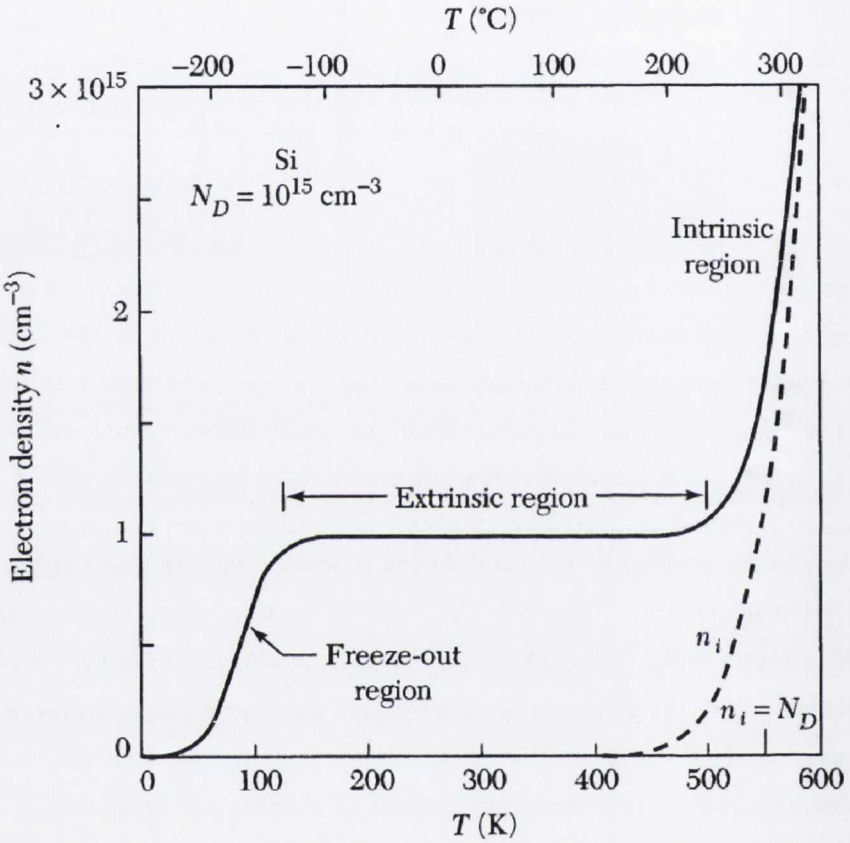

Figure 2.6: Electron density as a function of temperature for a Si sample with a donor concentration of 10^{15} cm^{-3} Sze (1985).

2.2.5 Carrier Transport Theory

In a semiconductor crystal, charge carriers move under either the inducement of an electric field or a density gradient. The former process is known as carrier drift, and the latter is carrier diffusion. Temperature gradients can also effect carrier movement, but for our purposes we will assume only slight deviations from thermal equilibrium conditions, thus minimising the effect.

2.2.5.1 Carrier Drift

An electric field exerting a constant force on electrons and holes in a semiconductor will accelerate them in opposite directions, provided there are empty states in the CB and VB to accommodate them. A constant electric field would lead to a linear increase in particle velocity over time were it not for the manifold collisions imposed upon them. The majority of which arise from ionised impurity scatterers and thermal lattice vibrations. Taking account of the scattering processes, the average particle drift velocity for a positively charged hole, $\boldsymbol{v}_{dp}$ in a low electric field, $\boldsymbol{\mathcal{E}}$, can be written as follows

$$\boldsymbol{v}_{dp} = \mu_p \boldsymbol{\mathcal{E}} \tag{2.22}$$

where μ_p is called the hole mobility, and μ is generally a tensor in crystalline semiconductors, hereafter the scalar version will be used. Similarly, but oppositely, the average drift velocity of an electron in a low field is

$$\boldsymbol{v}_{dn} = -\mu_n \boldsymbol{\mathcal{E}} \tag{2.23}$$

The total drift current density, due to both hole and electron motion is written

$$\boldsymbol{J}_d = e(\mu_n n + \mu_p p)\boldsymbol{\mathcal{E}} = \sigma \boldsymbol{\mathcal{E}} \tag{2.24}$$

where σ is the conductivity of the material, and the inverse of the resistivity ρ.

Mobility and Scattering The electron and hole mobilities can be described in terms of the electronic charge, e, the average time between collisions or relaxation time, τ_c, and the particle effective mass, m^*, and also in terms of their mean free paths, λ_{mfp}, as follows

$$\mu_n = \frac{e\tau_{cn}}{m_n^*} = \frac{e\lambda_{mfp}}{m_n^* \nu_{dn}} \tag{2.25}$$

and

$$\mu_p = \frac{e\tau_{cp}}{m_p^*} = \frac{e\lambda_{mfp}}{m_p^* \nu_{dp}} \tag{2.26}$$

There can be numerous origins of scattering in semiconductor crystals but, in general, lattice vibrations will always be present at temperatures above absolute zero, and collisions with ionised impurity atoms contribute strongly to the scattering term. These are two of the dominant scattering mechanisms in extrinsic semiconductors. Lattice or phonon scattering has a stronger impact at higher temperatures, due to increased lattice vibrations, this in turn reduces the mobility term that

results from lattice scattering. According to scattering theory this mobility, valid for scattering by accoustic phonons, to first order, is related to temperature according to the following relation

$$\mu_L \propto T^{-\frac{3}{2}} \tag{2.27}$$

The second major scattering mechanism, deriving from the presence of ionised impurities in the lattice, affects the motion of the charge carriers through coulomb interactions. Again, to first order, scattering theory recognises the relation between the mobility due to ionised impurity scattering and temperature to vary as follows

$$\mu_I \propto \frac{T^{+\frac{3}{2}}}{N_I} \tag{2.28}$$

where N_I is the total concentration of ionised impurities, both donor and acceptor, in the semiconductor. A temperature increase has the effect of augmenting the speed of the carriers, thus lessening the time spent proximate to the impurity scattering centre and diminishing the probability of a scattering event. This renders the carriers more mobile. Increasing the ionised impurity concentration, on the other hand, has the opposite effect. The inverse mobilities due to a number of different scattering mechanisms may be added, as a consequence of Matthiessen's rule, to obtain the reciprocal of the net carrier mobility

$$\frac{1}{\mu} = \sum_i \frac{1}{\mu_i} = \frac{1}{\mu_L} + \frac{1}{\mu_I} \tag{2.29}$$

Conductivity Ohm's law for a semiconductor is a rudimentary maxim of electronics, which relates the voltage applied across a sample to its resistance, and hence to its resistivity and sample geometry, as follows

$$V = \left(\frac{L}{\sigma A}\right) I = \left(\frac{\rho L}{A}\right) I = IR \tag{2.30}$$

where L is the sample length, and A is the cross-sectional area of a parallelepiped-shaped sample. The conductivity and resistivity of a completely ionised extrinsic semiconductor are predominantly a function of the majority carrier concentration and mobility. For a fully ionised p-type semiconductor with acceptor doping concentration, N_A,

$$\sigma = \frac{1}{\rho} = e(\mu_n n + \mu_p p) \approx e\mu_p N_A \tag{2.31}$$

For an n-type semiconductor in the extrinsic regime, the donor impurities are completely ionised rendering the electron concentration constant. In this region the mobility, and hence the conductivity, varies as a function of temperature. In the higher temperature intrinsic regime, the

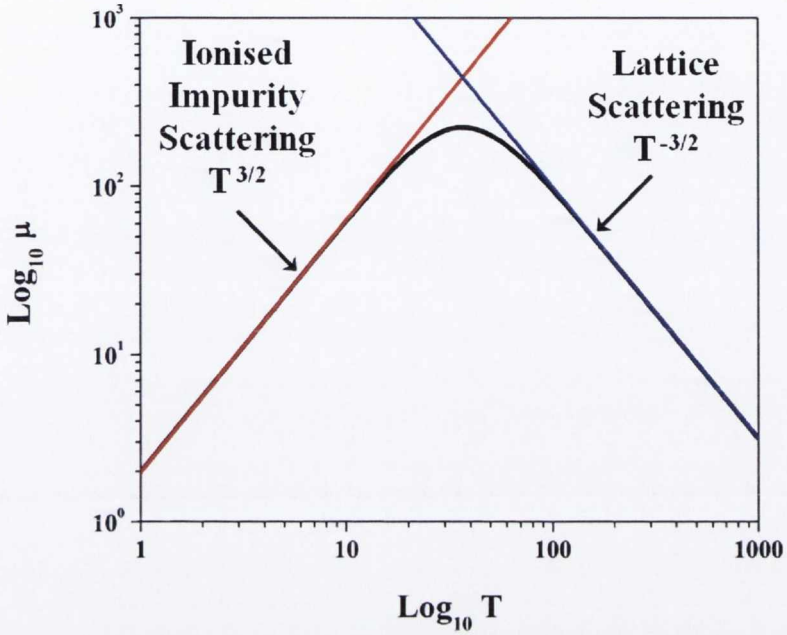

Figure 2.7: Theoretical temperature dependence of electron mobility.

contribution of the intrinsic carriers begins to dominate the conductivity. As temperatures tend towards absolute zero, the freeze-out regime sets in, and both electron concentration and conductivity are diminished with reducing temperature. In an intrinsic semiconductor, the electron and hole concentrations are equal, however their mobilities are not, therefore the intrinsic conductivity can be written as

$$\sigma_i = e(\mu_n + \mu_p)n_i \tag{2.32}$$

2.2.5.2 Carrier Diffusion

In the absence of an electric field, particles are induced to spread from a region of high concentration to one of low concentration. The motion of these electrically charged particles generates a diffusion current. The electron diffusion current density can be expressed in 1-dimension as

$$J_{ndif} = eD_n \frac{dn}{dx} \tag{2.33}$$

while the hole diffusion current density can be written

$$J_{pdif} = -eD_p \frac{dp}{dx} \tag{2.34}$$

where D_n and D_p are the electron and hole diffusion coefficients, $\frac{dn}{dx}$ and $\frac{dp}{dx}$ are the density gradients of the electron and hole concentrations respectively. The diffusion coefficients indicate the impact of a density gradient on the flux of current carriers.

The total current density is the sum of the current density terms for the current-inducing processes described above in the 1-dimensional case

$$J = en\mu_n\mathcal{E} + ep\mu_p\mathcal{E} + eD_n\frac{dn}{dx} + eD_p\frac{dp}{dx} \tag{2.35}$$

or in 3 dimensions

$$J = en\hat{\mu}_n\vec{\mathcal{E}} + ep\hat{\mu}_p\vec{\mathcal{E}} + eD_n\vec{\nabla}n + eD_p\vec{\nabla}p \tag{2.36}$$

Haynes and Shockley were the first to demonstrate drift and diffusion of minority carriers when they measured the minority carrier mobility, μ, and the diffusion coefficient, D, in an n-type semiconductor bar Haynes & Shockley (1951).

For a non-uniformly doped semiconductor in thermal equilibrium, the diffusion coefficient and the mobility are coupled according to the Einstein relation,

$$\frac{D_n}{\mu_n} = \frac{D_p}{\mu_p} = \frac{k_\mathrm{B}T}{e} \tag{2.37}$$

and both are highly temperature-dependent.

2.2.5.3 Generation and Recombination Processes

In thermal equilibrium the concentrations of electrons and holes in the CB and VB are independent of time and $pn = n_i^2$. Thermal processes, however, are continually at work exciting (generating) electrons directly from the VB to the CB, while other electrons are concurrently falling into the vacated states in the VB annihilating (recombining) both electron and hole and restoring equilibrium. In thermal equilibrium, the rate of generation of these electrons and holes must equal their rate of recombination. When an external excitation is applied to a semiconductor device, however, it no longer operates under equilibrium conditions, now $pn > n_i^2$, and excess electrons (holes) may exist in the CB (VB). This process is known as carrier injection. An abrupt increase of temperature or optical excitation by exposure to light can create or generate supplementary electrons and holes in excess of the thermal equilibrium concentrations.

As for the semiconductor in thermal equilibrium, the excess electrons may fall spontaneously from the CB to the VB in electron-hole recombination. The energy release upon recombination is either in the form of photon emission or heat dissipation. The former process is referred to as radiative recombination, and the latter as non-radiative recombination. These recombination

processes can be distinguished as either direct band-to-band recombination, which is prevalent in direct bandgap semiconductors, or indirect recombination which is encountered in indirect bandgap semiconductors.

Direct Recombination In thermal equilibrium, the straightforward direct band-to-band process for a direct bandgap semiconductor has already been described. With regard to the non-equilibrium case, the excess carrier electrons and holes introduced into a direct bandgap semiconductor are very likely to annihilate directly since the VB maximum and CB minimum are aligned at the same crystal symmetry position (k-value), and no further momentum is therefore required to facilitate the transition. The rate of direct recombination is proportional to the electron concentration and also to the hole concentration. Since excess electrons and holes are generated and recombine in pairs, their concentrations must be equal in order to preserve charge neutrality. Low-level carrier injection infers that the excess carrier concentration is greatly inferior to the thermal equilibrium majority carrier concentration. High-level carrier injection, on the other hand, is characterised by an excess carrier concentration that is on a par with or greater than the thermal equilibrium majority carrier concentration. In thermal equilibrium, the net recombination rate, $U = R - G_{th} = 0$, where R is the recombination rate, and G_{th} is the thermal equilibrium generation rate. However, for an n-type material undergoing low-level injection due to exposure to light, for example, the net recombination rate, is

$$U \equiv \frac{p_n - p_{n0}}{\tau_p} \tag{2.38}$$

where τ_p is the excess minority carrier lifetime,

$$\tau_p \equiv \frac{1}{\beta n_{n0}} \tag{2.39}$$

p_n is the non-equilibrium hole concentration, p_{n0} and n_{n0} are the thermal equilibrium hole and electron concentrations respectively, and β is the proportionality constant between the direct recombination rate, R, and the product of the overall hole and electron concentrations, pn,

$$R = \beta pn \tag{2.40}$$

Indirect Recombination Direct recombination proves difficult in indirect bandgap semiconductors since a change in crystal momentum is required to elicit a transition between the CB minimum and VB maximum, therefore indirect recombination processes are prevalent in such materials. These kinds of transitions are made possible by the presence of intermediate localised energy states or recombination centres within the bandgap.

Surface Recombination A high concentration of these localised energy states exist at the surface of a semiconductor due to discontinued or dangling bonds, thus recombination rates are greatly amplified in these regions. These surface states will be discussed in more detail in relation to semiconductor devices in chapter 6.

2.2.5.4 Continuity Equation

A semiconductor simultaneously experiences the processes of carrier drift, diffusion, and recombination, and the behaviour of such a system is described by the continuity equation which, in 1-dimension, expresses the net current flow into an infinitesimal thickness and the net carrier generation in that slice of material due to those processes subject to low-level injection. The linearised 1-dimensional continuity equation for minority carrier electrons in a p-type semiconductor is

$$\frac{\partial n_p}{\partial t} = n_p \mu_n \frac{\partial \mathcal{E}}{\partial x} + \mu_n \mathcal{E} \frac{\partial n_p}{\partial x} + D_n \frac{\partial^2 n_p}{\partial x^2} + G_n - \frac{n_p - n_{p0}}{\tau_n} \tag{2.41}$$

and for the minority carrier holes in an n-type semiconductor

$$\frac{\partial p_n}{\partial t} = -p_n \mu_p \frac{\partial \mathcal{E}}{\partial x} - \mu_p \mathcal{E} \frac{\partial p_n}{\partial x} + D_p \frac{\partial^2 p_n}{\partial x^2} + G_p - \frac{p_n - p_{n0}}{\tau_p} \tag{2.42}$$

The continuity equation in conjunction with Poisson's equation, together with the corresponding boundary conditions,

$$\frac{d\mathcal{E}}{dx} = \frac{\rho_s}{\epsilon_s} \tag{2.43}$$

where ϵ_s is the dielectric permittivity and ρ_s is the space charge density (the sum of the charge carrier densities and the ionised impurity concentrations), have an unique solution.

2.2.5.5 Ambipolar Transport

The excess electrons and holes injected under non-equilibrium conditions undergo the processes of diffusion, drift and recombination with the same effective diffusion coefficient, drift mobility and lifetime as one another, this behaviour is referred to as ambipolar transport. The assumption has, thus far, been that the electric field term, $\mathcal{E}$, arises solely from an external source and would cause the excess holes and electrons to drift apart from each other. However, since the excess carriers are charged, any separation between them will induce an internal electric field between the oppositely charged carriers attracting them towards one another. The electric field term is thus composed of an externally applied electric field together with an internal electric field,

$$\mathcal{E} = \mathcal{E}_{app} + \mathcal{E}_{int} \tag{2.44}$$

The ambipolar transport equation can be written as

$$D'\frac{\partial^2(\delta n)}{\partial x^2} + \mu'\mathcal{E}\frac{\partial(\delta n)}{\partial x} + G - R = \frac{\partial(\delta n)}{\partial t} \tag{2.45}$$

where δn is the excess carrier concentration, the ambipolar diffusion coefficient, D' is

$$D' = \frac{\mu_n n D_p + \mu_p p D_n}{\mu_n n + \mu_p p} \tag{2.46}$$

and the ambipolar mobility, μ' is

$$\mu' = \frac{\mu_n \mu_p (p - n)}{\mu_n n + \mu_p p} \tag{2.47}$$

The Einstein relation enables the ambipolar diffusion coefficient to be written

$$D' = \frac{D_n D_p (n + p)}{D_n n + D_p p} \tag{2.48}$$

2.3 Magnetic Field Effects

In the course of this dissertation, the behaviour of semiconductors under the influence of applied magnetic fields will be used to characterise these materials and also to examine their response. A brief description of the effects of the application of a magnetic field on a semiconductor is therefore required. This description will be carried out in c.g.s units for historical reasons.

The charge carriers of a metallic or semiconducting material, subject to an applied electric field, $\boldsymbol{\mathcal{E}}$, and an applied magnetic field, $\mathbf{B}$, will experience the Lorentz force,

$$\mathbf{F} = \frac{q}{c}(\boldsymbol{v} \times \mathbf{B}) \tag{2.49}$$

where $q = -e$ for electrons, and $q = +e$ for holes, and their motion will be governed by the Langevin equation,

$$\frac{d\boldsymbol{v}}{dt} = -\frac{e}{m^*}(\boldsymbol{\mathcal{E}} + \frac{1}{c}\boldsymbol{v} \times \mathbf{B}) - \frac{\boldsymbol{v}}{\tau} \tag{2.50}$$

where $\boldsymbol{v}$ is the average velocity and τ is the relaxation time. If the electric and magnetic fields are applied parallel, the electron will follow a helical path along the same direction. The Lorentz force deflects the electron in the plane perpendicular to $\mathbf{B}$ causing this cyclic motion. As the electron moves, however, it suffers collisions with impurities that restrict its velocity and introduce a drift current parallel to $\boldsymbol{\mathcal{E}}$.

2.3.1 Hall Effect

A current accelerating under an electric field, subject to a perpendicular applied magnetic field, experiences the same Lorentz force normal to the direction of both the magnetic field and the velocity of the charge carriers. A proportion of the charge is deflected, and this effect, first observed in 1879 Hall (1879), can be used to determine the sign of the majority charge carrier, the majority carrier concentration, and the mobility in a semiconductor.

The electric field, $\mathcal{E}$, is related to the conductivity, $\hat{\sigma}$, and resistivity, $\hat{\rho}$, tensors in the absence of a magnetic field as follows

$$\mathbf{j} = \hat{\sigma} \cdot \mathcal{E} \tag{2.51}$$

and

$$\mathcal{E} = \hat{\rho} \cdot \mathbf{j} \tag{2.52}$$

where the current density,

$$\mathbf{j} = -ne\boldsymbol{\nu} \tag{2.53}$$

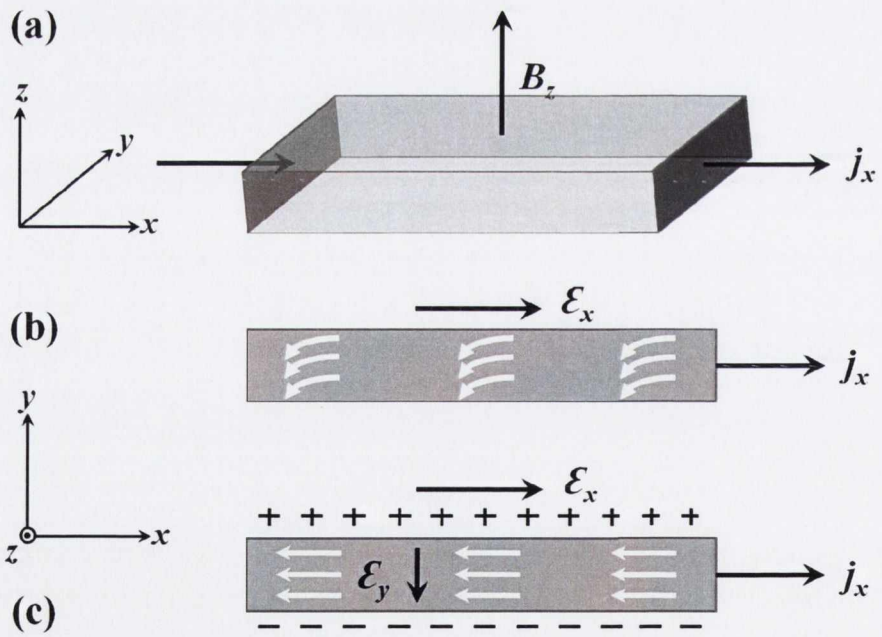

Figure 2.8: The Hall effect

Assuming the semiconductor layer is in the x-y plane, and the magnetic field, $\mathbf{B}$, is applied along the z-axis, if the electric field, $\mathcal{E}_x$, is applied in the x-direction, as in fig. 2.8 (a), in the

steady state the conductivity tensor reduces to

$$\sigma_0 \mathcal{E}_x = j_x + \omega_c \tau j_y \tag{2.54}$$

$$\sigma_0 \mathcal{E}_y = -\omega_c \tau j_x + j_y \tag{2.55}$$

Under the Drude model, σ_0 is the Drude conductivity

$$\sigma_0 = \frac{ne^2\tau}{m^*} \tag{2.56}$$

and ω_c is the cyclotron frequency

$$\omega_c = \frac{eB}{m^* c} \tag{2.57}$$

As the Lorentz force acts to deflect the charge carriers, they accumulate along the sides of the sample inducing an electric field, $\mathcal{E}_y$, in opposition to the Lorentz force which at some point exactly balances it, this is illustrated in fig. 2.8 (b) and (c).

The conductivity tensor is constructed

$$\hat{\sigma} = \begin{pmatrix} \sigma_{xx} & \sigma_{xy} \\ \sigma_{yx} & \sigma_{yy} \end{pmatrix} \tag{2.58}$$

where σ_{xx} are the longitudinal, and σ_{xy} the transverse components of the conductivity tensor Ashcroft & Mermin (1976), the resistivity tensor is treated similarly. We obtain the conductivity equations

$$\sigma_{xx} = \sigma_{yy} = \frac{\sigma_0}{1 + (\omega_c \tau)^2} \tag{2.59}$$

$$\sigma_{xy} = -\sigma_{yx} = -\frac{\sigma_0 \omega_c \tau}{1 + (\omega_c \tau)^2} \tag{2.60}$$

The transverse conductivity component can be written in the form

$$\sigma_{xy} = -\frac{\sigma_0}{\omega_c \tau} + \frac{1}{\omega_c \tau} \sigma_{xx} \tag{2.61}$$

In a strong magnetic field, and at low temperature, $\omega_c \tau \gg 1$, in these conditions the transverse current density, j_y, is balanced by the Lorentz force, and

$$\mathcal{E}_y = -\left(\frac{\omega_c \tau}{\sigma_0}\right) j_x \tag{2.62}$$

The longitudinal conductivity approaches the limit $\sigma_{xx} = 0$, and the transverse components give the Hall conductivity and Hall resistivity respectively as follows

$$\sigma_H = \sigma_{xy} = -\frac{nec}{B} \tag{2.63}$$

and

$$\rho_H = \rho_{xy} = -\frac{B}{nec} \tag{2.64}$$

where $R_H = -1/nec$ is the Hall coefficient.

2.3.2 Magnetoresistance

Magnetoresistance, first observed by Lord Kelvin Thomson (1857), and which is closely related to the Hall effect, presents as a change in resistance upon application of a magnetic field, **B**, due to the effect of the Lorentz force. Ordinary magnetoresistance is defined as

$$\frac{\Delta\rho}{\rho_0} = \frac{\rho_B - \rho_0}{\rho_0} \tag{2.65}$$

The longitudinal magnetoresistance is measured when **B** is applied parallel to the direction of the current, **j**. Conversely, the transverse magnetoresistance is measured with **B** applied perpendicular to **j**, this can vary markedly with the field. The longitudinal components of the conductivity and resistivity tensors, defined in the previous section, give the magnetoconductivity and magnetoresistivity respectively.

It has previously been mentioned that the Lorentz force induces electrons to move in a circular or helical orbit. The deflection of a charge carrier can be expressed as the ratio of the mean free path, λ_{mfp}, to the radius of curvature, r, for the carrier in the magnetic field

$$\frac{\lambda_{mfp}}{r} = \omega_c\tau = tan\theta_H \tag{2.66}$$

where θ_H is the angle between the current density, **j**, and the electric field, $\mathcal{E}$, and ω_c, the cyclotron frequency, is the angular frequency of revolution of the charge carrier. The ratio of magnetic field to resistance depends on the number of orbits the electrons can complete between collision events. Thus $\omega_c\tau$ is a measure of the deformation of the electronic orbits in the material due to the magnetic field.

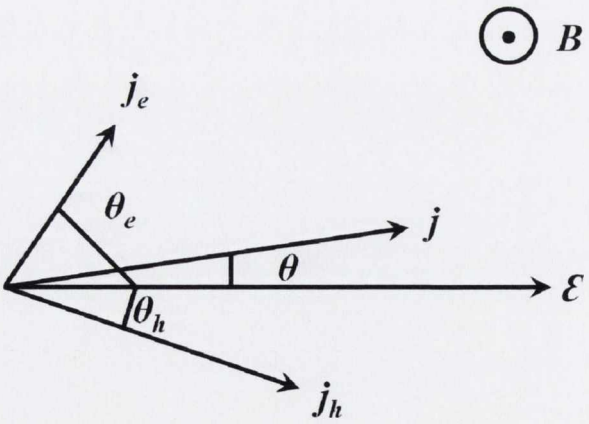

Figure 2.9: The electron and hole current density contributions and their Hall deflection angles, under the Two-Band model.

Calculation of magnetoresistance is more complicated than the Hall effect, since the free electron model will result in zero magnetoresistance. The Hall electric field cancels the Lorentz force due to the magnetic field, leaving ρ_{xx} independent of B. To remedy this situation, it is necessary to introduce two kinds of carriers, for example, electrons and holes or open and closed orbits, so that two drift velocities are introduced into the model. This technique is the customary model for analysing magnetoresistance, and it is known as the two-band model for magnetoresistance. The current density, $\mathbf{j}$, can be split into two distinct current densities, for electrons, $\boldsymbol{j_e}$, and for holes, $\boldsymbol{j_h}$, say. Similarly, the two carrier types are deflected by different Hall angles, θ_e and θ_h, as shown in fig. 2.9. The conductivity tensor for each band can be written as follows

$$\hat{\sigma}^i = \begin{pmatrix} \sigma^i_{xx} & \sigma^i_{xy} \\ \sigma^i_{yx} & \sigma^i_{yy} \end{pmatrix} \tag{2.67}$$

where $i = 1, 2$ correspond to the electron and hole bands respectively. The resistivity tensor can be calculated from this, since the scalar product of the two tensors is the identity

$$\hat{\sigma} \cdot \hat{\rho} = I \tag{2.68}$$

Using the expression for $tan\theta_H$, an expression can be derived for the magnetoresistance.

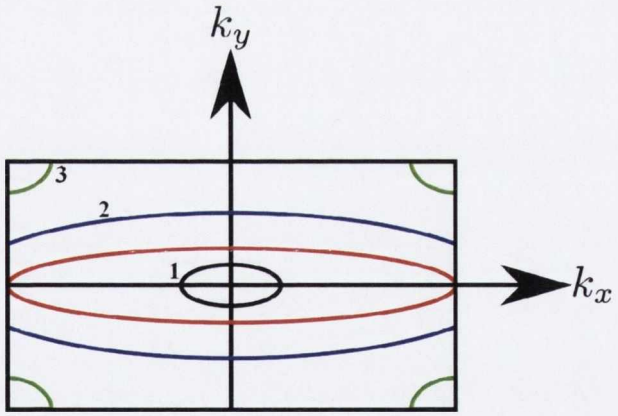

Figure 2.10: The Fermi surface in 2-dimensional Brillouin zone showing 1. closed orbit, 2. open orbit and 3. hole orbit.

There is no unique law deciding the magnetoresistance behaviour of materials, since there can be a number of contributing factors that are beyond the scope of this dissertation, however some general trends can be recognised from the various contributions to the magnetoresistance behaviour. Two magnetoresistance characters that can be identified according to the two-band model are the closed orbit and open orbit magnetoresistance effects. For crystals with a closed

Fermi surface that does not come in contact with the Brillouin zone boundary, carriers move along closed orbits, as shown in fig. 2.10. When the Fermi surface is in contact with the Brillouin zone boundary, on the other hand, the electrons travel in open orbits. In low magnetic fields it is not necessary to distinguish between open and closed orbits, since even a closed orbit ($\omega_c \tau \ll 1$) electron will have been scattered before it has completed a full cycle. Low magnetic fields elicit a positive magnetoresistive response that varies quadratically with the field for both closed and open orbit bands. Unlike open orbit magnetoresistance, however, closed orbit magnetoresistance saturates at high fields and can be described according to the relation

$$\frac{\Delta\rho^c}{\rho} = \frac{aB^2}{b + cB^2} \tag{2.69}$$

where the parameters a, b and c are related to the partial conductivities, σ^1 and σ^2, of the contributing electron and hole bands respectively. Open orbit magnetoresistance does not saturate at high fields. Although most magnetoresistance behaviour is typically positive, negative magnetoresistance effects related to impurity conduction and magnetic scattering have been observed in semiconductors Stamenov (2007).

2.4 Transparent Conducting Oxides

In the commercially recognised TCOs, the property of transparency permits optical access in the visible spectrum, while the conductivity can provide large area-electrical contact. This combination of properties is traditionally achieved in wide-bandgap oxides that become degenerate through the substitution of dopant ions, or native defects, while sustaining a conduction band minimum (n-type), or a valence band maximum (p-type), whose dispersion establishes a plasma-absorption edge in the infrared region of the optical spectrum, but maintains its wide energy bandgap (> 3 eV) Lewis & Paine (2000). The IR end of the transparency window is delimited by the plasma frequency which depends on the carrier concentration and the carrier effective mass, and will be defined in the next section.

Wide bandgap compounds are generally utilised as insulators, dielectrics, and optical materials in industry, however some of these materials exhibit considerable conductivity. The oxides of heavy-metal cations with electronic configuration ns^0, such as ZnO, CdO, Ga_2O_3, In_2O_3, Tl_2O_3, SnO_2, PbO_2, Sb_2O_5, and their mixed oxides all become n-type conductors upon electron doping Kawazoe *et al.* (2000). The electrical conduction mechanism operating in ITO, for example, is attributed to the presence of shallow donor impurity states, due to the substitution of Sn^{4+} donor ions for

In^{3+} in the lattice, situated in close proximity to the conduction band of the host compound Edwards *et al.* (2004). High levels of donor electrons are thermally ionised at room temperature and promoted to the degenerate conduction band structure inducing a plasma absorption in the far-infrared, but maintaining the fundamental wide bandgap. A schematic of the energy-band model for ITO is shown in fig. 2.11.

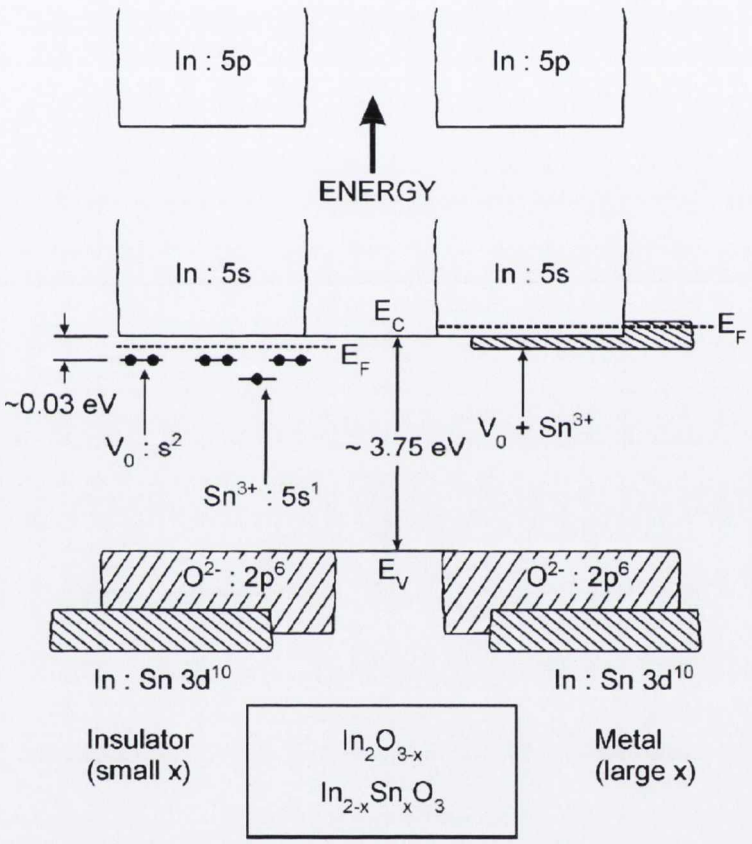

Figure 2.11: Energy-band model for $In_{2-x}Sn_xO_3$ with low-level doping (small x) and high-level doping (large x) adapted Edwards *et al.* (2004) from Fan & Goodenough (1977).

A profound understanding of the fundamental aspects of transparent semiconductors is required in order to improve either the properties of existing materials, or to design new types of TCOs. These insights are of great scientific importance whether or not the realisation of high-performance TCO hetero- and homo-junctions is possible. A vast amount of literature is available on different TCOs deposited by various growth techniques and their fundamental aspects, and some review articles concerning these issues have also been published Chopra *et al.* (1983) Exarhos & Zhou

(2007).

2.4.1 Electrical Properties of Transparent Conducting Oxides

The drift conductivity of carriers in a transparent conducting oxide is proportional to both the carrier concentration and mobility, as stated previously. Wide bandgap metal-oxide semiconductors typically have valence bands that are dominated by low-lying O $2p$ levels. Holes tend to become localised on the O^{2-} ions owing to their high electronegativity, and thus the hole mobility tends to be low. The low energy oxygen levels in the valence band, however, are responsible for the large bandgap in TCOs and hence their transparency. The bottom of conduction bands, on the other hand, are typically composed of cation s bands that are highly dispersed, and although these materials would not be conductors in their stoichiometric compositions, doping and non-stoichiometry can achieve high mobility charge carriers. At sufficiently high (donor) doping concentrations, the TCO becomes degenerate and the donor impurity level overlaps and merges with the conduction band minimum at room temperature giving rise to conduction electrons. The critical doping concentration, n_c, at which this transition from insulator to conductor occurs, can be estimated according to Mott's criterion Mott (1990)

$$n_c^{1/3} a_H^* = 0.26 \pm 0.05 \tag{2.70}$$

where a_H^* is the Bohr radius defined

$$a_H^* = \frac{\hbar}{m^*(e^2/\epsilon)} = \frac{a_0 \epsilon}{(m^*/m_0)} \tag{2.71}$$

where m^* is the carrier effective mass, a_0 is the hydrogen Bohr radius, m_0 is the hydrogen free electron mass and ϵ is the relative permittivity Edwards *et al.* (2004). Above n_c, the material is degenerately doped, the donor levels merge with the conduction band at room temperature, and create an effective free electron gas in accordance with the Drude model Drude (1900a) Drude (1900b). A consequence of the degenerate donor doping concentration, $n > n_c$, is that the plasma frequency, ω_p, for a free electron gas Ashcroft & Mermin (1976) defined as

$$\omega_p = \sqrt{\frac{n \cdot e^2}{\epsilon_0 \epsilon_\infty m^*}} \tag{2.72}$$

is shifted to higher energy, and plasma absorption begins to encroach upon transmission in the visible window of the spectrum, hence removing the transparency.

Electron densities are in general high for n-type TCOs, of the order $n \sim 10^{20}$ cm^{-3}, resulting in degenerate electron systems. The dispersion at the band edges can be approximated by parabolic

functions in these materials. The electrical conductivity is dominated by scattering mechanisms, which are strongly related to the electron concentration. All electronic scattering contributions together influence the mobility, and determine the upper limit of conductivity. For single-crystalline materials the ionised impurity scattering is considered to be the most important. Though, as the degree of crystallinity of the thin films decrease, the contribution of grain boundaries becomes ever more important in polycrystalline films.

2.4.2 Optical Properties of Transparent Conducting Oxides

2.4.2.1 Transparency

An important feature of TCOs is the existence of a transmission window covering most part of the visible spectrum, as illustrated in fig. 2.12. In the literature, the optical transmission is defined as the ratio between incoming light intensity and transmitted intensity averaged over all values in the visible range, between 400 nm and 700 nm, and the optical transparency is a percentage expression of this ratio. The transmission window is defined by two regions where no light is transmitted due to the two following phenomena.

TCOs are only transparent in the visible and near-infrared range between wavelengths of about $\lambda_g \sim 0.4$ and $\lambda_p \sim 1.6$ μm. For very short wavelengths ($\lambda < \lambda_g$) absorption is observed due to the fundamental energy gap. Photons of these wavelengths have energies in the UV range of the spectrum that are approximately equal to the bandgap energy ($3 - 4$ eV), they are absorbed to incite band-to-band transitions, and no light is transmitted. For long wavelengths ($\lambda > \lambda_p$), in the near IR range, high reflection occurs due to the plasma absorption edge as defined earlier under the Drude model Ashcroft & Mermin (1976).

Under the free electron model, the interaction of the electromagnetic field with the conduction electrons influences ϵ, the relative permittivity of the TCO material, a complex number, which is defined as follows

$$\epsilon(\omega) = (N(\omega) - i\kappa(\omega))^2 \tag{2.73}$$

where N is the real refractive index, and κ is the imaginary extinction coefficient. In the vicinity of the plasma frequency, ω_p, the reflectance and absorbance of the material are determined by these parameters. When $\omega < \omega_p$, the extinction coefficient dominates and the material is almost completely reflective. Approaching the fundamental absorption edge, λ_g, the reflectance becomes zero, and the absorption coefficient, α, can be deduced from the transmission curve as a function of the wavelength.

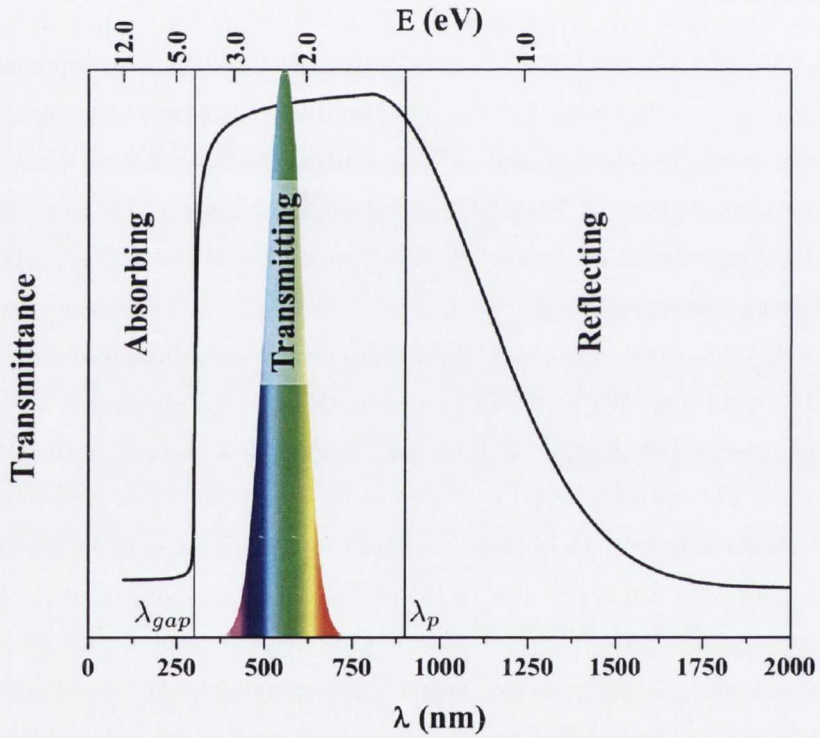

Figure 2.12: Optical transmission spectrum showing both the band edge and plasma edge.

The transmittance, T, and reflectance, R, data can be used to calculate absorption coefficients of the films at different wavelengths. The absorption coefficient, α, is given by the relation $\alpha = (1/d)\ ln[(1-R)^2/T]$ where d is the film thickness. The absorption coefficient data can be used to determine the bandgap, E_g, using the relation $\alpha h\nu = (h\nu - E_g)^{1/2}$ where $h\nu$ is the photon energy.

Both the fundamental bandgap and plasma absorption depend on the carrier density and the effective mass, which can be influenced by deposition conditions such as doping level, substrate deposition temperature, oxygen deposition pressure, and film thickness. In general, both edges shift toward lower wavelengths (higher energies) with increasing carrier density of the TCO film. The effect of reduced resistivity in SnO_2 thin films on the optical transmission spectrum is shown in fig. 2.13. The electrical resistivity of common n-type materials is around 10^{-4} Ωcm, whereas the transmission can be as high as 90 % in the visible regime. While the high transparency of the n-types has also been observed in the p-type TCOs, their conductivity is in general at least a factor of 1000 lower.

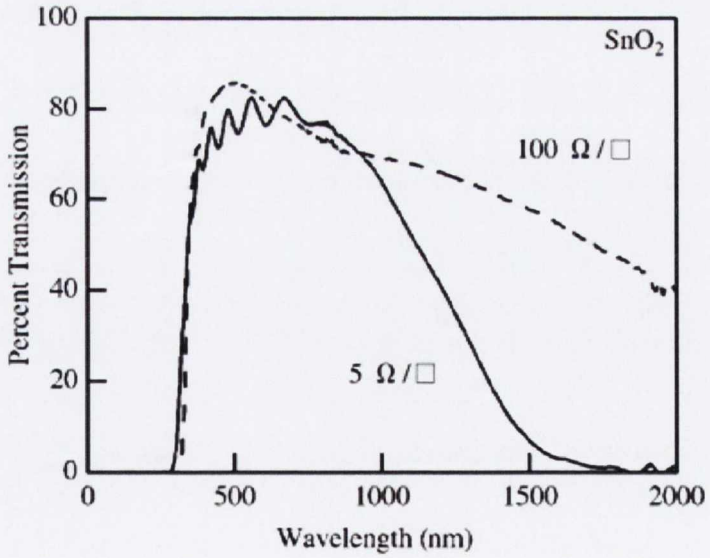

Figure 2.13: Optical transmission spectrum of two SnO_2 thin films with different resistivities Ginley & Bright (2000).

2.4.3 Combining Electrical and Optical Properties

2.4.3.1 Intrinsic Conductivity Limit

The primary contributors to scattering in extrinsic semiconductors, phonon scattering and ionised impurity scattering, have already been discussed with regard to carrier drift. Scattering in crystalline TCOs has been observed to be predominantly due to ionised impurity scattering Chen *et al.* (2000) Hamberg & Granqvist (1985). Scattering of the mobile carriers due to Coulomb interactions with the ionised donors/acceptors is a process that is inherent to these extrinsic conductors. In this way ionised impurity scattering can be seen conceptually to limit the conductivity achievable in TCOs. Brooks Brooks (1955) and Dingle Dingle (1955) independently calculated the resistivity for an electron gas of density n using this Coulombic interaction to be

$$\rho = \frac{N_i Z^2 e^2 m^{*2}}{24\pi^3(\epsilon_0\epsilon)^2 h^3 n^2} f(k_F) \tag{2.74}$$

where N_i is the concentration of impurity centres with charge Ze, ϵ is the relative permittivity at low frequency, m^* is the electron effective mass in the CB, and

$$f(k_F) = [ln(1+\beta^2) - \beta^2/(1+\beta^2)] \tag{2.75}$$

where $\beta = 2k_F/\kappa_{TF}$, and κ_{TF} is the Thomas-Fermi screening wave vector,

$$\kappa_{TF} = \left(\frac{3n}{\pi^4}\right)^{1/3} \frac{m^* e^2}{\hbar^2 \epsilon_s \epsilon_0} \tag{2.76}$$

where ϵ_s is the static dielectric constant.

The intrinsic performance limits in the doped In_2O_3, SnO_2 and ZnO TCO systems have been studied and found to depend mainly on ionised impurity scattering which sets a lower limit to the resistivity for an arbitrary doping concentration Bellingham *et al.* (1992). The added requirement of transparency in TCOs sets a further limit on the carrier concentration, n, and hence the attainable conductivity, due to the criterion that the plasma frequency, $\omega_p \propto \sqrt{n}$, cannot impinge on the visible spectrum Chen *et al.* (2000).

Aside from the intrinsic limitations upon TCO materials, it has also been pointed out that additional scattering mechanisms can arise due to processing conditions. Thin film depositions at low temperatures, for example, can result in reduced crystallinity in samples, an effect that may incur grain boundary scattering in these materials. The grain sizes within polycrystalline thin films are smaller than those within single crystalline samples, this translates to large densities of grain boundaries. In general, these boundaries, which correspond to dangling bonds, contain large

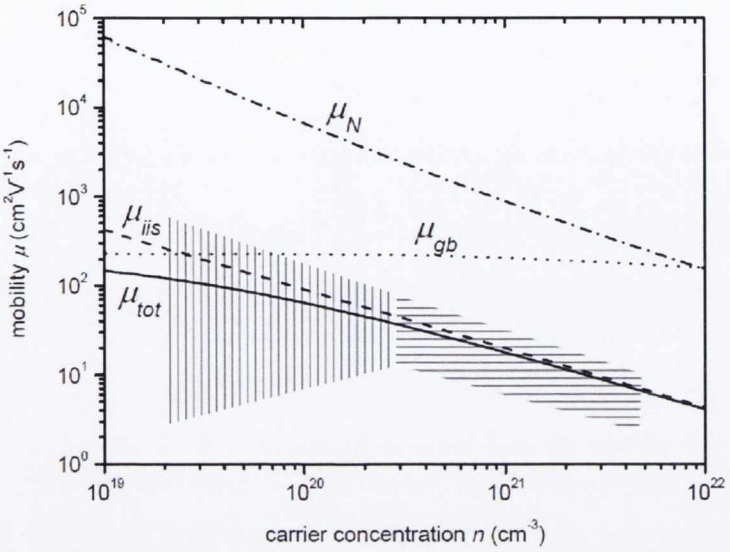

Figure 2.14: The upper mobility limit, μ_{tot}, indicated by the solid line, taking account of ionised impurity scattering, μ_{iis}, grain boundary scattering, μ_{gb}, and neutral impurity scattering, μ_N Dekkers (2007). The striped regions indicate the variations in reported data.

concentrations of interface states that tend to trap free carriers from the grain. A space charge region forms around the trapped charges at the grain boundary creating a potential barrier to charge transport. The impact of grain boundary scattering on mobility can be expressed

$$\mu_{gb} = \mu_0 exp\left(-\frac{\Phi_{gb}}{k_B T}\right) \tag{2.77}$$

where

$$\mu_0 = \left(\frac{L^2 e^2}{2\pi m^* k_B T}\right)^{1/2} \tag{2.78}$$

such that L is the grain size and Φ_{gb} is the grain boundary potential Petritz (1956). Grain boundary scattering will only affect the mobility if the grain size and the carrier mean free path are of the same scale. High level impurity substitution in samples can also conceivably induce neutral impurity scattering to occur in these degenerately doped TCOs for concentrations above the solubility limit, however this has a negligible effect on the overall mobility. The contributions of these scattering mechanisms to the upper limit of the mobility is shown in fig. 2.14.

2.4.3.2 Figure of Merit

A system has been devised to rate the performance of a transparent conducting oxide in terms of its electrical and optical properties. The ratio of the conductivity, α, to the optical absorption

coefficient, α, of the material is regarded as a figure-of-merit to gauge the efficacy of a TCO Exarhos & Zhou (2007). This quantity, which is dependent upon wavelength, is defined as follows

$$\frac{\sigma}{\alpha} = -R_s ln(T + R)^{-1} \tag{2.79}$$

where R_s is the sheet resistance, T is the total visible transmittance and R is the total visible reflectance. A larger value of σ/α indicates a higher performing TCO Gordon (2000).

2.4.4 *p*-Type Transparent Conducting Oxides

The first report of a p-type TCO was NiO Sato *et al.* (1993) in 1993. A 110 nm thick film showed a conductivity of 0.14 Scm^{-1} and 40 % transmission of visible light. A transparent rectifying junction was prepared by combining *p*-type NiO with *n*-type ZnO Sato *et al.* (1993). In 1997 there was a report of transparent *p*-type conducting films of $CuAlO_2$, a compound presenting with a delafossite structure, showing considerable improvement over NiO. The conductivity of 1 Scm^{-1}, however, was still about three orders of magnitude smaller than that of typical *n*-type materials. Since then, a number of promising *p*-type materials have been found as a consequence of material exploration efforts following the chemical modulation of the valence band (CMVB) design concept, which will be discussed later in this section. Work by the groups of Kawazoe and Hosono over the last few years has led to the description of a number of *p*-type TCOs Kawazoe *et al.* (1997); Kudo *et al.* (1998); Yanagi *et al.* (2000c, 2001a) based on Cu^+-bearing oxides. The discovery of *p*-type TCOs has led this class of material to the frontier of transparent oxide semiconductors. It thus becomes possible to fabricate transparent *p*-*n* junctions using an appropriate combination of *p*-type and *n*-type TCOs. Realisation of a *p*-*n* homojunction using a bipolar TCO would introduce the possibility of "invisible circuits" based on transparent oxides.

2.4.4.1 *p*-Type TCO Engineering

Chemical Modulation of the Valence Band It is difficult to prepare wide band gap binary metal oxides with *p*-type conductivity. In general, the top of the valence band of most of these oxides is dominated by closed shell $2p^6$ oxygen states. Because of the large electronegativity of oxygen, the valence band edge is strongly localised on the non-bonding oxygen $2p$ states. O $2p$ levels are far lower lying than the valence orbit of metallic atoms Fraga *et al.* (1976), leading to the formation of deep acceptor levels that trap the holes. The top of the valence bands in these wide band gap oxides, tend to have only slight dispersion Arnold *et al.* (2009), so that even when *p*-type doping is achieved, the hole effective masses are very large. The holes cannot

migrate within the crystal even under an applied electric field, resulting in poor conductivity and hole mobility. Kawazoe *et al.* proposed a possible solution, their approach is called "Chemical Modulation of the Valence Band (CMVB)" Kawazoe *et al.* (2000). The rationale behind the concept is that by introducing a "degree of covalency" in the metal oxygen bondings an extended valence band structure will form, where the valence band edge would be modified by mixing orbitals of appropriate counter cations that have filled energy-levels comparable to the O $2p$ level. This would reduce the strong coulombic force exerted by oxygen ions thereby delocalising the holes.

Investigations showed that the required cationic species are, among others, the $3d^{10}$-closed shell of Cu^{+} ions and $4d^{10}$-closed shell of Ag^{+} ions DeVault (1944); Kawazoe *et al.* (2000) which are degenerate with the O $2p$ states. The metal states interact with some of the O $2p$ states giving rise to increased band dispersion above the non-bonding O $2p$ or Cu $3d$ states, for example, and reducing the effective mass of the valence band maximum. Although some transition metal cations with an open d-shell may fulfil the energy requirement Bailar *et al.* (1973) for CMVB technique they usually show strong colouration due to a d-d transition, which is not desirable for transparent materials. Hence the focus has been concentrated towards the cations mentioned above, with closed ($d^{10}s^{0}$) electronic configuration. Fig.2.15 shows a schematic illustration of CMVB concept. Both of the atomic orbitals are occupied by electron pairs, and the resulting antibonding level becomes the highest occupied level, i.e. the valence band edge.

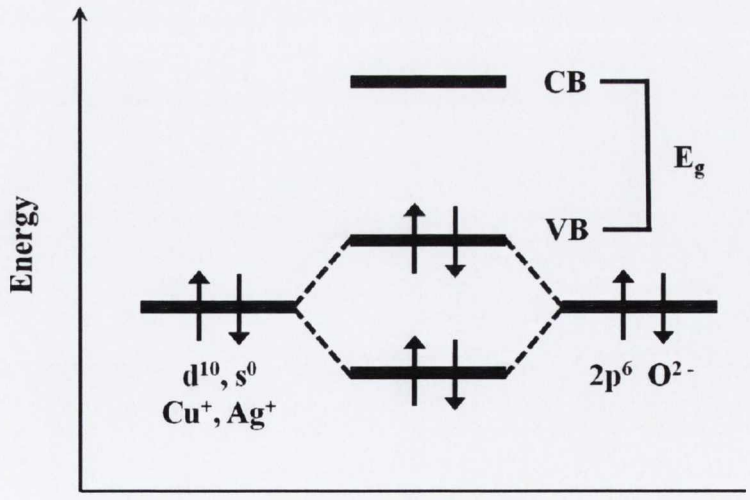

Figure 2.15: Schematic of the chemical bond between an oxide ion and a cation that has a closed shell electronic configuration. The energy of the closed shell electrons on the cation is assumed to be equivalent to that of O 2p electrons.

Next is the structural requirement for designing p-TCO materials. Tetrahedral coordination of oxide ions is advantageous for p-type conductivity, as it acts to reduce the localisation behavior of $2p$ electrons on oxide ions Kawazoe *et al.* (2000). The valence state of the oxide ions can be expressed as sp^3 in this conformation. Eight electrons (including $2s^2$) on an oxide ion are distributed in the four σ bonds with the coordination cations. This electronic configuration reduces the non-bonding nature of the oxide ions and increases the delocalisation of holes at the valence band edge.

Linearly Coordinated Cu^+ Oxides As we are interested in transparent conducting oxides, the bandgap of the material should be greater than 3.1 eV. The binary oxide Cu_2O is a p-type conducting oxide with quite a small bandgap of 2.17 eV Nikitine *et al.* (1961). The conduction band minimum of Cu_2O is dominated by Cu s states with a broad bandwidth Kleinman & Mednick (1980). Interactions between Cu s and O p levels and also mutual Cu s interactions on adjacent atoms are responsible for the breadth of the conduction band and therefore the reduced bandgap Kawazoe *et al.* (1997). The Cu_2O structure consists of a network of inter-penetrating O-Cu-O chains on a tetrahedral lattice, with Cu ions coordinated to six further Cu ions in the crystal Robertson *et al.* (2002). Lowering the dimension of cross-linking of Cu^+ ions should suppress these interactions. This led researchers to consider an aluminate of Cu^+, $CuAlO_2$, with the delafossite structure. Local symmetries around Cu^+ and O^{2-} ions in this phase are the same as those in Cu_2O, except that the nearest-neighbouring cations of the oxide ion are one Cu^+ and three Al^{3+} in the delafossite. The structure can be viewed as a layer structure with the sequence Cu-O-Al-O-Cu along the c-axis, and the 3-dimensional cross-linking of the Cu^+ network is reduced to 2-dimensional. This will give rise to a larger bandgap for the delafossite than for Cu_2O. Two families of Cu-based TCOs have been developed from this $CMVB$ technique, $CuMO_2$ ($M = Al, Ga, In, Sc$, etc.) with the delafossite structure and the non-delafossite structure $SrCu_2O_2$, $LaCuOCh$ ($Ch =$ chalcogen) Sheng *et al.* (2006).

Orgel proposed a d-s hybridised orbital model for linearly coordinated d^{10} ions such as Cu^+, Ag^+, Au^+ and Hg^{2+} Orgel (1966). Since the d^{10} ions have filled d orbitals, one would expect spherical electron-density distributions in these ions Ishiguro *et al.* (1983). However, since the energy difference between $3d$ and $4s$ orbitals is small, a symmetric displacement of anions can conceivably bring about a mixing of the d and s orbitals if the stabilisation due to the mixing can more than compensate for the energy lost through the distortion Orgel (1958). The $3d_{z^2}$, whose lobes extend toward the ligands in two-fold coordination, and the empty $4s$ orbitals in Cu_2O, for example, can thus form hybridised $\Psi_{d-s} = 1/\sqrt{2}(d_{z^2} - s)$ and $\Psi_{d+s} = 1/\sqrt{2}(d_{z^2} + s)$ orbitals, as illustrated

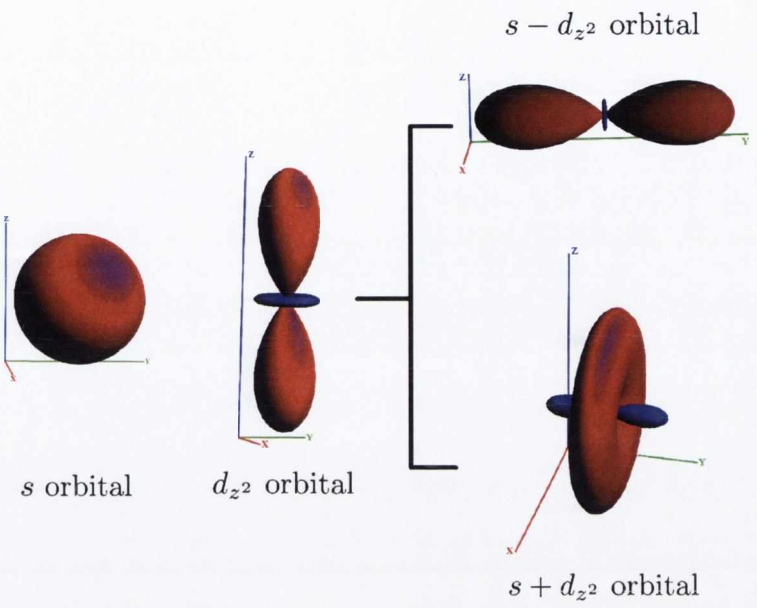

Figure 2.16: Schematic of the s and d_{z^2} orbitals and their linear combinations.

in fig. 2.16. The former orbital is mainly in the x-y plane, while the latter has dominant lobe contributions in the direction of the anion ligands, therefore linear coordination can be stabilised, with empty Ψ_{d+s} orbitals and filled Ψ_{d-s} orbitals, by aspherical electron configurations Ishiguro *et al.* (1983). Anisotropic electrical conductivity observed in delafossite $A^+B^{3+}O_2$ compounds has since been attributed to the d-s hybridisation of the A^+ ions Rogers *et al.* (1971) under the premise that electron transfer can occur via the overlap between non-bonding Ψ_{d-s} orbital, while the Ψ_{d+s} orbital is used to bond to the O^{2-} ions. The band diagram illustrating the chemical bond between the O^{2-} and the A^+ ion (where $A^+ = Cu^+$) in the delafossite compound is shown schematically in fig. 2.17.

2.4.5 Introduction to the Delafossite Family

2.4.5.1 History of the Delafossites

In 1873, Friedel first noted the existence of the compound $CuFeO_2$, shown in fig. 2.18 during the analysis of a mineral sample from Siberia Friedel (1873). The mineral was named delafossite in honour of the French mineralogist and crystallographer Gabriel Delafosse. Later work by Rogers confirmed the existence of the mineral in a number of copper mines in America Rogers (1913, 1922). The crystal structure of delafossite was established first by Soller and Thompson Soller &

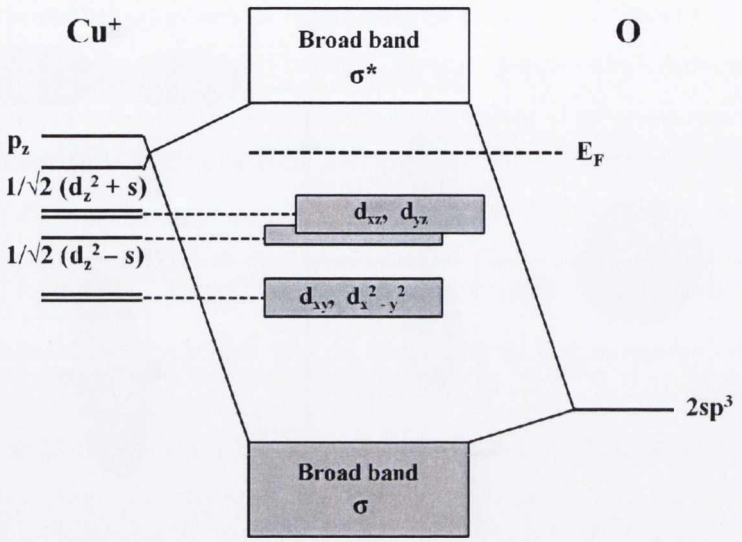

Figure 2.17: Schematic of the chemical bond between an oxide ion and a cation that has a closed shell electronic configuration. The energy of the closed shell electrons on the cation is assumed to be equivalent to that of O 2p electrons.

Thompson (1935) using a synthetically prepared sample and later by Pabst Pabst (1946) using a mineral sample.

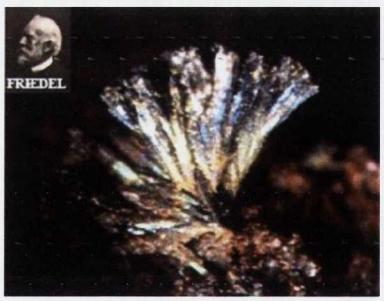

Figure 2.18: $CuFeO_2$ mineral with the delafossite structure discovered by Friedel.

A series of significant papers by Shannon, Rogers, and Prewitt detailed the synthesis, crystal structure, and electrical transport properties of a large family of compounds with the delafossite structure (e.g. $PtCoO_2$, $PdCoO_2$, $CuFeO_2$, and $AgFeO_2$) Prewitt *et al.* (1971); Rogers *et al.* (1971); Shannon *et al.* (1971). However, the crystal structure of cuprous chromite, $CuCrO_2$, single crystals had already been reported Dannhauser & Vaughan (1955).

The group of compounds possessing the $A^{1+}B^{3+}O_2$ chemical formula, of which the delafossite

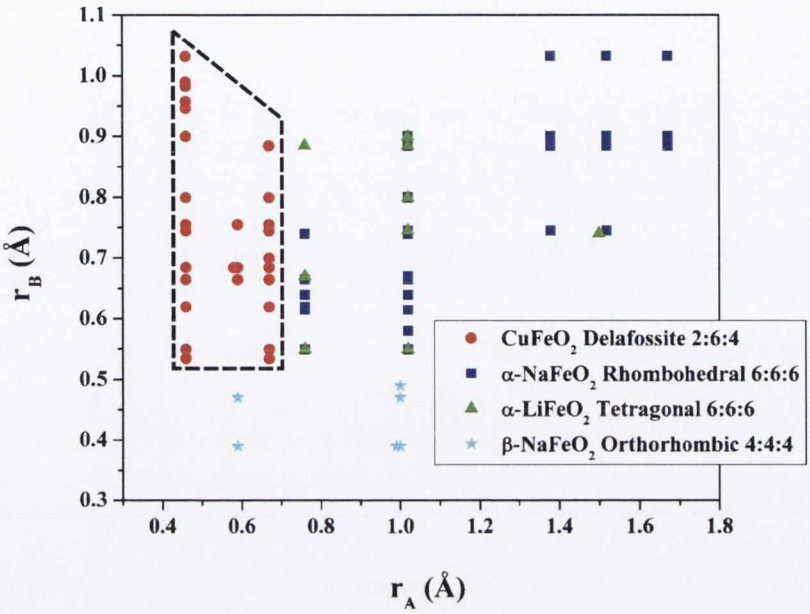

Figure 2.19: Sorting Map of ABO_2 compounds Shannon (1976).

structure is a member, can crystallise in the following prototype structures[1] Rogers *et al.* (1971),

- the $A^{VI}B^{VI}O_2^{VI}$ compounds consist of the tetragonal α-$LiFeO_2$ structures,
- the $A^{VI}B^{VI}O_2^{VI}$ compounds have the rhombohedral α-$NaFeO_2$ form,
- the $A^{IV}B^{IV}O_2^{IV}$ compounds are comprised of the orthorhombic β-$NaFeO_2$-type materials,
- and the $A^{II}B^{VI}O_2^{IV}$ compounds have the delafossite structure.

The coordination class of the ABO_2 material is decided by the ionic radii of the A^+ and B^{3+} cations, as illustrated in fig. 2.19. Larger cations demand higher coordination environments, while smaller cations require lower coordination, in order to bear the oxygen content. The A sites of the delafossite compounds are limited to the monovalent elements Cu, Ag, Pd, and Pt. The B sites, on the other hand, can range from a cation with the radius of B, up to a cation with a radius less than or equal to that of La, including the trivalent metal ions Al, Ga, In, Sc, Y, Cr, Fe, rare earths, etc. The Cu- and Ag-based delafossites are semiconductors, while the Pd- and Pt-based compounds are metallic Rogers *et al.* (1971). Corresponding Ag-based delafossite materials are

[1]The coordination class of each ion is given in roman numeric superscript.

difficult to synthesise by simple solid-state reaction Tate *et al.* (2002). It is, however, the Cu-based delafossites that are of interest to this study.

Although there has been renewed interest in the delafossites, due to recent reports on copper aluminium oxide ($CuAlO_2$), the material has been known to exist for nearly 50 years Hahn & Lorent (1955). Back in 1984 its p-type conductivity was first reported by Benko and Koffyberg Benko & Koffyberg (1984), although Kawazoe *et al.* Kawazoe *et al.* (1997) first prepared it in transparent thin film form for potential p-TCO technological application. Conductivities as high as 10 S/cm have been recorded, as well as favourable transparency over the visible spectrum ($E_g \sim 3.5$ eV). The structural properties of this material have been extensively studied by Ishiguro *et al.* Ishiguro *et al.* (1981, 1982, 1983). Other p-TCO thin films, belonging to this group, that have been examined are copper gallium oxide ($CuGaO_2$) and copper indium oxide ($CuInO_2$) Ueda *et al.* (2001); Yanagi *et al.* (2001a,b). The lattice parameters of these materials have reported in various literatures Benko & Koffyberg (1984); Kohler & Jansen (1986); Prewitt *et al.* (1971); Shimode *et al.* (2000). Also, the band structures of these materials were calculated by Yanagi *et al.* Yanagi *et al.* (2000a), Robertson *et al.* Robertson *et al.* (2002) and in detail by Ingram *et al.* Ingram *et al.* (2001). Doped versions of some similar types of p-TCO thin films have also been reported which include iron doped copper gallium oxide ($CuGaO_2$:Fe), ($CuInO_2$:Ca), ($CuScO_2$:Mg), ($CuCrO_2$:Mg), ($CuYO_2$:Ca) etc. Duan *et al.* (2000); Jayaraj *et al.* (2001); Nagarajan *et al.* (2001a); Tate *et al.* (2002); Yanagi *et al.* (2001a,b). Some interesting optical and electrical properties of these materials are presented in table 2.1.

2.4.5.2 Crystal Structure

As stated already, delafossite compounds belong to a family of ternary oxides with the general formula $A^+B^{3+}O_2$. The structure, which is illustrated in fig. 2.20, consists of two alternating layers, a planar layer of A cations in a triangular pattern and a layer of nominal BO_2 composition consisting of edge-sharing BO_6 octahedra flattened with respect to the c-axis. Each A atom is linearly coordinated with two oxygen atoms to form an O-A^+-O dumbbell unit placed parallel to the c-axis. The oxygen atoms of the O-A^+-O dumbbell link all A layers with the BO_2 layers. On the other hand each oxide ion in the BO_2 layer forms a favourable "pseudo-tetrahedral coordination (B_3AO)" Kawazoe *et al.* (2000) with the neighbouring B^{+3} and A^+ ions, as indicated in fig. 2.20 (c). Another amenable feature in this structure is the low coordination number of the A^+ ions, due to the large separation from oxygen ligands, which is the result of the strong coulombic repulsion between $2p$ electrons in oxygen ligands and A^+ d^{10} electrons.

Figure 2.20: Representation of (a) the delafossite structure ABO_2 for the $3R$ polytype, $R\bar{3}m$ space group symmetry, with (b) a view along the [001] direction showing the hexagonal structure, and (c) the octahedral coordination of the B^{3+} ions, the linearly coordinated A^{+} ions and the pseudo-tetrahedral coordination of the O^{2-} ions.

Material	x	d (nm)	T (%)	$E_{g\ Dir}$ (eV)	σ_{RT} (S/cm)	μ (cm^2/Vs)	S_{RT} (μVK^{-1})	Ref.
$CuAlO_2$		230	70	3.5	0.34	0.13	+214	[1]
$CuGaO_2$		500	80	3.6	0.063	0.23	+560	[2]
$CuGa_{1-x}Fe_xO_2$	0.5	150	60	3.4	1.0		+500	[3]
$CuIn_{1-x}Ca_xO_2$	0.07	170	70	3.9	0.0028		+480	[4]
$CuCrO_2$		250	40	3.1	1.0			[5]
$CuCr_{1-x}Mg_xO_2$	0.05	270	50	3.1	220	< 0.3	+150	[6]
$CuYO_2$		200	60	3.5	0.025	< 0.5		[7]
$CuY_{1-x}Ca_xO_2$	0.02	240	50	3.5	1.05	< 0.5	+275	[8]
$CuScO_2$		110	40	3.3	30.0	< 0.5		[9]
$CuSc_{1-x}Mg_xO_2$	0.05	220 - 250	80	3.3 - 3.6	0.07			[10]

Table 2.1: Optical and electrical properties of p-type TCO delafossite thin films. d = Thickness, T = average visible transmittance, $E_{g\ Dir}$ = direct bandgap, σ = conductivity, μ = mobility, S_{RT} = thermopower. Reference [1] = Yanagi *et al.* (2000a), [2] = Ueda *et al.* (2001), [3] = Tate *et al.* (2002), [4] = Yanagi *et al.* (2001a), [5] = Nagarajan *et al.* (2001a), [6] = Nagarajan *et al.* (2001a) Nagarajan *et al.* (2001b), [7] = Jayaraj *et al.* (2001) Nagarajan *et al.* (2001b), [8] = Jayaraj *et al.* (2001) Nagarajan *et al.* (2001b), [9] = Duan *et al.* (2000) Nagarajan *et al.* (2001b), [10] = Tate *et al.* (2002) Yanagi *et al.* (2003a)

Depending on the orientation of each layer in stacking, the delafossite structure can form as one of two polymorphs. By stacking the double layers with alternating A layers oriented 180^o relative to each other, the hexagonal $2H$ type is formed with $P6_3/mmc$ space group symmetry. If the double layers are stacked with the A layers oriented the same direction relative to one another but offset from each other in a three layer sequence, the rhombohedral $3R$ type is formed, with $R\bar{3}m$ space group symmetry. The $R\bar{3}m$ delafossites in the rhombohedral description, illustrated in fig.2.20 (a), have the lattice constants a = 2.8 - 3.8 Åand c = 17 - 19 Åand the unit cell contains three ABO_2.

2.4.5.3 Non-Stoichiometry and Doping

The potential for novel applications of TCOs is based on the fact that the electronic band gap of a TCO is higher than 3.1 eV (corresponding to the energy of a 400 nm blue photon). Visible photons (having energy between 2.1 and 3.1 eV) cannot, therefore, excite electrons from the valence band to the conduction band and are hence transmitted through it. They do, however, have enough energy to excite electrons from donor level to the CB (for n-type TCO) or holes from acceptor

level to the VB (for p-type TCO). And these acceptor or donor levels can be created in the TCOs by introducing cation or anion non-stoichiometry, and (or) appropriate dopants in a controlled manner.

The cause of p-type conductivity shown by many of these delafossite materials appears to be due to excess oxygen or metal deficiency within the crystallite sites of the material Ingram *et al.* (2004b). A defect complex of B cations occupying A cation-sites and stabilised by two bound oxygen interstitials has also been proposed to explain the p-type character of $CuAlO_2$, for example, which has a relatively small B cationic radius Ingram *et al.* (2004a). Deviation from stoichiometric composition of the components can be induced by regulating the preparation conditions of the materials. Intercalation of excess O^{2-} ions in the interstitial sites may trap electrons, leaving behind empty states in the valence band, which then act as holes. The formula for oxygen-excess delafossite films can be written $A^{+}B^{+3}O_{2+\delta}$, where δ, the proportion of excess oxygen, may vary from as low as 0.001 % in a $CuAlO_{2+x}$ thin film Thomas (1997) to more than 25 % in $CuYO_{2+x}$ polycrystalline powder and $CuScO_{2+x}$ thin films Nagarajan *et al.* (2001b)Cava *et al.* (1994)Cava *et al.* (1993)Jayaraj *et al.* (2000). Oxygen intercalation in delafossite p-TCOs has reportedly shown a maximum conductivity of $\sim 3 \times 10^1$ Scm^{-1} Duan *et al.* (2000). Although this represents a significant conductivity enhancement, it is still considerably lower than that of commercially available n-TCOs like indium tin oxide (ITO).

Substitutional doping of these materials by appropriate dopants in order to increase their conductivity has also been explored. Preparation of a solid solution of gallium doped copper aluminium oxide in the form of $CuAl_{1-x}Ga_xO_2$ ($0 \leq x \leq 0.5$) has been reported Shahriari *et al.* (2001). Heavy doping ($\sim$ 50%) of $CuGaO_2$ by Fe^{3+} in Ga sites has also been reported by Tate *et al.* (2002). Doping of $CuInO_2$, $CuYO_2$, $CuScO_2$, $CuCrO_2$ by divalent cations e.g. Ca^{2+}, Mg^{2+} *etc.* has been reported by various groups Duan *et al.* (2000); Jayaraj *et al.* (2001); Nagarajan *et al.* (2001a,b); Tate *et al.* (2002); Yanagi *et al.* (2001a,b). The corresponding electrical properties of these doped compounds are listed in table 2.1. When a trivalent cation is replaced by a divalent cation, one empty state in the valence band is created, which acts as a hole, thus increasing hole conductivity. The doping process can be described by the following relation:

$$(M^{III+3} + 3e^-) \uparrow = (M^{II+2} + 2e^-) \downarrow + V^- + h^+$$

where M^{III+3} and M^{II+2} are trivalent and divalent cations, V^- is the empty state, which is occupied by an electron, e^- and thus creating a "free" hole, h^+ Banerjee & Chattopadhyay (2005). The symbols $\uparrow$ and $\downarrow$ denote the replacement of the trivalent cation by a divalent one in the lattice

sites. Such doped delafossite films like $CuCr_{1-x}Mg_xO_2$ ($x = 0.05$), $CuY_{1-x}Ca_xO_2$ ($x = 0.01$ - 0.02), $CuSc_{1-x}Mg_xO_2$ ($x = 0.05$) showed better hole conductivity over the corresponding undoped films. There are also reports in the literature about the double substitution of trivalent M^{III} sites by divalent and pentavalent cations and triple substitution of trivalent cations has been reported Nagarajan *et al.* (2002); Tate *et al.* (2002).

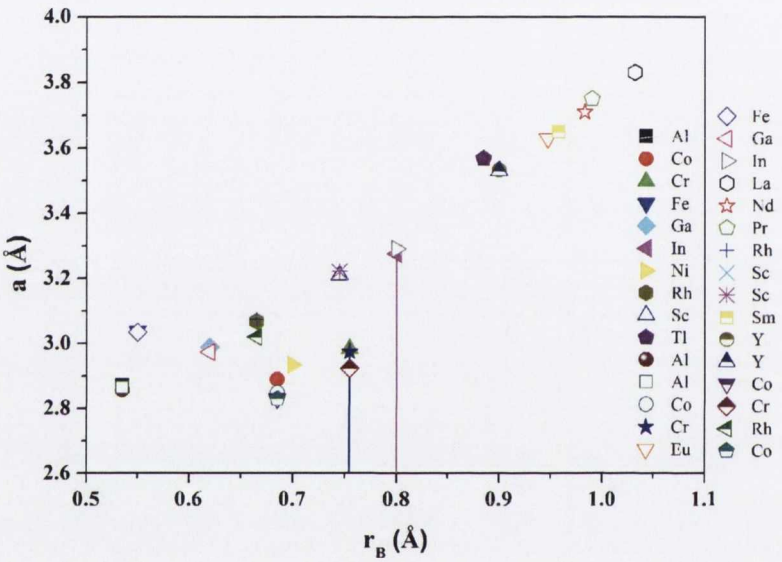

Figure 2.21: Variation of a lattice parameter with ionic radius of B cation in ABO_2 compounds.

The relationship between the lattice constants and the A and M^{III} cationic radii within the delafossite can influence the capacity for incorporation of a quantity of O^{2-} interstitial ions, and also the disposition of the structure to accepting substitutional impurity ions of a particular ionic size. The c lattice constant in the delafossites depends principally on the A ionic radius, while the a parameter depends on the M^{III} radius to a greater extent. A plot of the a lattice parameters corresponding to the ionic radius of their individual M ions is presented in fig. 2.21, from which the amenability of each distinct delafossite material to substitutional doping by ions of a relatively large or small size, compared to the M ion they are intended to replace, can be inferred. Large M-site delafossites, with increased a lattice parameter, greater than or equal to that of $CuScO_2$, are more conducive to allowing excess oxygen ions to permeate the lattice, and the layered delafossite structure allows the oxygen to diffuse easily through to the Cu plane via the open O-Cu-O layer and oxidise some of the Cu ions. The cation size and lattice parameter effects on the properties of

the delafossite materials will be discussed further in chapter 3.

Chapter 3

p-Type Delafossite $CuCrO_2$

3.1 McConnellite $CuCrO_2$

The synthetic mineral, McConnellite, copper chromium oxide ($CuCrO_2$) is a member of the delafossite family, possessing a number of favourable attributes. Reportedly a wide bandgap oxide, this ternary compound can be classified as a transparent conducting oxide, manifesting those seemingly incompatible properties of optical transparency together with semiconductivity. Member of an even more rare subclass of materials, the p-type TCOs, $CuCrO_2$ embodies the much anticipated complement to the more widely available, albeit higher performing, n-type TCOs. Together these polar transparent semiconductors have the potential to advance the electronics of transparent materials to the next generation of active transparent, all-oxide devices.

The p-type conductivity exhibited by this material is dramatically enhanced by the substitution of divalent Mg^{2+} ions for trivalent Cr^{3+} in the lattice, possessing the highest measured conductivity in the group of Cu-based delafossites Nagarajan *et al.* (2001a). The low carrier mobility observed in this material has hitherto prevented measurement of Hall effect in $CuCrO_2$ [1]. The carrier type has therefore been determined from thermoelectric measurements, and observation of a relatively high, positive Seebeck coefficient in this material suggests the potential for thermoelectric applications Tate *et al.* (2002). This material has also been investigated for its ozone-sensing capabilities Deng *et al.* (2009) Zhou *et al.* (2009).

The optical bandgap in $CuCrO_2$ is generally reported to be $\sim$ 3.1 eV involving direct band-to-band transitions Li *et al.* (2009b) Sadik *et al.* (2009), in adherence to the criterion to achieve optical transparency in the visible range of the electromagnetic spectrum. Thin films of this

[1] Apart from one report of $\mu = 11.16$ cm^2/Vs in thin films prepared by MOCVD Mahapatra & Shivashankar (2003), which far exceeded all other reports by at least two orders of magnitude.

promising material were 50% transparent to visible light [1] Nagarajan *et al.* (2001b). Calculations have determined the nature of the fundamental bandgap to derive from indirect transitions and to be significantly lower than the value obtained from optical absorption measurements Scanlon *et al.* (2009a), reasons for the discrepancy are as yet unclear.

$CuCrO_2$ crystallises in the delafossite crystal structure, depicted in fig. 2.20, which is described at length in chapter 2. Two polymorphs of $CuCrO_2$ can form, one with hexagonal $2H$ and a second with rhombohedral $3R$ crystal structures, the polytype of interest, however, is the rhombohedral, $3R$, crystal with space group $R\bar{3}m$ and group number 166 Marquardt *et al.* (2006). The lattice parameters of the $CuCrO_2$ rhombohedral unit cell are reported to be $a = b = 2.9734$ Å, and $c = 17.100$ Å, in the most recent powder diffraction file [2].

Along with fellow delafossite materials, $CuFeO_2$ and $AgCrO_2$ Dordor *et al.* (1988) Benko & Koffyberg (1987) Nagarajan *et al.* (2001b), $CuCrO_2$ exhibits antiferromagnetic ordering below a Néel temperature of ~ 25 K Attili *et al.* (1996). This triangular lattice antiferromagnet, with its effectively reduced-dimensional magnetic system is ideal for the study of spin frustration, and has therefore attracted appreciable interest in recent years Kadowaki *et al.* (1990) Okuda *et al.* (2008) Seki *et al.* (2008). The observation of ferroelectricity below T_N has excited further enthusiasm in the study of this complex magnetic structure Kimura *et al.* (2008). A curious correlation between the electrical and magnetic properties has also been observed in this, currently, topical material Okuda *et al.* (2007).

Polycrystalline samples of $CuCrO_2$ are generally synthesised by solid state reaction Maignan *et al.* (2009), the soft chemistry methods of sol-gel Götzendörfer *et al.* (2009) and hydrothermal technique Zhou *et al.* (2008) have also been used, however a marked improvement is observed in the conductivity of this delafossite in thin film form. $CuCrO_2$ thin films have been fabricated by rf sputtering Nagarajan *et al.* (2001b); Okuda *et al.* (2005), low pressure metal-organic chemical vapour deposition (MOCVD) Mahapatra & Shivashankar (2003), and recently by pulsed laser deposition Li *et al.* (2007) Sadik *et al.* (2009), with promising results.

3.1.1 Electronic Band Structure

Since the Cu-based delafossites were recently revisited for their suitability as transparent conducting oxides, under the "CMVB" design concept, several electronic band structure studies have been

[1] The films had a thickness of 250 nm

[2] PDF number 04-010-3330

conducted on these materials. $CuAlO_2$ has received the lion's share of attention in these investigations Buljan *et al.* (1999) Ingram *et al.* (2001) Robertson *et al.* (2002) Ingram *et al.* (2004a), with little examination of $CuCrO_2$ until very recently Scanlon *et al.* (2009a) Arnold *et al.* (2009) Maignan *et al.* (2009) Scanlon *et al.* (2010). For the purpose of examining the band structure and contributing densities of states of this material it is instructive to compare with other $CuMO_2$ delafossites with various M cations in the octahedral sites.

One of the initial investigations into the electronic structure and bonding in these delafossite oxides studied $CuMO_2$ with (M = Al, Ga, Y)[1] Buljan *et al.* (1999). Their work showed that in both the $2H$ and $3R$ polymorphs of $CuAlO_2$, the top of the VB was dominated by Cu $3d$ states, with some contribution of Cu $4s$ states indicating s-d_z^2 hybridisation in agreement with the Orgel model. The O $2p$ states were observed to overlap with the sharp Cu $3d$ peak and contribute significantly to the upper valence band, while the Al provided a negligible contribution to the valence band and the lower conduction band. Calculated electron density maps supported the covalent character of the $Cu - O$ bonds. Large indirect band gaps were calculated, however they were strongly overestimated compared to the existing experimental value of 1.65 eV determined for $3R$ $CuAlO_2$ Benko & Koffyberg (1984). A Mulliken population analysis of the three compounds under scrutiny, indicated that $CuAlO_2$ presented the most ionic MO_2 layer.

A subsequent electronic structure study[2] on $CuAlO_2$ Yanagi *et al.* (2000a) largely agreed with the results of Buljan *et al.* (1999) finding the top of the VB to be dominated by Cu-O bonding states, but with optical gaps of 1.7 eV (indirect) and 2.8 eV (direct), the former in good agreement with early experimental results Benko & Koffyberg (1984). From combined information on ultraviolet photoemission spectrum (UPS) with x-ray photoemission spectrum (XPS), it was inferred that an admixed state of Cu $3d$ and O $2p$ primarily constitutes the upper VB which determines the hole conduction.

In a more detailed study, the same method was employed[3] to calculate the band structure and densities of states of $CuAlO_2$ Ingram *et al.* (2001). An indirect fundamental gap of 1.95 eV, from F to Γ, was calculated with the smallest direct band gap reported to be 2.7 eV. This underestimated the experimental results of Yanagi *et al.* (2000a) and Kawazoe *et al.* (2000) Kawazoe *et al.* (1997) who both observed direct gaps of 3.5 eV.

This report further supported the Cu d_z^2-s hybrid orbitals proposed by Orgel Orgel (1966), and discussed in chapter 2, with the observation of a mixture of Cu s with Cu d states at the VB

[1] Hartree-Fock method with *a posteriori* density functional corrections
[2] Full-potential linearised augmented plane wave (FLAPW) method calculations
[3] Using the local-density approximation (LDA)

maximum, at F, in the electron charge density, and an isotropic charge density in the (001) plane. A linear antibonding structure between Cu d_z^2-s and O p_z was also observed at the VB maximum. This hybridisation, also seen in the calculated densities of states in the topmost VB, contributes to the band dispersion around F due to the strong coupling of the effective mass with the $Cu - O$ distance. The calculated electron density and decomposed electron charges at the CB minimum, at Γ, presented a dispersive band consisting mainly of Cu s and d states.

A comparison study was carried out into the band structure of three Cu-based delafossites with octahedral cations from the third column of the periodic table, $CuAlO_2$, $CuGaO_2$ and $CuInO_2$[1] Robertson *et al.* (2002). Successive replacement of the Al ion by Ga and then In, with increasing ionic radii, in the calculations increases the $Cu - Cu$ distance along the a axis. The bandgap was expected to increase due to reduced Cu-Cu interaction, as seen experimentally, however the calculated indirect bandgaps were observed to decrease monotonically, from 2.1 to 1.4 to 0.52 eV, as the cation moved down group III of the periodic table, a trend also observed by Nie et al. Nie *et al.* (2002). The Al, Ga and In cations in this study, however, increasingly contributed to the densities of states at the CB minimum, at Γ, and therefore had the effect of pulling down the Γ state.

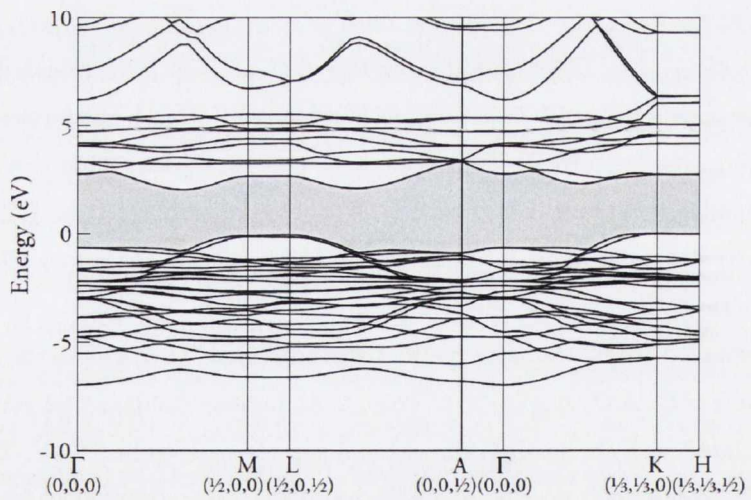

Figure 3.1: The electronic band structure of $CuCrO_2$ Scanlon *et al.* (2009a).

A recent study[2] examined the effect of replacing the Al ion in $CuAlO_2$ with Cr Scanlon *et al.* (2009a). The electronic band structure of $CuAl_{1-x}Cr_xO_2$ was calculated for $x = 0$, 0.5, 1. The

[1] Using the pseudopotential method within the local density formalism
[2] Using density-functional theory calculations

band structure of $CuAlO_2$ exhibited a conduction band minimum at Γ, and a broad valence band maximum between H and K, agreeing well with previous reports Nie *et al.* (2002) Robertson *et al.* (2002). An indirect band gap of 2.2 eV was identified, which differs slightly from the experimentally determined value of 1.8 eV Yanagi *et al.* (2000a). This difference may be due to intrinsic defect levels present in the optical absorption samples Robertson *et al.* (2002). Partial and total electronic densities of states indicate that both the top of the valence band and the bottom of the conduction band consist mainly of states derived from a mixture of Cu $3d$ and O $2p$ states, similar to previous results. The Al $3s$ and $3d$ states do not contribute significantly to the valence band, and Al states only participate in the upper conduction band.

Introduction of Cr ions into the lattice in $CuAl_{0.5}Cr_{0.5}O_2$, necessitates two spin components α and β. The octahedral crystal field induces a high spin t_{2g}^3 configuration. The fundamental indirect bandgap energy was observed to remain unchanged, however the conduction band minimum was seen to move to between L and A, with the valence band maximum close to the K point. The main contributions to the upper valence band were found to be due to Cu $3d$, O $2p$ and some Cr $3d$ states, where an increased density of states was observed. The Cr ions appear to influence the interaction between the Cu ions and the O ions they are coordinated to, supplying additional states to the α spin component at the valence band maximum. The bottom of the conduction band is dominated by Cr states, with the Al states only appearing in the upper conduction band. The oxygen coordinated to the Cr ions has a greater participation in the lower conduction band than in $CuAlO_2$, this may be responsible for the relocation of the valence band maximum in k-space in the doped compound.

Finally, calculations of the opposite endmember, $CuCrO_2$ were carried out, the band structure is shown in fig.3.1. The indirect band gap was observed to reduce to 2.04 eV, the conduction band minimum again occurring between the L and A symmetry points and the valence band maximum at M, while the direct band gap measured 2.55 eV. Antiferromagnetic ordering is stabilised within the simulated unit cell with a small energy advantage of 20 meV/f.u. over the ferromagnetic configuration, which is commensurate with the low Néel temperature observed in this material Okuda *et al.* (2005). Total and partial densities of states of $CuCrO_2$, shown in fig. 3.2, are similar to those of $CuAl_{0.5}Cr_{0.5}O_2$ with only slight changes in the Cr and Cu peak shapes in the valence band. The upper valence band again comprises contributions from Cu $3d$, Cr $3d$ and O $2p$ states. Increased contributions from Cr $3d$ levels dominate the lower conduction band. And enhanced interaction with the Cr $3d$ states extends the O $2p$ presence right the way from the conduction band minimum to the upper conduction band.

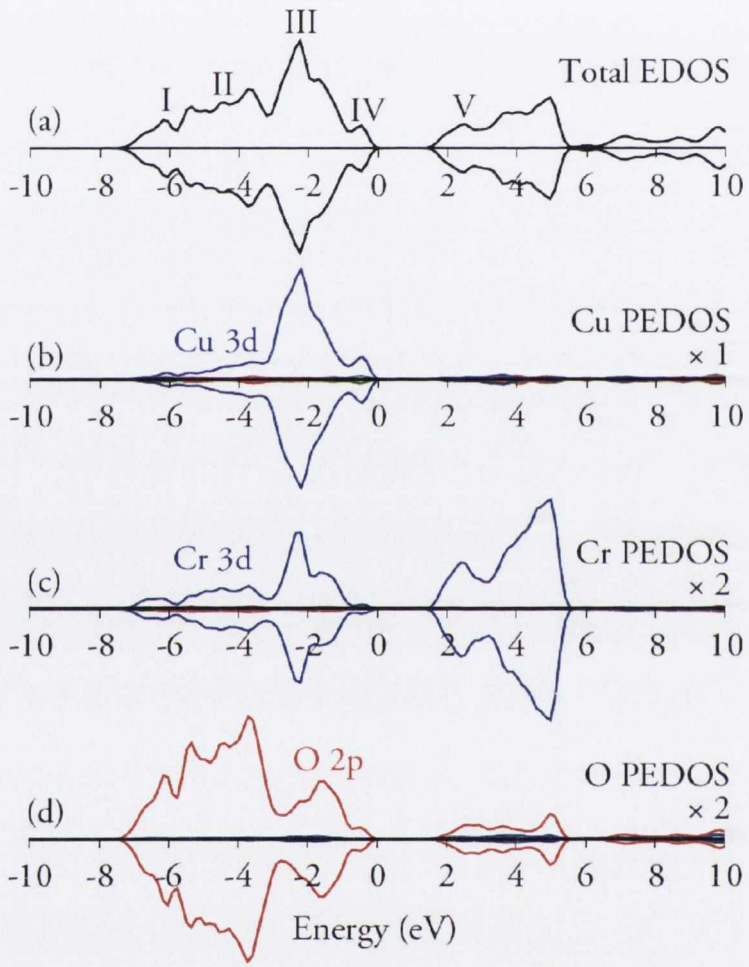

Figure 3.2: Total (EDOS) and partial (PEDOS) electronic densities of states for $CuCrO_2$ Scanlon *et al.* (2009a). The blue lines represent d states, green represent s states, and red represent p states.

Analysis of the ionicity of the charge distribution in these materials can indicate the degree to which the energy levels of the ions have hybridised within the lattice. Bader analysis was used in the study, to assess the partial charge localised on each ion. All three compounds were found to have less than the formal ionic charges of $+1$ on the Cu ions, and -2 on the O ions, indicating covalent mixing between these ions in agreement with the density of states calculations. The Al ion in the initial $CuAlO_2$ compound was found to have its full formal ionic charge of $+3$. The intermediate $CuAl_{0.5}Cr_{0.5}O_2$ compound exhibited equally ionic charge distribution on the Al ion with far less ionic Cr. Significantly reduced charge was also recorded on the O ions that were coordinated to the Cr, indicating partial charge transfer between them. An accompanying reduced charge redistribution between these O ions and the Cu was also observed. A similar result was found for the final $CuCrO_2$ compound, where valence charge was significantly distributed between the three elements. This finding is suggestive of an indirect interaction between Cu and Cr, mediated by the O ions that have already been observed to hybridise with Cr ions in the density of states calculations. The effect of the indirect Cu-O-Cr interaction appears to increase the density of states at the valence band maximum and thus influence the states that determine the conduction and mobility within the material. The comparison of the two endmember materials can lead us to attribute the flattening of the bottom of the conduction band in $CuCrO_2$, relative to the dispersive band in $CuAlO_2$, to the localised character of the Cr $3d$ states.

A theoretical study into the significance of covalency between the oxygen and the octahedral M^{III} cation in $Cu^I M^{III} O_2$ with ($M^{III} = Al, Cr, Sc, Y$) using density functional theory was very recently undertaken Scanlon *et al.* (2010). The band structures and densities of states of $CuAlO_2$ and $CuCrO_2$ were as reported above Scanlon *et al.* (2009a). The calculations for $CuScO_2$ arrived at a conduction band minimum at Γ and a valence band maximum located at H, with a fundamental indirect bandgap of 2.88 eV. The smallest direct bandgap was observed at the M point to be 2.98 eV, an underestimation of the 3.3 eV measured by optical spectrometry Duan *et al.* (2000). The partial densities of states study indicates a very slight input from the Sc states to the valence band which is dominated by Cu $3d$ and O $2p$ hybridised states, however a substantial contribution from the Sc d states is observed in the conduction band with some minor mixing with O $2p$ states. As for Al in the $CuAlO_2$, Sc states in $CuScO_2$ are consequently not expected to participate in the p-type electronic conduction. The conduction band minimum and valence band maximum are unchanged in $CuYO_2$, giving an indirect bandgap of 2.93 eV, and a direct bandgap of 3.15 eV occurring at Γ, again underestimating the experimental value of 3.5 eV Jayaraj *et al.* (2001). Cu and O states participate in the conduction and valence bands of $CuYO_2$ in a similar way to the

$CuScO_2$ density of states calculations, and while the Y cation p and d states only constitute a minor part of the valence states, the Y d states dominate the conduction band with some O $2p$ mixing. Of the four materials studied, the M^{III} ion of $CuCrO_2$ participated the most in the upper valence band density of states responsible for the p-type conduction properties, while both the Sc in $CuScO_2$ and the Y in $CuYO_2$ displayed a greater degree of interaction with the O $2p$ states in the conduction band than did the Al in $CuAlO_2$. Bader partial charge analysis was again used to compare the charge distribution within the four compounds, where $CuCrO_2$ exhibited the greatest partial charge transfer between Cr and O, and the Al and O in $CuAlO_2$ retained the greatest portion of their formal ionic states, consistent with previous results Scanlon *et al.* (2009a). The Sc and O in $CuScO_2$ were slightly more ionic than Cr and O in $CuCrO_2$, while the Y and O in $CuYO_2$ were less covalent yet again. This analysis indicates that covalency in these four materials increases in the following sequence $CuAlO_2$ – $CuYO_2$ – $CuScO_2$ – $CuCrO_2$, in agreement with the experimentally observed increasing conductivity trend in their optimally doped or oxygen intercalated samples Kawazoe *et al.* (1997) Jayaraj *et al.* (2001) Nagarajan *et al.* (2001b).

XPS A number of investigations into the band structure of the more studied Cu-based delafossites have been carried out. $CuCrO_2$, on the other hand, has come to the fore more recently and is therefore less studied. A dedicated spectroscopic study, however, has lately been carried out on this system, and some preliminary band structure calculations have been reported. Arnold *et al.* studied the electronic structure of $CuCrO_2$ by x-ray spectroscopies Arnold *et al.* (2009). They found the electronic structure of $CuCrO_2$ to be very similar to that of other Cu (I) oxides where Cu is found in a linear coordination environment. The upper part of the VB was observed to derive mainly from Cu $3d$ and Cr $3d$ states while the lower VB states were of dominant O $2p$ atomic character, but with pronounced mutual hybridisation among Cu $3d$, Cr $3d$, and O $2p$ states. Admitting the difficulty in locating the Cr $3d$ states experimentally, they compared their experimental data to electronic structure calculations on $CuCrO_2$ which were carried out. This indicated that the Cr $3d$ states straddled most of the VB and hybridised strongly with O $2p$ states at the bottom of the VB. The significant Cr $3d$ contribution to the top of the VB indicated that holes introduced into $CuCrO_2$ by p-type doping were partially delocalised onto Cr which could account for the higher conductivity of $CuCrO_2$ compared to $CuAlO_2$. Substitution of Mg on Cr sites in the $CuCrO_2$ lattice was observed to induce a shift in the Fermi level closer to the valence band edge, as would be expected for p-type doping.

3.1.1.1 Size Dependence Theory

Rationalising the optical properties and the electrical conductivity variation within the delafossite family is no easy task. And although electronic band structure calculations have shed some light on the influence of the different M^{III} cations in these $CuM^{III}O_2$ materials, the structural and bonding implications of the varying sizes of the cations must also be considered. It is generally thought that a small polaronic conduction mechanism is responsible for the electrical transport properties within these systems Benko & Koffyberg (1984) Rogers *et al.* (1971) Ingram *et al.* (2001) Ingram *et al.* (2004b). This mechanism will be discussed in greater detail in a later section, however it suffices to note that the *Cu-Cu* separation within the lattice has a significant influence upon polaron hopping, and therefore conductivity, in these materials, with reduced *Cu-Cu* separation expected to correspond to an increase in the rate of hopping. Upon inspection, a decrease in conductivity along the series $Mg{:}CuCrO_2$ – $Mg{:}CuScO_2$ – $Ca{:}CuYO_2$ was noted to coincide with an increase in the size of the ionic radius of the M^{III} ion Nagarajan *et al.* (2001a). A consequence of increasing the size of the M^{III} ion is an increase in the *a* lattice parameter and hence the *Cu-Cu* distance in the *a-b* plane Ingram *et al.* (2005). This reduces the *Cu d-d* overlap and possibly the mobility within the crystal. The effect, however, does not follow for *Mg*-doped $CuAlO_2$, in which the Al^{3+} ion in octahedral coordination has an even smaller ionic radius than Cr^{3+}, but which displays a lower conductivity than *Mg*-doped $CuCrO_2$. Nevertheless, it has been noted that higher conductivity in undoped $CuAlO_2$ than both undoped $CuScO_2$ and $CuYO_2$ may be associated with its reduced M^{III} cation size, but this cannot explain the higher conductivity in undoped $CuCrO_2$ than in $CuAlO_2$ Marquardt *et al.* (2006).

It has been observed that an increase in the *Cu-O* bond length is accompanied by a decrease in both the *Cu-Cu* distance and the incidental *a* lattice parameter, resulting in an increase along the *c* axis Marquardt *et al.* (2006). This has been attributed to a mutually compensating relation between the two bonds in $CuM^{III}O_2$ delafossites. It has also been suggested that Coulomb repulsion between *Cu* ions with filled outer shells, whose repulsive force is further enhanced by polarisation due to the linear two-fold coordination of *Cu* along the *c* axis, depends upon the *Cu-Cu* separation. As this separation reduces, due to replacement of *M* with a smaller cation, the polarisation is forced to decrease, thus weakening the *Cu-O* bonds along the *c* axis and lengthening them Nagarajan *et al.* (2001b).

Another factor to consider is that the size of the *M* cation also affects the ability to dope or to introduce oxygen interstitials into the material. Extrinsic doping of the delafossites has been seen to have a dramatic effect on the conductivity of these materials Banerjee & Chattopadhyay

(2005). However, low dopant solubility limits are generally observed in their lattices Maignan *et al.* (2009). It is logical to assume that the larger the M ion in the crystal the greater the capacity for accepting replacement ions and oxygen interstitials in the lattice. However, the lower conductivity recorded in Mg-doped $CuScO_2$ and Ca-doped $CuYO_2$ when compared with Mg-doped $CuCrO_2$ has been alluded to already.

Size dependence theory alone, therefore, cannot explain the conductivity trend within these materials, and the electronic structure of the M must also be taken into account. Evidence of a pattern of increasing covalency with oxygen that matches the trend of increasing conductivity in the series of delafossites, with M cations in the order Al-Y-Sc-Cr, has been published recently Scanlon *et al.* (2010). It has been observed that the higher conductivities observed for $CuCrO_2$ and $CuFeO_2$ may be due to favourable mixing between the $3d$ states on the M ion in the Cu-O-M-O-Cu chains Nagarajan *et al.* (2001a). It would appear that finding a compromise between the size factors, the electronic structure and the chemical factors is necessary to explain the conductivity behaviour in the Cu-based delafossites.

3.1.2 Magnetic Properties

Aside from the simultaneous transparency and semiconducting features of $CuCrO_2$, this material exhibits magnetic ordering. $CuCrO_2$ is an antiferromagnet with a reported Néel temperature of approximately 25 K Kadowaki *et al.* (1990). The magnetic properties of this particular delafossite have excited considerable interest over the last few years, and researchers are increasingly performing studies into the somewhat complicated incommensurate magnetic structure of this oxide. The classical antiferromagnetic ordering state, the Néel state, can be envisaged as the formation of two interpenetrating magnetic sublattices with antiparallel spin structures in which the overall magnetisation cancels apart from minor contributions from thermal excitations. This definition, however, is a little simplistic and neglects the cases where the spin substructures are non-collinear or where there are more than two magnetic sublattices in operation, triangular antiferromagnets for example, which have particular relevance here. The fundamentals of magnetic exchange interactions giving rise to magnetic ordering have been reviewed in appendix C in the context of this dissertation.

3.1.2.1 Crystal Field Interaction

The energy levels of an ion occupying a site in a crystal are influenced by the anisotropic environment or the crystal field. The effect of this is to lift the degeneracy of the energy levels or to incur

level splitting. The significance of the crystal field varies between different groups of elements, for example the crystal field is less consequential for the $4f$ rare earth ions and is dominated by the exchange splitting and also spin-orbit interactions, this is considered the weak crystal field case. The strong crystal field dominates the other interactions in some $4d$ and $5d$ transition metal compounds, due to mixing of the d-orbitals with the p-orbitals of the surrounding anions. And the medium case, which holds most relevance to the discussion at hand, applies to the $3d$ transition metal ions, where the crystal field overshadows the spin-orbit interaction, but inferior to the exchange splitting. The crystal field contribution to the Hamiltonian can be expressed

$$\mathcal{H}_{CF} = \int \rho(\mathbf{r}) V(\mathbf{r}) d^3r \tag{3.1}$$

where $\rho(\mathbf{r})$ is the ionic charge density, and $V(\mathbf{r})$ is the electrostatic potential from the rest of the charges in the crystal. Two important effects of the crystal field on the $3d$ ions are the quenching of the orbital angular momentum, and the introduction of magnetocrystalline anisotropy which favours magnetisation along certain easy-axis orientations.

In oxides and other ionic compounds, the $3d$ ions are generally found to have either octahedral (6-fold) or tetrahedral (4-fold) coordination, both of which have cubic symmetry unless they are distorted. In a free $3d$ transition metal ion $n = 3$, $l = 2$, and the electron orbitals are 5-fold degenerate with $m = 0, \pm 1, \pm 2$. An orthogonal set of $3d$ orbitals can be constructed from the radial function $f(r)$ for the principal quantum number and the spherical harmonics $Y_l^m(\theta, \phi)$ Figgis (1966) as follows

$$d_{z^2} = \psi_0 \approx f(r) \cdot Y_2^0(\theta, \phi) \tag{3.2}$$

$$d_{yz} = \frac{1}{\sqrt{2}}(\psi_1 - \psi_{-1}) \approx f(r) \cdot \frac{Y_2^1(\theta, \phi) - Y_2^{-1}(\theta, \phi)}{\sqrt{2}} \tag{3.3}$$

$$d_{xz} = \frac{1}{\sqrt{2}}(\psi_1 + \psi_{-1}) \approx f(r) \cdot \frac{Y_2^1(\theta, \phi) + Y_2^{-1}(\theta, \phi)}{\sqrt{2}} \tag{3.4}$$

$$d_{xy} = \frac{1}{\sqrt{2}}(\psi_2 - \psi_{-2}) \approx f(r) \cdot \frac{Y_2^2(\theta, \phi) - Y_2^{-2}(\theta, \phi)}{\sqrt{2}} \tag{3.5}$$

$$d_{x^2-y^2} = \frac{1}{\sqrt{2}}(\psi_2 + \psi_{-2}) \approx f(r) \cdot \frac{Y_2^2(\theta, \phi) + Y_2^{-2}(\theta, \phi)}{\sqrt{2}} \tag{3.6}$$

In an octahedral crystal field the five degenerate orbitals split into two groups, t_{2g} and e_g, with an energy difference Δ_{oct} (the octahedral crystal field splitting), as indicated in fig. 3.3. The d_{xy}, d_{yz} and d_{xz} orbitals belong to the lower energy t_{2g} group, whose lobes project between the Cartesian axes, while the $d_{x^2-y^2}$ and d_{z^2} orbitals belong to the higher energy e_g group, whose lobes

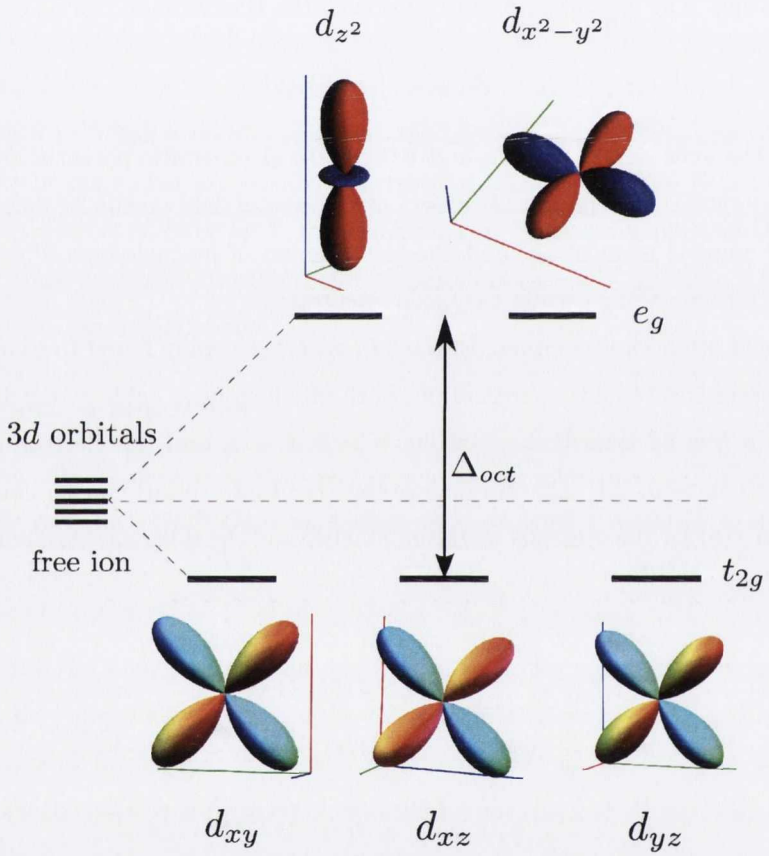

Figure 3.3: Octahedral crystal field splitting

project along the axes and point directly towards the octahedral oxygen anions located on the axes. The e_g orbitals experience a greater Coulomb repulsive force from the oxygen anion ligands than the t_{2g} orbitals that have a greater separation from them. A large Δ_{oct} splitting of the $3d$ orbitals in a strong crystal field can result in a low-spin configuration since the energy cost of filling the e_g orbitals is greater than the double-occupancy Coulomb energy cost of completely filling the t_{2g} orbitals. Conversely, a weak crystal field can bring about small Δ_{oct} splitting and give rise to a high-spin configuration, where Hund's rules are adhered to. Thus for $3d^3$ Cr^{3+}, for example, the high spin t_{2g} configuration has $S = 3/2$, while the low spin configuration has $S = 1/2$. The crystal field splitting for Cr^{3+} ions in octahedral coordination will be considered in the context of the delafossite $CuCrO_2$ crystal structure.

3.1.2.2 Literature Review of Magnetic Properties

Spin frustration can arise from geometrical frustration in antiferromagnetic triangular lattices. The ground state of such a frustrated spin system is typically highly degenerate Okuda *et al.* (2008), and this can bring about interesting magnetic characteristics such as spin glass Ramirez *et al.* (1992), spin ice Ramirez *et al.* (1999) and quantum spin liquid states Sindzingre *et al.* (2000), and also multiferroic properties Kimura *et al.* (2006). As a result there has been appreciable interest in the study of triangular lattice antiferromagnets (TLA). It was for this reason that the initial magnetic structure study of the $3R$ phase of $CuCrO_2$, which presents planes of Cr^{3+} ions arranged in a triangular pattern, was performed Kadowaki *et al.* (1990). This initial powder neutron diffraction experiment reported a quasi-two-dimensional behaviour in the paramagnetic phase and attempted to decipher the magnetic structure in the magnetically ordered phase. In this study the $(1/3, 1/3, l)$ and $(2/3, 2/3, l)$ magnetic peaks, where $l \in \mathbb{Z}$, were observed below the ordering temperature, T_N 25 K. The material was thus identified as having a commensurate 120^o spin structure wave vector $k = (q, q, 0)$ where $q = (1/3)$ in the a-c plane, with long-range magnetic order established in the c plane, but finite correlation along the c axis.

In the $CuCrO_2$ crystal structure the magnetic Cr^{3+} cation is at the centre of an octahedron with O^{2-} anions at the vertices. The effect of the octahedral surroundings is to quench the orbital moment of the $3d^3$ electronic state of the Cr^{3+}, with $S = \frac{3}{2}$. Since Cu^+ $(3d^{10})$ is nonmagnetic, Cr^{3+} $(3d^3)$ is mainly responsible for the magnetic properties of $CuCrO_2$ Ono *et al.* (2007). If the effective moment is $\mu_{eff} = 2[S_i(S_i + 1)]^{1/2}$ where i can signify a high-spin (HS) or low-spin (LS) state (i = HS or LS), the effective magnetic moments of Cr^{3+} are $\mu_{eff} = 3.87\mu_B$ for the HS state $(S_{HS} = 3/2)$, and $\mu_{eff} = 1.73\mu_B$ for the LS state $(S_{LS} = 1/2)$.

A number of magnetisation studies have reported the measurement of Néel temperatures that are slightly at variance with one another, this can be seen in table 3.1. Figures varying from T_{N} = 23.6 K Kimura *et al.* (2008), 24 K Poienar *et al.* (2009), 24.5 K Okuda *et al.* (2007), 25 K Ono *et al.* (2007) Seki *et al.* (2008) Li *et al.* (2009b) , 25.8 K Okuda *et al.* (2008), and 26 K Okuda *et al.* (2005), to 27 K Doumerc *et al.* (1986) have been measured in undoped $CuCrO_2$. The susceptibility, χ, was observed to follow Curie-Weiss behaviour, $\chi = (C/(T - \theta_{\mathrm{CW}}))$, down to a crossover temperature, T_{cross} Okuda *et al.* (2005). And the extracted Curie-Weiss temperatures for the $CuCrO_2$ endmember ranged from θ_{CW} = -215 K Ono *et al.* (2007) to -170 K Maignan *et al.* (2009). The effective moments due to the magnetic ions in $CuCrO_2$, which are determined from the linear part of the inverse susceptibility curves, are also listed in table 3.1, and range from μ_{eff} = 3.1 μ_B/Cr to $\sim$ 4.0 μ_B/Cr, indicating that Cr^{3+} is in the high-spin state.

Composition	Sample type	T_N (K)	$\theta_{CW}(K)$	μ_{eff} (μ_B/Cr)	Ref
$CuCrO_2$	Polycrystalline	27	-199	3.88	Doumerc *et al.* (1986)
$CuCrO_2$	Polycrystalline	25 ± 0.5		3.1 ± 0.2	Kadowaki *et al.* (1990)
$CuCrO_2$	Polycrystalline	26	≤ 0		Okuda *et al.* (2005)
$CuCr_{0.97}Mg_{0.03}O_2$	Polycrystalline	26	≤ 0		Okuda *et al.* (2005)
$CuCrO_2$	Polycrystalline	25	-215(2)	3.653(9)	Ono *et al.* (2007)
$CuCr_{0.99}Mg_{0.01}O_2$	Polycrystalline	25	-186(3)	3.78	Ono *et al.* (2007)
$CuCr_{0.98}Mg_{0.02}O_2$	Polycrystalline	25	-163.6(8)	3.590(3)	Ono *et al.* (2007)
$CuCr_{0.97}Mg_{0.03}O_2$	Polycrystalline	25	-149.2(6)	3.519(3)	Ono *et al.* (2007)
$CuCrO_2$	Polycrystalline	24.5	< 0		Okuda *et al.* (2007)
$CuCr_{0.96}Mg_{0.04}O_2$	Polycrystalline	26	< 0		Okuda *et al.* (2007)
$CuCrO_2$	Polycrystalline	25.8			Okuda *et al.* (2008)
$CuCrO_2$	Single crystal	$T_{N2} = 24.2$	-211 (χ_c)		Kimura *et al.* (2008)
		$T_{N1} = 23.6$	-203 (χ_{ab})		
$CuCrO_2$	Polycrystalline	24			Seki *et al.* (2008)
$CuCrO_2$	Polycrystalline	24	-202	3.89	Poienar *et al.* (2009)
$CuCr_{0.98}Mg_{0.02}O_2$	Polycrystalline	25.5			Poienar *et al.* (2009)
$CuCrO_2$	Polycrystalline	24	-170	3.7 − 4.0	Maignan *et al.* (2009)
$CuCr_{0.98}Mg_{0.02}O_2$	Polycrystalline	25		3.7 − 4.0	Maignan *et al.* (2009)
$CuCrO_2$	Polycrystalline	25	-190		Li *et al.* (2009b)

Table 3.1: Basic magnetic properties of $CuCrO_2$ triangular-lattice antiferromagnet

In the first study on single crystals of $CuCrO_2$, two transitions were observed in both the susceptibility and specific heat measurements, around the previously reported ordering temperature, at $T_{N2} = 24.2$ K and $T_{N1} = 23.6$ K Kimura *et al.* (2008). The higher temperature anomaly, T_{N2}, has been attributed to the transition from the paramagnetic phase to a collinear antiferromagnetic spin structure, while the lower transition, T_{N1}, appears to result from an out-of-plane 120^o spin structure. Below the Néel temperature, the magnetic degeneracy is lifted and the noncollinear 120^o magnetic structure is realised in the antiferromagnetic regime, to resolve the magnetic frustration, as is often observed in the triangular lattice antiferromagnets. Neutron diffraction experiments have determined that the system has easy-axis type anisotropy (i.e. with the spin-spiral perpendicular to the triangular-lattice plane (TLP)) Seki *et al.* (2008). The collinear spin structure has ordered spin components parallel to the hexagonal c axis, while the spin components of the out-of-plane 120^o spin structure are ordered perpendicular to the c axis. The out-of-plane 120^o structure has two possible spin configurations, the first arrangement has the spiral plane parallel to the (110) plane, while the second has the spiral plane parallel to the $(1\bar{1}0)$ plane.

High resolution powder neutron diffraction measurements were used to study, in detail, the structural modification of the $CuCrO_2$ lattice with reducing temperature Poienar *et al.* (2009). The comprehensive lattice parameter examination indicated that the a lattice parameter increased, while the c parameter and the cell volume V decreased, with reducing temperature from 300 K down to T_N, and below T_N all three parameters became virtually constant. The $[CrO_2]_\infty$ layers exhibited a thickness increase as the temperature reduced, and the Cr-O distances within the CrO_6 octahedron decreased. This deformation of the octahedron arises from the deviation of the O-Cr-O angles from 90^o, and is thought to be related to the ordering of the spin structure below T_N. Broad magnetic peaks observed in the neutron diffractograms indicated an incommensurate propagation vector $k = (q, q, 0)$, where q was refined to 0.329 for the undoped sample, and 0.326 for a 2 % Mg doped sample. This corresponds to an incommensurate 118^o spin structure which is very close to the commensurate 120^o structure previously reported in the original neutron diffraction study Kadowaki *et al.* (1990).

A recent spin-polarised neutron diffraction study on $CuCrO_2$ single crystals confirmed that an incommensurate proper screw spin structure operates in this TLA Soda *et al.* (2009). Both the commensurate 120^o spin structure and cycloidal ordering of the spiral plane failed to describe the system.

Exchange Mechanism A number of models have been suggested to explain the exchange mechanism at work in this TLA Poienar *et al.* (2009) Arima (2007). An indirect intralayer *Cr-O-Cr* superexchange interaction has been invoked to account for the magnetic behaviour of this system. A weak direct exchange interaction has also been suggested between Cr^{3+}-Cr^{3+}, since according to Goodenough Goodenough (1960), interactions between edge-sharing octahedral cations do not involve an intermediate anion. Because of the 3-dimensional magnetic order, indirect superexchange interactions via *O-Cu-O* links must be considered. Interlayer coupling via *Cr-O-Cu-O-Cr* "super-superexchange" interactions, indicated in the figure, must be taken into consideration to account for the difference between the experimentally observed Néel temperature and the theoretically determined transition temperature $T_{KM} = 15.9$ K Kadowaki *et al.* (1990). The *Cu-O-Cr* angle has been observed to increase upon cooling to 10 K. Since this angle mediates the interlayer superexchange interaction, interlayer coupling is increased as the temperature reduces. Conversely, a weakening of the intralayer *Cr-Cr* interaction is expected to arise due to the increased *Cr-Cr* layer separation as the temperature decreases. With the onset of the antiferromagnetic transition, the CrO_6 octahedron has been reported to relax slightly in the *c* direction Poienar *et al.* (2009), this may be linked to the incommensurate helicoidal magnetic structure. These competing effects may strongly affect the magnetic order at low temperature. These possible exchange mechanisms and their various paths are illustrated in fig. 3.4.

Inelastic neutron scattering has been used to study the spin dynamics in single crystals of $CuCrO_2$ material, and the results have been compared to energy calculations based on the Heisenberg model in order to explore the deviation from the commensurate 120^o spin structure Poienar *et al.* (2010). In-plane antiferromagnetic nearest-neighbour interactions, J_{ab} and J'_{ab}, where J_{ab}, $J'_{ab} > 0$, have been considered in conjunction with in-plane next nearest-neighbour couplings, J_{NN}. The inter-plane contribution, J_c, has also been taken into account, although a weak interaction is expected due to the short magnetic correlation length reported along *c*. In the isotropic or perfectly triangular case, i.e. with $J'_{ab}/J_{ab} = 1$, $J_c = 0$ results in the classical commensurate 120^o spin structure, however $J_c \neq 0$ achieves an incommensurate spin structure with q close but not equal to $1/3$, unless a strong antiferromagnetic coupling with next nearest-neighbours, J_{NN}, acts to stabilise a collinear phase with $k = (1/2, 1/2, 0)$. In the anisotropic case, with $J'_{ab}/J_{ab} = 1.1$, for example, the incommensurate structure with $q \approx 1/3$ is stabilised, whether or not $J_c = 0$. An even higher J_{NN} coupling is required to maintain the collinear phase in this scenario. Two helicoidal magnetic structures were used to model the experimental dispersion, the circular spin-rotation (or non-modulated) structure, where $S = 3/2$ on each *Cr* site, and the elliptic spin (or

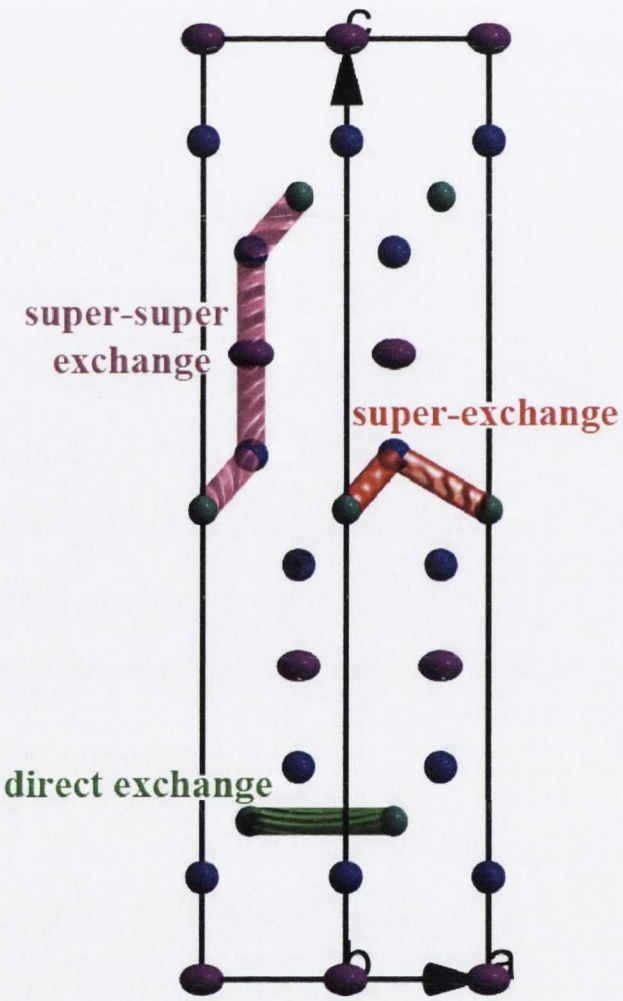

Figure 3.4: Possible exchange mechanisms in $CuCrO_2$

modulated) structure, where the spin on the Cr sites varied due to out-of-plane components. Both the non-modulated and modulated structures required weak antiferromagnetic J_{NN} contributions to stabilise the helicoidal structure, and although J_c could not be quantified it was estimated to be insignificant. It should be noted that the helicoidal magnetic structure of $CuCrO_2$ is very close to that of the classical 120^o structure, in light of the considerable participation of J_{NN}.

The Effect of Doping on the Magnetic Properties It is predicted that the introduction of charge carriers into such a system could induce some interesting effects, since the carriers will be entering a system with a highly degenerate magnetic state. One report observed that the magnetic ordering seemed to be promoted by Mg doping Okuda *et al.* (2008). Despite the introduction of a degree of randomness into the compound, that would usually suppress the order, the residual magnetic frustration appeared to be lifted upon substitution of the nonmagnetic ion. The peak of the antiferromagnetic transition in the magnetic part of the specific heat reportedly became sharper with increasing doping concentration, x, and the temperature at which the peak was observed also increased slightly with increasing x. This effect was also noticed in the magnetisation measurements, the inflection at the antiferromagnetic transition was seen to become increasingly sharp with an increased magnetisation for greater values of x. The conclusion here was that the introduction of holes by substitution of the divalent impurity was responsible for the variations in both magnetisation and resistivity, and crucially, the degree of itinerancy of the doped hole, perhaps stemming from the difference in lattice constant Okuda *et al.* (2007), may have influenced this effect.

Apart from increasing the conductivity, Mg doping was seen to affect only the sharpness of the antiferromagnetic transition and to shift it to a slightly higher temperature. The pronounced transition is indicative of an amplified 3-dimensional character, which could be explained either by a dilution of the magnetic ions alleviating the frustration in the triangular lattice, or by an increase in interlayer coupling. Although the magnitude of the magnetic moment is barely affected and the c component of the spin structure remains, narrower diffraction peaks were reported for 2 % Mg doped $CuCrO_2$ than for the endmember Poienar *et al.* (2009). This could indicate reduced disorder in the impurity doped sample. In terms of the experimental work, particular emphasis was placed on the doping process, and a thorough study of the Mg solubility in the lattice and possible nonstoichiometry effects was carried out. X-ray diffraction revealed a very low solubility limit of 1 % Mg substitution Maignan *et al.* (2009), above which doping concentration, an impurity phase corresponding to the spinel $MgCr_2O_4$ was observed. Variation of the doping concentration

did not significantly impact the effective moment, however the distinctive sharpening of the T_N transition in the susceptibility data with increased Mg substitution was observed. This behaviour is highly suggestive of coupling between the localised spin and itinerant hole.

3.1.3 Electrical Properties

Over the past two decades a vast amount of literature has been published reporting varying electrical properties of the many Cu-based delafossite materials and their doped members. A selection of these reports have been summarised in table 3.2. The wide variation in measured electrical and optical quantities is thought to arise from deviations in stoichiometry Tate *et al.* (2002) Isawa *et al.* (1997) Ashmore & Cann (2005), differences in synthesising techniques Banerjee & Chattopadhyay (2005) Mahapatra & Shivashankar (2003), the presence of both intrinsic and extrinsic defects Ingram *et al.* (2005) Kawazoe *et al.* (2000) Ingram *et al.* (2004a) Ingram *et al.* (2004b) and compensation Robertson *et al.* (2002).

Composition	x	Form	σ (S/cm)	μ (cm^2/Vs)	Type	Bandgap (eV)	Reference
$CuAlO_2$		Bulk	17	0.1	p	1.65 Indirect	Benko & Koffyberg (1984)
$CuAlO_2$		Film	0.3	0.13	p	1.8 Indirect	Yanagi *et al.* (2000a)
$CuAlO_2$		Film	0.95	10.4 [1]	p	3.5 Direct	Kawazoe *et al.* (1997)
$CuAlO_2$		Film	0.34		p	3.5 Direct	Yanagi *et al.* (2000b)
$CuAl_{1-x}Mn_xO_2$	0.03	Bulk	$< 10^{-6}$		p		Kim *et al.* (2004)
$CuAlO_2$		Bulk	0.03	$\sim 8.9 \times 10^{-3}$	p		Ingram *et al.* (2004a)
$CuAlO_2$		Film	0.39		p		Banerjee *et al.* (2005)
$CuAl_{1-x}Mg_xO_2$	0.01	Film	4×10^{-4}		p		Stauber *et al.* (2000)
$CuCrO_2$		Bulk	1×10^{-5}		p		Benko & Koffyberg (1986)
$CuCr_{1-x}Ca_xO_2$	0.05	Bulk	0.01	< 0.1	p	1.28 Indirect	Benko & Koffyberg (1986)
$CuCrO_2$		Film	1	< 1	p	3.1 Direct	Nagarajan *et al.* (2001a)
$CuCr_{1-x}Mg_xO_2$	0.05	Film	220	< 1	p	3.1 Direct	Nagarajan *et al.* (2001a)
$CuCr_{1-x}Mg_xO_2$	0.05	Film	100	< 0.1	p	3.02 – 3.19 Direct	Sadik *et al.* (2009)
$CuCr_{1-x}Mg_xO_2$	0.05	Film	40		p	3.2 Direct	Li *et al.* (2009a)
$CuCrO_2$		Bulk	9.49×10^{-4}		p		Zheng *et al.* (2006)
$CuCr_{1-x}Ni_xO_2$	0.06	Bulk	0.047		p		Zheng *et al.* (2006)
$CuCr_{1-x}Mg_xO_2$	0.07	Film	1		p	2.58 Indirect	Rastogi *et al.* (2008)
$CuCrO_2$		Film	0.86	11.16	p	3.08 Direct	Mahapatra & Shivashankar (2003)
$CuGaO_2$		Film	6.3×10^{-2}	0.23	p	3.6 Direct	Ueda *et al.* (2001)
$CuGaO_2$		Film	5.6×10^{-3}		p	3.4 Direct	Yanagi *et al.* (2000b)
$CuGaO_2$		Film	0.02		p	4.3 Direct	Tate *et al.* (2002)
$CuGa_{1-x}Fe_xO_{2+y}$	0.5	Film	1		p	3.4 Direct	Tate *et al.* (2002)
$CuSc_{1-x}Mg_xO_{2+y}$	0.05	Film	20		p		Tate *et al.* (2002)
$CuScO_2$		Film	1.16×10^{-4}			3.7 Direct	Kakehi *et al.* (2003)
$CuScO_{2+y}$		Film	0.2		p	3.6 Direct	Kykyneshi *et al.* (2004)
$CuSc_{1-x}Mg_xO_2$	0.06	Film	1.5×10^{-2}		p	3.6 Direct	Kykyneshi *et al.* (2004)
$CuSc_{1-x}Mg_xO_{2+y}$	0.05	Film	25		p	3.6 Direct	Kykyneshi *et al.* (2004)
$CuScO_2$		Bulk	0.37 [2]	0.05	p		Ingram *et al.* (2004b)
$CuSc_{1-x}Mg_xO_2$	0.05	Bulk	2.28 [2]	0.03	p		Ingram *et al.* (2004b)
$CuScO_{2+y}$		Film	30		p		Duan *et al.* (2000)
$CuYO_{2+y}$		Films	0.02		p	3.5 Direct	Jayaraj *et al.* (2001)

Continued on next page ···

[1] This value was later revised down to 0.13 cm^2/Vs Yanagi *et al.* (2000a)

[2] Measured at 740 °C

Composition Continued ···	x	Form	σ (S/cm)	μ (cm^2/Vs)	Type	Bandgap (eV)	Reference
$CuY_{1-x}Ca_xO_2$	~ 0.02	Films	1	< 1	p	3.5 Direct	Jayaraj *et al.* (2001)
$CuYO_2$		Bulk	0.018 [2]	0.04	p		Ingram *et al.* (2004b)
$CuY_{1-x}Ca_xO_2$	0.05	Bulk	0.26 [2]	0.05	p		Ingram *et al.* (2004b)
$CuYO_2$		Films	0.025		p	3.5 Direct	Nagarajan *et al.* (2001b)
$CuY_{1-x}Ca_xO_2$	~ 0.02	Films	1.05		p	3.5 Direct	Nagarajan *et al.* (2001b)
$CuIn_{1-x}Sn_xO_2$	0.05	Film	3.8×10^{-3}		n	$\sim$ 3.9 Direct	Yanagi *et al.* (2001a)
$CuIn_{1-x}Ca_xO_2$	0.07	Film	2.8×10^{-3}		p	$\sim$ 3.9 Direct	Yanagi *et al.* (2001a)
$CuIn_{1-x}Sn_xO_2$	0.05	Bulk	4.4×10^{-1} [1]		n	1.44 Indirect	Sasaki & Shimode (2003)
$CuIn_{1-x}Ca_xO_2$	0.05	Bulk	2.7×10^{-4} [1]		p	1.44 Indirect	Sasaki & Shimode (2003)
$CuIn_{1-x}Ca_xO_2$	0.05	Film	3×10^{-3}		p	4.15 Direct	Teplin *et al.* (2004)
$CuNi_{2/3}Sb_{(1-x)/3}Sn_{x/3}O_2$	0.1	Film	0.05		p	3.4 Direct	Tate *et al.* (2002)
$CuCoO_2$		Single crystal	5×10^{-6}				Rogers *et al.* (1971)
$CuEuO_{2.65}$		Bulk	0.065				Isawa *et al.* (1997)
$CuLaO_2$		Bulk	0.032		p	2.8	Takahashi *et al.* (2007)
$CuNdO_{2.62}$		Bulk	1.8				Isawa *et al.* (1997)
$CuPrO_{2.62}$		Bulk	0.13				Isawa *et al.* (1997)
$CuSmO_{2.63}$		Bulk	0.22				Isawa *et al.* (1997)
$CuBO_2$		Film	1.65		p	2.2 Indirect	Snure & Tiwari (2007)
$CuFeO_2$		Single crystal	2				Rogers *et al.* (1971)
$CuFeO_2$		Single crystal [2]	3.1×10^{-4} [3]	1.1×10^{-4}	n	1.26 Indirect	Dordor *et al.* (1988)
$CuFe_{1-x}Sn_xO_2$	0.01	Bulk	3.2×10^{-5}	1.1×10^{-6}	n	1.26 Indirect	Dordor *et al.* (1988)
$CuFeO_2$		Bulk	1.5	0.27	p	1.15 Indirect	Benko & Koffyberg (1987)
$CuFe_{1-x}Mg_xO_2$	0.05	Bulk	8.9	0.12	p	1.15 Indirect	Benko & Koffyberg (1987)
$CuFe_{1-x}Sn_xO_2$	0.05	Bulk	2.4×10^{-4}	2.7×10^{-6}	n	1.15 Indirect	Benko & Koffyberg (1987)

Table 3.2: Basic electrical properties of some delafossite oxides

[1] Measured at 600 K

[2] Crystals were synthesised by flux in a Cu crucible with a $LiBO_2$ flux

[3] Conductivity was highly anisotropic

Conductivity The mechanism behind the electrical transport in the Cu-based delafossites is a topic that has engaged many research groups in recent years, and explanation of the extremely high conductivity reported in 5 % Mg-doped $CuCrO_2$, which currently holds the record at 220 S/cm Nagarajan *et al.* (2001a), remains a contentious issue. In second place, Mg-doped $CuScO_2$ has been reported to exhibit a conductivity of 30 S/cm Nagarajan *et al.* (2001b), an order of magnitude lower than the paragon of p-type TCO conductivity, Mg:$CuCrO_2$, but yet far greater than the undoped, stoichiometric compound. The influence of both the electronic band structure and the crystal chemistry of these materials on their electrical properties has been discussed conceptually in previous sections, here we examine the experimental observations.

The potency of extrinsic impurity doping in enhancing electrical conductivity is clear in a number, but not all, of these materials. The electrical properties of some of the lesser conducting undoped delafossites have been observed to ameliorate upon exposure to an oxidising environment due to the intercalation of excess oxygen ions in the interstices of the lattice Cava *et al.* (1993) Nagarajan *et al.* (2001b) Kawazoe *et al.* (1997). The $CuCrO_2$ lattice is reputed to be a poor acceptor of excess oxygen Tate *et al.* (2002) Rastogi *et al.* (2008), however the conductivity of $CuScO_2$ and $CuYO_2$ have been widely reported to profit from annealing in oxygen atmosphere Duan *et al.* (2000) Isawa *et al.* (1997). This would appear to indicate that there is more than one conduction mechanism operating in these materials. Conductivity improvements in other delafossites, such as $CuAlO_2$, have been attributed to cation vacancy defects Marquardt *et al.* (2006) Hamada & Katayama-Yoshida (2006) or nonstoichiometric cation ratios Ingram *et al.* (2005) Ingram *et al.* (2004a).

The various deposition techniques employed in thin film fabrication and powder synthesis methods can influence the phase Rastogi *et al.* (2008), crystallinity Li *et al.* (2007), grain size and grain homogeneity, and porosity McLachlan *et al.* (1990) of the material, thereby also affecting the sample conductivity. Pulsed laser deposition (PLD) has been found effective in realising oriented thin films of $CuCrO_2$ with low impurity levels and high crystallinity Li *et al.* (2007) Sadik *et al.* (2009). Metal-organic chemical vapour deposition (MOCVD) Mahapatra & Shivashankar (2003) and rf sputtering Nagarajan *et al.* (2001a) Tate *et al.* (2002) have also been employed for film deposition, and some of the lower temperature fabrication processes, such as spray pyrolysis, require post-deposition annealing to eliminate additional impurity phases Rastogi *et al.* (2008). Single crystals have been grown by a flux decomposition method Crottaz *et al.* (1996) Kimura *et al.* (2008)[1]. Powder samples have been prepared by solid state reaction Doumerc *et al.* (1986) Okuda *et al.*

[1] Using a Bi_2O_3 flux

(2005) Kadowaki *et al.* (1990) Poienar *et al.* (2009), hydrothermal synthesis Zhou *et al.* (2008) and the sol-gel method Deng *et al.* (2009). Grain boundary scattering has been speculated to inhibit the conductivity in the Cu-based delafossites Isawa *et al.* (1997) Isawa *et al.* (1998) Rastogi *et al.* (2008), whereas increased crystallinity in thin film samples is expected to enhance the conductivity. The low dopant solubility levels observed in bulk delafossite materials may also be a conductivity limiting factor Maignan *et al.* (2009) Rastogi *et al.* (2008), however, as is often the case, the solubility level itself may increase in thin film samples with high crystallinity, thereby increasing the supply of holes.

Conductivity measurements provide useful insights into the electrical transport mechanism in operation in a material. Arrhenius plots of the thermal conductivity variation, $ln\ \sigma$ as a function of $10^3/T$, permit extraction of the activation energy of the defect levels within the material according to the relation $\sigma = \sigma_0\ exp(-E_a/k_BT)$ where E_a is the activation energy. Initial studies of the electrical performance of these materials were persuaded by a mechanism of small polaron hopping conduction between Cu^{1+} and Cu^{2+} ions [1] Benko & Koffyberg (1986) Benko & Koffyberg (1984) Benko & Koffyberg (1987) since the Hall mobility was found to be extremely low[2]. It is currently generally accepted, however, that there are two transport regimes in operation in the cuprous-delafossites Okuda *et al.* (2005). Activated conductivity, characteristic of band model behaviour, functions in the higher regime (close to room temperature and above) Rastogi *et al.* (2008), while variable range hopping small polaronic conduction, $ln\ \sigma \propto -T^{-1/4}$, prevails in the lower temperature region Ingram *et al.* (2001). These reports have supported their assertions of small polaronic behaviour with thermoelectric measurements and high temperature electrical characterisation that indicate extremely low carrier mobility in the delafossite materials, and thermopower (hole content) that is essentially independent of temperature while the conductivity, and hence mobility, is thermally activated Ingram *et al.* (2001).

Mobility The mobility of many of the lesser conducting delafossites have been reported, as evidenced in the reported electrical properties in table 3.2, however these values are found to be extremely low, in some cases too low to measure. Thermoelectricity measurements are used to determined the carrier mobility from the thermopower Ingram *et al.* (2005), however these measurements are ineffective on thin film samples due to the inhibiting substrate. To the author's knowledge, Hall effect data has been measured on Cu-based delafossite samples only twice Kawazoe

[1] The Cu^{2+} being formed from Cu^{1+} by a charge-compensating process initiated by M^{II} divalent cation substitution for the M^{III} cation

[2] $\mu < 0.1\ cm^2/Vs$

et al. (1997) Mahapatra & Shivashankar (2003), giving Hall mobilities of 10.4 cm^2/Vs and 11.16 cm^2/Vs for undoped $CuAlO_2$ and $CuCrO_2$ thin film samples respectively. The former figure was later retracted in favour of 0.13 cm^2/Vs Yanagi *et al.* (2000a), which perhaps gives an indication of the difficulty in acquiring Hall effect parameters in these low conductivity, low mobility materials.

Effective mass theory relates the effective mass, and hence the mobility of electrical carriers, to the shape of the conduction band minimum (n-type conduction) or valence band maximum (p-type conduction) in a semiconductors band structure, as described in chapter 2, assuming the bands are parabolic at the band edges Scanlon *et al.* (2009b). The effective masses of $CuAlO_2$, $CuYO_2$, $CuScO_2$ and $CuCrO_2$ were calculated in this way revealing $CuCrO_2$ to have the lowest hole effective mass at the valence band maximum. However, studies on the band structure of a number of the Cu-based delafossites have revealed little dispersion and high densities of states at the valence band maxima rendering the assumption of parabolic bands invalid Scanlon *et al.* (2010). A theoretical study of the valence band alignment of $CuAlO_2$, $CuYO_2$ and $CuScO_2$ Shi *et al.* (2008) revealed that, of the three materials, $CuScO_2$ has both the lowest carrier effective mass, and the highest valence band maximum relative to the vacuum level, which suggests that it is easier to dope p-type according to the doping limit rule Zhang *et al.* (1998) Zhang *et al.* (2000). This finding is in agreement with the experimental observation that it has the highest conductivity Duan *et al.* (2000) of the three. In calculations for $CuCrO_2$, covalent interactions between the Cr $3d$ states and their O neighbours, that have in turn hybridised with Cu $3d$ states, ensures an increased density of states at the valence band maximum and a narrowing of the bandwidth. The consequential low curvature of the valence band maximum indicate a high effective mass for the holes and hence a low carrier mobility Scanlon *et al.* (2009a).

Small Polarons The Cu-based delafossites share some properties in common with the much studied, p-type antiferromagnetic transition metal oxide NiO. In general, they both exhibit low mobilities and narrow bandwidths Morin (1954). NiO was found to exhibit a large activation energy which initially showed a dramatic decrease upon low-level doping with Li but was observed to converge to a virtually constant activation energy above 2 % Li doping concentration Heikes & Johnston (1957), which was attributed to a mobility activation energy in the thermally activated hopping mechanism of conduction Bosman & van Daal (1970).

The electronic transport mechanism in operation in ionic materials differs from that of the Drude free electron gas in that there are interactions between the ions and the charge carriers. As a consequence of this, ionic materials can exhibit far greater carrier effective masses and far

inferior mobilities to those of metals and the degenerate n-type transparent semiconductors that have been discussed in chapter 2. The polar interactions between the ions and the carriers are Coulombic in nature, and this has the effect of forming a potential well that can trap the carriers. A trapped carrier interacts with the crystal lattice via phonons creating a distortion in the lattice, and this "dressed" carrier is known as a polaron Hirsch (1995). The polaron can be large or small depending on the range of its influence over the lattice. We are more concerned with small polarons, however, whose distortion of the lattice extends no further than one interatomic spacing. Significant carrier-lattice interactions and narrow bandwidths are peculiar to these quasi-particles Bosman & van Daal (1970).

Small polaron transport of the trapped carriers is conducted by hopping between localised sites. At low temperatures small polaron band conduction or variable range hopping mechanism operates, while small polaron hopping transport, a diffusion process characterised by an activated mobility, functions at high temperatures. Variable range hopping conduction refers to the tunnelling of the trapped carriers between sites. The temperature dependence of this conduction mechanism has been described by the following relation Mott (1968)

$$\sigma = \sigma_{VRH} exp(-BT^{-1/4}) \tag{3.7}$$

where

$$B = 2\left(\frac{3}{2\pi}\right)^{\frac{1}{4}}\left(\frac{\alpha^3}{k_{\mathrm{B}}N(E_F)}\right)^{\frac{1}{4}} \tag{3.8}$$

and

$$\sigma_{VRH} = \frac{3}{2}e^2\nu\sqrt{\frac{N(E_{\mathrm{F}})}{2\pi\alpha k_{\mathrm{B}}T}} \tag{3.9}$$

assuming α is a coupling constant, $N(E_{\mathrm{F}})$ is the density of states at the Fermi level, and ν is the phonon vibration frequency. This description of the conduction is still disputed however, and a more general formalism of the conduction mechanism has been put forth with $ln\ \sigma \propto T^{-n}$ where $1/4 < n < 1/2$ Hamilton (1972).

Despite the general consensus that a variable range hopping conduction mechanism operates in the lower regime, while activated behaviour dominates at higher temperatures in the Cu-delafossites, there has been one report of high temperature resistivity measurements on polycrystalline $CuCr_{1-x}Mg_xO_2$ ($x = 0.01, 0.02$) samples Maignan *et al.* (2009) that indicate small polaron hopping behaviour[1] in the higher temperature region wherein thermal activation is observed for the undoped materials.

[1] $ln(\rho/T) \propto T^{-1}$ Maignan *et al.* (2009)

Magnetoresistance Resistivity measurements in reducing temperatures carried out on antiferromagnetic polycrystalline Mg-doped $CuCrO_2$ samples have revealed an anomalous profile at low temperatures Okuda *et al.* (2005) Maignan *et al.* (2009). A kink appears in the resistivity around the Néel temperature in the otherwise semiconducting ρ versus T characteristics for 2 % and 3 % doping concentrations. Interesting magnetoresistance behaviour has also been reported for Mg-doped $CuCrO_2$ polycrystalline samples, suggesting that there is a coupling between the doped hole and the local spin at the Cr-site Okuda *et al.* (2005) Okuda *et al.* (2007). The magnetoresistance, defined by the relation $MR(\%) = 100 \times [\rho(H) - \rho(H = 0)]/\rho(H = 0)$, as discussed in chapter 2, has been observed to be negative in the variable range hopping temperature regime in $CuCr_{0.96}Mg_{0.04}O_2$ samples. Moreover, the negative MR in this region has been observed to increase to a maximum at $\sim$ 30 K, just above the Néel temperature, and then to fall sharply to a minimum value at $\sim$ 20 K, just below T_N, after which point the MR begins to increase again with reducing temperature. In another report, a similarly non-monotonic MR effect has been discerned, again in 4 % Mg-doped $CuCrO_2$ bulk samples Maignan *et al.* (2009). The measurement exhibits a maximum MR = 19 % at 5 K in a 7 T field, above which temperature the MR decreases to $\sim$ 0 at 25 K. A sharp increase in the magnitude of the MR has again been observed at 30 K, which then decreases progressively until it can no longer be measured above around 70 K. This negative MR behaviour above T_N has been attributed to reduced spin scattering upon application of a magnetic field, and the onset of the antiferromagnetic ordering at T_N has been deemed responsible for the subsequent MR drop, by blocking the charge hopping until the former behaviour resumes at lower temperature.

3.1.4 Motivation

One of the foremost objectives of this project was to fabricate thin films of a p-type delafossite transparent conducting oxide possessing semiconducting properties that were suitable for implementation in an operational transparent electronic device while maintaining a certain degree of film transparency, and $CuCrO_2$, with its high conductivity was the ideal candidate. In order to achieve this goal, each step in the development process from powder synthesis through to thin film deposition had to be optimised using structural and electrical characterisation to determine the most appropriate synthesis and growth conditions. To this end, a number of powder preparation methods have been investigated and a thorough scan of the growth conditions has been carried out.

In particular it was necessary to determine the electrical properties that could be achieved through acceptor-impurity substitution and the further implications of doping on the material. A study of the dopant solubility limit in the powder material, together with an investigation of high level impurity substitution in the typically more receptive thin films has allowed us to gain an insight into the effects of doping in this material. This would enable the determination of the optimum doping concentration to use in the potential device in the subsequent part of this project. A further aim of the study was to examine the interesting relation between the electric and magnetic properties of $CuCrO_2$ that have excited some interest in the research community for whom the conduction mechanism in operation in the delafossite materials is not fully understood. This aspect has been considered in relation to the effect of increased impurity doping in the system. In view of these objectives, structural, optical, magnetic, and electrical investigations have been carried out on a number thin film samples with varying doping levels.

3.2 Powder Preparation and Analysis

The initial step towards achieving high quality, crystalline $CuCrO_2$ thin films by the technique of PLD is to prepare powder-derived, dense, stoichiometric targets to use as the source material for ablation. It was necessary, therefore, to examine the basic structural and morphological properties of these polycrystalline samples.

3.2.1 Synthesis

A number of powder synthesis techniques have been reported for this material. In this work, the methods of solid state reaction and sol-gel were compared with a view to obtaining an optimally sintered target, which is essential for effective growth in the PLD process.

3.2.1.1 Solid State Reaction

The preparation of synthetic minerals involving high temperature reactions has traditionally been carried out by solid state reaction. The basic principle behind this method is the mixing of a number of reactants under exposure to an external energy source (usually heat) which initiates the reaction. If this energy is sufficiently high to activate the reaction, the resultant products will correspond to a thermodynamically stable compound. In order to obtain the desired material, a knowledge of the phase diagram of the reactants is necessary in order to choose the correct set of experimental conditions (pressure, temperature, etc.).

The most renowned Cu-based delafossite TCO, $CuAlO_2$, presents a phase diagram with a peritectic point, which places an upper limit on the reaction temperature for this compound Misra & Chaklader (1963). $CuCrO_2$ reportedly presents a contrasting scenario Jacob *et al.* (1986). At temperatures below $\sim$ 1170 K, a stoichiometric mixture of copper oxide and chromium oxide will not form the desired $CuCrO_2$ phase, a mixture of the spinel $CuCr_2O_4$ and CuO will form instead. For higher reaction temperatures $CuCrO_2$ will form, and the experimental phase diagram does not indicate any decomposition of this phase up to at least 1600 K Gadalla & White (1964). $CuCrO_2$ powder was, therefore, prepared by solid state reaction, the technical details for which are described in appendix A.

To investigate the evolution of the electrical properties of $CuCrO_2$ thin films doped with Mg, it was necessary to prepare targets thus doped. In order to determine the solubility limit of Mg in $CuCrO_2$ the doped compounds $CuCr_{1-x}Mg_xO_2$ with (x = 0 %, 0.5 %, 1.0 %, 1.5 %, ... , 4.0 %) were prepared. Despite reports of a relatively low solubility limit Okuda *et al.* (2005) Maignan *et al.* (2009), it was decided to synthesise powders of $CuCr_{1-x}Mg_xO_2$ with (x = 5 %, 8 %, 10 %) from which to prepare targets for ablation. It is generally believed that thin film samples are more receptive to impurity substitution than their bulk counterparts [1].

3.2.1.2 Sol-gel

One way to improve the sintered quality of polycrystalline ceramics is to start with smaller grains, thereby increasing the exposed surface area for reaction. This can be achieved by either mechanical grinding or through a soft chemistry technique, where the reaction temperatures are much lower compared to the standard solid state reaction. We chose to use a sol-gel method adapted from Li *et al.* (2007). The basic principle of the sol-gel technique is to form a colloidal solution of a metal salt (the "sol") in a polymeric network (the "gel"). After the gelling process, the removal of the solvent, produces a precursor that forms the end compound upon firing. The experimental conditions are described in more detail in appendix A. The precursor was heated to various temperatures in the range, 973 to 1223 K in 50 K intervals, in order to determine the best conditions to achieve the $CuCrO_2$ phase.

3.2.2 Structural Characterisation

Phase analysis of the powders produced by the above methods was carried out using powder x-ray diffraction as detailed in appendix B. The x-ray diffraction patterns of the $CuCrO_2$ powder

[1] Although, it is not certain whether full stoichiometric transfer is completed during PLD.

prepared by solid state reaction at various temperatures are presented in fig.3.5. The phases present in the diffractograms were identified initially by comparison with the JCPDS database. Patterns without any traces of byproduct impurities, such as Cu_2O, CuO, and $CuCr_2O_4$, are obtained for reaction temperatures above 1173 K. Similar behaviour is observed for the polycrystalline sample synthesised by sol-gel method. This finding makes the perceived advantage of the reduced temperature sol-gel method irrelevant, and the technique therefore redundant. As a consequence of this finding, all of the Mg-doped $CuCrO_2$ powder samples were produced by solid state reaction at the optimised temperature of 1173 K.

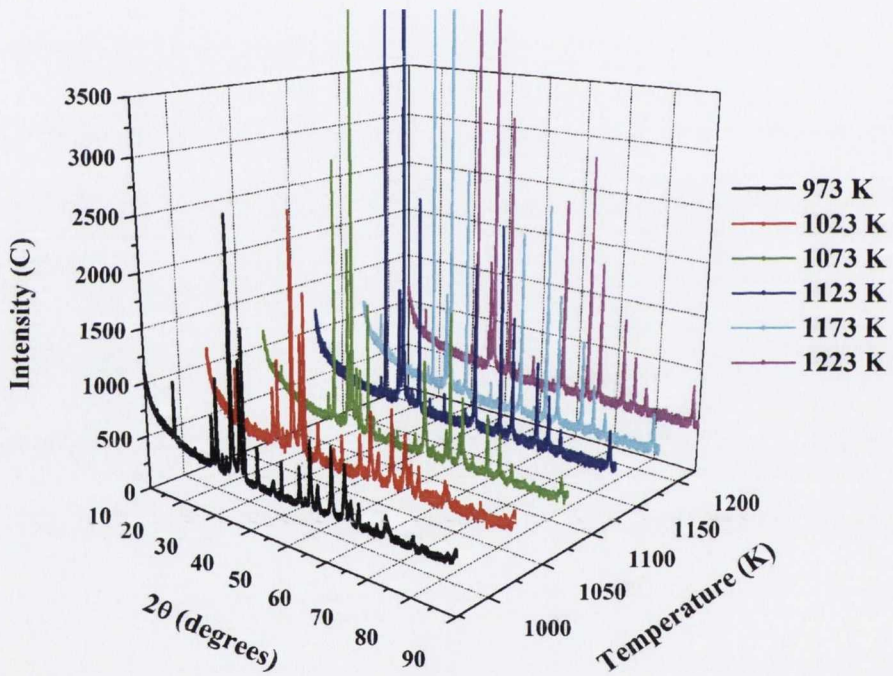

Figure 3.5: Reaction temperature scan of $CuCrO_2$ powder prepared by solid state reaction.

In order to extract further crystallographic information from the undoped $CuCrO_2$ powder synthesised at 1173 K, the diffraction pattern was refined, using the Rietveld method[1], with the delafossite structure, whose crystallographic parameters are presented in table 3.3. All of the Bragg peaks in the diffraction pattern are indexed with the space group $R\bar{3}m$ and with lattice parameters $a = b = 2.9705(6)$ Åand $c = 17.0999(1)$ Å.

The diffraction peaks have a narrow profile that is characteristic of a sample with highly crystallised large grains. The rhombohedral symmetry of the compound often results in the growth

[1]The FullProf Suite freeware was used for all of the refinements.

Crystal System			Rhombohedral	
Space Group			$R\bar{3}m$	
Group Number			166	
Atom	Wyckoff Notation	x	y	z
Cu	3(a)	0	0	0
Cr	3(b)	0	0	1/2
O	6(c)	0	0	z

Table 3.3: Fractional Atomic Coordinates of Rhombohedral Cuprous Chromite $CuCrO_2$.

of crystal platelets, which has the effect of creating non-random orientation of the powder specimen, particularly in the geometry used for the measurement, thereby distorting the intensity. To overcome this, the problematic (006) and (104) peaks were excluded from the dataset used for the refinement[1] which is shown in fig. 3.6.

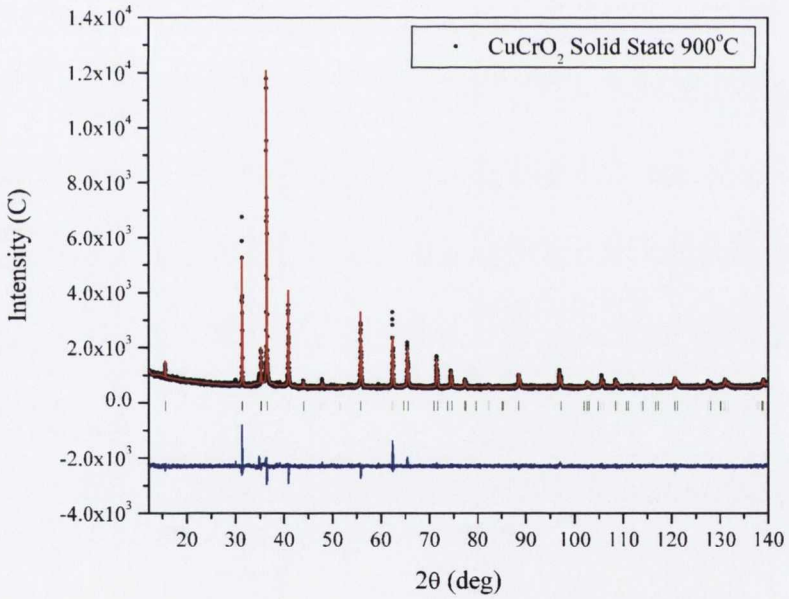

Figure 3.6: Rietveld powder refinement of $CuCrO_2$ powder. The powder was prepared by solid state method and sintered at 1173 K

Although the previous issue of preferential orientation in the powder sample was inherent to

[1]The atomic thermal displacements used for the refinements were set to the values obtained by Poienar *et al.* (2009)

the material microstructure, a further refinement issue arose due parasitic wavelengths in the XRD system. Deterioration of the tungsten filament in the sealed Cu x-ray tube used in the diffractometer over time leads to the production of x-rays with the W L_α wavelength ($\lambda = 1.47642$ Å). A secondary pattern arises in the diffractogram due this additional wavelength radiation, the resulting Bragg peaks are identified in the 3.7.

The Mg-doped $CuCrO_2$ powders were also characterised by XRD and their diffraction patterns are presented in fig. 3.7. The powder remained single phase for values $0\ \% \leq x \leq 1.0\ \%$ but the emergence of a $MgCr_2O_4$ impurity phase was observed in the diffractograms for higher doping concentrations, hence the doping limit of the $CuCrO_2$ powder was found to be $x = 1.0\ \%$, considerably less than the 4 % and 3 % values previously reported Okuda *et al.* (2005)Okuda *et al.* (2008) Maignan *et al.* (2009). The low solubility limit of Mg ions in the lattice can be explained by considering the ionic radii of the Cr^{3+} ions (0.615 Å) that are substituted by Mg^{2+} ions (0.72 Å) in octahedral coordination. The substitution of an ion with a radius, larger than the original by 17 %, is likely to induce significant strain in the CrO_2 layers, rendering this substitution energetically unfavourable.

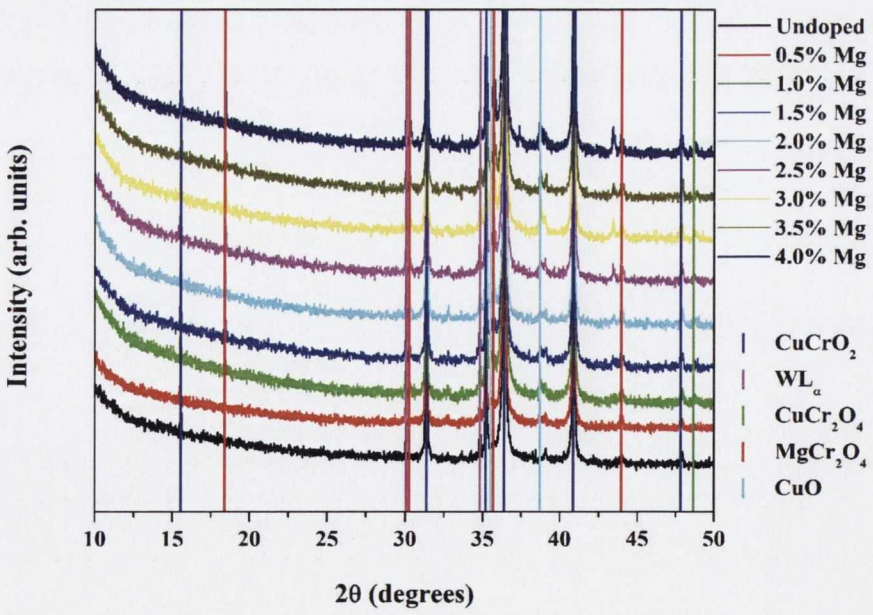

Figure 3.7: X-Ray diffraction patterns of $CuCr_{1-x}Mg_xO_2$ powders with $0\ \% \leq x < 4.0\ \%$, showing impurity phases

The previous work on Mg substitution in the $CuCrO_2$ lattice showed an inverse relationship between the a parameter, which should decrease, and the c, which should expand with increased doping Poienar *et al.* (2009) Okuda *et al.* (2005). A maximum change of -0.04 % change in the a parameter and 0.06 % for the c lattice parameter were observed, while the volume of the cell remained constant. The variation of a and c lattice parameters with doping concentration x, obtained from Rietveld refinement, is presented in fig. 3.8. The results do not indicate a particular monotonic trend in the evolution of the lattice parameters. However, the appearance of the $MgCr_2O_4$ impurity phase above 1 % Mg doping concentration precludes the accurate determination of the values of a and c.

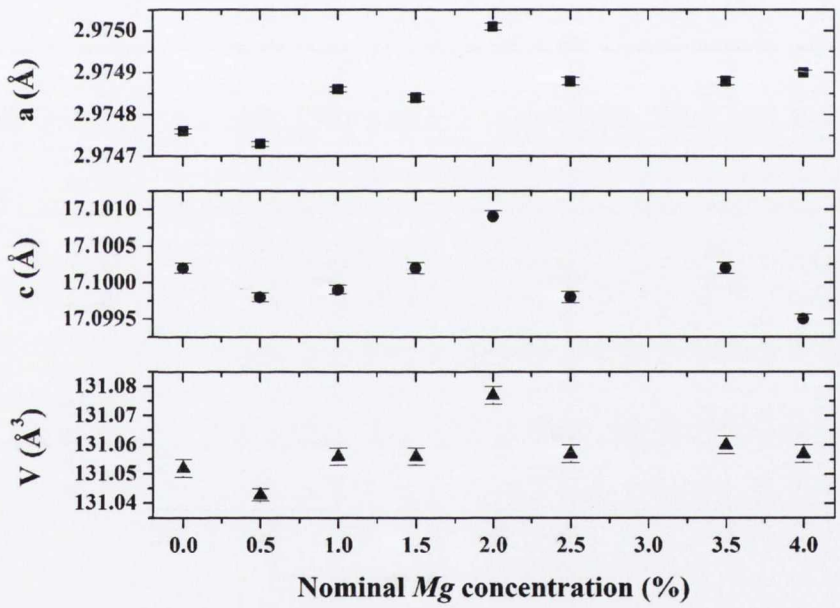

Figure 3.8: Variation of a and c lattice parameters and cell volume, V, of $CuCrO_2$ powder with Mg doping concentration x

3.2.3 Morphological Characterisation

Although an earlier powder diffraction file, number 00-039-0247, from the JCPDF database agreed with the experimentally observed ratio of intensities, the latest revision of the $CuCrO_2$ powder diffraction file, number 04-010-3330, has recorded an intensity ratio of (325:340) between the (006) and (104) peaks. The relative intensities of the (006) and (104) peaks in the diffractograms,

(600:300), did not agree with their simulated intensities, indicating a strongly oriented character in the powder samples. In order to investigate the microstructural properties of the polycrystalline samples, scanning electron microscopy was carried out by Cédric Leuvrey, on undoped and 10 % Mg-doped $CuCrO_2$ powders.

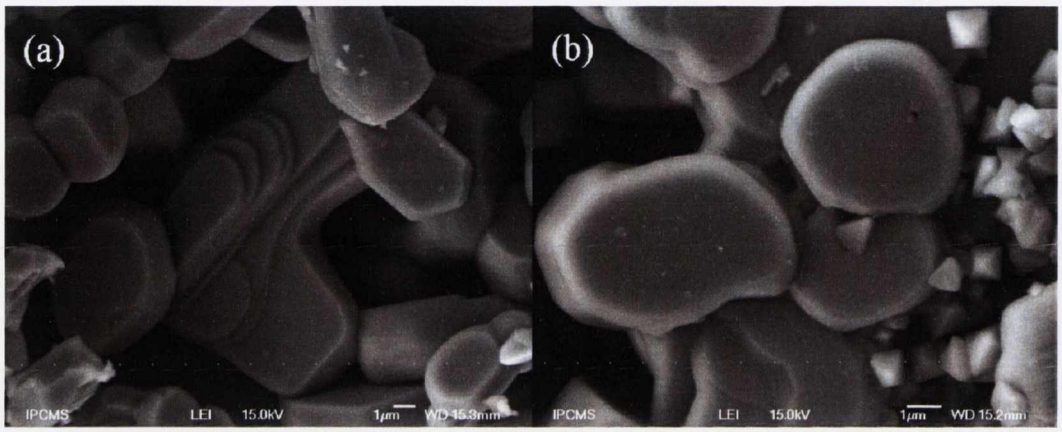

Figure 3.9: SEM images of (a) $CuCrO_2$ and (b) 10 % Mg-doped $CuCrO_2$ powder samples

SEM examination of the undoped powder, shown in fig. 3.9 (a), revealed that the powder was composed of large platelets, an effect also observed by Maignan *et al.* (2009). The observed morphology is expected for a compound with a rhombohedral crystal structure, the c axis being normal to the face of the platelets, verifying the preferred orientation observed by x-ray diffraction. The appearance of steps on the plate surface is a typical feature of layered systems.

Analysis of the 10 % Mg-doped bulk sample revealed a segregated phase consisting of smaller octahedral crystallites amid the large delafossite platelets in fig. 3.9 (b). Energy dispersive x-ray spectroscopy (EDX) analysis indicated that the global Mg stoichiometry corresponded to the nominal doping concentration. Spot analysis of a platelet revealed that the relative stoichiometry corresponded to $CuCrO_2$ with a very minor concentration of Mg (< 2 %). Conversely, spot analysis on two distinct octahedrons, indicated that the relative stoichiometry of ions corresponded to $MgCr_2O_4$ and $CuCr_2O_4$ spinel phases respectively. Observation of the spinel phase, $MgCr_2O_4$, is unsurprising since the Mg-doping concentration has far exceeded the solubility limit of $CuCrO_2$ in powder form, confirming the previous x-ray diffraction observations. Although the powder used to prepare targets for PLD was not entirely the pure $CuCrO_2$ phase, this is not prohibitive for deposition of thin films containing the nominal doping concentration once the overall stoichiometric ratio of the elements is correct, and their distribution on a scale of millimetres is homogenous.

3.2.4 Magnetic Properties

The magnetic properties of the doped and undoped $CuCrO_2$ powders were examined by SQUID (Superconducting Quantum Interference Device) magnetometry. The magnetic moment per unit mass, σ, of the material was measured as a function of temperature for varying Mg-doping concentrations with Dr. M. Venkatesan, x, in the range $0\ \% \leq x < 4.0\ \%$ at 0.5 % increments. The measurements were carried out in an applied magnetic field of 0.5 T and they are presented in fig. 3.10. The main feature in the measurement is the antiferromagnetic transition, observed at approximately 25 K, which corresponds to the Néel temperature of $CuCrO_2$. Another transition was also exhibited in the magnetisation of the undoped $CuCrO_2$ powder at around 135 K. This can be attributed to the presence of an impurity phase of $CuCr_2O_4$, a ferrimagnet with a Curie temperature of 135 K Ok *et al.* (1989). The rest of the doped powders also exhibit this inflection feature, but to a lesser extent. A further feature to emerge in this measurement was an upturn below the Néel temperature of $CuCrO_2$. Upon closer examination and comparison with x-ray diffraction patterns the occurrence of this feature coincided with the presence of the impurity phase $MgCr_2O_4$, a reputed antiferromagnet with a Néel temperature of 16 K Shaked *et al.* (1970). Observation of the spinel impurity, $CuCr_2O_4$, by magnetometry and its absence in the x-ray diffraction pattern is a good example of the surpassing of the limit of detection of XRD.

Attempts were made to remove the spinel impurity phases from the $CuCrO_2$ powder by washing it with HNO_3 acid. This, however, was found to achieve the opposite effect removing the delafossite and leaving only the $CuCr_2O_4$ spinel behind. In a subsequent effort to produce phase pure $CuCrO_2$ powder and, in particular, to eliminate the $CuCr_2O_4$ spinel impurity phase observed above, the powder preparation was carried out in a Pt crucible under a flow of Ar gas, in order to perform the reaction in a less oxidising medium. $CuCrO_2$ powder with a 2 % Mg doping concentration was also prepared using this method. The evolution of the magnetic moment of these samples as a function of temperature is shown in fig. 3.11. In this case, the inflection in the region of 135 K is no longer observed. This confirms the magnetic phase purity of the sample prepared in less oxidising conditions than in air.

The data exhibited essentially linear κ^{-1} vs T behaviour in the paramagnetic region at temperatures above 160 K, as shown in fig. 3.12 (a), in accordance with the Curie-Weiss law $\kappa = C/(T + \theta_{\mathrm{CW}})$ where κ is the dimensionless susceptibility, $C = (\mu_0 N \mu_{eff}^2)/(3k_{\mathrm{B}})$[1] is the Curie constant, $\mu_{eff} = 2\sqrt{S(S+1)}$ is the spin-only effective magnetic moment[2], and θ_{CW} is the Curie

[1] N is the concentration of spins per m^3

[2] For Cr^{3+} ions, the orbital moment is quenched.

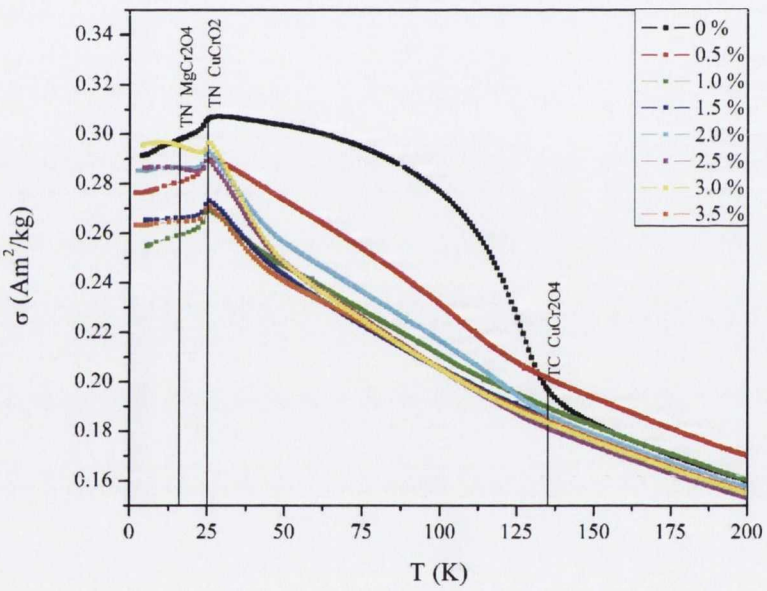

Figure 3.10: The temperature dependence of the magnetic moment per unit mass, σ, of $CuCr_{1-x}Mg_xO_2$ powders with 0 % $\leq x <$ 4.0 % measured in an applied magnetic field of 0.5 T

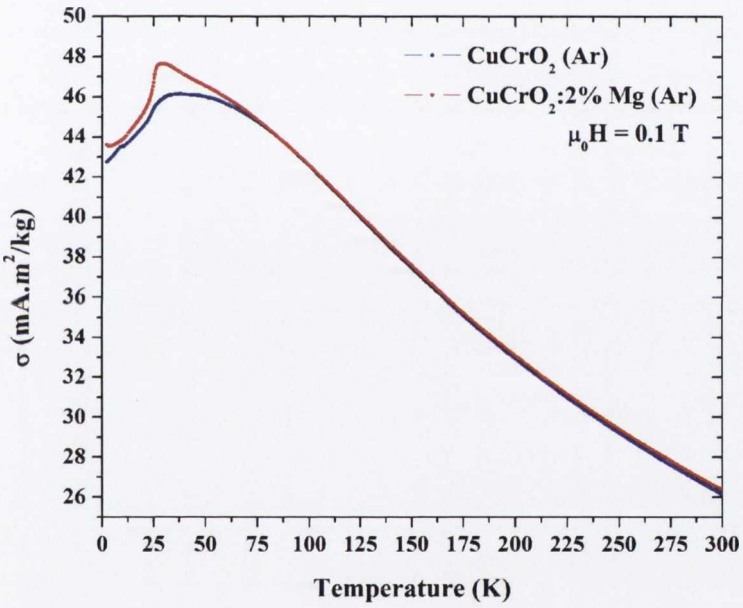

Figure 3.11: The temperature dependence of the magnetic moment, σ, of $CuCr_{1-x}Mg_xO_2$ powders with $x = 0$ %, 2 % measured in an applied magnetic field of 0.1 T

temperature. A very slight deviation from linearity was observed at higher temperatures, this has been explained by higher order corrections using the high temperature series expansion of the reciprocal susceptibility Doumerc *et al.* (1986).

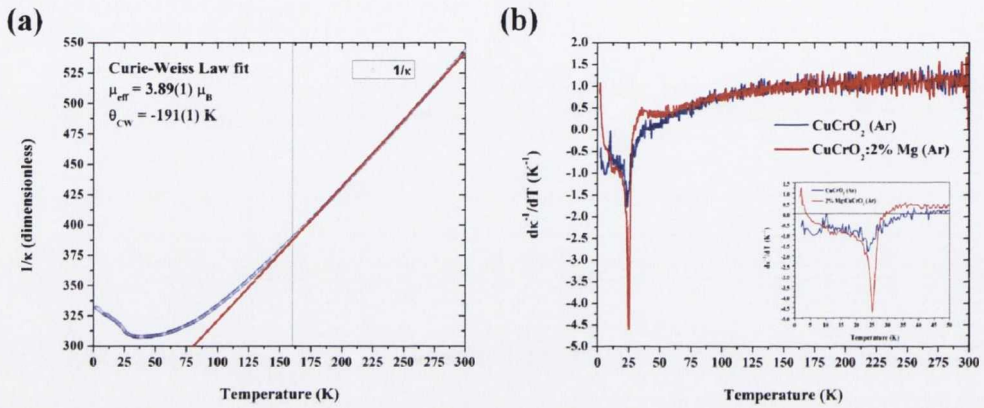

Figure 3.12: (a) Curie-Weiss law fit of the temperature dependence of the inverse dimensionless susceptibility, κ^{-1}, of undoped $CuCrO_2$ powder measured in an applied magnetic field of 0.1 T. (b) First derivative of the inverse molar susceptibility as a function of temperature, $\partial\kappa^{-1}/\partial T$ vs T, of both the undoped $CuCrO_2$ and 2 % Mg-doped powders measured in an applied magnetic field of 0.1 T.

The Curie-Weiss temperature that has been extracted from the fitting gave a value of θ_{CW} = -191(1) K which is largely in agreement with reported figures, many of which are displayed in table 3.1. The effective magnetic moment has been determined to be μ_{eff} = 3.89(1) μ_B/Cr, which is extremely close to the expected spin-only effective moment of 3.87 μ_B/Cr for $S = 3/2$ Cr^{3+} ions in high spin octahedral coordination t_{2g}^3. The slight overestimation of the effective moment on the Cr ions is a result of the minor digression of the inverse susceptibility from linearity at high temperature explained by Doumerc *et al.* (1986).

At low temperatures, evolution of the first derivative, $\partial\kappa^{-1}/\partial T$ of the inverse susceptibility, shown in fig. 3.12 (b), exhibited a sharp negative discontinuity at $\sim$ 25 K corresponding to the Néel point. This value agrees well with previously reported measurements Kadowaki *et al.* (1990) Ono *et al.* (2007) Li *et al.* (2009b). The results of this magnetic study indicate that phase pure $CuCrO_2$ and 2 % Mg-doped $CuCrO_2$ were achieved by synthesising the powders under an Ar gas flow. To confirm that the spinel impurities were reduced under the detection limit of the SQUID magnometer a hysteresis loop has been measured at 1.8 K. To confirm that the spinel impurities have been reduced below the detection limit of the SQUID magnometer a hysteresis loop has been

measured at 1.8 K. The magnetisation as a function of magnetic field of the undoped powder, shown in fig. 3.13, was linear with no hysteretic behaviour, confirming the absence of ferromagnetism in the compound.

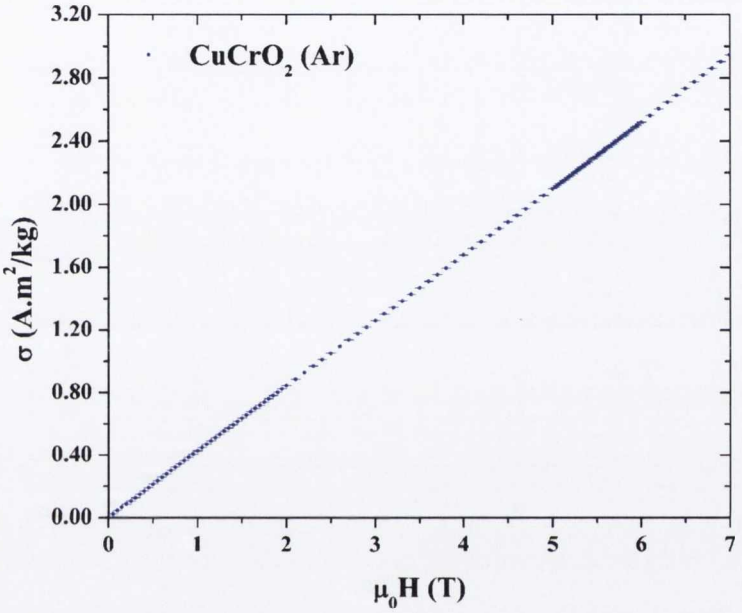

Figure 3.13: Magnetisation as a function of field at 1.8 K for the undoped $CuCrO_2$ powder prepared under Ar gas flow.

3.2.5 Discussion

The powder synthesis study has revealed that $CuCrO_2$ exhibits preferential orientation in bulk form, and taking account of this in the x-ray scattering analysis, no advantage has been observed in employing the sol-gel synthesis technique over standard solid state reaction, and the powder reaction temperature has been optimised to 1173 K. An x-ray diffraction study of the solubility limit of the Mg impurity ion in the $CuCrO_2$ lattice and the evolution of the lattice parameters and cell volume with increasing dopant concentration by Rietveld refinement yielded a surprisingly low 1 % Mg solubility level, above which a $MgCr_2O_4$ impurity phase was observed. A non-monotonic relationship was observed between the a and c lattice parameters of the unit cell and the doping concentration.

SEM examination of the microstructure of the $CuCrO_2$ powder samples confirmed the oriented granular nature of the powder through the observation of large platelets in the images. Analysis of the 10 % Mg-doped sample verified the presence of an impurity phase with octahedral symmetry, however EDX analysis established that the global Mg-doping concentration agreed with the nominal concentration, and that the distribution of the dopant ions in the powder was sufficiently homogeneous for PLD.

SQUID magnetometry measurements revealed an impurity phase, unseen by x-ray diffraction analysis of the undoped bulk $CuCrO_2$ specimen prepared in air, corresponding to the ferrimagnetic spinel $CuCr_2O_4$. This necessitated powder synthesis under Ar atmosphere to eradicate the spinel phase and achieve single phase $CuCrO_2$. As anticipated, the presence of the $MgCr_2O_4$ spinel phase, for doping concentrations above 1 %, was confirmed by the observation of an antiferromagnetic transition in the magnetisation at $\sim$ 16 K. The antiferromagnetic ordering of the $CuCrO_2$ compound in each of the samples measured has been confirmed by the observation of a transition corresponding to the Néel point at $\sim$ 25 K. The temperature dependence of the susceptibility of phase pure undoped and 2 % Mg-doped $CuCrO_2$ powder samples have been observed to adhere to the Curie-Weiss behaviour above 160 K. The effective moment of the undoped sample has been determined to be 3.89 μ_B/Cr, and the Curie temperature has been extracted to be -191 K, in good agreement with published reports.

3.3 Thin Film Fabrication

The technique of pulsed laser deposition is particularly suited to oxide growth, with an adaptable range of achievable substrate temperature and oxygen partial pressure conditions. High temperature pulsed laser deposition has been successful in achieving the stoichiometric transfer of multication compounds, and this process is described at length in appendix A. The technique of PLD was selected for the growth of $CuCrO_2$ thin films.

3.3.1 Optimised Thin Film Growth

Although PLD has become a widely used technique for the deposition of oxides, it is by no means a standardised process. Optimised deposition conditions are not transferable from system to system, and the range of controllable and uncontrollable growth conditions are too numerous to achieve precise reproducibility. It is therefore important to explore the window of deposition conditions

comprehensively, and to control as many variables as possible, to optimise the growth process in a material.

Thin films of undoped and Mg-doped $CuCrO_2$ were grown on single crystal Al_2O_3 (0001) substrates by PLD. A wide range of oxygen background pressure (1×10^{-3} μbar to 100 μbar) and temperature (773 to 973 K) combinations were investigated, as shown in Fig. 3.14, to find the optimum deposition conditions. All of the films were characterised by the x-ray scattering techniques of x-ray reflectivity and diffraction, as described in appendix B, to determine the film thickness and crystallographic phases present in the samples. A summary of the phases obtained for the various temperatures and pressures investigated is presented in fig. 3.14. Crystallographically, the best conditions for growth of undoped $CuCrO_2$ were determined to be an oxygen partial pressure of the order of 10 μbar and a substrate temperature in the range 873 – 973 K. The introduction of Mg-doping in the thin films allowed further optimisation based on minimising the electrical resistance measured by two probes. Enhanced conductance was then observed for films grown under the more precise conditions of 20 μbar of oxygen and a temperature of 923 K at the substrate. The optimum deposition conditions for these films are summarised in table 3.4.

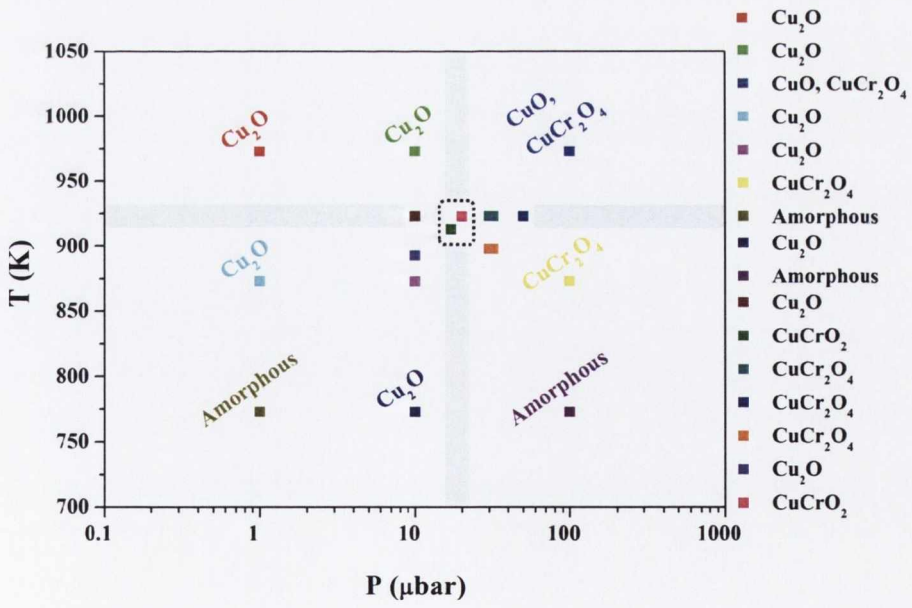

Figure 3.14: Window of deposition conditions investigated indicating the impurity phases observed during optimisation of $CuCrO_2$ thin film growth

	Dopant	Pressure O_2 (μbar)	Temperature (K)	Energy Density (Jcm^{-2})	Rep Rate (Hz)	Substrate
$CuCrO_2$		10	873 – 973	1.9	5	c-Al_2O_3
$CuCrO_2$	10 % Mg	20	923	1.5	2	c-Al_2O_3

Table 3.4: Summary of optimum growth conditions for $CuCrO_2$ thin films

3.3.2 Structural Characterisation

The structural characterisation of optimised thin films was performed using reflection high energy electron diffraction (RHEED) during the deposition, x-ray reflectivity (XRR), x-ray diffraction (XRD) and atomic force microscopy (AFM), the details of these techniques can be found in appendix B.

3.3.2.1 RHEED

The RHEED patterns of a blank c-cut sapphire substrate perpendicular to the $[\bar{1}10]$ and $[\bar{1}00]$ directions are shown in fig. 3.15 (a) and (b) respectively. An angle of 30^o separates these two directions. An atomically flat sapphire surface is characterised by narrow spots in the diffraction pattern. At the initial stages of the deposition of $CuCrO_2$ the spots disappeared rapidly leaving a blurry background. After a few seconds streaks appeared in the pattern, this is characteristic of 2-dimensional growth. The profile of this streaky pattern corresponds to $CuCrO_2$ with a 30^o rotation in the plane. After a considerable duration of deposition, spots are observed to be superimposed on the streaks, this is characteristic of a transition from 2-dimensional to 3-dimensional growth. The final RHEED patterns, after the deposition, are presented in fig. 3.15 (c) and (d). The (a) and (c) patterns, and similarly the (b) and (d) patterns, correspond to the same rotation of the substrate relative to the beam, 0 and 30^o respectively.

3.3.2.2 X-Ray Reflectivity

X-ray reflectivity is a useful technique to obtain information on the density, thickness and interfacial roughness of thin film samples. The reflectivity of 2 % and 5 % Mg-doped $CuCrO_2$ samples are shown in fig. 3.16. The observation of Kiessig fringes in the reflectivity scan indicate that the thin film has a certain level of smoothness. The critical angle is proportional to the density of the film, and together with the period of the oscillations this can be used to determine the thickness of the layer in the manner described in appendix B. The reflectivity can be fitted using IMD freeware and the resulting fits are shown in fig. 3.16. The good agreement between the experimental and

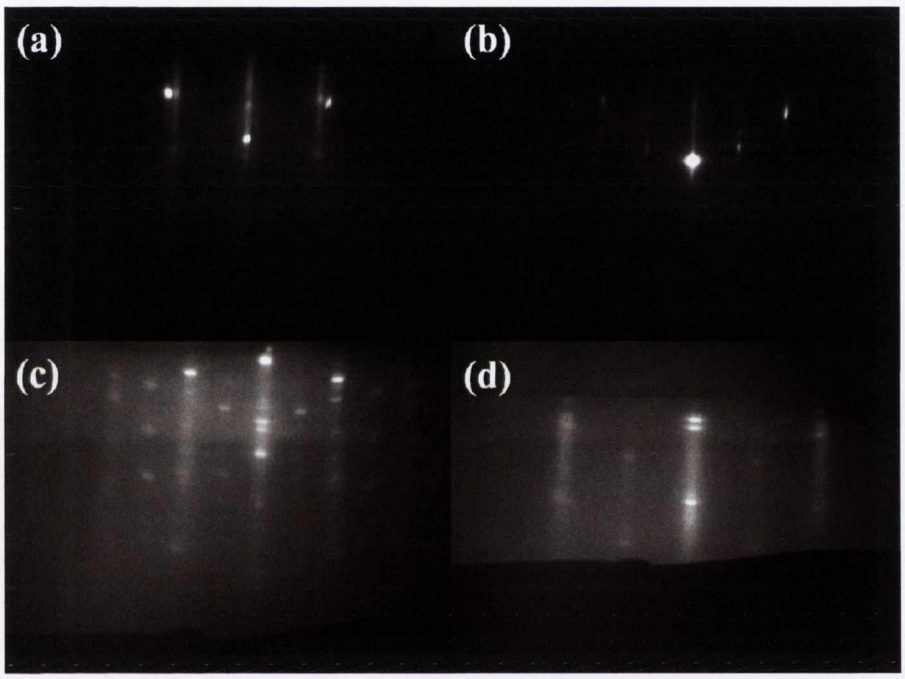

Figure 3.15: RHEED pattern of (a) the [$\bar{1}$10] and (b) the [$\bar{1}$00] orientations of the c-cut sapphire substrate before deposition, and after deposition of a $CuCrO_2$ thin film relative to (c) the [$\bar{1}$10] and (d) the [$\bar{1}$00] orientations of the substrate.

calculated data indicate that both of the samples have little surface and interfacial roughness with the substrate. A similar effect has been observed in $2\theta - \omega$ x-ray diffraction scans of a number of the thin film samples, grown at a low deposition rate, with Pendellösung fringes about the Bragg peaks, as presented in fig. 3.17.

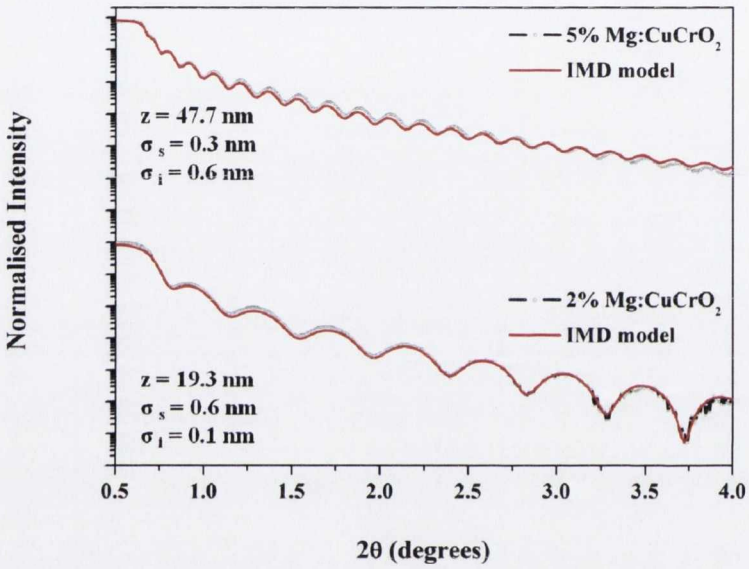

Figure 3.16: XRR analysis of thickness of 2 % and 5 % Mg doped $CuCrO_2$ thin films together with the IMD models.

3.3.2.3 X-Ray Diffraction

A typical $2\theta - \omega$ scan for an optimised 5 % Mg-doped thin film is presented in fig. 3.18. The $CuCrO_2$ peaks are labelled with their Miller indices(003), (006), (101), (009), (0012), (202), (0018). The Al_2O_3 (003), (006) and (0012) peaks of the substrate correspond to the remaining unidentified peaks in the diffraction pattern. The $CuCrO_2$ $(00l)$ family of planes is observed, indicating a strong preferred orientation of the thin film following the c-axis orientation of the Al_2O_3 substrate. No impurity phases are observed in this film, and a very minor additional (101) orientation of the $CuCrO_2$ thin film emerges. The observation of the second orientation of the material in some of the films may be due to the great lattice mismatch between the thin film and the sapphire substrate.

The systematic measurement of $2\theta - \omega$ scans on thin films produced with various doping

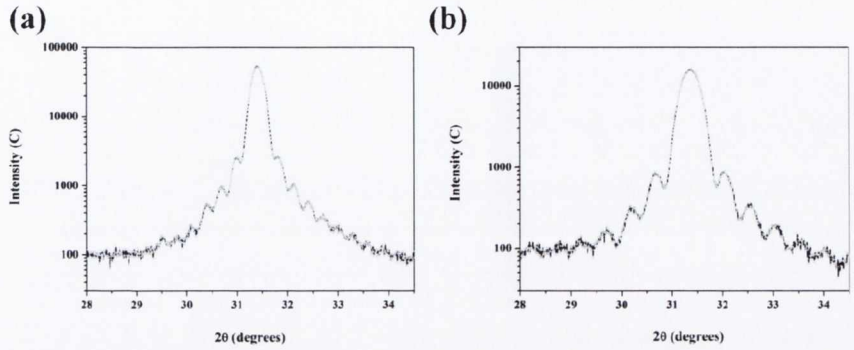

Figure 3.17: Pendellösung fringes observed about the primary $CuCrO_2$ (006) peak of (a) an undoped and (b) a 2 % Mg doped $CuCrO_2$ thin film.

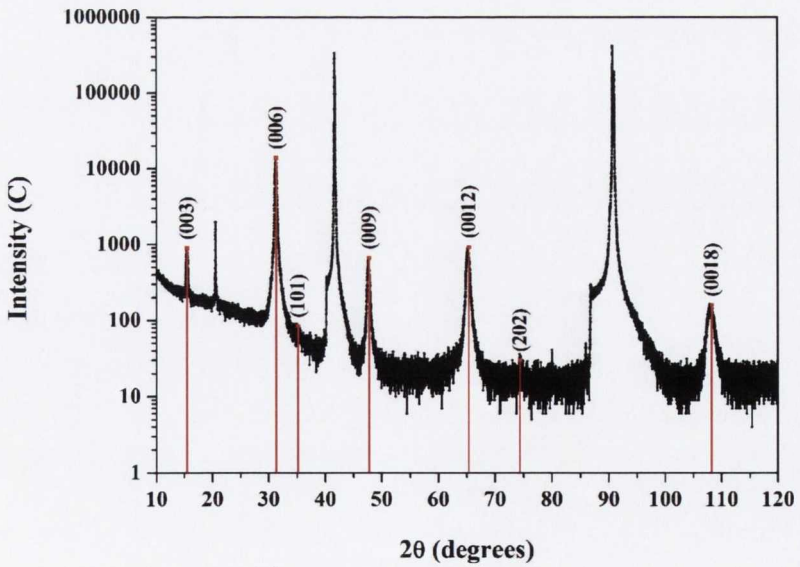

Figure 3.18: XRD phase examination of a 5 % Mg doped $CuCrO_2$ thin film.

concentrations indicated similar behaviour, showing the identical $(00l)$ growth direction with a minor secondary (101) orientation. A selection of these scans with doping concentrations, x, in the range $0 \leq x \leq 10$ % are presented in fig. 3.19. The deterioration of the source target during ablation may be responsible for the sporadic observation of the Cu_2O impurity phase in the diffraction patterns as indicated in the figure. Nevertheless, the intensity of these impurity peaks is minimal and can only be seen above the background on logarithmic scales with longer counting times and therefore improved statistics. Observation of this impurity phase did not correlate with increased doping concentration in the thin films, and furthermore, no $MgCr_2O_4$ phase was observed up to 10 % Mg-doping levels. This would indicate that the solubility limit of Mg in the $CuCrO_2$ thin film lattice far exceeds that of the bulk.

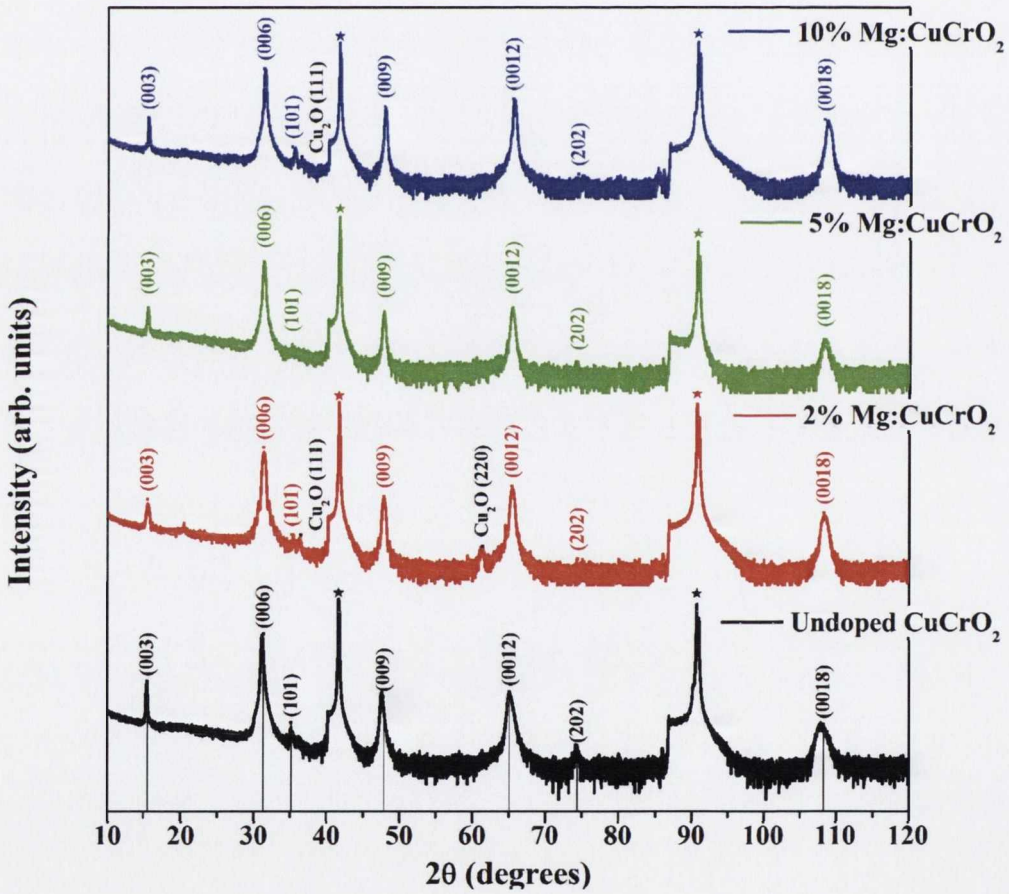

Figure 3.19: Phase examination of an undoped, 2 % Mg doped, 5 % Mg doped, and 10 % Mg doped $CuCrO_2$ thin films.

To further assess the crystalline quality and orientation of the thin films, ω scans were measured

on the $CuCrO_2$ (006) Bragg peak. A typical rocking curve of a 5 % Mg-doped thin film deposited under the optimum growth conditions is presented in fig. 3.20. A feature observed in the majority of the rocking curves examined was the superposition of two peaks with differing full width at half maximum height (FWHM) ω. The curve shown in the figure was fitted with two pseudo-voigt functions sharing a common centre. The FWHM ω values calculated for each function were found to be 0.284 ± 0.004^o for the broader, lower intensity diffuse component, and 0.0316 ± 0.0001^o for the narrow, high intensity peak.

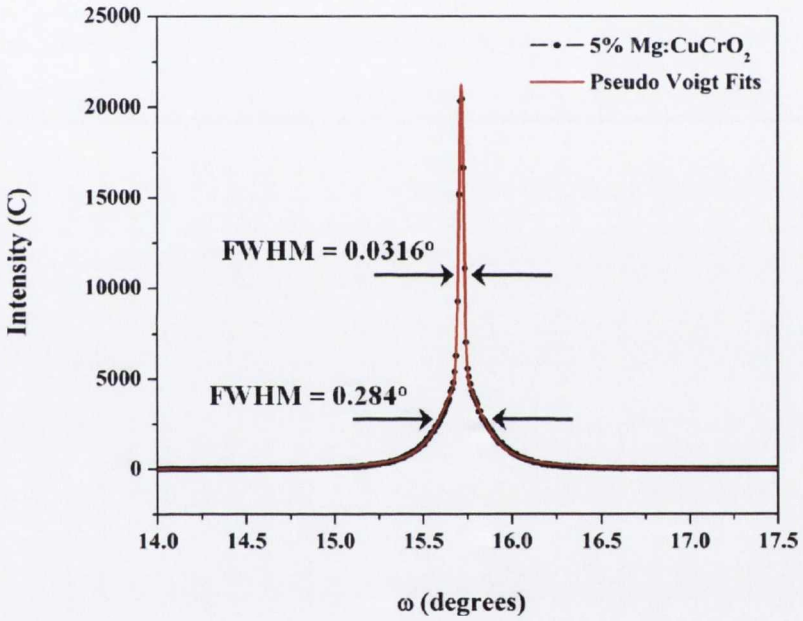

Figure 3.20: Rocking curve of 5 % Mg-doped $CuCrO_2$ thin film.

Reports on similar rocking curve profiles have attributed this behaviour to two distinct growth modes in the film Stifter & Sitter (1995). The narrow high intensity peak corresponds to the initial 2-dimensional island growth. Once a critical film thickness is exceeded, the growth reportedly becomes three dimensional with a tilting of the grains and the formation of mosaic blocks. A disorder, due to misfit dislocations, occurring at the substrate/thin film interface has also been proposed to explain this anomaly, which has also been observed in the AlN system Heinke *et al.* (2001). This latter hypothesis may apply to the $CuCrO_2$ system as grown on Al_2O_3 substrates due to the similarity between the AlN and $CuCrO_2$ crystal structures.

Since the samples show a strong preferred orientation with the relation $[00l]_{CuCrO_2} \parallel [00l]_{Al_2O_3}$, in-plane measurements were carrier out in order to further assess the orientational relationship between the film and substrate. Having considered the relative intensities of the diffraction peaks of $CuCrO_2$, the (104) plane was selected for examination. The angle ψ between the $(00l)$ plane and the (104) plane was calculated according to the following equation:

$$cos\psi = \frac{h_1h_2 + k_1k_2 + \frac{1}{2}(h_1k_2 + h_2k_1) + \frac{3a^2}{4c^2}l_1l_2}{\sqrt{(h_1^2 + k_1^2 + h_1k_1 + \frac{3a^2}{4c^2}l_1^2)(h_2^2 + k_2^2 + h_2k_2 + \frac{3a^2}{4c^2}l_2^2)}} \tag{3.10}$$

The value of ψ is reported in table 3.5, together with the ψ angular position of the Al_2O_3 (113) plane. The values of ψ and 2θ for these two planes are relatively close together, suggesting the possibility of the existence of an orientational relationship between them. A ϕ scan was measured for each of these planes, and this data is shown in fig. 3.21.

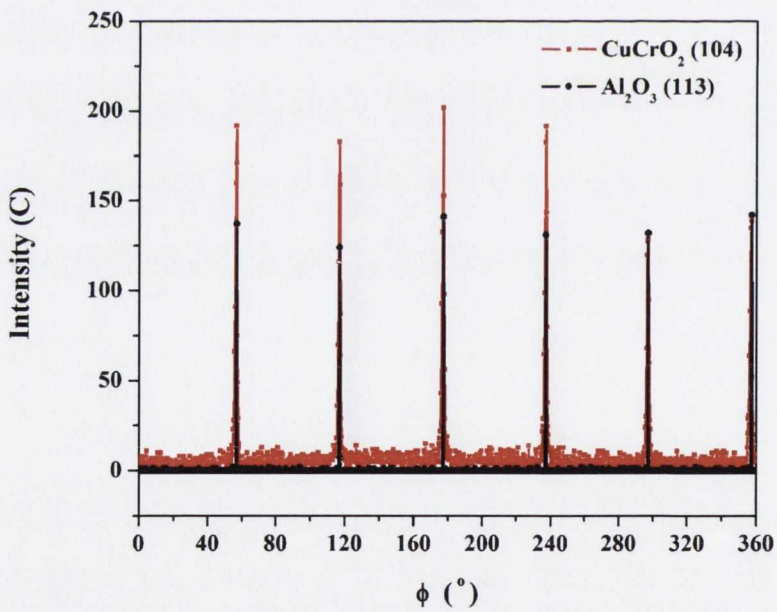

Figure 3.21: In-plane ϕ scan of $CuCrO_2$ thin film in (104) direction and the (113) direction of its Al_2O_3 substrate.

Each of the scans reveal a six-fold rotational symmetry. The peaks of the $CuCrO_2$ (104) plane overlap perfectly with those of the Al_2O_3 (113), indicating that the in-plane axis of the delafossite are rotated 30^o relative to that for the substrate. The expected three-fold symmetry of

the delafossite (104) plane is thus observed to be twinned. This has also been observed in $CuGaO_2$ Ueda *et al.* (2001) and $CuAlO_2$ Stauber *et al.* (1999).

This rotation can be understood by considering the atomic scale scheme of the crystal structures, illustrated in fig. 3.22, which explains the epitaxial growth of $CuCrO_2$ on c-cut sapphire substrates. The figure indicates that there are two possible stacking modes, if it is assumed that the oxygen layers of $CuCrO_2$ are stacked upon the oxygen layers of Al_2O_3, and that the close packed structure of the oxygen ions is sustained. The direction of the a-axis in $CuCrO_2$ is rotated by 60^o between the two distinct cases, and it differs from the a-axis in Al_2O_3 by $\pm$ 30^o. These two stacking modes explain the six diffraction peaks in the $CuCrO_2$ ϕ scan.

To confirm the observed relationship between the $CuCrO_2$ (104) and Al_2O_3 (113) planes, pole figures of the (104) and (113) Al_2O_3 planes were measured, the data is presented in fig. 3.23 (a) and (b). The 30^o difference between the sapphire (104) and (113) planes is evident in these figures. The pole figures of 5 % Mg-doped and 10 % Mg-doped $CuCrO_2$ (104) peaks are presented in fig. 3.23 (c) and (f), both showing the six-fold rotational symmetry already encountered in the ϕ scan of fig. 3.21. The introduction of Mg into the lattice appears to induce a degree of disorder, as evidenced by the broadening of the peaks in the pole figure. At low ψ angles, a feature possessing the same six-fold symmetry, is observed, and its intensity increases with enhanced doping. This could be due to a long range ordering of the substituted Mg-dopant. The fig. 3.23 (e), which consists of the superposition of the pole figures (a), (b) and (c), highlights the 30^o rotation of the a parameter of $CuCrO_2$ with respect to that of the Al_2O_3.

In order to determine the a lattice parameter and to confirm the preferred orientation relationship between the $CuCrO_2$ (104) and Al_2O_3 (113) planes, reciprocal space maps around those Bragg peaks were measured, and a set of data is presented in fig. 3.24. Fig. 3.24 (a) represents the portion of the reciprocal space map containing the $CuCrO_2$ (006) and Al_2O_3 (006) peaks. The high intensity, narrow peak in the upper part of the reciprocal space map corresponds to the sapphire peak, and the broader, lower intensity peak in the lower part of the map represents the film peak. Although the distance between the film and substrate peaks is large, the presence of Pendellösung fringes can be observed about the film peak.

The reciprocal space map presented in fig. 3.24 (b) consists of the $CuCrO_2$ (104) and the Al_2O_3 (113) peaks. The alignment of the two peaks along the $2\theta - \omega$ axis confirms the orientational relationship between these planes. The 2θ angular position of the (104) peak permits the calculation of the a lattice parameter using the c parameter, which is determined from the position of the out-of-plane (006) peak, using the equation for the lattice plane spacing below. The lattice parameters

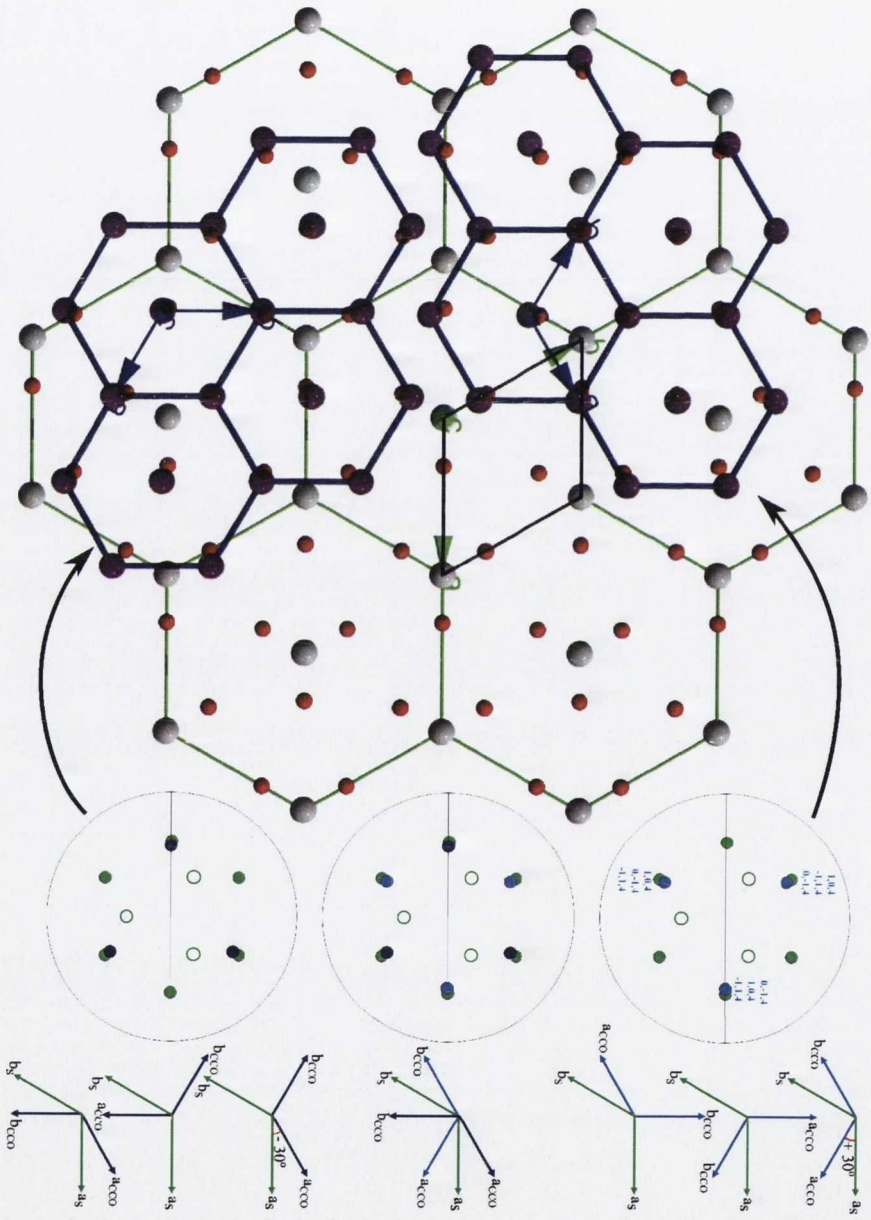

Figure 3.22: Lattice mismatch between $CuCrO_2$ thin film and Al_2O_3 substrate.

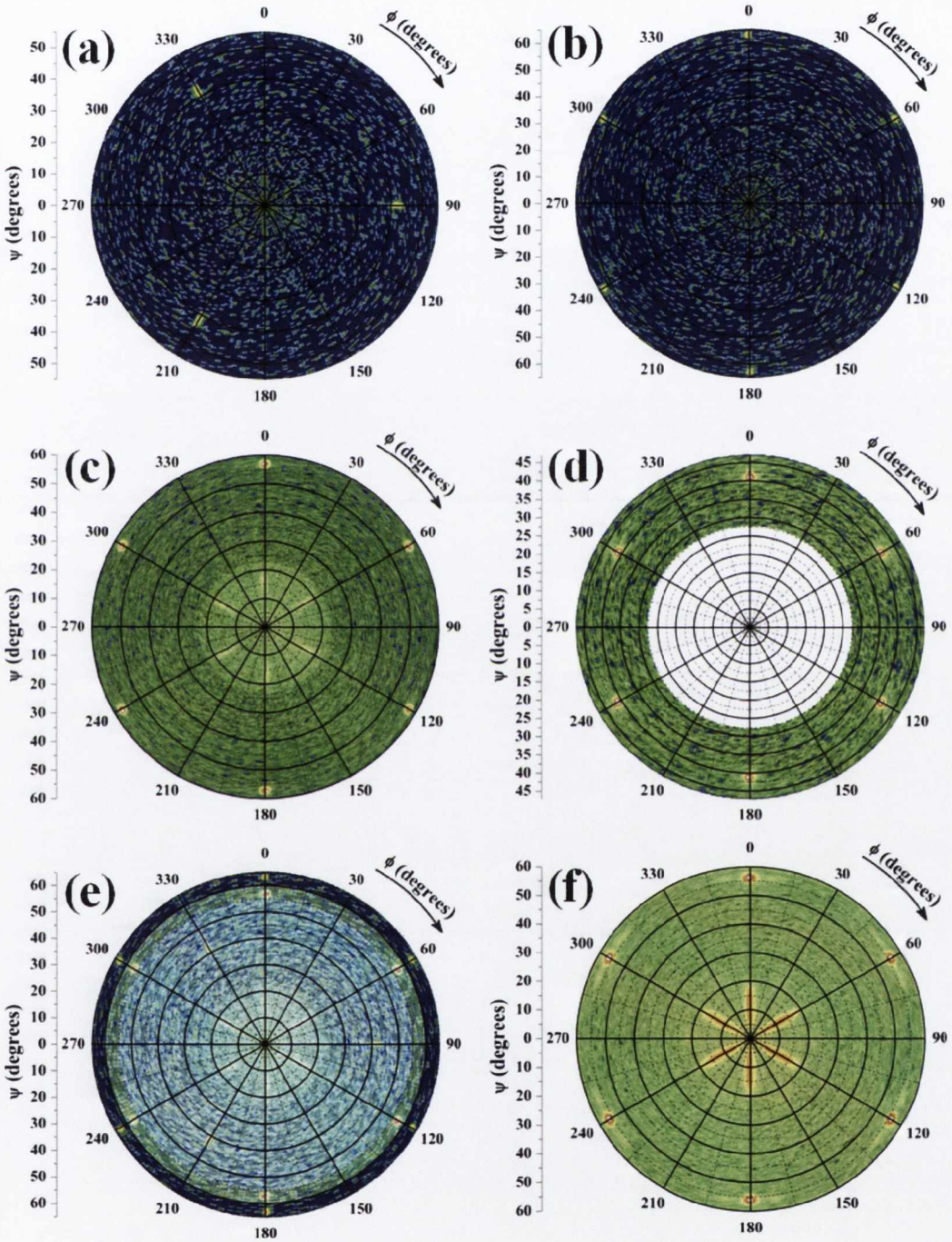

Figure 3.23: Pole figures of (a) Al_2O_3 single crystal substrate in (104) direction; (b) Al_2O_3 in (113) direction; (c) 5 % Mg:$CuCrO_2$ in (104) direction; (d) 5 % Mg:$CuCrO_2$ in (108) direction; (e) 5 % Mg:$CuCrO_2$ (104) with Al_2O_3 (104) and (113) peaks superimposed; (f) 10 % Mg:$CuCrO_2$ (104) peaks.

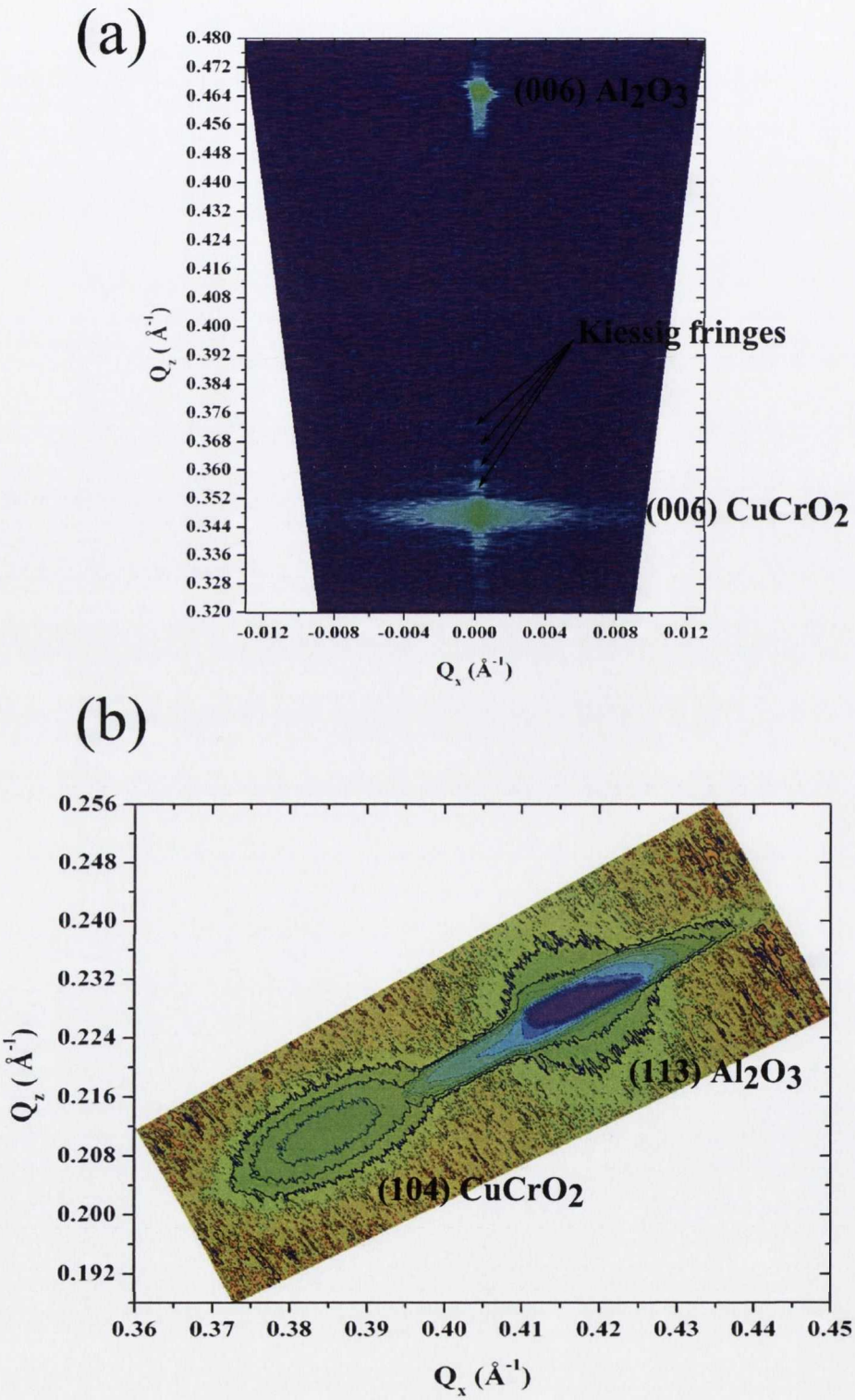

Figure 3.24: Out-of-plane and in-plane reciprocal space maps of $CuCrO_2$ film on Al_2O_3 substrate. (a) Shows the (006) $CuCrO_2$ peaks with the (006) sapphire peak. (b) Shows the (104) $CuCrO_2$ peak with the (113) sapphire. The Kiessig fringes in this film can also be seen in the reciprocal space map.

of the films are summarised in table 3.5. The doping concentration in the films is not observed to significantly influence the lattice parameters, which are found to be close to the bulk values.

$$\frac{1}{d^2} = \frac{4}{3}\left(\frac{h^2 + hk + k^2}{a^2}\right) + \frac{l^2}{c^2} \tag{3.11}$$

for (006)

$$c = 6d \tag{3.12}$$

for (104)

$$a = \sqrt{\frac{4d^2c^2}{3(c^2 - 16d^2)}} \tag{3.13}$$

Material	Dopant	a (Å)	c (Å)	Thickness (nm)
$CuCrO_2$ [1]	undoped	2.9734	17.100	Bulk
$CuCrO_2$	undoped	3.00	17.197	62.7
$CuCrO_2$	2 % Mg	3.00	17.095	19.3
$CuCrO_2$	5 % Mg	3.07	17.068	13.5
$CuCrO_2$	5 % Mg	3.06	17.107	30.7
$CuCrO_2$	10 % Mg	2.97	17.054	39.5

Plane	2θ	ω	ψ	ϕ scan
$CuCrO_2$ (104)	40.852^o	20.426^o	58.90^o	6 peaks
Al_2O_3 (113)	43.34^o	21.62^o	61.21^o	6 peaks

Table 3.5: Table of lattice parameters and angular positions of asymmetric planes

3.3.2.4 Atomic Force Microscopy

The surface morphology of the $CuCrO_2$ thin films has been examined by Dr. S. Colis, using tapping mode AFM. Figure 3.25 shows images of $CuCrO_2$ thin films grown over varying deposition durations, ranging from 45 mins to 9 hrs, increasing from (a) to (d), at a substrate temperature of 923 K in 20 μ bar of O_2. The images on the left hand side have been scanned over a range of 15 μm^2, while the images on the right hand side have been scanned over the narrower range of $\sim 1 \mu m^2$. The thinnest film, shown in fig. 3.25 (a), exhibited small spherical particles of approximately 200 nm diameter. The root mean square roughness over a 5 μm^2 range of this sample is found to be 5 nm, whereas the r.m.s. roughness on a 300 nm^2 range in between the small grains is 1 nm. The maximum vertical peak to peak value on the wider range being 50 nm. These particles may

be droplets formed on the film during deposition. The images presented in fig. 3.25 (b) show the appearance of rod-like particles on the surface of the films. These particles have a typical length of 200 nm and a width of approximately 40 nm. The profile of the rod is prism-like in accordance with the 3-fold symmetry of $3R$ $CuCrO_2$. The r.m.s. roughness on a 1 μm^2 scale is 12 nm, while the inter-particle r.m.s. roughness on a 250 nm^2 range is just 1.5 nm. For this film the maximum vertical peak to peak value on the wider range was evaluated to be 250 nm. The images of the final two films, shown in figs. 3.25 (c) and (d), exhibit triangular and hexagonal particulates ranging in lateral size from 300 nm to 1 μm. The surface between these crystallites displays a similar morphology to that of the previous film, shown in fig. 3.25 (b), with an r.m.s. roughness of 1 nm on a 900 nm^2 sampling window. The volume density of the crystallites has been observed to increase with deposition time, as illustrated by fig. 3.25 (c) and (d) and the height of this crystallites is found to be around 250 nm. Observation of the directional alignment of the particles with 3-fold symmetry at 60^o (and multiples of 60^o) relative orientation, provides further evidence of the 60^o crystal twinning observed by x-ray diffraction.

The thickness of the films in fig. 3.25 (a) and (b) have been determined by XRR to be 27 nm and 40 nm respectively. The AFM images indicate a transition in the growth mode from 2-dimensional to 3-dimensional, in agreement with RHEED analysis of the growth. The 3-dimensional growth of the crystal continues to be highly-oriented as shown in the images above, in agreement with the XRD analysis.

3.3.3 Optical Characterisation

The films were analysed by optical spectrometry in the UV-visible range of the electromagnetic spectrum. This was done in order to determine the "transparency" of the thin films, which is defined as the transmittance (%) over the visible range (i.e. 400 - 700 nm wavelength, or 2.1 eV - 3.1 eV energy range), and also to determine the optical bandgap of the materials. Details of the experimental measurement are provided in appendix B. It is clear from fig. 3.26 that the thickness of the films has a large influence over the transmittance. The thicker films exhibit relatively lower transmittance, while the thinner ones transmit more visible light. On average, the transparency is between 40 and 80% for the samples measured. A summary of the observed optical transmission properties is given in table 3.6.

The undoped films exhibit a sharp absorption at the band-edge while the doped films, which vary largely in conductivity, exhibit a more gradual absorption. Although it would appear that

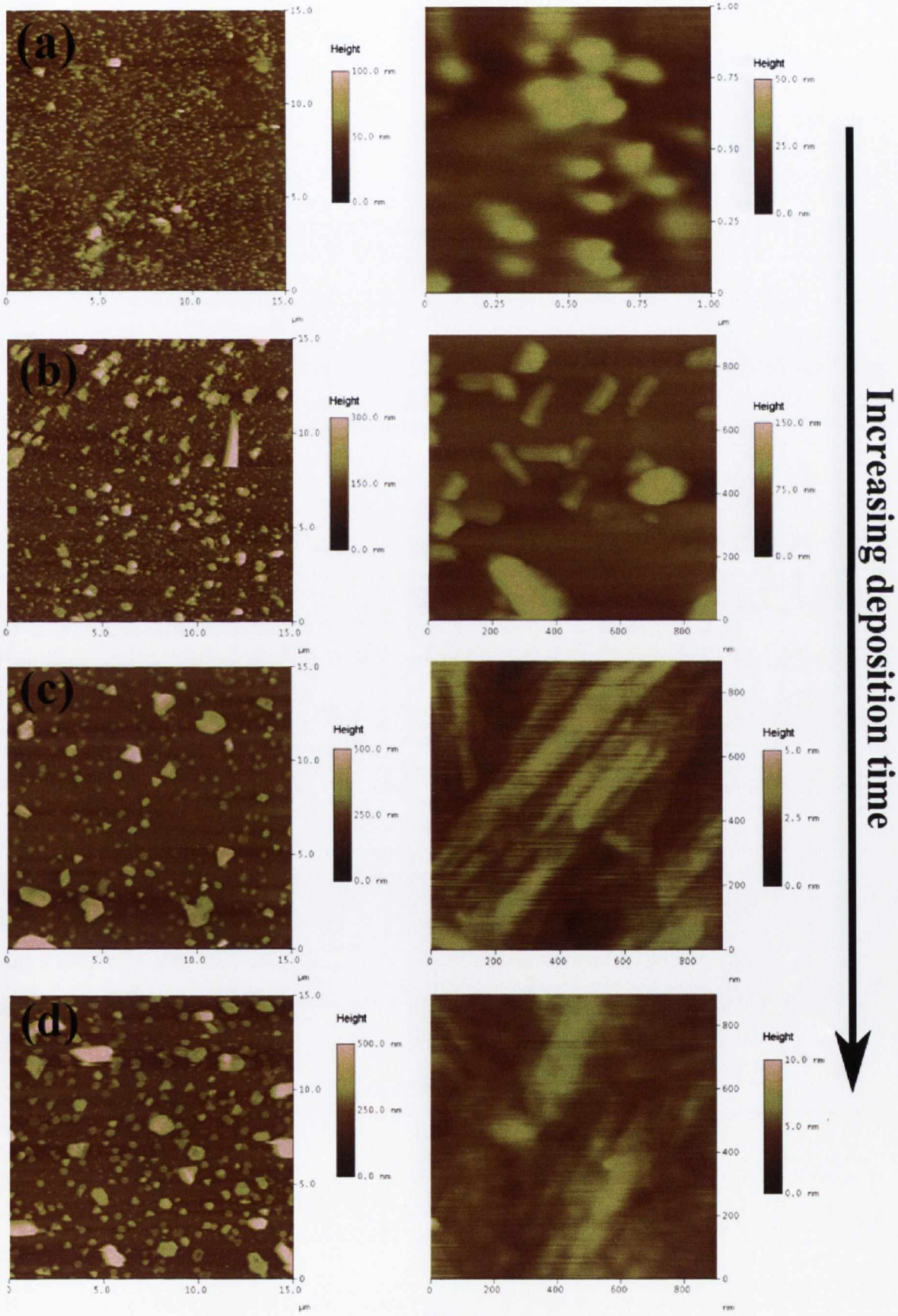

Figure 3.25: AFM images of $CuCrO_2$ thin films of varying thicknesses.

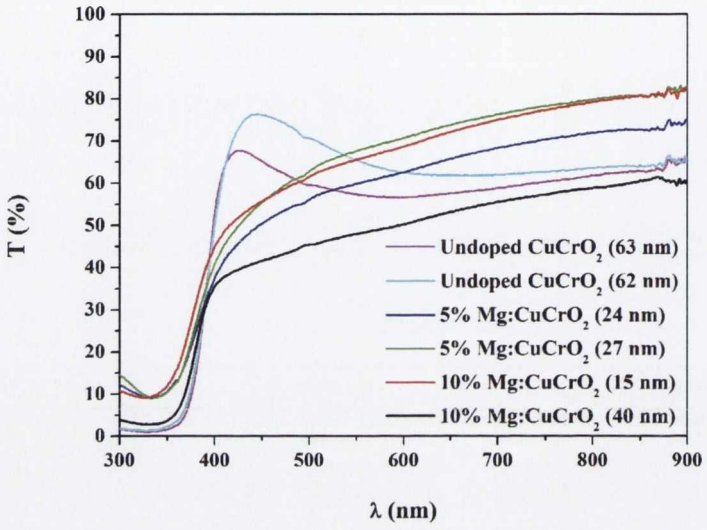

Figure 3.26: UV-Visible spectrometry of $CuCrO_2$ thin films

the absorption edge varies to an extent with doping, shifting to lower energy with increased doping this is not the case, since the thickness of the films must be taken into account.

The bandgaps of the thin films were calculated from the axis intercept of the slope of the straight-line portion of the Tauc plots Tauc *et al.* (1966) for the above data according to the equation

$$(\alpha h\nu)^{1/n} = A(h\nu - E_g) \tag{3.14}$$

$$\alpha d = ln\frac{100}{\%T} \tag{3.15}$$

where α[1] is the absorption coefficient, d is the film thickness, A is a constant, ν is the frequency, E_g is the optical bandgap, and the exponent n depends on the type of optical transition. For a direct transition $n = 1/2$, while for an indirect transition $n = 2$. The Tauc plot for a direct transition of the samples measured is presented in fig. 3.27 (a) and the values of the bandgap obtained for the various doping concentrations are summarised in table 3.6. The observed bandgaps for the samples range from 3.15 eV to 3.22 eV, and all were found to be in better agreement with a direct transition.

[1]This definition of α assumes that the reflectance, R, is essentially zero close to the absorption edge.

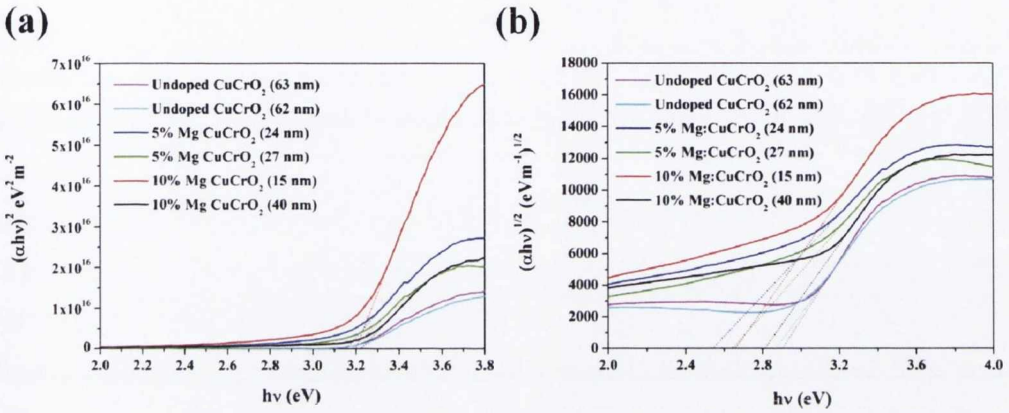

Figure 3.27: Tauc plot to determine (a) the direct optical bandgap (b) the indirect bandgap of $CuCrO_2$ thin films.

Compound	Dopant	d (nm)	T (%)	Bandgap (eV)	
				Direct	Indirect
$CuCrO_2$	Undoped	62.7	55 - 70	3.22 ± 0.05	2.90 ± 0.04
$CuCrO_2$	Undoped	61.9	60 - 75	3.21 ± 0.06	2.87 ± 0.02
$CuCrO_2$	5 % Mg	26.8	60 - 80	3.18 ± 0.06	2.64 ± 0.03
$CuCrO_2$	5 % Mg	23.6	60 - 80	3.15 ± 0.08	2.54 ± 0.02
$CuCrO_2$	10 % Mg	15.4	50 - 70	3.20 ± 0.06	2.66 ± 0.02
$CuCrO_2$	10 % Mg	39.5	40 - 60	3.22 ± 0.03	2.81 ± 0.02

Table 3.6: Table of optical bandgap and transparency of $CuCrO_2$ films.

3.3.4 X-Ray Photoelectron Spectroscopy

XPS experiments were carried out with Dr. C. McGuinness and Dr. J. Alaria, on the thin film samples to compare the endmember $CuCrO_2$ films with the Mg-doped samples. The x-ray photoemission spectrometer consisted of a hemispherical analyser equipped with a rotating anode $Al\ K\alpha$ x-ray source ($h\nu = 1486.6$ eV). The UHV chamber had an incorporated Ar sputtering system to prepare the sample for this surface sensitive technique. Similarities were observed between the obtained data and that reported in the literature Rastogi *et al.* (2008) Arnold *et al.* (2009).

Survey scans of undoped and nominally 10% Mg-doped $CuCrO_2$ thin films are presented in fig. 3.28. The survey scan of the undoped sample presents only lines corresponding to Cu, Cr, O and some traces of C[1] indicating the chemical purity of the sample. In the case of the doped sample, the same general spectrum is observed with an additional peak at 1305 eV corresponding to the Mg $1s$ transition. This suggests that a certain amount of Mg has been inserted into the lattice. A quantitative analysis was not possible since no standard sample for Mg was available.

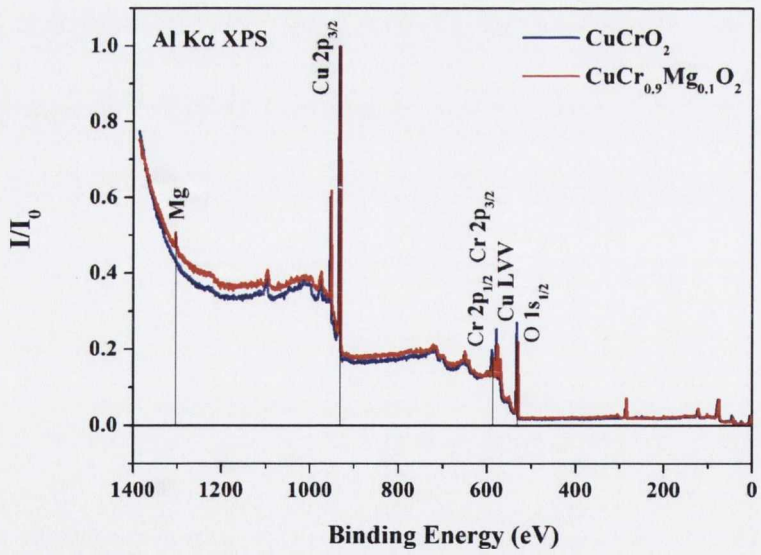

Figure 3.28: $Al\ K\alpha$ X-ray photoelectron spectra of both undoped $CuCrO_2$ and 10% Mg doped $CuCrO_2$ showing full energy survey

XPS spectra of Cr $2p$, Cu $2p$ and O $1s$ lines were recorded and are shown in fig. 3.29 (a),(b),

[1] Since the samples were relatively insulating, a charge neutraliser was used during the measurement, the C lines were then used as a reference.

and (c) respectively. The Cu $2p$ spectrum of the undoped sample presents a symmetric peak at 931.5 eV, corresponding to Cu^+, with no evidence of the satellite characteristic of the presence of Cu^{2+} at 942.0 eV Christopher & Swamy (1992). The profile of the Cu $2p$ spectrum of the doped sample is similar to that of the undoped film, with a binding energy shifted to higher energy in contrast with the observations of a polycrystalline study Arnold *et al.* (2009). The XPS spectra of the Cr $2p$ lines for both the undoped and doped samples show similar profiles, however no shift in the binding energy is observed. The Cr $2p3/2$ peak, observed at 576 eV, indicates that the valence state of Cr ion is 3+ Li *et al.* (2009b). The O $1s$ core level spectra of the undoped and Mg-doped $CuCrO_2$ films are shown in fig. 3.29 (c). The undoped film presents one peak at a binding energy of $\sim$ 530 eV. According to reported data for O $1s$ mixed metal oxides, this corresponds to a species with two negative charges, O^{2-} Christopher & Swamy (1992). The higher energy peak, observed for the doped sample, is normally associated with an oxygen species that has one negative charge such as CO_3^{2-}, HO^- or O^-. However, the symmetric C $1s$ peak, observed for these oxides, rules out the possibility of carbonate-type species on the sample surface. Moreover, considering that the films were sputtered *in situ* to prepare the surface for measurement, a substantial reduction in adsorbed oxygen species, such as the potential hydroxide layer which is absent in the undoped film, is expected.

The valence band photoemission spectra of undoped and Mg-doped $CuCrO_2$ are presented in fig.3.30. The figure indicates that in both cases the Fermi level lies just above the valence band edge in the lower part of the band gap, as expected for a p-type semiconductor. The profiles of these spectra are similar to that reported by Arnold *et al.* (2009), showing that the experimental spectra are dominated by Cu $3d$ states. For higher resolution measurements in the upper valence band region, however, UPS measurements are required.

3.3.5 Electrical Properties

3.3.5.1 Temperature dependence of conductivity

The temperature dependence of the resistance of undoped, 2, 5, 8 and 10 % Mg-doped $CuCrO_2$ thin films were measured with Dr. P. Stamenov, in order to investigate the nature of the conductivity and its dependence on Mg-doping. DC measurements were carried out in a Quantum Design PPMS (Physical Properties Measurement System) between 300 K and 2 K.

Two electrical contacts were made to all of the samples, except the 10 % Mg-doped films, with Au wire and In contacts, and these samples were measured using the high impedance set-up. The 10 % Mg-doped films were contacted in the Van der Pauw geometry. All of the samples exhibited

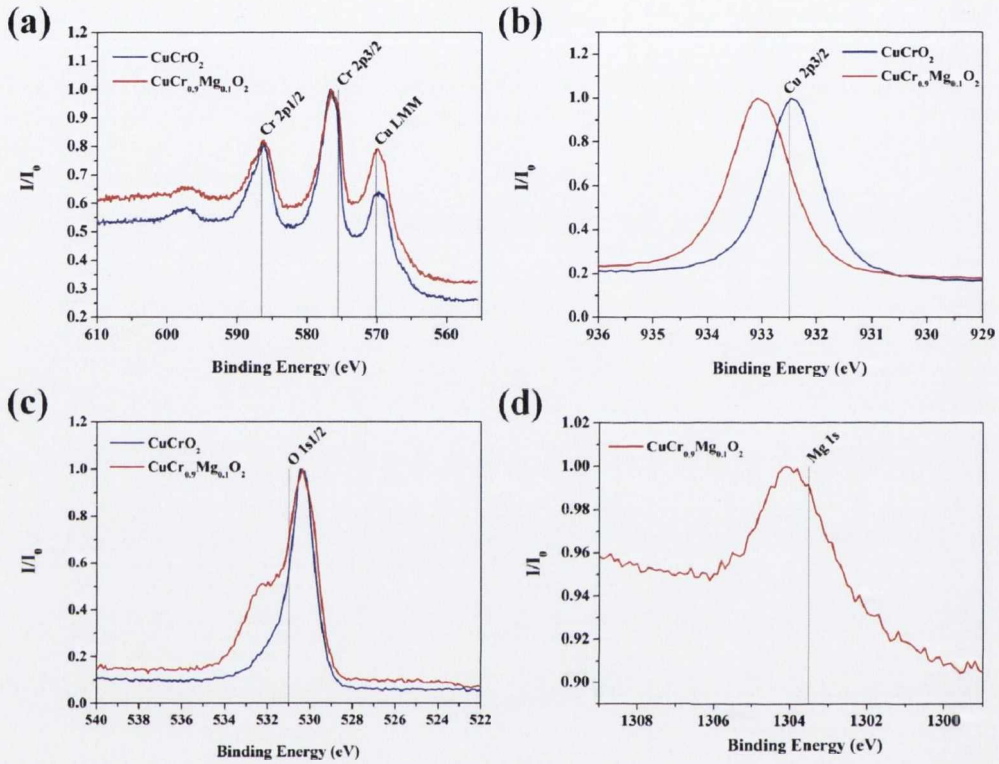

Figure 3.29: *Al* $K\alpha$ X-ray photoelectron spectra of both undoped $CuCrO_2$ and 10% Mg doped $CuCrO_2$ showing (a) Cr $2p$ structure, (b) Cu $2p_{3/2}$ core line, (c) O $1s_{1/2}$ emission line and (d) Mg $1s$ structure in the doped sample

Composition	d (nm)	E_{a1} (meV)	T range (K)
Undoped $CuCrO_2$	63	78.340±0.076	158.5 – 250.3
2 % Mg:$CuCrO_2$	23	73.861±0.062	163.5 – 263.8
5 % Mg:$CuCrO_2$	75	21.363±0.022	156.5 – 250.3
8 % Mg:$CuCrO_2$	70	11.015±0.006	87.2 – 300.0
10 % Mg:$CuCrO_2$	40	12.017±0.014	76.8 – 299.9
10 % Mg:$CuCrO_2$	135	20.608±0.032	134.3 – 299.9

Table 3.7: Activation energy values calculated from Arrhenius plots shown in fig. 3.32. E_{a1} corresponds to high temperature values (from 100 to 300 K).

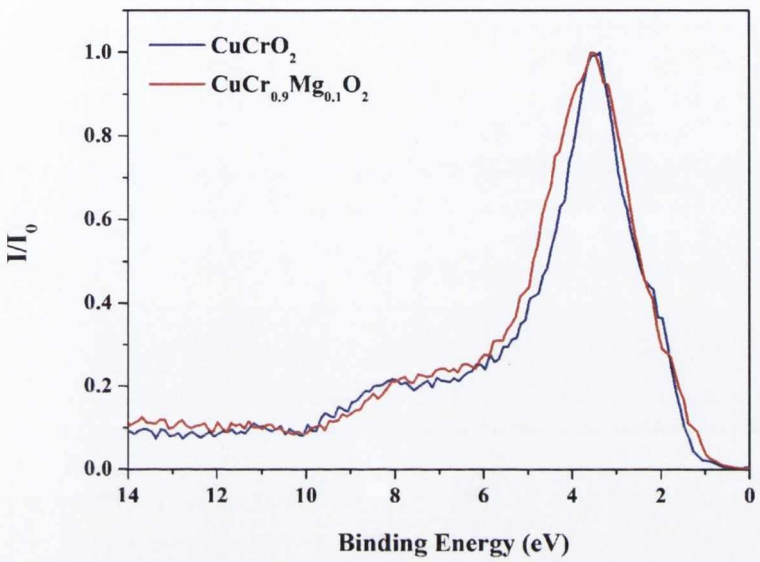

Figure 3.30: *Al Kα* X-ray photoelectron spectra of both undoped $CuCrO_2$ and 10% Mg doped $CuCrO_2$ showing the valence band structure.

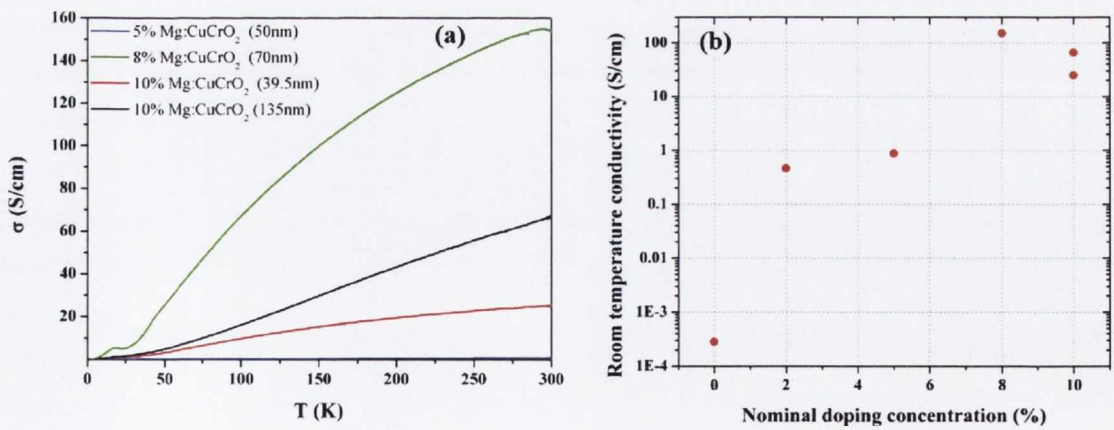

Figure 3.31: (a) The temperature evolution of the conductivity of 5 %, 8 % and two 10 % Mg-$CuCrO_2$ thin films, (b) Room temperature conductivity values of these films.

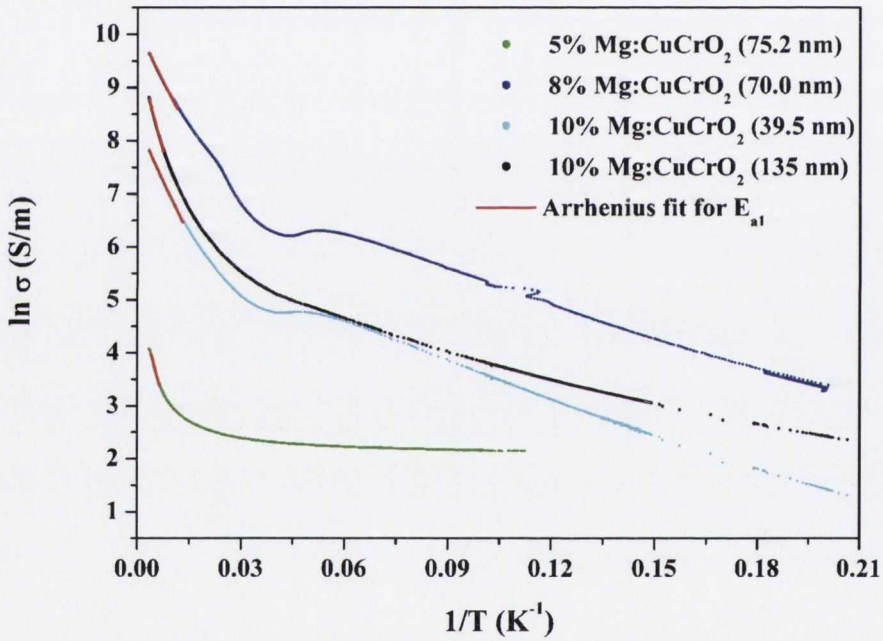

Figure 3.32: Arrhenius plot of 5 %, 8 % and two 10 % Mg-doped $CuCrO_2$ thin films with temperature with the linear fit (red line) at high temperature to determine the activation energy.

exponential resistance behaviour as a function of temperature, characteristic of a semiconductor. The room temperature conductivities for undoped, 2 %, 5 %, 8 % and two 10 % Mg-doped samples of differing thicknesses are shown in fig. 3.31.

To gain some insight into the position of the impurity band with respect to the valence band (assuming that the material is indeed p-type), the activation energy was extracted from the temperature dependence of the conductivity. The correct way to extract the position of the impurity level in a doped semiconductor would be to measure both the mobility and the carrier concentration as a function of temperature. The carrier concentration in the temperature region where the carrier are thermally ionised can be written in the case of a p-type semiconductor as

$$p = \propto e^{\left(\frac{-E_a}{k_B T}\right)} \tag{3.16}$$

using a Maxwell-Boltzmann type function for the occupancy factor, which is generally valid for $E_a > 3kT$. Since the carrier concentration and mobility are not easily determined in this type of material, an attempt to extract E_a from the variation of the conductivity as a function of temperature can be made. Assuming that the relation 2.32 is valid, and that the mobility follows a power low as a function of temperature, the exponential term of the carrier concentration will dominate the conductivity. In that case, the activation energies, E_a, can be calculated from a linear fit of the plot in the temperature ranges indicated on table 3.7 according to the equation:

$$ln\sigma = -\frac{E_a}{k_B T} + ln\sigma_0 \tag{3.17}$$

Arrhenius plots of the results of the measurements are shown in fig. 3.32 for thin films with 5, 8 and 10 % doping concentrations and the calculated activation energy are summarised in table 3.7.

Plots of $ln\sigma$ against $T^{-1/4}$ in the low temperature regime (below 50 K) were not observed to be linear in the entire temperature region, and therefore no further variable range hopping analysis was conducted. In samples with a nominal doping concentration higher than 5 % an anomaly is observed around 25 K, and is attributed to the antiferromagnetic transition. The temperature dependence of the resistivity, ρ, of 40 nm and 135 nm thick 10 % Mg-doped films are shown in fig. 3.33 (a). The anomaly around the magnetic transition is not as pronounced in the thicker film. This could be due to a non-homogenous conduction through the entire thickness of the thicker films, where other scattering mechanisms such as surface or grain boundary scattering would contribute to the conduction mechanism, therefore diluting the contribution to the scattering of the carriers from the localised moments. In order to avoid this, all subsequent layers and structures were limited to less than $\sim$ 70 nm.

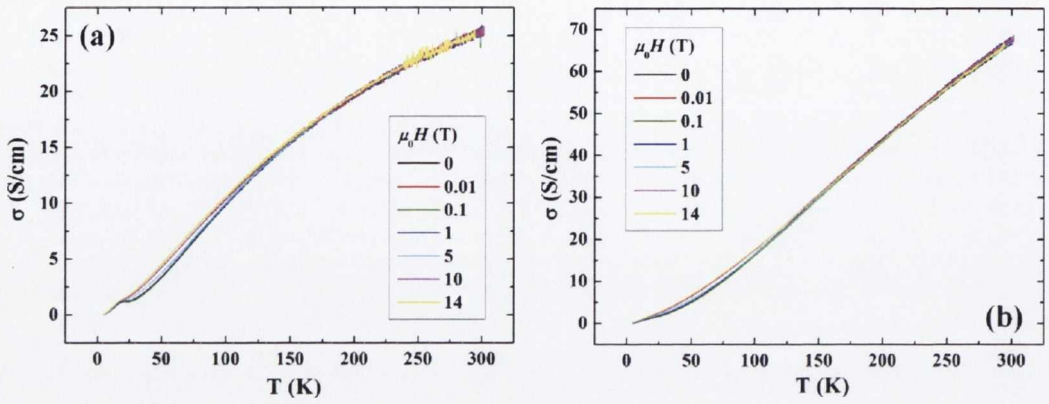

Figure 3.33: Graph of σ vs T of (a) a 40 nm thick 10 % Mg-$CuCrO_2$ thin film and (b) a 135 nm thick 10 % Mg-$CuCrO_2$ thin film in various applied magnetic fields.

3.3.5.2 Magnetotransport

Magnetoconductance The magnetoconductance of 2 %, 5 %, 8 % and 10 % Mg-doped $CuCrO_2$ thin film samples were measured with Dr. P. Stamenov, in the same physical properties measurement system, with magnetic fields varying in the range -14 T $\leq \mu_0 H \leq$ +14 T and temperatures varying from 300 K to $\sim$ 2 K. The samples were contacted with Au wire and In soldered contacts in the Van der Pauw configuration, which is described in appendix B. The measurements were carried out with the field applied in the direction perpendicular to the sample plane (transverse) unless otherwise stipulated on the graph. The results are presented in fig. 3.36, 3.37 and 3.38 below.

Since samples were measured in UHV conditions (cryosorption pump, better than 10^{-8} mbar), and sample cooling relies on radiation transfer, resulting thermal RC constants are on the order of 1 hr. For small temperature drifts, the system is close to linear and is therefore simply described by a first order linear differential equation for the temperature offset between sample and thermometer, the solution of which is a simple exponential time dependence of the isothermal offset. This causes a conductance drift during an isothermal magnetic field scan and the raw data have to be corrected. An example of untreated data is presented in fig. 3.34 for a 2 % Mg-doped $CuCrO_2$ thin film measured at 100 K. To correct the data for this thermal drift during a scan field, the exponential decay (when the field scans were recorded incrementally from low temperature to high temperature) is determined in the time domain shown by the red line in fig. 3.35. This offset is subtracted in the time domain to obtain the raw current, before the data is examined in field domain. This data processing procedure is illustrated in fig. 3.35.

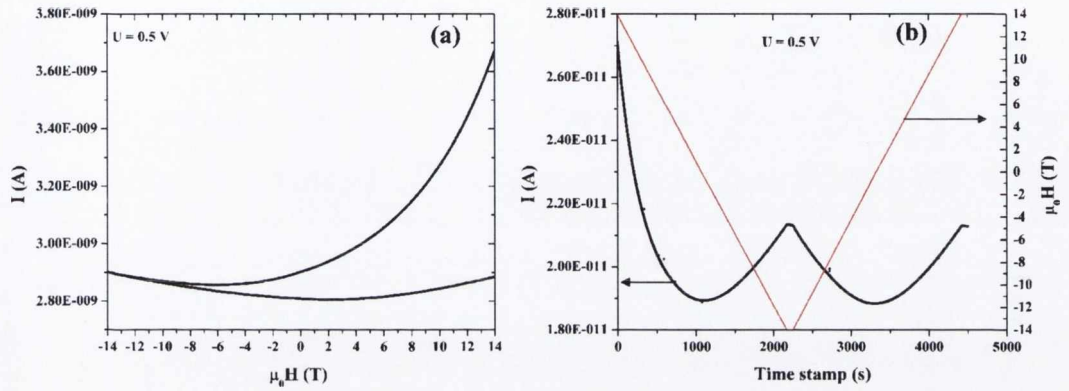

Figure 3.34: Raw data of an isothermal field scan for 2 % Mg-doped $CuCrO_2$ thin film sample at 100 K, (a) in field domain, (b) in time domain (the variation of the applied magnetic field is also shown in red).

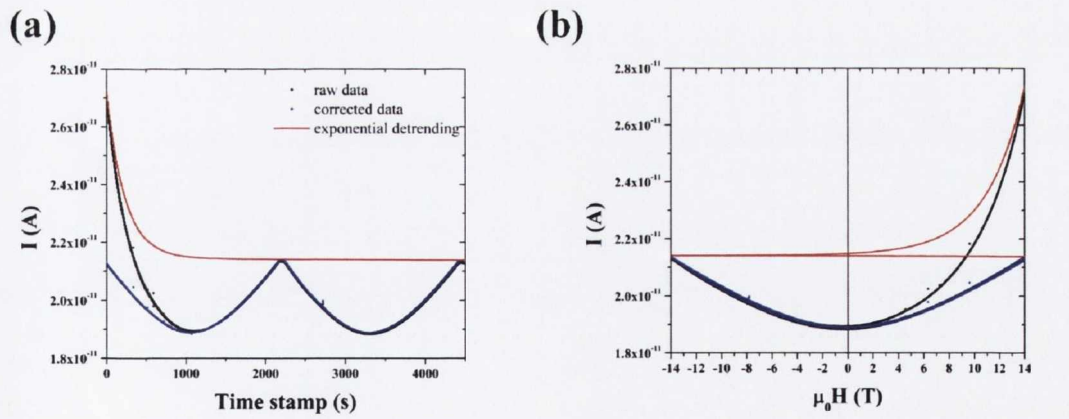

Figure 3.35: Example of the detrending procedure, (a) in time domain, for 2 % Mg-doped $CuCrO_2$ thin film sample at 100 K showing the raw data (black), the detrending exponent (red) and the corrected data (blue), (b) in field domain.

The undoped $CuCrO_2$ thin film was too resistive to measure magnetoconductance, MC, below $\sim$ 150 K. For all samples, in all temperatures, positive magnetoconductance was observed, which can only be associated with carrier delocalisation or direct influence of exchange splitting on the carrier concentration. One possibility is that below and in the vicinity of the Néel point small spin canting (of the order of 1^o) may alter the position of the exchange split impurity level in the gap sufficiently to change the carrier concentration by a factor of $\sim$ 2. In most cases the magnetoconductance was negligible above 100 K.

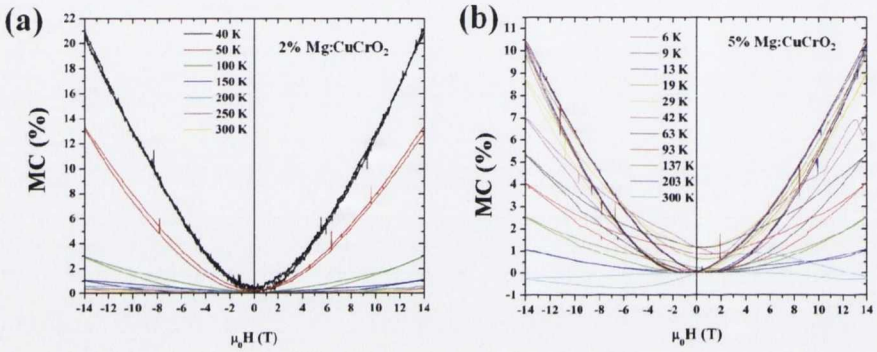

Figure 3.36: Magnetoconductance of (a) 2 % Mg-$CuCrO_2$ and (b) 5 % Mg-$CuCrO_2$ thin films

The 2 % Mg sample was successfully measured down to 40 K, where it reached a maximum positive MC of $\sim$ 21 % shown in fig. 3.36 (a). The 5 % Mg sample also exhibited positive MC of $\sim$ 10.5 % down as far as 6 K in fig. 3.36 (b).

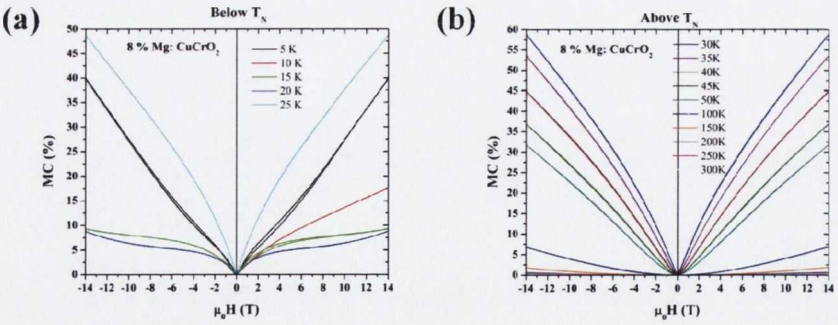

Figure 3.37: Magnetoconductance of 8 % Mg-$CuCrO_2$ thin film (a) below T_N and (b) above T_N.

Measurement of the 8 % Mg-doped sample revealed an interesting feature in the magnetotransport properties of $CuCrO_2$. The positive MC was observed to increase with reducing temperature in the range 50 K to 30 K, where the maximum of $\sim$ 60 % was achieved. Further cooling resulted

in a decrease in the MC around the Néel temperature $\sim$ 25 K and below, until a minimum of $\sim$ 10 % was measured at 20 K. In further reduced temperatures the MC was observed to resume increasing, resulting in a MC of $\sim$ 40 % at 5 K. Similar observations can be made based on temperature scans shown in fig. 3.33. Similar non-monotonic behaviour, with a maximum just above T_N was observed in polycrystalline samples in a number of publications Okuda *et al.* (2005) Maignan *et al.* (2009) Okuda *et al.* (2007). The shape of the magnetoconductance at high field is linear and no bending due to the breaking of the antiferromagnetic order is observable up to 14 T. In order to observe a spin flop, a field in excess of 3-10 times the exchange energy would be necessary. Since the exchange is on the order of 2 meV, the required field would be about 40-100 T.

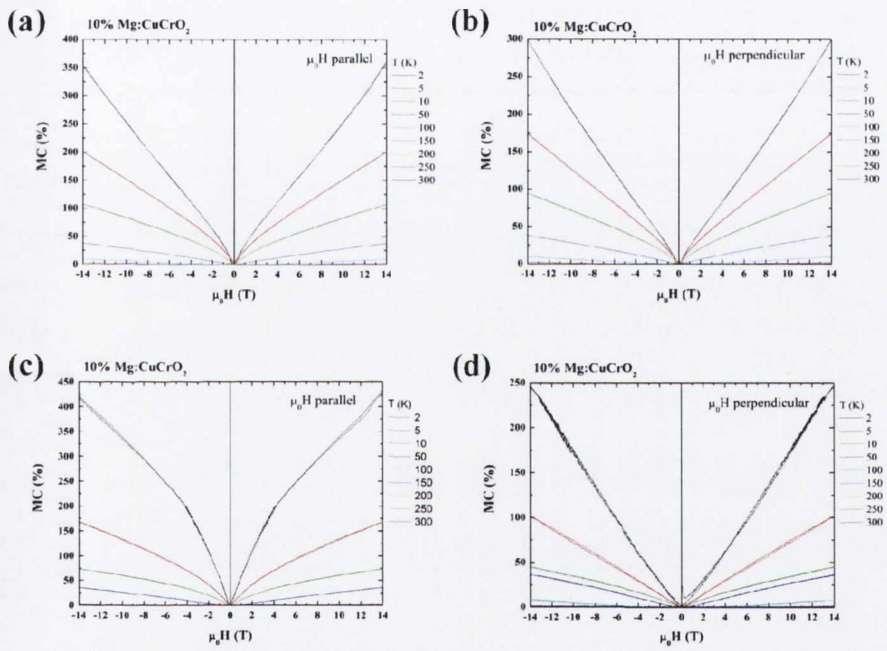

Figure 3.38: Magnetoconductance of two 10 % Mg-$CuCrO_2$ thin films in both the field parallel and field perpendicular configurations. The magnetoconductance of a 135 nm thick 10 % Mg-$CuCrO_2$ film measured with the field (a) parallel and (b) perpendicular to the sample plane. The magnetoconductance of a 40 nm thick 10 % Mg-$CuCrO_2$ film measured with the field (c) parallel and (d) perpendicular to the sample plane.

The most sizeable positive magnetoconductance value was measured in the 10 % Mg-$CuCrO_2$ thin films. A degree of anisotropy ($\sim$ 20 %) was also observed between the transverse and longitudinal configurations. Anisotropy in the physical properties is expected in this type of layered system and the observation of such anisotropy provides further evidence of the good microcrys-

talline orientation of the films on length scales comparable to the Fermi wavelength of the holes (of the order of 10 nm). The 135 nm thick sample yielded a 350 % MC in the field parallel scheme, shown in fig. 3.38 (a), while the thinner 40 nm thick sample exhibited $\sim$ 410 % MC in the same set-up, fig. 3.38 (b). A significant digression from these climactic values was observed in the field perpendicular regime, wherein the thicker sample measured $\sim$ 300 % magnetoconductance and the thinner sample demonstrated a $\sim$ 250 % value. Although these values remain significant, they are considerably lower than their parallel counterparts.

Considerable investigation of the magneto-electric coupling reported in $CuCrO_2$ thin films has been underway in very recent years Poienar *et al.* (2009) Okuda *et al.* (2005). The large magnetoconductance reported in this work appears to be further evidence of such interactions.

Hall Effect It has previously been noted that the direct measurement of the Hall effect has proved too difficult due to the low mobility of the carriers in $CuCrO_2$ and Mg-$CuCrO_2$. A more sensitive method must therefore be employed. One possibility is to use low frequency AC excitation ($\sim$ 17.5 Hz), high impedance preamplifiers, and bridge nulling in order to achieve stability on the time scale of hours and signal-to-noise ratios of the order of 10^3 and allow for the extraction of Hall voltages of the order of 1 % of the residual resistance drop. This type of AC Hall effect measurement, carried out with Dr. P. Stamenov, has allowed us to obtain the basic effective transport parameters, resistivity, mobility and electronic carrier concentration, shown in table 3.9. Sample impedance below 100 K became comparable to the input impedance of the preamplifiers used introducing significant fluctuations in amplifier bias currents, thus prohibiting measurement below this temperature.

Parameter	Value	Standard error
A	0.00373	1.70301×10^{-6}
B	4.95276×10^{-9}	5.43891×10^{-11}
C	7.85334×10^{-14}	3.64703×10^{-16}
D	1.32007×10^{-11}	6.87035×10^{-12}

Table 3.8: AC Hall effect fitting parameters for 10 % Mg:$CuCrO_2$ thin film measured at 150 K

Fitting the AC Hall effect data, as shown in the examples above fig. 3.39 with the equation

$$y = A + B \cdot |x| + C \cdot x^2 + D \cdot x \tag{3.18}$$

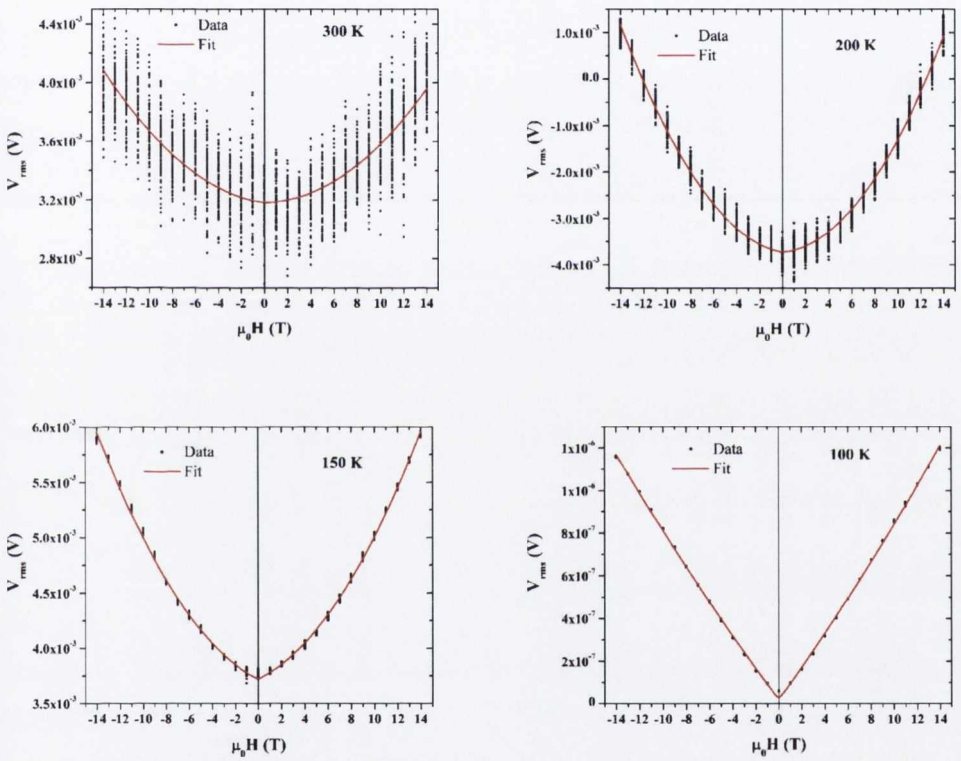

Figure 3.39: AC Hall effect measurement of a 10 % Mg-doped $CuCrO_2$ thin film, showing a sample fitting of data collected at 100, 150, 200 and 300 K.

where A is the residual resistive voltage, B is the coefficient of proportionality for the linear magnetoresistance, C is the conventional parabolic positive magnetoresistance and D is the Hall slope. The extracted D parameter is used to calculate the actual AC Hall voltage and hence the effective transport parameters reported in table 3.9. The error on the absolute value of the Hall voltage extracted in a Van der Pauw geometry can be as high as 10 % depending on the size of the contact, distance between contacts and possibility of inhomogeneity in the thickness of the film, however the level of reproducibility, or the relative uncertainty between different temperatures on the same sample and contact configurations is better than that, allowing the comparison between different temperatures. Moreover it should be emphasised that with the low mobilities encountered in this material a distinct separation of hole and electron concentrations from transport measurement is not possible. Therefore all the transport parameters given are effective parameters (for all types of carrier).

T (K)	ρ (Ωcm)	μ_{eff} (cm^2/Vs)	n_{eff} (cm^{-3})
100	0.101	5.6(8) $\times$ 10^{-3}	-1.1(2) $\times$ 10^{22}
150	0.064	8(5) $\times$ 10^{-5}	-1.2(8) $\times$ 10^{24}
200	0.051	7(1) $\times$ 10^{-3}	1.7(3) $\times$ 10^{22}
300	0.040	5(1) $\times$ 10^{-3}	3.4(7) $\times$ 10^{22}

Table 3.9: Effective transport parameters calculated from AC Hall effect measurement of 10 % Mg:$CuCrO_2$ thin film

The data clearly indicate that there is a crossover from a hole-dominated conduction regime at the lower temperatures to an electron-dominated conduction regime demarcated by a change in the sign of the effective carrier concentration, with the compensation point in the region between 150 and 200 K[1]. Although the origin of the donor level, located approximately 20 - 70 meV (as indicated by E_{a1} in table 3.7) below the CB, is unclear, carrier compensation would be expected in exactly this temperature region. The anomalously low value for the effective mobility, μ_{eff}, and the anomalously high value for the effective carrier concentration, n_{eff}, in the region of 150 K are characteristic of the two band scheme discussed in section 2.3.2, and the fact that only effective parameters are accessible as signal-to-noise ratio does not permit the simultaneous fitting of conductivity and Hall resistance as a function of magnetic field. The possibility of incorporation

[1] It is the effective carrier type that changes in the measurement, and that is a function of both the partial signed mobilities, and the partial carrier concentrations, therefore the Hall resistance going through zero does not imply automatically that ρ goes to infinity.

of this material into a device functioning at room temperature is prohibited by the fact that n-type behaviour is observed in this temperature region.

3.3.6 Discussion

The powders synthesised in the previous section have been used as the source materials to fabricate targets of the parent material $CuCrO_2$, and its Mg-doped compound, for pulsed laser deposition of thin film samples of the same phase on c-cut sapphire substrates. The deposition process has been optimised in terms of substrate temperature and oxygen partial pressure conditions to achieve the desired single phase material, and a complete survey of the conditions for successful growth of $CuCrO_2$ thin films has been carried out determining a temperature of 923 K and 20 μbar of O_2 to produce the optimum results. Low growth rates and laser fluences just above the ablation threshold have been favoured over the faster, higher energy growth modes in order to avoid degradation of the crystal during deposition. X-ray diffraction inspection of the thin film samples indicates a higher solubility limit for Mg in the $CuCrO_2$ lattice than in the bulk specimens, due to the absence of the $MgCr_2O_4$ phase in the scans. The films have been observed to grow highly c-axis oriented with the appearance of a very minor secondary (101) orientation of the films. A small Cu_2O impurity phase has been observed in some of the samples, however the appearance of this phase does not correlate with increased doping concentration, and may be due to target deterioration during ablation. Rocking curves of the thin films have exhibited narrow FWHM ω values indicating coherent growth. The a and c lattice parameters of the films have been determined by in-plane and out-of-plane XRD analysis, they agree well with the reported bulk values, and they appear to vary independently of Mg-doping concentration in the substituted samples. The undoped and Mg-doped thin film samples have been characterised by optical transmission measurements in the UV-visible range, the transparencies of the films have been observed to vary from 40 to 80 % in the visible spectral range, and these values are evidently influenced by the film thicknesses. The bandgaps of the films have been determined by the method of Tauc, returning values between 3.15 and 3.22 eV corresponding to direct transitions, which did not exhibit any obvious dependence on doping. Confirmation of Mg-incorporation into the $CuCrO_2$ lattice for a 10 % Mg-doped thin film sample was provided by the observation of a peak corresponding to the Mg $1s$ line in the x-ray photoelectron spectrum of the doped film, which was absent in the undoped sample. The conductivity of the doped films has been observed to increase with increasing Mg content. For doping concentrations higher than 5 %, the conductivity increases by four orders of magnitude. The conductance and magnetoconductance of the thin films of higher Mg doping have shown an anomaly around the Néel temperature of

the compound. This feature may be an indication of a strong interaction between the carriers and the localised spin on the Cr atoms. The magnetoconductance in all the measured samples has been observed to be positive and linear at high fields. It has been observed to increase at low temperature, and at 5 K the magnetoconductance of the higher doped samples reaches several hundred percent. Although the origin of these large values remains unclear, this is another indication of strong spin-carrier coupling. An attempt has been made to determine the sign and magnitude of the effective carrier concentration using an ac Hall effect method in a Van der Pauw configuration. Although this method may not be the most accurate in determining the actual carrier concentration, it did provide clear evidence of hole conduction below 150 K.

3.4 Conclusions

The furtherance of the $CuCrO_2$ delafossite with respect to both its optical and electrical properties has involved investigation of the optimum preparation techniques and conditions, examination of the effect of impurity substitution, and characterisation of the obtained species. The powder study has revealed a very low Mg ion solubility limit of 1 % in the $CuCrO_2$ lattice. Reaction under an Ar atmosphere has been found necessary to achieve a single $CuCrO_2$ phase in the bulk samples. The powders synthesised under the optimised conditions are highly suitable source materials for PLD of $CuCrO_2$ thin films, producing densely packed and well-sintered targets with an observed global doping concentration in good agreement with the nominal doping concentration, and an appropriately homogeneous Mg impurity distribution. The Néel point was determined to be just below 25 K, and is unaltered by Mg-doping. The effective moment was found to be 3.89 μ_B/Cr with a Curie temperature of -191 K, whose absolute value is far above the Néel transition temperature, implying that the transition is driven by local disorder and frustration. This is to be expected because of the triangular antiferromagnetic ordering, which can be seen in fig. 2.20.

High quality thin films were grown on sapphire substrates with a 30^o rotation. Various levels of Mg-doping were investigated, both in terms of their optical and electrical properties. No discrete surface or interface layers were resolved by x-ray reflectivity. The disorder induced by the introduction of Mg into the lattice was clearly observed by 3 axis x-ray diffraction and evidence for long-range ordering of the Mg dopant was observed. For very thick deposits (very long deposition times, up to 9 hrs) heterogeneous microcrystalline growth was observed. Even though the top surface roughness of the films immediately after growth was of the order of 2 nm r.m.s., after long term (two years) exposure to ambient atmosphere significant surface precipitates ($\sim$ 40 nm)

were seen. The direct optical bandgap was confirmed to be 3.1(1) eV. No systematic relation was observed with Mg-dopant concentration up to 10 %. Significant ($\sim$ 5 %) free carrier absorption and reflection was observed owing to the high carrier concentration (of the order 10^{22} cm^{-3}). Visible optical transparencies as high as 70 % have been observed for thicknesses of $\sim$ 30 nm, with maximal transmission in the IR estimated at $\sim$ 85 %. The incorporation of the Mg-dopant was confirmed by x-ray photoemission spectroscopy. The temperature dependance of the conductivity obeys an exponential law in the temperature region 100 K - 300 K, where an activation energy on the order of 70 meV is extracted. This shows that, at least at high temperature, a band conduction occurs in this material. For the first time effective carrier concentrations and mobilities have been successfully measured in this system. Very large magnetoconductance (in excess of 300 % at 14 T) has been observed below the Néel point in highly doped thin film samples (10 % Mg concentrations). This is also well manifested in the temperature-dependence of the conductivity in the vicinity of the antiferromagnetic transition.

Chapter 4

Bipolar Delafossite $CuInO_2$

4.1 Introduction to $CuInO_2$

Of the copper-based delafossites, the $CuInO_2$ system is particularly interesting because of its reported bipolar dopability Sheng *et al.* (2006). $CuInO_2$ has a rhombohedral crystal structure with space group $R\bar{3}m$ Liu *et al.* (2005a). The lattice parameters of the structure have been experimentally determined to be $a = 3.292$ Å and $c = 17.388$ ÅShimode *et al.* (2000). Thin films of $CuInO_2$ delafossite exhibit both p-type and n-type conduction by doping with an appropriate impurity and tuning the deposition conditions. By substituting Sn^{4+} for In^{3+} in the lattice, it becomes n-type, while doping with Ca^{2+} induces p-type semiconductivity, allowing the possibility for p-n homojunctions to be produced Yanagi *et al.* (2001a,b).

Unfortunately, the conductivity of $CuInO_2$ films has, thus far, been smaller than that of the other p-type TCOs. According to most of the reports, the conductivity values of Ca- and Sn-doped $CuInO_2$ are of the order of 10^{-3} S/cm [1], which can be increased by one order of magnitude by optimising the deposition parameters Kudo *et al.* (1998). No figures for the Hall mobility of either material have been reported. The activation energy of n-type Sn-doped $CuInO_2$, which was reported to be 0.077 eV, is far lower than that of the p-type Ca-doped compound which was 0.190 eV Kawazoe *et al.* (1997); Yanagi *et al.* (2001a). The thermopower gave similar results with -50 μVK^{-1} for the Sn doping and +480 μVK^{-1} for the Ca Yanagi *et al.* (2001a). The band gap of the material was estimated to be 3.9 eV Kawazoe *et al.* (1997), the largest reported bandgap of the delafossite TCOs.

[1] There was one report of a conductivity of 10^{-6} S/cm in $CuInO_2$:Ca Yanagi *et al.* (2001a)

Yanagi *et al.* reported the growth of *p*-type $CuInO_2$ films by PLD from phase-pure $CuInO_2$ targets Yanagi *et al.* (2001a). However, producing phase-pure targets is still challenging and has likely limited the subsequent research on $CuInO_2$. Almost phase-pure targets have reportedly been fabricated by the method of cation exchange reaction Shimode *et al.* (2000). However, the oxygen-rich $Cu_2In_2O_5$ phase of *Cu-In-O* is easily prepared by solid-state synthesis in air. Therefore, Teplin et al. reportedly used $Cu_2In_2O_5$ as a target to deposit single-phase undoped and $Ca-$doped $CuInO_2$ thin films Teplin *et al.* (2004). Yanagi *et al.* later fabricated a homogeneous transparent rectifying *p-n* junction with this material Yanagi *et al.* (2000c). The diode, which had a total thickness of 1.8 μm, exhibited an optical transmission of 60 - 80 % in the visible region and had a turn-on voltage of $\sim 1.8\ V$.

A number of theoretical papers have been published in the attempt to explain the properties of $CuInO_2$. Using first-principles methods, Nie *et al.* interpret the bipolar dopability observed in $CuInO_2$ to be due to the exceptionally large disparity between its fundamental indirect bandgap and apparent direct band gap Nie *et al.* (2002). Liu *et al.* found a discrepancy between their calculated conductivity values for undoped $CuInO_2$, and *Ca-* and *Sn*-doped $CuInO_2$ and the experimentally observed values. They propose that the presence of amorphous In_2O_3 may be responsible for the differences between the experimental reports and the modelling. They further suggest that the XRD spectra presented in the experimental reports do not preclude the existence of In_2O_3 particularly in the amorphous state. Both In_2O_3:*Sn* and In_2O_3 with oxygen deficiency are proven *n*-type TCOs with high mobility, even in amorphous phase. Ginley *et al.* report that In_2O_3 coexists in deposited films of $CuInO_2$:*Ca* for a deposition temperature of 873 K or above Ginley *et al.* (2003).

4.1.1 Electronic Band Structure

The nature of the bandgap in $CuInO_2$ is a source of discord in the research community. Experimentally, the fundamental bandgap of $CuInO_2$ has been determined by optical absorption measurements to be approximately 3.9 eV or greater Yanagi *et al.* (2001a) Teplin *et al.* (2004), and the transition has been identified as a direct band-to-band transition. Conversely, density functional theory reports an indirect fundamental bandgap between the VB maximum, which appears at the *F* symmetry point, and the CB minimum, which is at the Γ point of the Brillouin zone Falabretti & Robertson (2007), with values between 0.32 eV and 0.52 eV, as indicated in table 4.1.

Calculations have determined the smallest direct gap to occur at Γ, however this transition is dipole forbidden Pellicer-Porres *et al.* (2006) Makhova *et al.* (2006). Absorption near the smallest

E_g Direct (eV)	Symmetry	E_g Indirect (eV)	Symmetry	Reference
0.73	Γ [1]	0.41	$F - \Gamma$	Nie *et al.* (2002)
0.68 [2]	Γ	0.32	$F - \Gamma$	Liu *et al.* (2005a) Liu *et al.* (2005b)
		0.49		Sasaki & Shimode (2003)
0.96	Γ	0.52	$F - \Gamma$	Robertson *et al.* (2002)

Table 4.1: Theoretical bandgap values of $CuInO_2$.

direct bandgap at Γ is therefore thought to be of low level, only increasing slightly with increasing energy until a subsequent higher energy transition occurs. One study reports that the lowest direct allowed transition occurs at the L point, and the authors attribute the observed optical bandgap to this transition, defining it to be an apparent bandgap, since optical absorption measurements are only sensitive to the more intense direct transitions Nie *et al.* (2002). There has been a report of some optical absorption in $CuInO_2$ thin films, below the optical bandgap between 1 and 2 eV, measured by spectroscopic ellipsometry Teplin *et al.* (2004), which could be attributed to either the fundamental indirect transition or the lowest direct transition at Γ which, although small, is nonetheless nonzero.

A density of states study on the electronic band structure has indicated a broad valence band that is composed mainly of Cu d and O p states, with some Cu s and In d states contributing to the upper valence band. The conduction band minimum mainly consists of Cu d, In s and O s states Liu *et al.* (2005a). A DFT study of the Ca and Sn doping in $CuInO_2$ has reported that Ca substitutes for In in the lattice, forming quite a deep acceptor level 0.41 eV above the VB maximum Liu *et al.* (2005b), consistent with experimental reports of resultant p-type conductivity. Substitution of Sn on In sites was found to form deep donor levels in the bandgap. This publication infers that these deep donor and deep acceptor impurities are unlikely to account for the increased conductivity described in experimental reports, suggesting that amorphous In_2O_3, unseen by x-ray diffraction, may be somewhat responsible for the enhancement in the electrical properties. The observation of the coexistence of an In_2O_3 impurity phase in thin films of $CuInO_2$ Ginley *et al.* (2003) has been reported.

4.1.1.1 Bipolar Doping

The bipolar character of the delafossite $CuInO_2$ is puzzling, considering it is a wide bandgap oxide. However, reports that the optical bandgap is merely an apparent bandgap, and that the fundamental gap is indirect in nature, may explain this unusual property. It has also been noted

that the CB minimum for $CuInO_2$ is low-lying in comparison with another $CuM^{III}O_2$ delafossite, $CuAlO_2$, that also has a group (III) M cation, which should imply that the material is conducive to n-type doping Nie *et al.* (2002).

4.1.2 Electrical Properties

The reported electrical and optical properties of $CuInO_2$ thin films and donor and acceptor doped compounds are summarised in table 4.2.

Material	Dopant	σ (S/cm)	E_a (eV)	E_g Direct (eV)	E_g Indirect (eV)	T (%)	Reference
$CuInO_2$	Undoped	$\sim 10^{-6}$ [1]		4.45	1.44		[1]
$CuInO_2$	5 % Ca	2.7×10^{-6} [2]		4.45	1.44		[1]
$CuInO_2$	5 % Sn	4.4×10^{-3} [3]		4.45	1.44		[1]
$CuInO_2$	5 % Sn	3.8×10^{-3}	0.077	~ 3.9		~ 70	[2]
$CuInO_2$	7 % Ca	2.8×10^{-3}	0.190	~ 3.9		~ 70	[2]
$CuInO_2$	5 % Ca	5.8×10^{-2}					[3]
$CuInO_2$	5 % Ca	$\sim 3 \times 10^{-3}$		4.15			[4]

Table 4.2: Summary of electrical and optical properties reported for $CuInO_2$ thin films. Reference [1] = Sasaki & Shimode (2003), [2] = Yanagi *et al.* (2001a) Ohta *et al.* (2003c) Hosono *et al.* (2002), [3] = Ginley *et al.* (2003), [4] = Teplin *et al.* (2004) (T = Transparency).

4.1.3 Motivation

The primary advantage of an amphoteric semiconductor is the opportunity to produce a homoepitaxial $p-n$ homojunction diode, as has been reported for $CuInO_2$ Yanagi *et al.* (2001b). The lattice matching between the polar layers of such a structure can result in greatly improved interface morphology and crystallinity in the structure, properties that have significant influence in optoelectronics applications. The question arises, however, as to how bipolarity of doping can emerge in such a wide bandgap oxide.

The difficulty in preparing single phase $CuInO_2$ in bulk has been well documented Ginley *et al.* (2003). In this study the objective was to determine the optimum growth conditions necessary to achieve phase pure, highly crystalline thin films of both donor and acceptor doped $CuInO_2$. A further goal was to assess their candidacy for implementation in an active transparent device

in terms of their electrical and structural properties. In studying this member of the delafossite family, optical measurements have been carried out in an attempt to determine the nature of the bandgap in this bipolar material.

In the existing report of *p-n* transparent homojunction fabrication, the authors described contacting the respective *n* and *p*-type $CuInO_2$ layers of the structure with highly conductive layers of ITO to provide transparent contacts to the junction. Although contacting the sample with transparent layers would appear to be a practical next step after measuring rectification in a transparent *p-n* homojunction, it may have been a premature measure to take before confirming that the $CuInO_2$ *n* and *p* layers are solely responsible for this electrical behaviour. We aimed to verify whether or not we could achieve rectification in a $CuInO_2$ homojunction without the influence of post-deposited highly conductive layers.

4.2 Powder Synthesis

4.2.1 Solid State Reaction

Synthesis of the $CuInO_2$ powder by simple solid state reaction proved more difficult than $CuCrO_2$. As described earlier, single phase $Cu_2In_2O_5$ powder can more easily be prepared by solid state reaction than $CuInO_2$, and it has successfully been used to deposit thin films of $CuInO_2$ Teplin *et al.* (2004). Therefore, powder of undoped $Cu_2In_2O_5$ and the doped powders, $Cu_2In_{2(1-x)}M_{2x}O_5$ where for $M = Ca$, $x = 1, 2, 3, 5, 8$ %, and for $M = Sn$, $x = 1, 2, 3, 5$ %, were prepared by this method. The procedure described in chapter 3 and appendix A was repeated and the $Cu_2In_2O_5$ target was prepared in accordance with the equation:

$$2CuO + (1-x)In_2O_3 + (2x)SnO_2/CaO \longrightarrow Cu_2In_{2(1-x)}Sn/Ca_{2x}O_5$$

4.2.2 Ion Exchange Reaction

$CuInO_2$ is a ternary compound which, according to the literature Liu *et al.* (2005b), is metastable compared to its end-point binary compounds Cu_2O and In_2O_3. The synthesis of $CuInO_2$ in either powder or thin film form is difficult. In addition to the report in which solid state reaction was employed, another method for preparation of $CuInO_2$ powder has been reported Shimode *et al.* (2000). Cation exchange reaction, as the name suggests, involves the exchange of one cation in the reactant for the desired cation. This technique has also been employed in the synthesis of $CuScO_2$

Doumerc *et al.* (1987). In this case, $LiInO_2$ was used as a reactant for an exchange reaction with $CuCl$ according to the following reaction equation Shimode *et al.* (2000), Gessner (1970):

$$LiInO_2 + CuCl \longrightarrow CuInO_2 + LiCl$$

The $LiInO_2$ was prepared by solid state reaction of stoichiometric amounts of Li_2O (97%) and In_2O_3 (99.99%) according to the equation:

$$\frac{1}{2}Li_2O + \frac{1}{2}In_2O_3 \longrightarrow LiInO_2$$

The powders were mixed together and ground before sintering in a silver tube at 798 K for 5 days. The rate of heating and cooling was 10 K/hr. The phase of the $LiInO_2$ powder obtained was analysed by x-ray diffraction before the second stage of the process was carried out. This powder was then mixed with $CuCl$ (97 % pure) in a dry process. The mixture was then sealed in an evacuated quartz tube and heated at 873 K for 24 hrs. The resultant species was then rinsed with distilled water to leach out the remaining $LiCl$ and finally dried in a heating cupboard.

4.2.3 Structural Characterisation

X-Ray analysis of the precursor $LiInO_2$ powder, prepared by solid state reaction, was not found to be single phase. The x-ray powder diffraction pattern is shown on fig. 4.1, with two phases identified as the desired $LiInO_2$ compound (shown in red) and the impurity phase In_2O_3 (shown in blue). This is due either to the volatility of the LiO_2, or to its reaction with the silver tube in which the reaction took place. The ion exchange reaction was not, therefore, carried out since this impurity phase remain throughout the process. This result is in agreement with the findings reported by Shimode *et al.* (2000), who obtained the $CuInO_2$ phase with traces of the additional phases, CuO and In_2O_3, arising from the unreacted $CuCl$ powder and already present In_2O_3.

Since the objective in studying the powder synthesis was to procure a stoichiometric target from which $CuInO_2$ thin films could be deposited, the $Cu_2In_2O_5$ was equally suitable. The $Cu_2In_2O_5$ powder prepared by solid state reaction was also found to contain some small impurity phases, CuO and In_2O_3, as shown in fig. 4.2, however this method was more amenable to synthesising powders with various stoichiometries of the Ca and Sn impurities respectively, and in the absence of any advantage in using the cation exchange prepared powder, $Cu_2In_2O_5$ was found to suffice. In order to produce thin films of $CuInO_2$ by PLD, $Cu_2In_2O_5$ powder was therefore used as the source material. The cations in this material are present in equal proportions and the nature of the PLD process allows sufficient control over the oxygen content in the films to achieve the requisite phase.

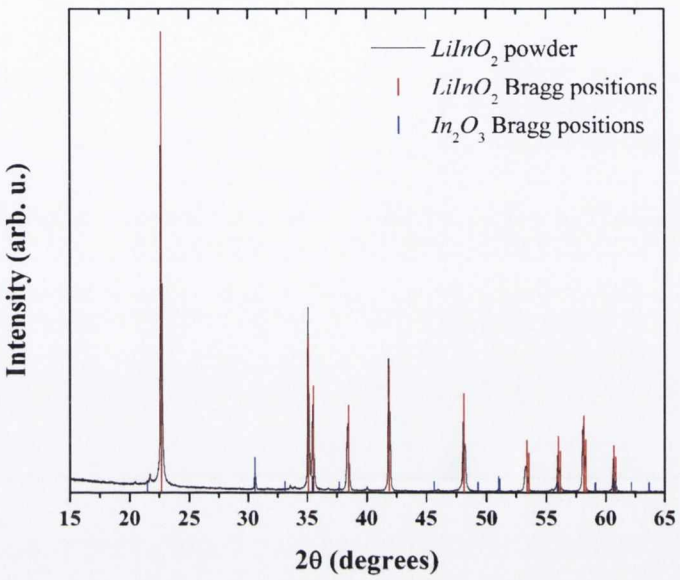

Figure 4.1: X-Ray diffraction analysis of $LiInO_2$ powder.

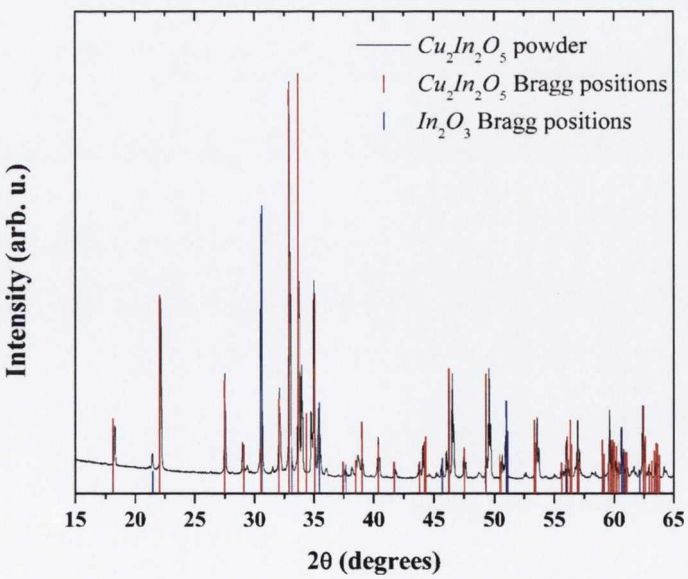

Figure 4.2: X-Ray diffraction analysis of $Cu_2In_2O_5$ powder.

4.3 Thin Film Fabrication

Thin films of $CuInO_2$ doped with both Sn and Ca have been grown on $(00l)$ oriented sapphire substrates by PLD, and the deposition conditions have been optimised to achieve single phase films with a high degree of crystallinity. As with the powder synthesis, $CuInO_2$ thin films are more difficult to fabricate than their $CuCrO_2$ counterparts. The most obvious difficulty to date has been described already, that is the inability to make a phase pure $CuInO_2$ target, although the PLD system has sufficient control over the oxygen partial pressure during deposition to allow a certain level of control over the oxygen content in the thin films and hence the $Cu_2In_2O_5$ is an adequate source material. This solution raises another issue, that of the laser interaction with the target, which has the effect of altering the target stoichiometry in the ablated pellet. This problem was also observed in relation to the ablation of $CuCrO_2$ thin films, and it was overcome by polishing the target surface to reveal a new stoichiometric layer between depositions.

Having investigated a number of substrate temperature and oxygen partial pressure combinations, it has been observed that the range of deposition conditions that result in the successful growth of delafossite copper indium oxide thin films is narrow. An average oxygen partial pressure of 1 μbar, one order of magnitude lower than that required for the previous delafossite, was required to achieve the optimum growth of these films. This is to be expected since the source material, $Cu_2In_2O_5$ is oxygen rich compared with the required stoichiometric ratio of cations and anions for obtaining the delafossite phase $CuInO_2$. It is worth noting that this material is known to accept excess oxygen in the lattice Park & Keszler (2003) Yaicle *et al.* (2007) Liu *et al.* (2005a). The optimal substrate temperature during deposition was found to be 773 K, significantly lower than the 923 K required for $CuCrO_2$ thin film growth, but in agreement with reports that $CuInO_2$ decomposes above 873 K Park & Keszler (2003). The resultant thin films were noted to be transparent and colourless to the eye. The optimum growth conditions for these materials are summarised in table 4.3.

	Dopant	Pressure O_2 (μbar)	Temperature (K)	Energy Density (Jcm^{-2})	Rep. Rate (Hz)
$CuInO_2$		10	773	1.5	2
$CuInO_2$	1 % Sn	1	773	1.5	2
$CuInO_2$	3, 5, 8 % Ca	0.5 – 10	773	1.5	2

Table 4.3: Summary of optimum growth conditions for $CuInO_2$ thin films.

4.3.1 Structural Characterisation

The growth of the $CuInO_2$ thin films was monitored *in situ* by RHEED during the deposition. The diffraction patterns of a bare *c*-cut sapphire substrate in two directions are shown in figs. 4.3 (a) and (b) before the deposition. The diffraction patterns of the $CuInO_2$ film in the same directions, after the deposition in the optimised growth conditions, are shown in fig. 4.3 (c) and (d). The spotty patterns observed after the deposition, are characteristic of 3-dimensional growth, the arrangement of the diffraction spots in line with those of the underlying Al_2O_3 substrate are indicative of a crystalline film with oriented growth.

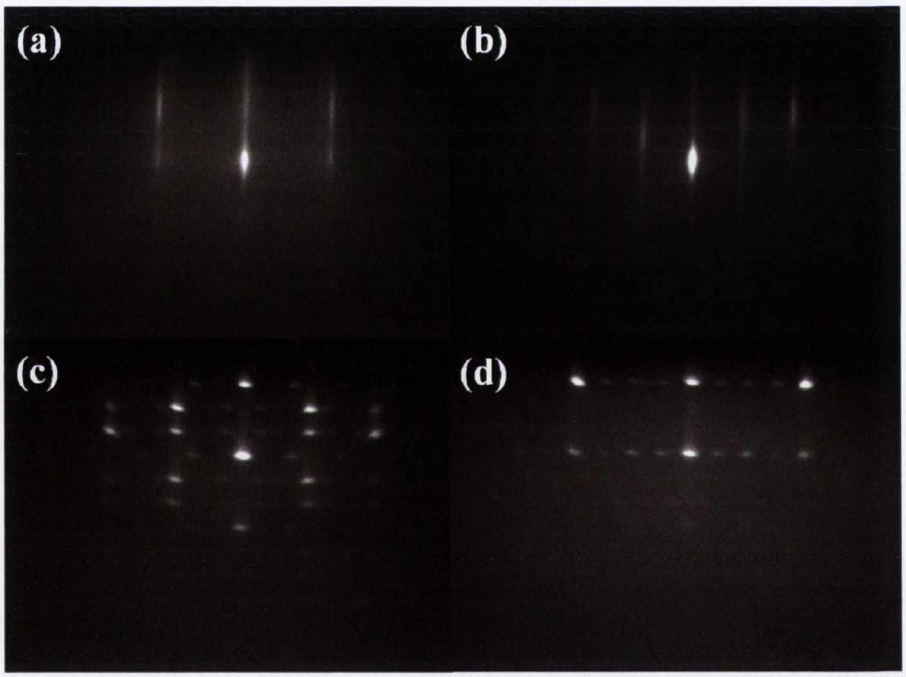

Figure 4.3: RHEED patterns of (a) $[\bar{1}10]$ and $[\bar{1}\bar{1}0]$ orientations of the *c*-cut sapphire substrate before deposition and corresponding views (c) and (d) underneath after deposition of a $CuInO_2$ thin film.

The $CuInO_2$ thin films were characterised by x-ray diffraction analysis. Diffraction patterns of an undoped $CuInO_2$ thin film, grown under the optimised deposition conditions is shown in fig. 4.4 (a). All of the peaks are indexed with the $CuInO_2$ $(00l)$ family of planes, apart from the (006) and (0012) peaks of the sapphire substrate. This pattern indicates similarities between the growth of $CuInO_2$ thin films and that of the other delafossite $CuCrO_2$ thin films examined in chapter 3. The quality of the samples have been examined by rocking curve analysis, a typical ω scan is

shown in fig. 4.4 (b). As for $CuCrO_2$, the rocking curve is composed of two distinct superimposed pseudo-voigt peaks about a common centre. The thickness of the analysed film was measured to be 15 nm by XRR, and the fact that the area under the narrow peak is smaller than the area under the broad peak confirms that misfit dislocations occurring at the substrate/thin film interface is the origin of this behaviour[1]. In order to illustrate the narrow range of deposition conditions, and the difficulty in obtaining phase pure $CuInO_2$ thin films and to distinguish an In_2O_3 impurity phase within these samples, the profile of the (006) peak of a film prepared at 823 K in 10μbar of O_2 is presented in fig. 4.4 (c). The peak exhibits a small shoulder on the low-angle side, the deconvolution of which resolves into three pseudo-voigt functions. The two more intense peaks correspond to the Cu $K_{\alpha 1}$ and $K_{\alpha 2}$ wavelength reflections of the $CuInO_2$ (006) planes. The least intense peak is identified as an impurity phase of In_2O_3.

X-Ray reflectivity analysis was used to determine the thickness of the thin films. The grazing angle 2θ scan of a 3 % Ca-doped $CuInO_2$ thin film sample is shown in fig. 4.5. The scan was fitted using the IMD software package, and the fitting is also shown in the figure. Additional information can be obtained from the simulation on the roughness of the thin film surface, which is shown on the graph, and the roughness at the film/substrate interface.

Diffraction patterns corresponding to 3, 5, and 8 % Ca-doped thin films are presented in fig. 4.6. The $2\theta - \omega$ scans revealed the single phase nature of all of the Ca acceptor-doped films. Despite the relatively high doping concentrations of up to 5 %, and the considerable lattice mismatch between the $CuInO_2$ film and the Al_2O_3 substrate, no impurity phases or secondary orientations were observed in these films up to concentrations of 8 % Ca where a minor additional peak was observed at $2\theta = 66.3°$. The films were all highly c-axis oriented as indicated by the $(00l)$ reflections of the Bragg peaks.

Surprisingly, however, the 1 % Sn doped sample did reveal a number of minor impurity phases despite this low level impurity doping. Additional phases of In_2O_3 and CuO were observed in the $2\theta - \omega$ scans of the donor-doped films, as indicated in fig. 4.7, however the thin film, which had a greater thickness compared with the other films, remained highly c-axis oriented. This indicated that the dopant solubility limit for Ca far exceeded that for Sn upon substitution for In in the lattice of the $CuInO_2$ thin film samples.

Asymmetric x-ray diffraction analysis was carried out on a number of the thin film samples to assess the in-plane nature of the thin film crystal. In-plane ϕ scans examining the (012) and (104)

[1] So in the case of thin films with a thickness on the order of 10 nm the narrow peak represents a smaller part of the layer

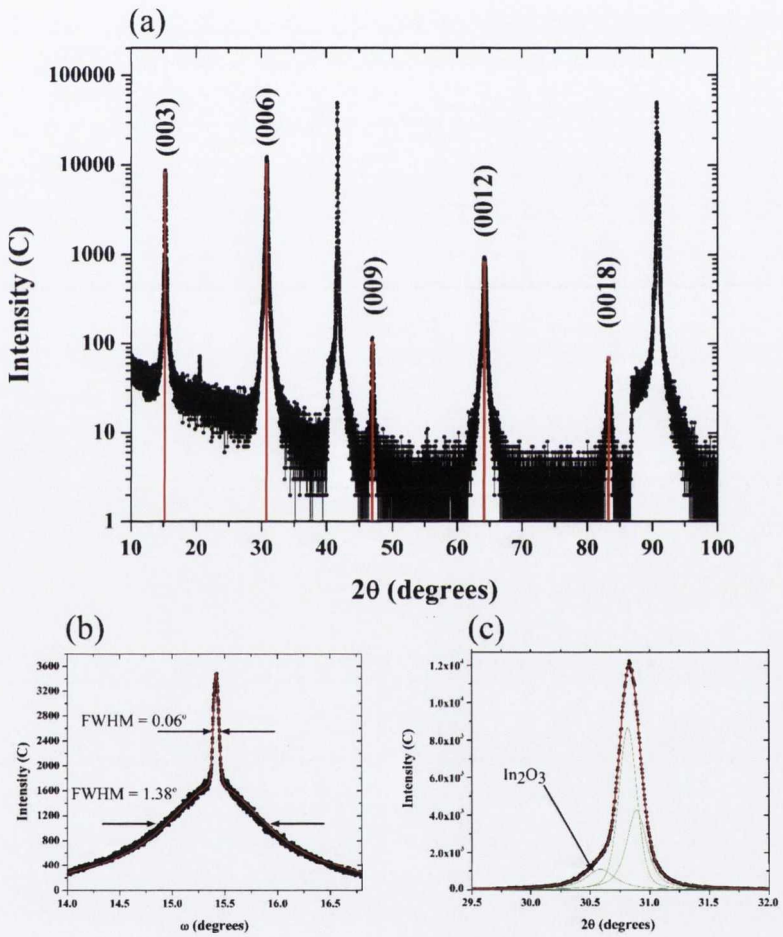

Figure 4.4: X-Ray diffraction (a) $2\theta - \omega$ scan, (b) rocking curve, and (c) $2\theta - \omega$ peak profile including peak fit, of undoped $CuInO_2$ thin film.

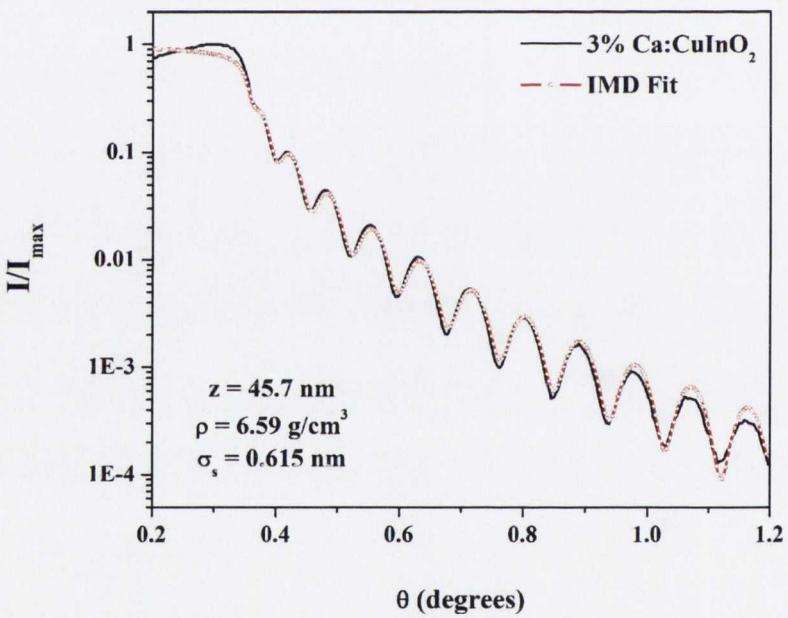

Figure 4.5: XRR scan of a 3 % Ca-doped $CuInO_2$ thin film fitted with IMD software package to obtain film thickness.

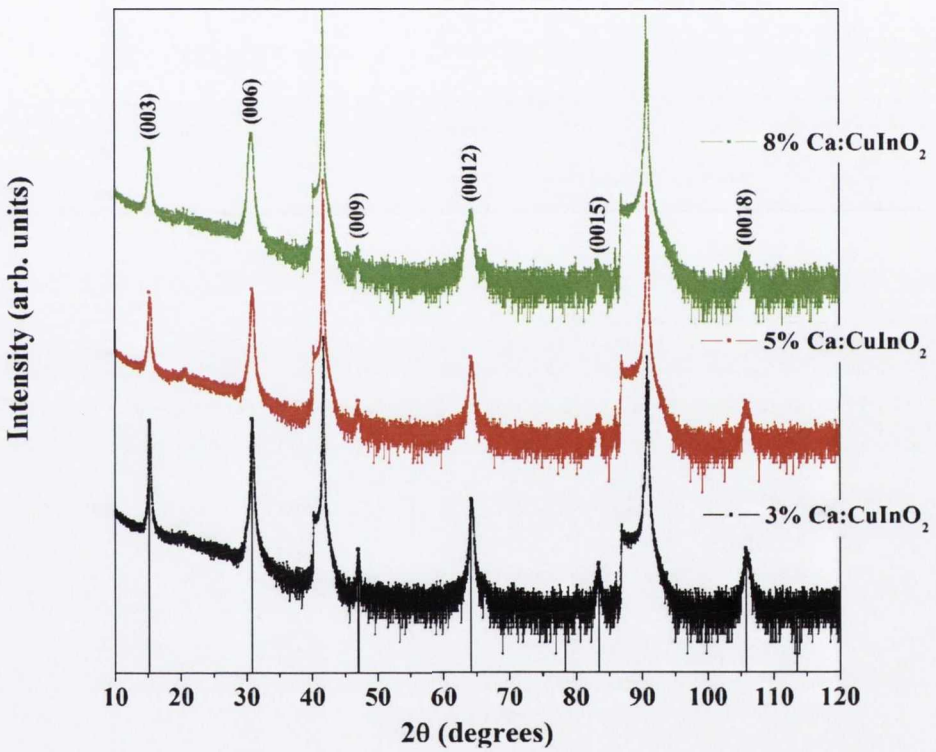

Figure 4.6: XRD $2\theta - \omega$ scans of $CuInO_2$ thin films with 3 % Ca doping, 5 % Ca doping, and 8 % Ca doping as indicated.

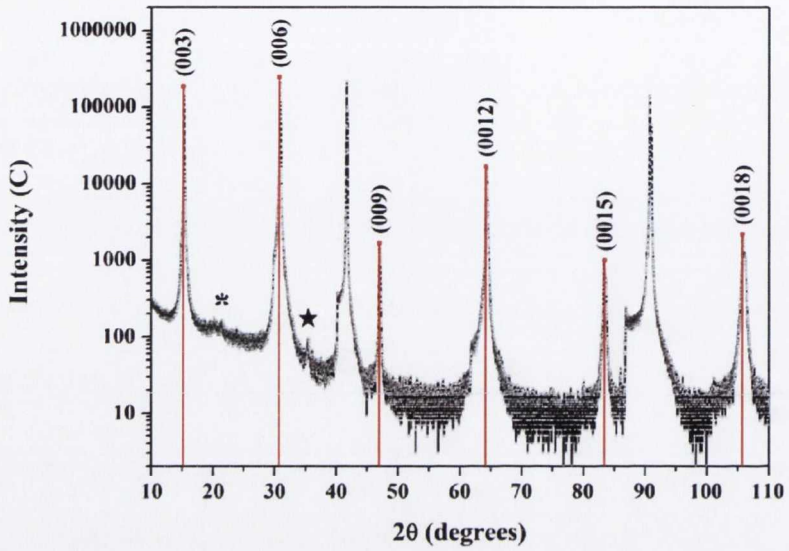

Figure 4.7: $2\theta - \omega$ scan of 1 % Sn-doped $CuInO_2$ thin film. The asterisk identifies an In_2O_3 (211) reflection, and the star identifies a CuO (002) peak.

planes of the 1 % Sn-doped $CuInO_2$ film are shown in fig. 4.8. Both the (012) and (104) planes of the film exhibit a multiplicity of 12, while a multiplicity of 6 is expected for the [012] and [104] directions. A similar effect was noted for the $CuCrO_2$ in chapter 3, and this was attributed to a 30^o in-plane rotation of the thin film in order to relax the considerable strain due to the large lattice mismatch with the sapphire substrate at the interface. The sapphire peaks had a multiplicity of 3 as expected.

An asymmetric $2\theta - \omega$ scan was carried out to determine the in-plane a lattice parameter of the film. The (104) film peak was observed to be sizeably shifted from the standard 2θ position published in the powder diffraction file. This may, to an extent, be due to sample misalignment for the in-plane measurement. The peak profile was also distorted due to the inappropriate focusing geometry of the XRD, which is habitually used in line-focusing geometry.

The ψ angular position of the (104) plane was calculated to be 56.7^o, and the in-plane scan was carried out with the sample positioned at this angle. The a and c lattice parameters determined from the combination of symmetric and asymmetric scans were found to be 3,570(1) Å and 17.362(7) Å respectively. The c lattice parameter compares tolerably well with the value in the powder diffraction file, 17.388 Å, while the a lattice parameter deviates slightly from the 3.292 Å

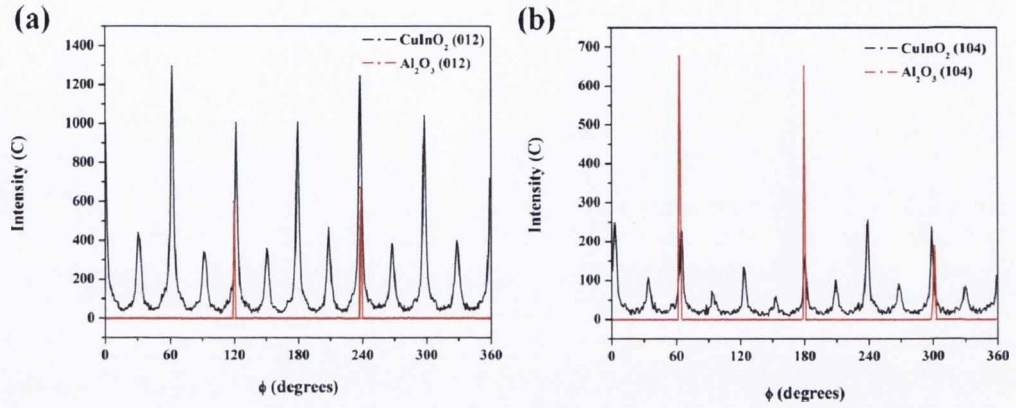

Figure 4.8: In-plane ϕ scans of (a) (012) and (b) (104) directions of a 1 % Sn-doped $CuInO_2$ thin film by XRD.

reported, however this is most likely due to the error introduced as a result of misalignment with the sample during scanning.

4.3.1.1 Atomic Force Microscopy

The surface morphology of a $CuInO_2$ thin film was analysed by AFM, by Dr. S. Colis, the resulting images are shown in fig. 4.9. The sample exhibits a smooth surface morphology on each of the scales examined, as indicated by fig. 4.9 (a), (b) and (c). The r.m.s. roughness of the surface was found to range from 4 nm, for the 15 μm^2 sampling window, down to 0.7 nm, for the 900 nm^2 sampling range. The maximum vertical peak to peak height was found to be 30 nm.

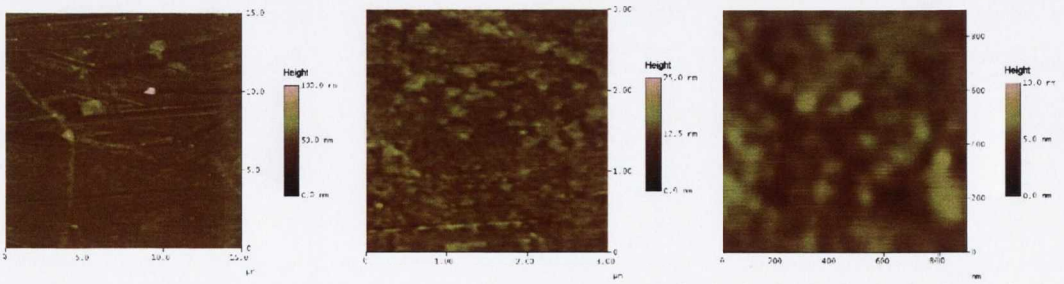

Figure 4.9: AFM images of a Ca-doped $CuInO_2$ thin film in different areal ranges.

4.3.2 Optical Characterisation

Optical spectrometry analysis in the UV-visible range of the electromagnetic spectrum was carried out on the $CuInO_2$ thin film samples. The purpose of this was to measure the transparency of the thin films of this delafossite material in the visible region and also to examine the optical bandgap and its dependence on doping.

The optical spectra of a number of Ca- and Sn-doped $CuInO_2$ thin films with varying impurity concentrations are presented in figs. 4.10 and 4.11. Similar results to those of the previous delafossite have been observed for the $CuInO_2$ thin films, in that the absorption edge for the films with higher impurity concentration is less sharp than that for the undoped and low-level doped films. In the case of $CuInO_2$ the average transmittance over the visible range is elevated in comparison to $CuCrO_2$, with values ranging from 55 to 90 % transparency. The appearance of transitions in the visible region for the 3 and 5 % Sn-doped $CuInO_2$ films may be due to the presence of CuO and In_2O_3 impurities which were observed for doping concentrations as low as 1 % by x-ray diffraction. The transmittance curves presented have not been corrected for sample thicknesses, and the apparent increase of transmittance with the introduction of the dopant could be due either to this effect or the varying incorporation of the silver paint-stainless steel composite on the back of the substrate. For this reason, and for reasons stated in appendix B, no attempt is made to compare the transparency between different films, and all transmittance values are reported with their corresponding film thickness. No improvement in the optical transparency of the materials is expected, or observed with the introduction of the dopant.

The optical bandgap and the nature of the transitions responsible for the absorption were calculated in accordance with the method of Tauc, as described in chapter 3. Graphs of $(\alpha h\nu)^{1/n}$ as a function of $h\nu$, where $n = 1/2$ for direct transitions, $n = 2$ for indirect transitions, were plotted as shown in figs. 4.12 and 4.13. The linear portion of the Tauc plots were extrapolated to the $h\nu$ axis to determine the energy gap corresponding to the transition. And the linearity was used to assess the nature of the transition.

Both the direct and indirect optical bandgaps for the $CuInO_2$ thin films appeared at higher energies than those for the $CuCrO_2$ films, the results are presented in table 4.4. The character of the fundamental bandgap in the Cu-based delafossites has been a source of disagreement broadly between experimentalists and theoreticians Liu *et al.* (2005a) Teplin *et al.* (2004). The Tauc plots indicate that the direct transition is responsible for the optical absorption edge, despite theoretical reports that the fundamental bandgap is indirect in nature Nie *et al.* (2002).

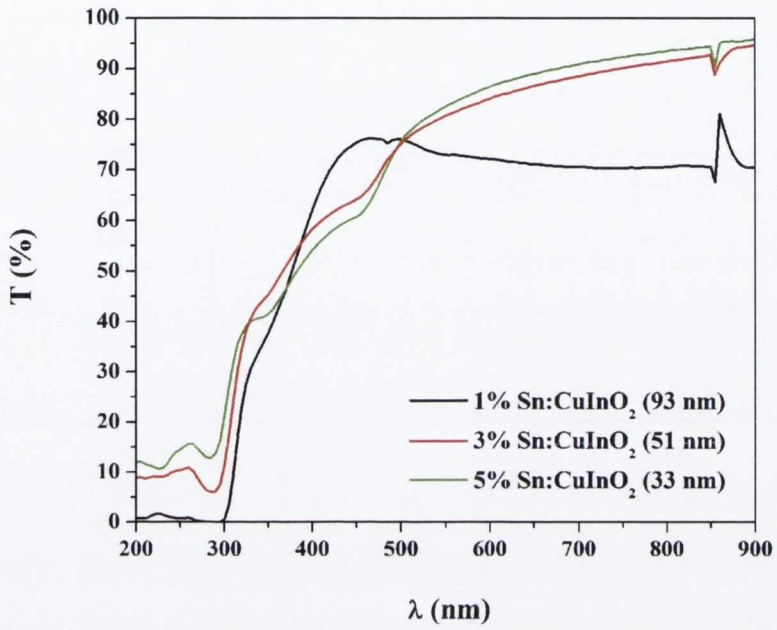

Figure 4.10: UV-Visible spectrometry of 1, 3, and 5 % Sn-doped $CuInO_2$ thin films showing optical transmission as a function of wavelength.

Compound	Dopant	d (nm)	T (%)	Bandgap (eV)	
				Direct	Indirect
$CuInO_2$	1 % Sn	93.0	70 - 80	4.1	3.8
$CuInO_2$	3 % Sn	51.0	55 - 90	4.0	3.5
$CuInO_2$	5 % Sn	33.0	55 - 90	4.0	3.3
$CuInO_2$	3 % Ca	45.7	60 - 85	4.1	3.9
$CuInO_2$	5 % Ca	55.0	60 - 85	4.1	3.9
$CuInO_2$	8 % Ca	70.0	60 - 75	4.0	3.6

Table 4.4: Table of Optical Bandgap and Transparency of Ca/Sn-$CuInO_2$ films (T = Transparency, d = thickness).

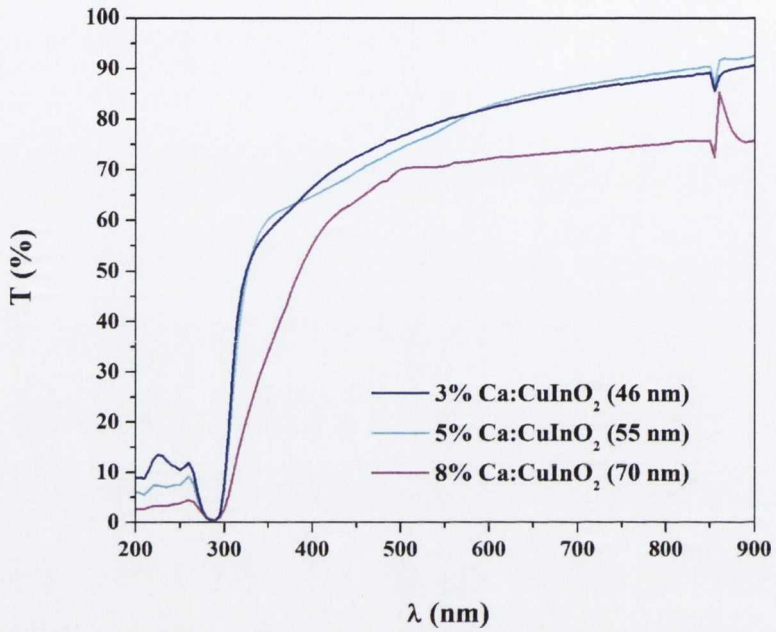

Figure 4.11: UV-Visible spectrometry of 3, 5, and 8 % Ca-doped $CuInO_2$ thin films showing optical transmission as a function of wavelength.

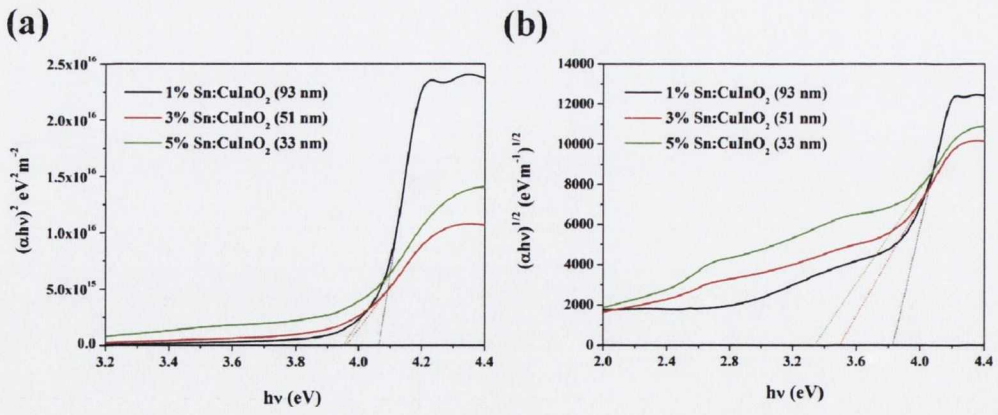

Figure 4.12: UV-Visible spectrometry of 1, 3 and 5% Sn-doped $CuInO_2$ thin films showing Tauc plots for (a) $n = 1/2$ direct bandgap calculation and (b) $n = 2$ indirect bandgap calculation.

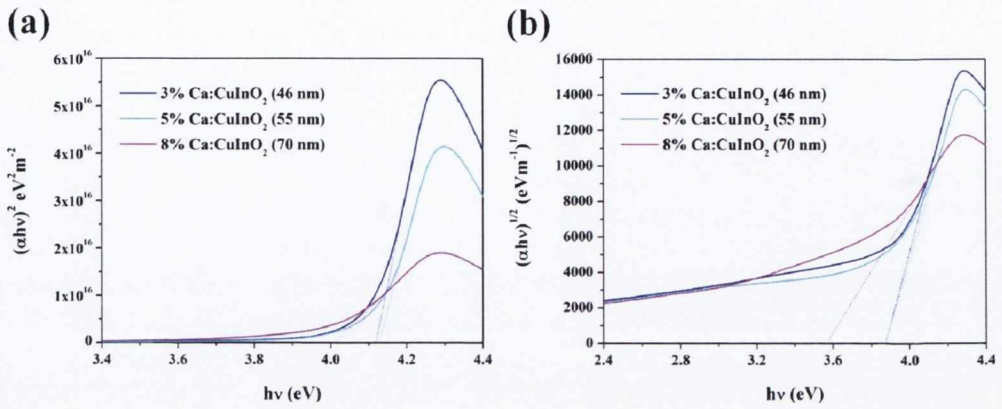

Figure 4.13: UV-Visible spectrometry of 3, 5 and 8% Ca-doped $CuInO_2$ thin films showing Tauc plots for (a) $n = 1/2$ direct bandgap calculation and (b) $n = 2$ indirect bandgap calculation.

4.3.3 Electrical Properties

Preliminary measurement of the sheet resistance, $R_s = R/d$, of the $CuInO_2$ thin films, using two probe contacts and a Keithley 6430, indicated extremely low electrical conductivity levels, despite the heavy doping levels. The results are shown in table 4.5. Large fluctuations were observed in the electrical sheet resistance of the thin films. Two factors could be responsible for these fluctuations:

- the existence of a depletion layer
- poor reproducibility of physical properties

Neither explanation can be ruled out, however to confirm the existence of a depletion layer would require the production of more films with various thicknesses. As for the irreproducibility of properties, the stabilisation of the $CuInO_2$ phase alone is not an easy task, and is therefore a likely explanation. The samples were not found to be sufficiently conductive for further electrical measurements.

Sample	Dopant	Thickness (nm)	Resistance (Ω)	Sheet Resistance (Ω/m)
$CuInO_2$	1 % Sn	93.0	1.0×10^{12}	1.08×10^{19}
$CuInO_2$	5 % Ca	55.0	3.3×10^{9}	6.06×10^{16}
$CuInO_2$	5 % Ca	26.2	2.0×10^{11}	7.63×10^{18}
$CuInO_2$	5 % Ca	40.4	8.3×10^{10}	2.06×10^{18}

Table 4.5: Table of basic electrical properties of Ca/Sn-$CuInO_2$ films.

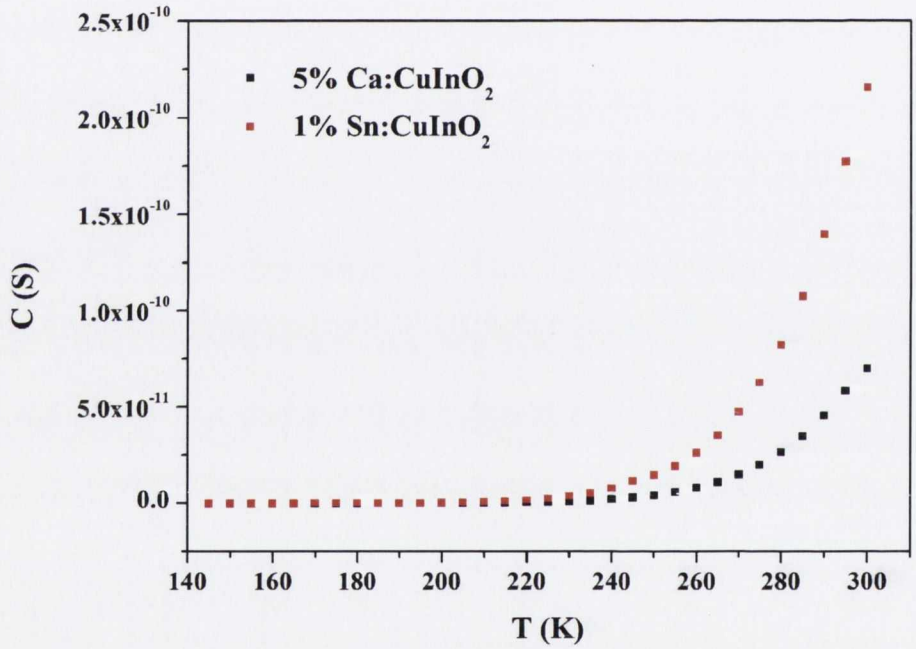

Figure 4.14: Conductance of 5 % Ca-doped and 1 % Sn-doped $CuInO_2$ thin films as a function of temperature.

The temperature dependence of the conductance through supposedly p-type Ca-doped $CuInO_2$ and supposedly n-type Sn-doped $CuInO_2$ have been measured on a high-impedance set-up in the PPMS with Dr. P. Stamenov, and is shown in fig. 4.14 for the range just below room temperature. A single high temperature activation energy could be reliably extracted in either case. Corresponding values are 0.37 eV for the Ca-doped and 0.34 eV for the Sn-doped sample. Even though hints of a lower activation energy scale were visible (not shown on fig. 4.15) that could not be reliably extracted because of the prohibitively high impedance of the layers below about 150 K. It is likely that the absorption features shown in figs. 4.11 and 4.10 between 450 and 500 nm are due to the acceptor (donor) level to the VB (CB) transitions respectively. Unfortunately due to the intrinsically low mobility and relatively high activation energies scale for both p and n-type $CuInO_2$ they were not deemed suitable for the construction of either diffuse p-n diodes or homojunction transistors.

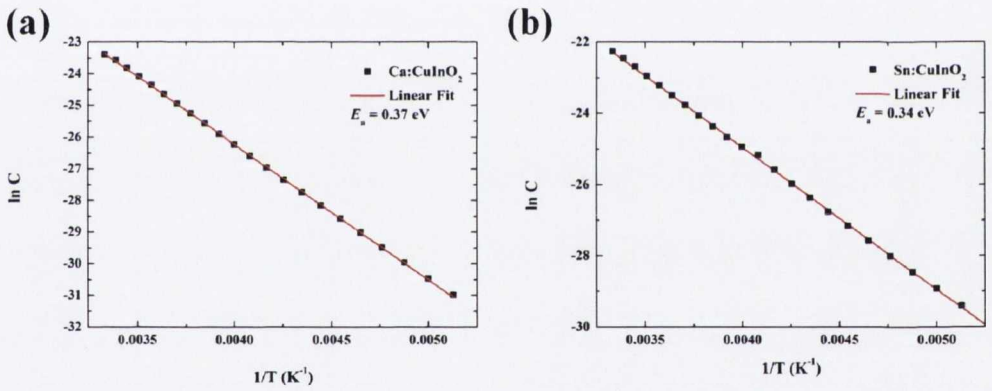

Figure 4.15: Arrhenius plots of (a) Ca and (b) Sn-doped $CuInO_2$ thin films.

4.4 Conclusion

Highly crystalline, single phase, semiconducting thin films of the reputed bipolar delafossite $CuInO_2$ with Ca and Sn substitutional impurities, with c-axis orientation, have been fabricated by pulsed laser deposition from $Cu_2In_2O_5$ source materials. Only minute amounts of secondary phases CuO and In_2O_3 have been detected by x-ray diffraction. Films were sufficiently flat, with short range surface roughness on the order of 4 nm r.m.s. Films were found to be sufficiently transparent (between 50 and 80 % in the visible region for thicknesses close to 100 nm). The direct gap was found to be of the order of 4.1 eV. Systematic increase of about 5 % in quasi-free carrier reflection

and absorption was observed between 2 and 4 eV. All samples prepared were found to be highly resistive with room temperature sheet resistances of the order of 10^{18} - 10^{19} Ω/m. The acceptor and donor activation energies were found to be 0.37 and 0.34 eV, respectively. A single p-n homojunction device was fabricated, which will be described in chapter 6. Because of the prohibitively high sheet resistance, low mobility, and high donor and acceptor activation energies no efforts were made to fabricate a homojunction transistor.

Chapter 5

n-Type Transparent Conducting Oxide ZnO

5.1 n-Type TCOs

The TCO materials market has been dominated by an elite few, as mentioned in the introduction, based on SnO_2, In_2O_3, ZnO and ITO Chopra *et al.* (1983). These materials are known to exhibit both high conductivity and optical transmissivity, they are reproducible, environmentally stable and have good surface morphology. They are also all n-type. Indium tin oxide (ITO) commands the flat panel displays division of the industry as a transparent electrode, and is in fact the most widely commercially applied TCO material, also finding applications in aerospace and solar energy commerce Lewis & Paine (2000). Growth in passive architectural applications, such as low-emissivity energy-efficient windows, use vast and increasing quantities of F-doped SnO_2 coatings deposited by the economical spray pyrolysis method Ginley & Bright (2000), to prevent heat loss by radiation. Although inferior to ITO in terms of electrical conductivity and surface morphology[1], SnO_2 has greater IR reflectivity and high transparency, and is more cost effective to fabricate than the commonly sputtered ITO. SnO_2 coatings are also used glass freezer doors, photovoltaics, plasma and touch screens. n-Type TCOs also find other applications in functional glass structures, such as electrically activated electrochromic (EC) windows also known as "smart windows" for privacy, thin film defrosting resistive elements and antistatic coatings, in electromagnetic shielding in video display terminals Banerjee & Chattopadhyay (2005).

In addition to the traditional binary TCOs, ternary compounds such as Cadmium stannate,

[1] Good surface morphology is required for flat panel display (FPD) applications

Cd_2SnO_4 [1] Nozik (1972), $CdIn_2O_4$, Zn_2SnO_4, $MgIn_2O_4$, $ZnSnO_3$, $GaInO_3$, $Zn_2In_2O_5$ and $In_4Sn_3O_{12}$ and many other ternary n-type TCOs Ginley & Bright (2000) Minami (2000), containing combinations of the cations, Zn^{2+}, Cd^{2+}, In^{3+}, Ga^{3+} and Sn^{4+}, have been developed to achieve enhanced properties over the conventional n-type TCOs Freeman *et al.* (2000).

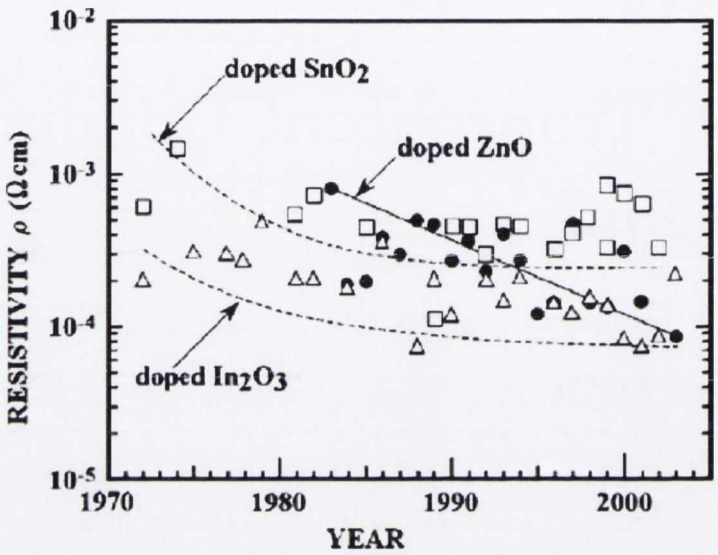

Figure 5.1: Reported resistivities of impurity-doped binary TCO films, including doped-SnO_2,doped-In_2O_3 and doped-ZnO,over the last number of years Minami (2005).

Advances in deposition techniques and material characterisation, as a result of the drive for high-temperature superconductors, have resulted in the possibility of achieving large area deposition of thin films with improved performance. The use of impurity-doped ZnO, whose electrical properties are catching up with those of the industry leader, as shown in fig. 5.1, and whose abundant supply and price stability can reassure the market, has been proposed as an alternative to ITO in transparent applications Minami (2005). Thin films of both materials can be fabricated by magnetron sputtering, however resistivity-lowering improvements have been observed in films grown by pulsed laser deposition. A resistivity of 8.45×10^{-5} Ωcm has been observed in ITO, with a measured carrier concentration of 1.38×10^{21} cm^{-3} and a Hall mobility of 53.5 cm^2/Vs Suzuki *et al.* (2002), while thin films of Al-doped ZnO, also grown by PLD, have exhibited a resistivity as low as 8.5×10^{-5} Ωcm, with a corresponding carrier concentration and Hall mobility of 1.5×10^{21} cm^{-3} and 47.6 cm^2/Vs respectively Agura *et al.* (2003). The Hall mobility of Al-ZnO thin

[1] Cd_2SnO_4 shows mobility improvements over the more established SnO_2

films with a carrier concentration in the region 10^{20} - 10^{21} cm^{-3} is thought to be predominantly affected by ionised impurity scattering due to the elevated density of carriers.

5.2 Zinc Oxide, ZnO

Wurtzite zinc oxide, ZnO, is an extremely widely used and versatile oxide material, with great potential for semiconductor device applications. This material is a wide bandgap semiconductor, whose direct gap of $\sim$ 3.4 eV renders it a very promising candidate for transparent electronics and UV optoelectronics device constituents. ZnO has recently come to the fore in the area of dilute magnetic semiconductors (DMS), where doping with $3d$ transition metal ions such as Co, Fe and Mn is intended to induce a ferromagnetic ordering in this otherwise diamagnetic oxide Coey (2006). In addition, the useful features of resistance to radiation, high temperatures and other harsh environmental conditions, and also its predisposition to wet chemical etching depict a highly attractive material for device applications.

5.2.1 Crystal Structure

ZnO belongs to the II-VI family of semiconductors, which crystallise in either cubic zinc-blende or wurtzite structure[1]. In ambient temperature and pressure, ZnO crystallises in the hexagonal wurtzite structure where each cation is at the centre of a tetrahedron (4-fold coordination) with anions occupying the vertices. This coordination is typical of sp^3 covalent bonding, but the electronegativity of O places ZnO at the cusp between covalent and ionic semiconductors.

The wurtzite crystal structure consists of the stacking of two hexagonal-close-packed sublattices (space group $P6_3mc$), with the lattice parameter ratio $c/a = \sqrt{3/8} \approx 1.6$. Each layer is formed with one atom type displaced with respect to the next along the threefold c-axis by the amount $u = 3/8$ in an ideal wurtzite structure. In a real ZnO crystal, the wurtzite structure deviates from the ideal arrangement, by changing the c/a ratio or the u value. A schematic representation of the crystal structure of ZnO is presented in fig. 5.2 and the main crystallographic parameters are summarised in table 5.1.

5.2.2 Literature Review

Fabrication The crystal fabrication process has been optimised for this material, to the extent that very large single crystals, although costly, are readily available, and ZnO crystals have been

[1] ZnO crystallises in three different polymorphs: wurtzite, zinc-blende and rock-salt.

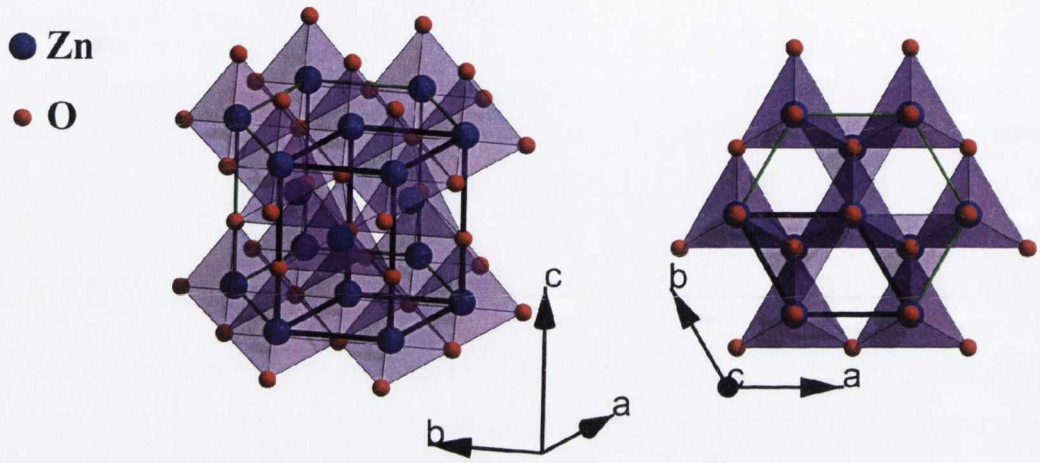

Figure 5.2: Crystal structure of wurtzite *ZnO*.

Wurtzite $P6_3mc$		
a	c	c/a
3.25	5.21	1.6
Wyckoff positions		
Zn	$2a$	1/3, 1/3, 0
O	$2b$	1/3, 2/3, 0.38

Table 5.1: Summary of the crystallographic parameter of wurtzite ZnO

used as substrates to grow closely lattice-matched GaN thin films. High purity polycrystalline ZnO is most commonly used in applications at present. Bulk crystals are fabricated by a number of different techniques such as vapour transport Dodson & Savage (1968), hydrothermal Ohshima *et al.* (2004), and pressurised melt growth Nause & Nemeth (2005), a modified Bridgman process, each of which deliver varying growth rates and impurity levels. Homoepitaxial growth of zinc oxide thin films on native substrates was expected to present reduced defect concentrations in the films due to the absence of a potentially contaminating substrate and also film-substrate lattice matching. However, reports of homoepitaxial thin film growth on ZnO substrates are sparse. This apparent tendency away from ZnO substrates is thought to be due to their high price and the absence of optimised surface preparation techniques, with researchers favouring Al_2O_3, $GaAs$, $ScAlMgO_4$, InP, $LiTaO_3$, Si and GaN substrates for film growth.

For many of the current applications of ZnO, polycrystalline thin films are sufficient to fulfil their function, and low temperature techniques such as spray pyrolysis Castaneda *et al.* (2006), electrochemistry Gu & Fahidy (1999), sol-gel Choi *et al.* (1996) and oxidation of metallic Zn layers on glass substrates are adequate. However, electronic and optoelectronic devices generally require far higher quality single crystalline films with low defect concentrations and disciplined dopant incorporation. To achieve this level of improved thin film growth such techniques as molecular-beam epitaxy (MBE) Johnson *et al.* (1996), metal-organic chemical vapour deposition (MOCVD) Heinze *et al.* (2007), pulsed laser deposition (PLD) Lorentz *et al.* (2005) and, to a lesser extent, sputtering Coutts *et al.* (2006) have been employed, with single crystal substrates replacing the glass ones. These processes allow increased regulation of the temperatures and oxygen partial pressures during film growth. Despite the large lattice mismatch, Al_2O_3 substrates are most commonly used for ZnO growth by PLD because of their relatively low cost. A consequence of this is that film quality must be sacrificed. Deposited ZnO films consist of large crystallites separated by grain boundaries which adversely affect the conductivity of the layers due to increased scattering. The recent use of $ScAlMgO_4$ substrates as an alternative to sapphire have shown marked improvements in the electrical properties of the ZnO films Tsukazaki *et al.* (2003). The minimal lattice mismatch of 0.09 % is responsible for the reported enhancement of the Hall mobility to 440 cm^2/Vs.

Donor and Acceptor Doping ZnO crystals are essentially always n-type regardless of growth method. Failed attempts to synthesise p-type ZnO in the 1970s and 1980s, and the hindrance of this unintentional n-type doping in as-grown crystals, led the scientific community to lose interest in this semiconducting oxide for electronic devices, for which precise control is required over the electrical

properties. This involuntary n-type conductivity has been attributed to oxygen vacancies Harrison (1954) and zinc interstitials in the lattice Hutson (1957). And until recently, these point defects were widely accepted to be the culprits. Recent theoretical reports, corroborated by experiment, indicate that the oxygen vacancies are deep donors and do not contribute to the conductivity Janotti & de Walle (2005) Vlasenko & Watkins (2005) have led to uncertainty in the mechanism behind this inadvertent conductivity. Furthermore, despite being shallow donors, Zn interstitial ions and antisites are unstable and have high formation energies and therefore unlikely to be responsible for the conduction Janotti & de Walle (2007b). Incorporated H impurities have been considered as a possible offender since they are typically present in most growth environments and hydrogen incorporated on oxygen vacancy sites act as shallow donors in ZnO Janotti & de Walle (2007a) Lavrov *et al.* (2009).

The electronic band structure of ZnO is typical of most wide bandgap transition metal oxides in that the $4s$ states of the Zn^{2+} ions form the bottom of the conduction band, while the valence band maximum consists of O^{2-} $2p$ levels or the bonding sp^3 orbitals Klingshirn (2007). The low-lying nature of the $2p$ band of the electronegative O ions makes it challenging to achieve p-type conductivity in this material, as described in chapter 2. Despite the apparent difficulty in synthesising p-type ZnO, achievement of this goal has frequently been reported in the literature Look *et al.* (2002) Ryu *et al.* (2000) Guo *et al.* (2001) Hwang *et al.* (2003) Bian *et al.* (2004). However, the wide variation and irreproducibility of the transport parameters have cast doubt on the reliability of the measurements and the interpretation of the data Zhao *et al.* (2007).

Attempts have been made to control the n-type electrical conductivity in ZnO by intentional donor doping. The group III elements, Al, Ga and In, have been investigated as intentional donor impurities in ZnO, substituting as shallow donors on the Zn site Myong *et al.* (1997) Ataev *et al.* (1995) Hu & Gordon (1993). Electron concentrations of up to 8×10^{20} cm^{-3} were measured in Al-doped ZnO films produced by CVD Hu & Gordon (1992). Fluorine also behaves as a shallow donor in ZnO when substituted for O Hu & Gordon (1991). The group I elements, Li, Na and K, have been explored with a view to acceptor doping. Li can potentially behave as both a donor, as an interstitial impurity, and an acceptor, by substituting for a Zn ion. However, reports of p-type conductivity resulting from Li doping are lacking Lander (1960) Zeng *et al.* (2006). Copper reportedly acts as a deep acceptor in ZnO, compensating the n-type carriers Müller (1976) and thus reducing the electron concentration. Nitrogen is considered to be a suitable candidate for acceptor doping of ZnO, since it has a similar size and electronic structure to oxygen. There have been a number of reports on N-doping of ZnO by CVD, MBE and PLD, resulting in p-type conductivity,

with mobilities ranging from $2 - 12$ cm^2/Vs Look *et al.* (2002) Minegishi *et al.* (1997). Theoretical investigations of the compensation effect of nitrogen doping by intrinsic defects are still debating the compensation mechanism at work Lee *et al.* (2001) Fons *et al.* (2006). Acceptor doping with arsenic has been reported to achieve p-type conductivity, however possible interference due to the *GaAs* substrate was admitted Ryu *et al.* (2000). Antimony doping of *ZnO* also resulted in p-doping with a large hole concentration of 2×10^{18} cm^{-3} Xiu *et al.* (2005). Finally, co-doping with donors and acceptors in order to compensate during the growth process, and the subsequent removal of the donors, *H* for example, has been proposed to achieve p-type *ZnO*. Co-doping of *ZnO* with *N* and *Ga* has reportedly resulted in hole concentrations of 4×10^{19} cm^{-3} Joseph *et al.* (1999).

5.3 Motivation

One of the primary goals of this thesis was to synthesise TCO materials and advance them to a point where they could, in principle, be implemented in a functioning all-oxide transparent electronic device. To achieve this objective an n-type transparent semiconductor that allowed control over its carrier concentration and hence mobility was required. An oxide material with a broad temperature and pressure stability range was favoured.

The properties of the less developed p-type delafossite TCOs are still under study, however the furtherance of n-type TCOs is far advanced relative to that of their p-type counterparts. The behaviour and growth techniques of the n-type TCO, *ZnO*, are well understood, thus making this material an obvious candidate for the role of the n-type TCO in a potential transparent electronic device. The advantages of such low cost, non-toxic, transparent oxide materials have already been discussed in the introduction. In the context of this study, however, *ZnO* holds particular appeal because it has a certain degree of crystallographic matching with the rhombohedral delafossite materials, in addition to a compatibility of growth in terms of temperature and oxygen partial pressures. For these reasons, *ZnO* was selected to form the n-type base layer in a p-n-p heterojunction bipolar transistor device structure, that will be expanded upon in chapter 6.

In order to realise this unconventional device, it was necessary to understand and gain a certain level of control over the properties of its constituent semiconducting materials. The optimisation of cation and anion stoichiometries in *ZnO* was a necessary step in order to avoid crystal deterioration and degenerate conductivity due to the presence of unintentional impurities. To this end, the initial goal was to determine the optimum growth conditions resulting in the preparation of insulating thin films of undoped *ZnO*. The secondary aim was to utilise these conditions to grow *Al*-doped

ZnO, so that the resulting electrical conductivity could be attributed mainly to intentional doping, and thereby controlled to a certain extent.

5.4 Thin Film Fabrication

Thin films of ZnO were grown on single crystal (001) oriented Al_2O_3 substrates by pulsed laser deposition, which is described in detail in appendix A. Targets were prepared by the methods described in the following passages, and a range of growth temperatures and oxygen partial pressures were investigated in order to determine the optimum deposition conditions. It was clear that relatively high oxygen partial pressures would be required in order to minimise the occurrence of oxygen vacancy defects in the film samples. While it has been shown that oxygen vacancies are not directly responsible for the unintentional n-type conductivity in ZnO, they have been indirectly implicated in that they provide empty sites in which to accommodate unintentional impurities such as hydrogen. The high vacuum PLD system cannot avoid the presence and possible incorporation of H impurity ions. High substrate temperatures during growth were also expected to result in high crystalline quality of the thin films.

5.4.1 Target Preparation

Targets composed of commercial $4N$ pure ZnO powder and powder prepared by the precipitation method, explained in the following passage, were prepared for comparison. Solution-based methods of powder synthesis were favoured over solid state reaction since it was elected to use extremely low doping concentrations in the impurity doped compounds. Such low concentrations are difficult to achieve in a controlled way otherwise. Only very low impurity densities were required since they resulted in sufficiently high carrier concentrations without inducing degenerate behaviour and maintaining the semiconducting properties. The powders were hydraulically pressed into pellets and then sintered in air at 1073 K for 12 hrs.

5.4.1.1 Precipitation

ZnO powder was synthesised by the method of precipitation, which is described in appendix A, using the starter salt zinc acetate and oxalic acid. Summarily speaking, solutions were made with both of these initial species in de-ionised water, the solutions were added together stirred and then left to settle or precipitate. The residual powder at the bottom of the beaker was filtered from the solution, dried and then sintered at 1073 K.

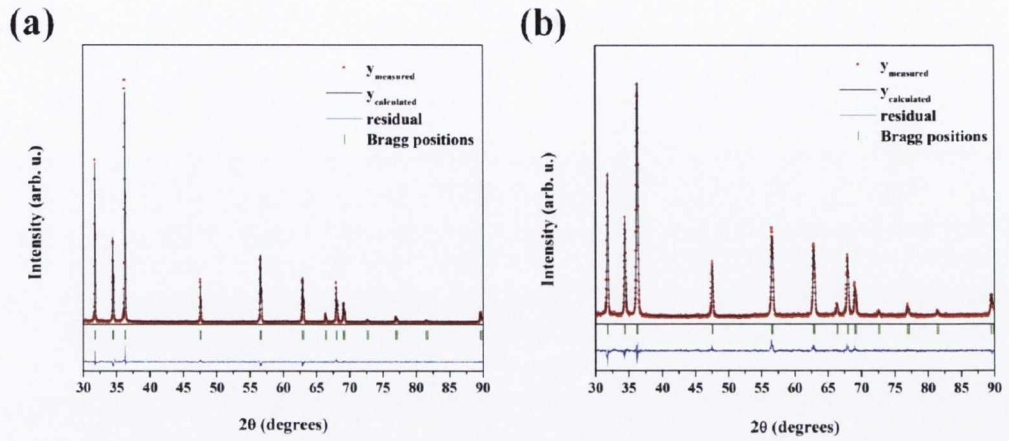

Figure 5.3: Rietveld refinement of 2θ scans of (a) a target of commercial ZnO powder that was sintered at 1073 K, and (b) a target of ZnO powder prepared by the co-precipitation method and subsequently sintered at 1073 K.

The structures of both of the targets that were prepared were analysed by x-ray diffraction. Rietveld refinement was carried out on the 2θ scans of each target for comparison, and the fittings are shown in fig. 5.3. Each scan can be well fitted with the wurtzite ZnO model, with a very slight residual arising mainly from preferred orientation. Minor differences in residuals may arise due to the difficulty in fitting broadened peaks that are adversely affected by non-monochromatic x-rays.

The Bragg peaks in the 2θ XRD scans can be analysed from the refinements to obtain information on the crystallinity of the sample specimens. Examination of the breadth of the peaks in the 2θ scans of each powder indicate broader full widths at half maximum height (FWHM) for the powder prepared by co-precipitation, as evidenced by fig. 5.4. This trend is an indication that the powder prepared by precipitation has a smaller average grain-size than the target made from the commercial powder.

5.4.2 Optimisation of Oxygen Stoichiometry

Thin films of the undoped ZnO were deposited using the co-precipitation target as the source material. Temperatures in the range 923 – 1173 K were scanned with relatively high oxygen partial pressures varied between 100 and 220 μbar. Low laser repetition rates and fluences were chosen, delivering a reduced deposition rate relative to those generally reported in the literature, in order to avoid deterioration of the growing thin film. The properties of crystalline quality and electrical resistivity in the preparatory samples were scrutinised in order to determine the

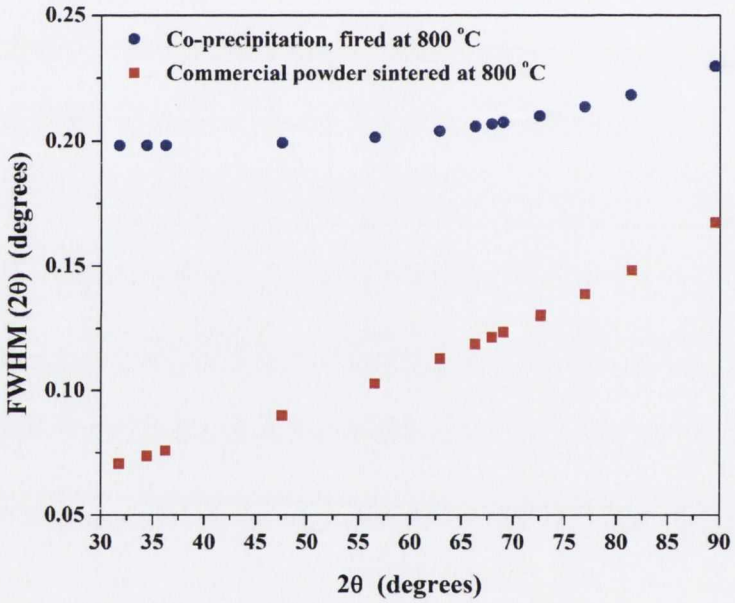

Figure 5.4: Full width at half maximum height of Bragg peaks of a 2θ scan of a target of ZnO powder prepared by the co-precipitation method and subsequently sintered at 1073 K, compared with a target of commercial ZnO powder that was sintered at 1073 K.

optimum growth conditions for our purposes. The phase and orientation of the thin films were confirmed by 2θ-ω XRD scans and the quality of the thin film crystal was examined by carrying out rocking curves (ω scans) on the primary peaks of the samples. Current-voltage characteristics were measured at room temperature, on a high impendence measurement set-up, to determine the resistivity of the samples.

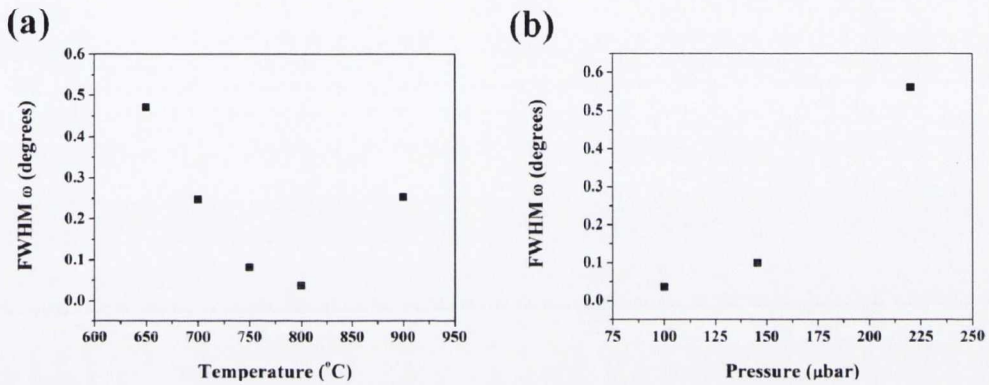

Figure 5.5: Full width at half maximum height of rocking curves of undoped *ZnO* thin films deposited (a) at various temperatures and (b) pressures in order to determine optimum deposition conditions required to achieve high crystallinity.

All of the samples were found to be single phase and to exhibit Bragg peaks corresponding to the wurtzite *ZnO* diffraction pattern. The thin films were also singly-oriented displaying (002) and higher order reflections indicating that the grains of the crystal all grew in the same direction. It was desirable to obtain narrow FWHMs in the ω scans, since this corresponded to oriented character in the grains of the films. The criterion of high crystalline quality was fulfilled therefore for samples with distinguishing narrow rocking curves. The FWHM of the rocking curves are plotted against the deposition substrate temperature and oxygen partial pressure in fig. 5.5 (a) and (b) respectively. From these graphs it is clear that the narrowest peaks are obtained for temperatures between 1023 and 1073 K and for gas pressures of approximately 100μbar. Partial pressures lower than this value were directly found to be conductive by two probe resistance measurement, and were therefore discounted from the study. The deposition system was also limited in the range of controllable oxygen partial pressures that could be used. A partial pressure of 220 μbar was relatively inaccurately controlled with a flow of oxygen regulated by needle valve with the gate valve to the turbo molecular pump closed and monitoring on a pressure gauge. A partial pressure of 145 μbar was controlled with the mass flow controller again with the gate valve closed. A partial

pressure of 100 μbar, was again controlled with the mass flow controller which was approaching its upper limit since the chamber was simultaneously pumped with the turbo pump as the high purity oxygen gas was introduced into the chamber. This last partial pressure was found to be the most reproducible for this gas control configuration.

Room temperature *I-V* characteristics were measured on each of the undoped *ZnO* thin films to determine the most resistive film and therefore the growth conditions that promoted stoichiometry in the samples. The samples were contacted with high purity *Ag* wires and *Ag* paint, and connected to a high impedance measurement rig. Five data points were measured in the range -1 to $+1$ V in 0.5 V intervals for each of the samples and all of the characteristics were linear. The inverse slope of each was corrected for film thickness in order to determine the sample resistivity.

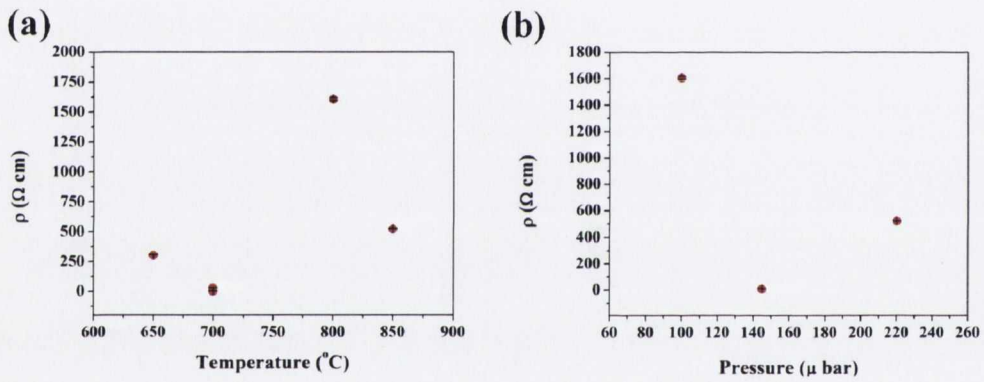

Figure 5.6: Room temperature resistivity of undoped *ZnO* thin films deposited at various temperature and pressure combinations.

The resistivity was then plotted as a function of the deposition substrate temperature and partial pressure as shown in fig. 5.6 (a) and (b) respectively. The growth temperature resulting maximum resistivity in the films was found to be 1073 K, and a partial pressure of 100 μbar. The maximum in resistivity observed in these films is not a direct proof of the optimum stoichiometry as it could also be due to poor mobilities and inferior crystalline quality. As there is no straightforward method to analyse the oxygen stoichiometry in the thin films, the resistivity in conjunction with XRD analysis of sample crystallinity is used as an indicator. These results considered in tandem with the XRD study of the rocking curves suggest that the conditions required for the promotion of both high resistivity together with thin film crystallinity coincide in the temperature range 1023 – 1073 K and for an oxygen partial pressure of 100 μbar. This result was carried forward and utilised in the next part of the *ZnO* study, the growth of semiconducting *Al*-doped *ZnO* thin films

of low doping concentration. For this purpose, the conditions to promote maximal resistivity and crystal quality were expected to translate to the intentional impurity-doped samples, and films of somewhat controlled carrier concentration and hence conductivity were therefore anticipated.

5.4.2.1 Structural Characterisation

The thin films grown within the optimum temperature and pressure range have been studied by x-ray diffraction. As previously mentioned, the phase pure thin films of single (002) orientation have a high degree of crystallinity, this can be seen in the 2θ-ω scan of an undoped ZnO film shown below in fig. 5.7. The ZnO peaks of this relatively thick film have a very high intensity, and the c lattice parameter of the hexagonal film was deduced from the position of the (002) reflection. The three extremely sharp, highly intense, unidentified peaks correspond to the (003), (006) and (0012) reflections of the (00l) oriented Al_2O_3 substrate.

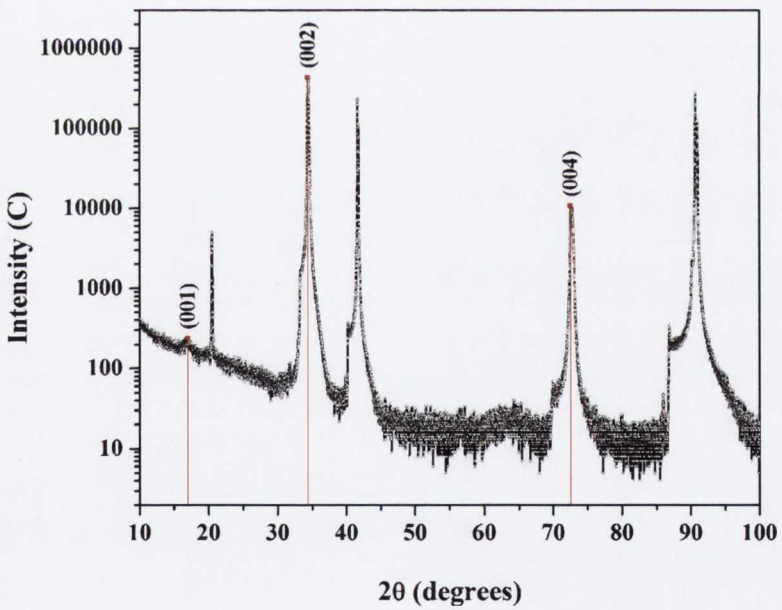

Figure 5.7: XRD pattern of an undoped ZnO thin film grown at optimum conditions on a c-cut Al_2O_3 substrate.

The thicknesses of the thin films were determined by x-ray reflectivity measurement, and wide variations in deposition rate were observed in the different temperature and pressure combinations. Some of the samples were too thick for the thickness to be accurately determined from XRR data,

and their thicknesses were therefore estimated by extrapolation from measurements of thinner films, with shorter deposition times, produced under the same conditions. Analysis of the rocking curve of quite a thin undoped ZnO film, of 40 nm, is shown in fig. 5.8. Two pseudo-voigt functions were necessary to fit this ω scan, as it is clear from the base of the peak there is a contribution from a broader but lower intensity peak. The broad peak at the base of the rocking curve is thought to arise from the initial ZnO layers at the interface with the substrate. The large lattice mismatch of 31.6 % between the ZnO $(1\bar{2}10)$ and sapphire $(11\bar{2}0)$ planes induces significant strain in the first number of atomic layers of the thin film, and a 30^o rotation of the crystal is known to occur about the c axis of ZnO in order to relax the strain. The effect of this is to reduce the mismatch between the ZnO $(10\bar{1}0)$ and the Al_2O_3 $(11\bar{2}0)$ planes to 18.4 % Ozgur *et al.* (2005). This rotation occurs within the first few nanometres of the thin film sample, and it is expected that this region of the thin film will manifest a poor crystalline quality. This assumption could well explain the apparent observation of two effective ZnO thin films, one with a poorer crystalline quality characterised by a broader FWHM ω of 0.168^o, and a second with an improved crystalline quality as evidenced by an extremely narrow FWHM ω of 0.033^o comparable to that of the single crystal substrate, as measured with the narrowest slits. The rotated ZnO layer acts as a natural buffer to compensate for the lattice mismatch, and subsequent ZnO growth is lattice matched to the effective buffer layer. A similar effect has been observed and discussed in chapter 3.

Asymmetric XRD scans were performed on the undoped ZnO thin film sample in order to determine the multiplicity of the peaks in-plane. The a lattice parameter was then calculated from an in-plane 2θ-ω scan. The corresponding ψ angle for the chosen in-plane orientation was calculated using the formula for interplanar angles in the hexagonal structure. A ϕ scan of the reflections of the (101) plane of the ZnO film is compared with a ϕ scan of the sapphire (113) plane in fig. 5.9. The (113) plane of the hexagonal Al_2O_3 substrate exhibited 6 peaks, while the ZnO (101) plane was observed to have a multiplicity of 12, in agreement with some reports Fons *et al.* (1999) Chen *et al.* (1998). The multiplicity of the ZnO (101) reflection is expected to be 6, however two types of in-plane rotational domains are sometimes observed as a result of the alignments: ZnO $[1\bar{2}10]$ $\parallel$ Al_2O_3 $[1\bar{1}00]$ and ZnO $[10\bar{1}0]$ $\parallel$ Al_2O_3 $[11\bar{2}0]$. This corresponds to a 30 ^{o} rotation between the ZnO and sapphire a axes. The (113) ϕ peaks of the substrate coincided with the (101) peaks of the film confirming the predicted 30^o rotation of the ZnO thin film relative to the substrate.

The c lattice parameter of the film was determined from the position of the (002) peak obtained from the symmetric 2θ-ω scan. The 2θ position of the (101) Bragg peak in the asymmetric 2θ-ω

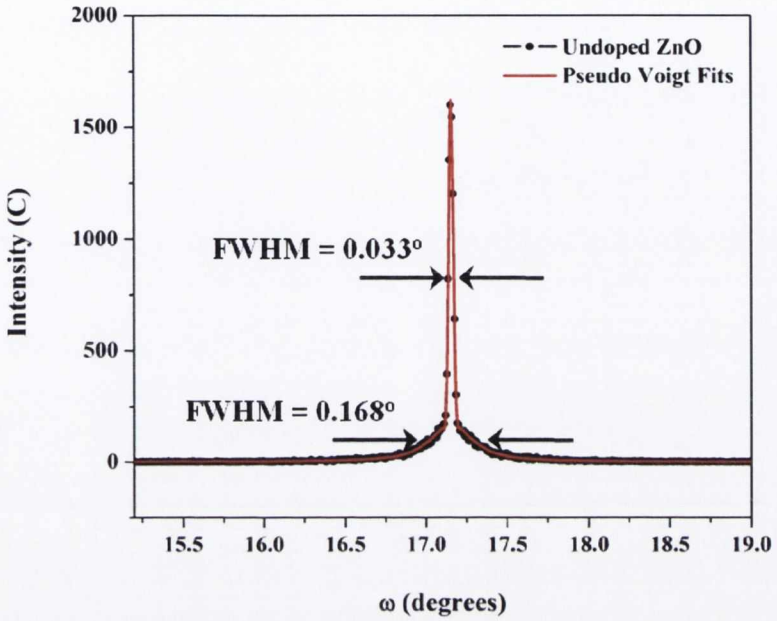

Figure 5.8: Rocking curve of *ZnO* (002) peak for an undoped *ZnO* thin film.

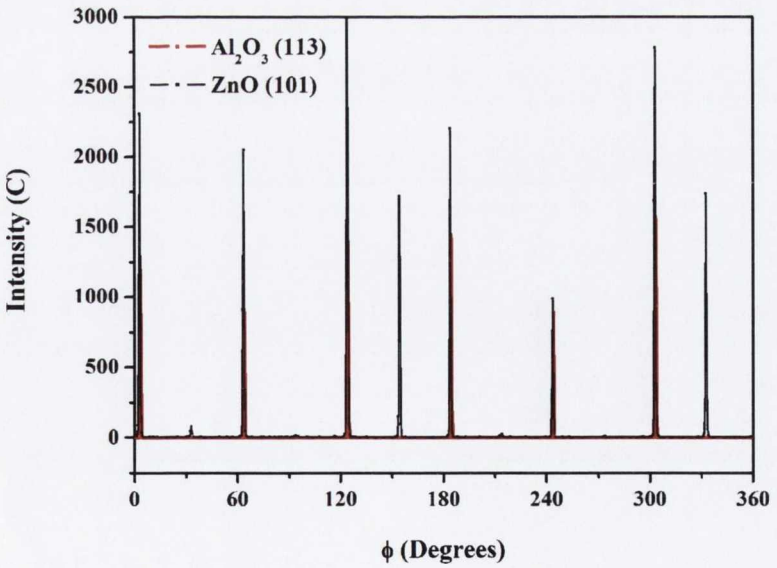

Figure 5.9: In-plane ϕ scan about the *ZnO* (101) direction showing the coincidence of the peaks with the Al_2O_3 (113) peaks.

scan of the *ZnO* thin film, shown in fig. 5.10, in conjunction with the previously determined c parameter, allowed determination of the a parameter of the *ZnO* cell according to the d-spacing relation described in chapter 3, where

for (002)

$$c = 2d \tag{5.1}$$

and for (101)

$$a = \sqrt{\frac{4d^2c^2}{3(c^2 - d^2)}} \tag{5.2}$$

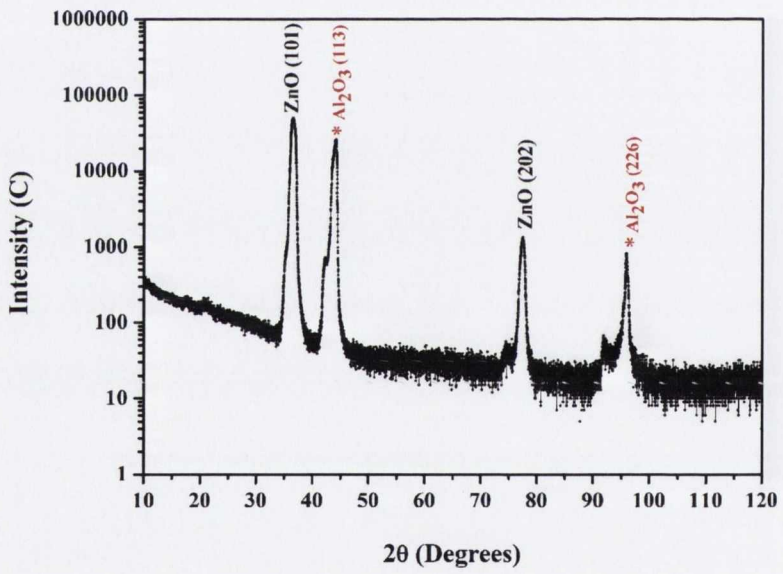

Figure 5.10: In-plane XRD pattern of a ZnO thin film showing the (101) orientation of ZnO and the (113) of the sapphire substrate.

A summary of the structural information acquired from the x-ray diffraction studies is presented in table 5.2.

The extracted a and c lattice parameters for the undoped *ZnO* thin film compare favourably with the bulk parameters in the powder diffraction file (04-003-2106), 3.2501(1) Å and 5.2071(1) Å respectively. The multiplicity of the asymmetric planes of both the thin film and substrate agree with the expected values.

Material		a (Å)		c (Å)	
ZnO		3.221(8)		5.206(4)	
Material	Plane	2θ	ω	ψ	ϕ scan
ZnO	(002)	34.42°	17.21°	0°	1 peak
Al_2O_3	(006)	41.68°	20.84°	0°	1 peak
ZnO	(101)	36.50°	18.25°	62.17°	12 peaks
Al_2O_3	(113)	43.34°	21.62°	61.21°	6 peaks

Table 5.2: Table of lattice parameters and angular positions of symmetric and asymmetric planes

5.4.2.2 Electrical Properties

The resistivity of an undoped *ZnO* thin film sample, prepared under the optimal deposition conditions described above, was measured with Dr. P. Stamenov, using a dedicated high impedance set-up. A two point contact configuration was used, in the manner described in appendix B and the measurements were performed at biases for which the contacts would be expected to be sufficiently transparent in the entire temperature range. The data was acquired in the PPMS system with temperatures varying from room temperature down to 5 K. Measurement of samples with extremely high resistivity is normally difficult, due to leakage currents in the connecting wires, however the set-up used allows greater sensitivity in measurements of this resistivity range.

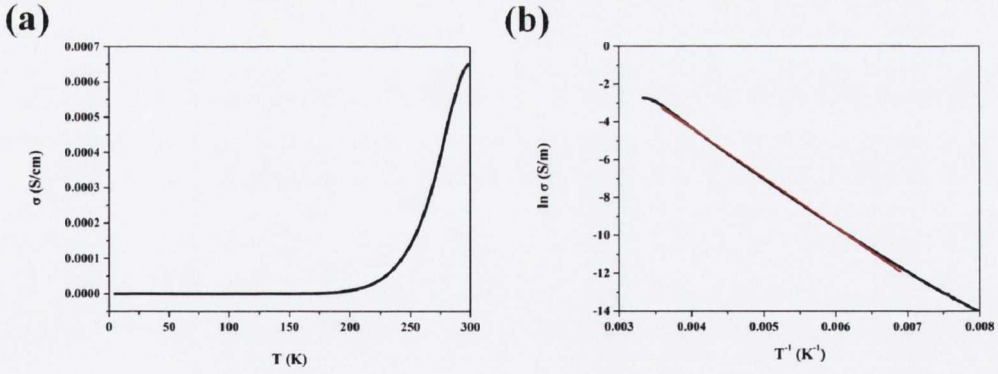

Figure 5.11: (a) Temperature dependence of the conductivity of an undoped *ZnO* thin film. (b) Arrhenius plot of the same undoped *ZnO* film.

The conductivity of the undoped sample as a function of temperature is plotted in fig. 5.11 (a). The shape of the conductivity curve is characteristic of a semiconductor, however the room temperature conductivity of just 6.5×10^{-4} S/cm is sufficiently low for our purposes, and close to insulating. An Arrhenius plot of the conductivity is presented in fig. 5.11 (b), where behaviour in

agreement with the relation $ln\ \sigma \propto T^{-1}$ was observed in the temperature range 278.4 to 145.0 K. The linear slope was extracted in order to calculate the activation energy of the sample, which was determined to be 225.3 $\pm$ 0.1 meV. This value exceeded the activation energy extracted from the conductivity data of the undoped $CuCrO_2$ thin film, indicating that the ZnO film was sufficiently resistive, and that the film stoichiometry did not induce unwanted carriers.

5.4.3 Preparation of Al-doped ZnO Thin Films

The next objective in the ZnO study was to grow highly crystalline Al-doped ZnO thin films in the optimum deposition conditions, determined above. Moreover, it was necessary to produce samples that were not degenerately doped for subsequent incorporation into a semiconductor device in the final stage of this work. Previous experience of the electrical characterisation of this system in the research group led us to select 0.1 % as the nominal Al-doping level to achieve these properties.

5.4.3.1 Target Preparation

A target of ZnO with 0.1 % Al impurity composition was synthesised by co-precipitation, as described previously, however $AlCl_3$ was used as a source of the Al dopant. It has already been mentioned that synthesis of powders with low doping concentrations by solid state reaction can give rise to sizeable deviations from nominal composition, and therefore co-precipitation was deemed to be the most appropriate technique. The resultant precipitate was sintered, pressed into a pellet, and re-sintered at 1073 K, in the usual way to produce the $Zn_{0.999}Al_{0.001}O$ target.

Thin films of nominally 0.1 % Al-doped ZnO were deposited by PLD as before, utilising the previously determined optimum growth conditions, this time with the $Zn_{0.999}Al_{0.001}O$ target. The phase and orientation of the samples were then characterised by 2θ-ω XRD scans, as shown in fig. 5.12. The x-ray analysis confirmed that the thin films again crystallised in the wurtzite ZnO structure. The films all grew in the c-axis orientation, with the (001), (002) and (004) ZnO reflections indicated on the figure. The unidentified peaks correspond to the c-cut Al_2O_3 substrate. Close inspection of the high intensity film peaks reveals a slight splitting due to the non-monochromatic x-ray wavelength in the XRD system. The two resolved peaks correspond to the $Cu\ K_{\alpha 1}$ and $K_{\alpha 2}$ wavelengths from the x-ray source, this is habitually observed for well-aligned single crystal substrates and here it is an indication of a large grain-size in the film.

Rocking curves were measured to assess the orientation of the planes of the thin films. The FWHM ω for this relatively thick Al-doped ZnO thin film was determined to be 0.075°, again using the narrowest slits available, as shown in fig. 5.13. This narrow width of the rocking curve

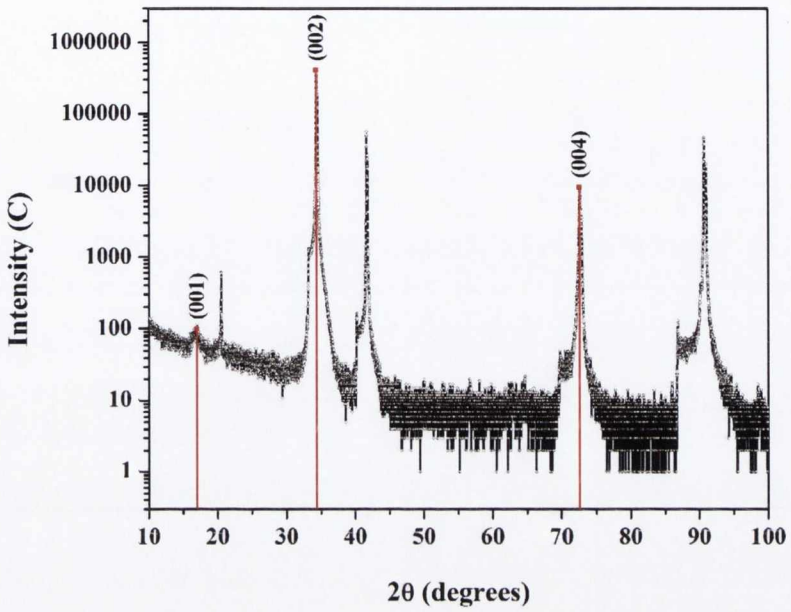

Figure 5.12: XRD pattern of a 0.1 % Al:ZnO thin film grown on a *c*-cut Al_2O_3 substrate.

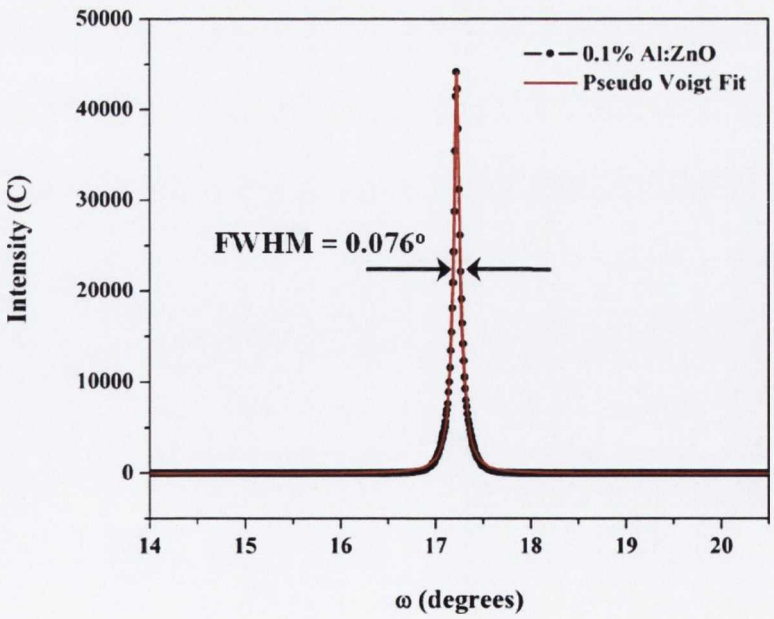

Figure 5.13: Rocking curve of *ZnO* (002) peak for a 0.1 % *Al*-doped *ZnO* thin film.

is an indication that the planes perpendicular to the c axis of the thin film have grown with a high degree of parallelism. This ω scan about the primary ZnO peak was fitted with a single pseudo-voigt function. It is probable that the greater intensity of this peak, due to increased film thickness, negates the contribution of another possible peak at the base.

5.4.3.2 Optical Characterisation

The optical transmittance of an undoped and a 0.1 % Al-doped ZnO thin film were measured by optical spectrometry and the spectra are presented in fig. 5.14. The transparency of the films was observed to be between 55 and 90 % in the visible range. A sharp transition is observed below 400 nm corresponding to the absorption band edge. The difference in transmittance between the two films can be explained by the variation in the thickness. Interference oscillations observed after the band edge correspond to thickness fringes in the doped sample.

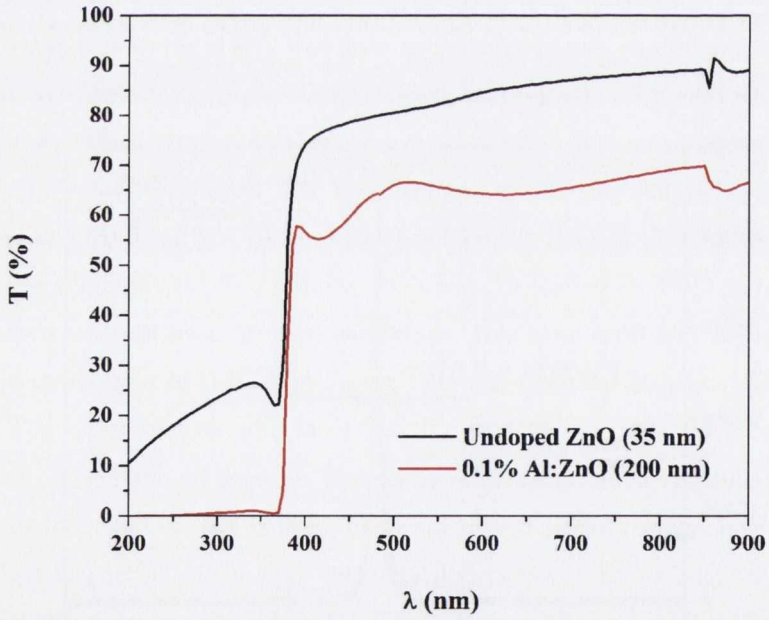

Figure 5.14: Optical transmission as a function of wavelength of undoped and 0.1 % Al-doped ZnO thin films.

The optical bandgap of the undoped and Al-doped ZnO thin films were extracted from the transmission spectra according to the method of Tauc, described in chapter 3, and shown in fig.

5.15. Direct transitions were observed to be responsible for the bandgaps, which were calculated to be 3.2 and 3.3 eV for the undoped and *Al*-doped films respectively.

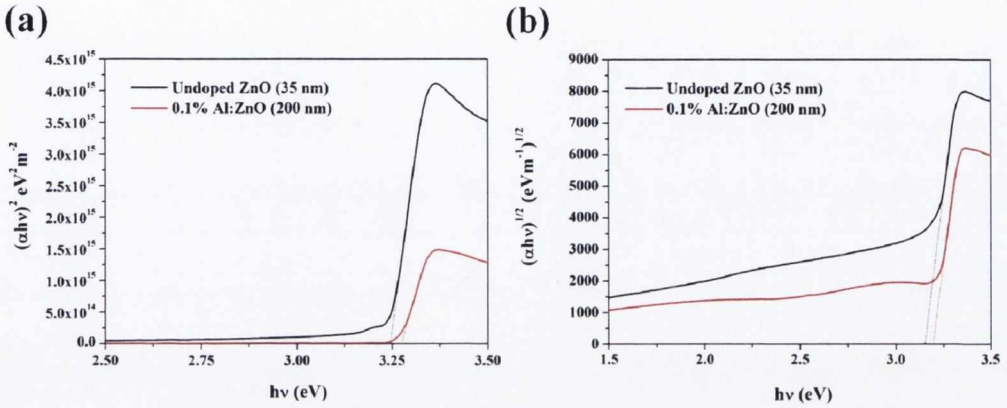

Figure 5.15: Tauc plots of undoped and 0.1 % *Al*-doped *ZnO* thin films to ascertain (a) the direct and (b) indirect bandgaps.

The resulting optical properties are summarised in table 5.3.

Compound	Dopant	d (nm)	T (%)	Direct Bandgap (eV)
ZnO	Undoped	35	75 - 85	3.24(3)
ZnO	0.1 % *Al*	200	55 - 65	3.27(2)

Table 5.3: Table of Optical Bandgap and Transparency of an undoped and an *Al*-doped $CuInO_2$ thin film (T = Transparency, d = thickness).

5.4.3.3 Electrical Properties

The electrical properties of the far more conductive *Al*-doped *ZnO* thin film, whose structural features have been presented above, was measured with Dr. P. Stamenov, in the PPMS system. The thin film was contacted in an acceptable geometry of Van der Pauw configuration, as shown in fig. 5.17, for Hall voltage measurement, using high purity *In* soldered contacts and high purity *Au* wires in accordance with the method described in appendix B[1].

Conductivity The conductivity at room temperature has been calculated using the Van der Pauw geometry by measuring the horizontal R_{xx} and vertical R_{yy} resistances[2] using reciprocal

[1] Although this is not the original geometry proposed by Van der Pauw and not the optimal choice for minimising errors, it is a widely used and accepted geometry for square samples Thurber (2008).

[2] No reverse current polarity measurements were performed to correct for possible voltage offset due to Seebeck effect.

measurement:

$$R_{xx} = \frac{R_{23,41} + R_{41,23}}{2} = 214.8\Omega \tag{5.3}$$

$$R_{yy} = \frac{R_{12,34} + R_{34,12}}{2} = 209.9\Omega \tag{5.4}$$

The sheet resistance R_s was then computed by solving the equation

$$e^{-\frac{\pi R_{yy}}{R_s}} + e^{-\frac{\pi R_{xx}}{R_s}} = 1 \tag{5.5}$$

using the Mathcad root function, and was found to be $R_s = 962.4\ \Omega$. The conductivity was calculated from $\rho = R_s \cdot t = 25$ mΩ·cm, where t is the thickness of the film, corresponding to a conductivity of 40 S/cm, which is 5 orders of magnitude higher than the conductivity of the undoped thin film deposited under the same conditions. Since switching the contacts during a variable temperature measurement is not possible with this setup, the evolution of the resistivity as a function of the temperature of the film was measured by following the change in resistance R_{xx}. If the value does not correspond to the absolute value of the film resistance, its relative change as a function of temperature is attributable the sample. The data have been acquired in the temperature range 300-5 K, as represented in fig. 5.16 (a). The temperature dependence of the resistivity of the *Al*-doped thin films exhibits the characteristic semiconductor curve shape.

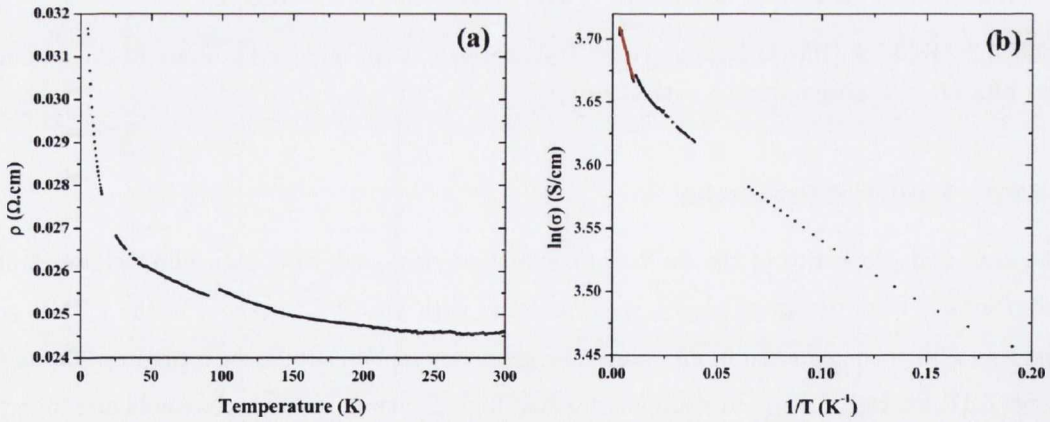

Figure 5.16: (a) Temperature dependence of the resistivity of a 0.1 % *Al*-doped *ZnO* thin film. (b) Arrhenius plot of the same doped *ZnO* film.

The activation energy of the doped sample was deduced from an Arrhenius plot of $ln\ \sigma$ against T^{-1} which is presented in fig. 5.16 (b). A value of 16.1 ± 0.1 meV was obtained from the slope of the linear region in the temperature range 231 - 115 K. This activation energy is far lower than that of the undoped *ZnO* thin film reported above, indicating that the charge carriers introduced

into the doped *ZnO*, that are responsible for the sizeable increase in conductivity, arise solely due to the *Al*-impurity doping.

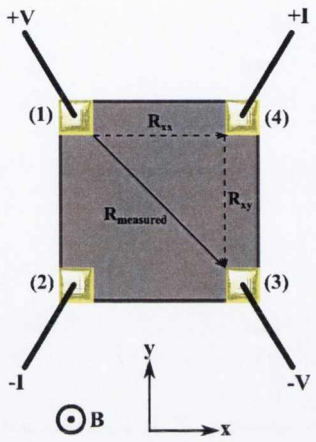

Figure 5.17: Van der Pauw electrical configuration for measurement of Hall effect in thin film samples.

Hall Effect For an ideal square, with contacts perfectly aligned R_{xx} should be zero. This is never achieved experimentally, and one of the main advantages of this measurement configuration is the possibility of correcting for contact misalignment and other thermomagnetic effects[1]. Since the conductivity tensor obeys the Onsager relations, $R_{xx}(B) = R_{xx}(-B)$ and $R_{xy}(B) = -R_{xy}(-B)$, by measuring the voltage and reversing the polarity of the field, the true Hall voltage drop correspond to the antisymmetric (R_{xy}) components of the measured resistance

$$R_{xy}(B) = \frac{|R_{measured}(B) - R_{measured}(-B)|}{2} \tag{5.6}$$

The correction is done in several steps and an example of the raw data processing practise is shown in fig. 5.18.

1. The black dots in fig. 5.18 (a) correspond to the raw measured data of an *Al*-doped *ZnO* film at 300 K.

2. The resistance drop is interpolated to a straight line with a constant field increment and is represented as the red and blue lines for the positive and negative parts of the applied magnetic field respectively.

[1]Except for the Ettinghausen effect.

3. From the interpolated data, the true Hall resistive drop is calculated using equation 5.6. The true Hall resistive drop after data processing is shown in fig. 5.18 (b).

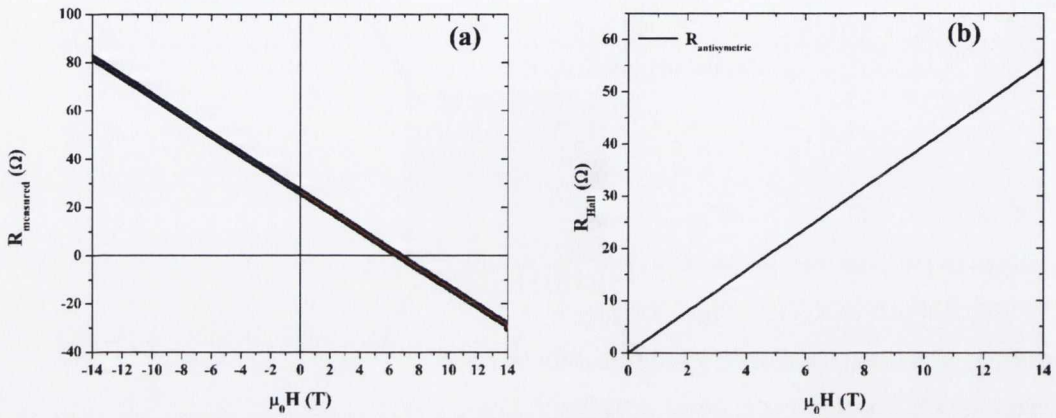

Figure 5.18: (a)Raw measured Hall resistance data (black dots) with the interpolated curve in positive magnetic fields (red line) and in negative magnetic fields (blue line) (b) Corrected Hall resistance data from contact misalignment as described in the text. All the data are for an *Al*-doped *ZnO* sample measured at room temperature.

To gain greater insight into the transport properties of the mobile charge carriers in *Al*-doped *ZnO*, Hall effect measurements have been carried out on the above thin film. The sample was contacted in the Van der Pauw configuration, as previously described, and measured in the PPMS. The Hall resistance of the sample was measured with Dr. P. Stamenov in an applied magnetic field which was varied between -14 and 14 T at a number of temperature settings between 300 and 7 K. The measured resistance was decomposed into its symmetric and antisymmetric components.

The antisymmetric contribution to the measured resistance has been extracted and is shown in fig. 5.19 for the *Al*-doped *ZnO* thin film, this linear component is attributed to the Hall effect. The negative slope of the field dependence of the antisymmetric resistance identifies the majority electrical carriers in the sample to be negatively charged electrons. This is to be expected for an *n*-type donor doped semiconductor.

The effective transport parameters for the *Al*-doped *ZnO* sample have been calculated as a function of temperature, and the effective carrier concentration and effective carrier mobility are presented in figs. 5.20 and 5.21 respectively. The film clearly exhibits semiconducting behaviour with a room temperature effective carrier concentration and effective mobility of about 6 $\pm$ $\times$ 10^{18} cm^{-3} and 40 cm^2/Vs respectively, in line with our objective to produce *ZnO* with reasonable transport parameters.

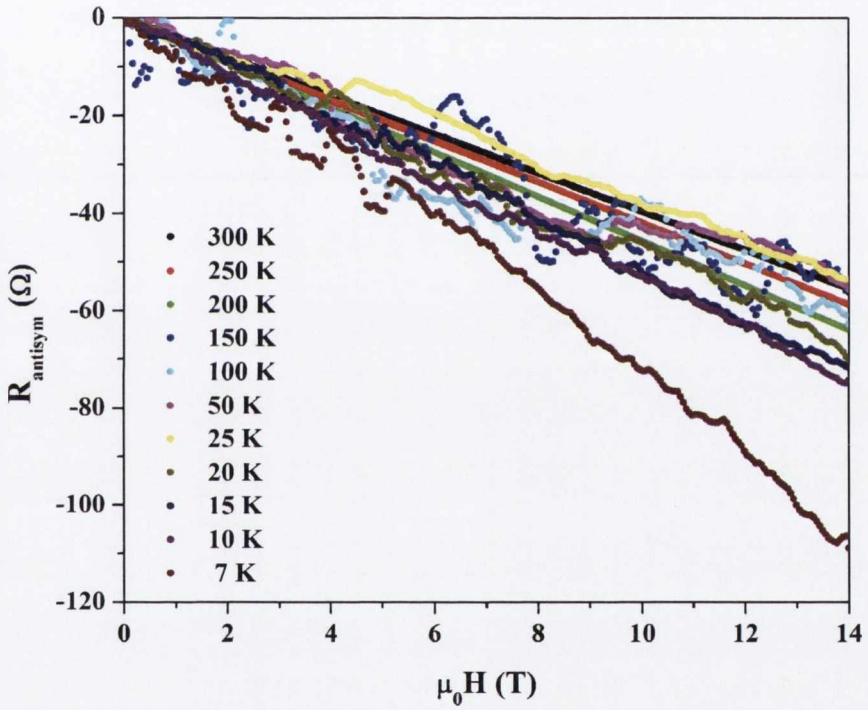

Figure 5.19: Field dependence of Hall resistance for a 0.1 % *Al*-doped *ZnO* thin film at various temperatures.

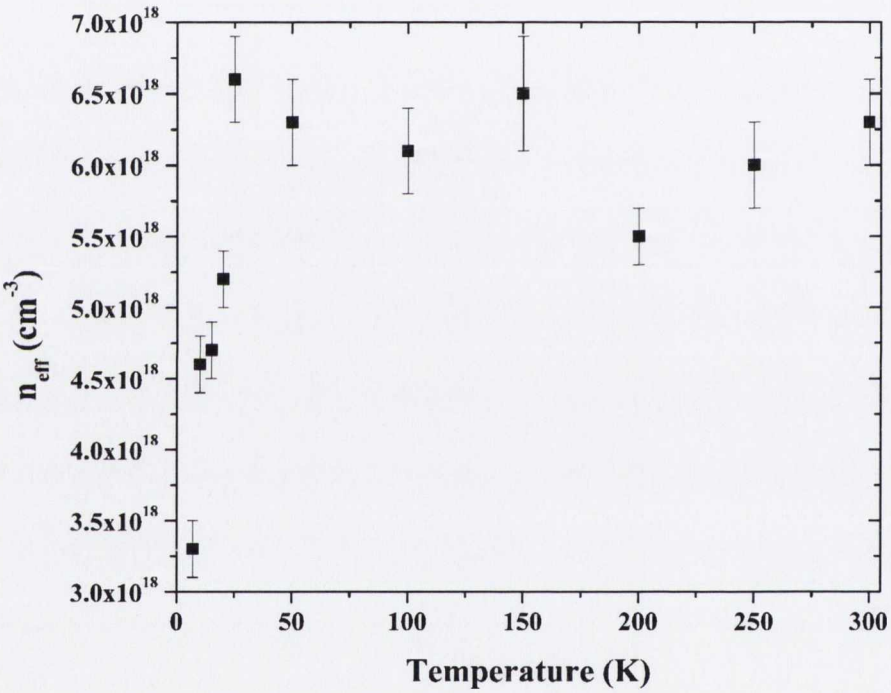

Figure 5.20: Temperature dependence of effective carrier concentration for a 0.1 % *Al*-doped *ZnO* thin film.

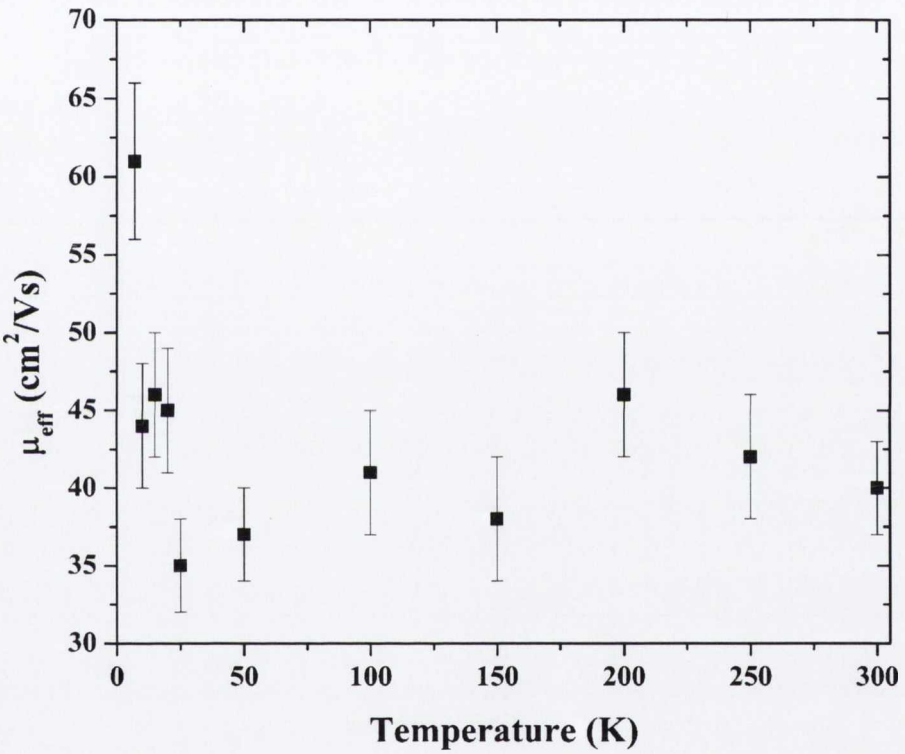

Figure 5.21: Temperature dependence of effective carrier mobility for a 0.1 % *Al*-doped *ZnO* thin film.

The effective transport properties determined from Hall effect measurements in a 0.1 % *Al*-doped *ZnO* thin film are presented in table 5.4, together with a comparison of the activation energies and room temperature conductivities of both the doped and undoped optimised *ZnO* thin films.

Composition	E_a (meV)	T range (K)	σ_{RT} (S/cm)
Undoped *ZnO*	225.3(1)	278.4 – 145.0	6.49×10^{-4}
0.1 % *Al:ZnO*	16.1(1)	231.0 – 114.9	40
Composition		n_{eff} (cm^{-3})	μ_{eff} (cm^2/Vs)
0.1 % *Al:ZnO*		$6.3(3) \times 10^{18}$	40(3)

Table 5.4: Table of effective transport parameters undoped and *Al*-doped *ZnO* thin films.

5.5 Conclusion

A two-step optimisation of the growth process for *n*-type *Al*-doped *ZnO* has been realised. First the room temperature resistivity of undoped films, prepared at various deposition conditions (substrate temperature and oxygen partial pressure) was maximised. Second, a fixed nominal dopant concentration of 0.1 % *Al* was used, in order to have a reproducible carrier concentration well below the degeneration limit (reached at about 0.25 %), and growth parameters were fine-tuned. Structural characterisation by means of x-ray diffraction confirmed a high degree of orientation, a FWHM ω as low as 0.033^o was observed in the rocking curve. Films were confirmed to be non-degenerate in the entire temperature region between *He* temperatures and room temperature. Optical absorption measurements confirmed the direct gap to be $\sim$ 3.2 eV. Finally, room temperature mobility was found to exceed 0.1 cm^2/Vs at the relatively high carrier concentration of $5{\cdot}10^{22}$ cm^{-3}. Therefore the films were deemed to have sufficient structural, morphological and electrical quality to serve as an active layer in bipolar heterojunction transistor structures, which will be examined in chapter 6.

Chapter 6

Transparent Devices

6.1 Literature Review

The primary applications of TCO materials as passive transparent conducting layers, taking advantage of their degenerate semiconducting properties, has previously been discussed. In recent years, however, major advances in materials processing and characterisation, and in particular, progress in thin film layer deposition with controlled carrier concentration, have improved the prospect of utilising these materials in active transparent electrical applications where their semiconducting properties are exploited.

There have been great strides made in the area of transparent electronic devices in the past few years. An ultraviolet light-emitting diode (UVLED) composed of p-type $SrCu_2O_2$ and n-type ZnO transparent conductive layers was fabricated by PLD Ohta *et al.* (2000a) Ohta *et al.* (2000b) Ohta *et al.* (2001) Kudo *et al.* (1999). Thin films of the transparent semiconductor $InGaO_3(ZnO)_5$ were used to fabricate a transparent field-effect transistor (FET) Nomura *et al.* (2003). And well-known p-type NiO was used in conjunction with n-type ZnO to form a transparent oxide-based pn-heterojunction diode Ohta *et al.* (2003a). Room temperature pulsed laser deposited n-type amorphous indium gallium zinc oxide (IGZO), $InGaZn_5O_8$, has been used together with p-type transparent $LaCuOSe$ to produce a light emitting p-n junction Hiramatsu *et al.* (2005). Since then a variety of transparent oxide pn junctions have been reported, namely, p-$CuYO_2$:Ca / n-ZnO Hoffman *et al.* (2001), p-$CuAlO_2$ / n-ZnO Tonooka *et al.* (2003) Takahata *et al.* (2009), p-$CuCrO_2$:Mg / n-ZnO Tonooka & Kikuchi (2006) Chiu *et al.* (2009), p-ZnO:N / n-ZnO Aoki *et al.* (2000), p-$CuInO_2$:Ca / n-$CuInO_2$:Sn Yanagi *et al.* (2001b) and p-$ZnRh_2O_4$ / n-ZnO Ohta *et al.* (2003b).

The majority of attention has focused on fabricating transparent thin film transistors (TFTs), since the first reports of such a device based on ZnO by Masuda *et al.* (2003) and Hoffman *et al.* (2003) in 2003. Further studies have been carried out using wide bandgap $Zn_{0.9}Mg_{0.1}O$ for the semiconducting layer of the device Ohtomo *et al.* (2006), and doping it with P to increase the mobility Kwon *et al.* (2004). The inexpensive non-vacuum techniques of chemical bath deposition and spin coating have been used to fabricate TFTs with respective semiconductor channels ZnO and $Zn_{0.97}Zr_{0.03}O$ Cheng *et al.* (2005) Lee *et al.* (2006). And active matrix liquid crystal displays (AMLCDs) and active matrix organic light emitting diodes (AMOLEDs) have been produced with ZnO TFTs Hirao *et al.* (2006) Park *et al.* (2006). Apart from ZnO, a number of the binary oxide semiconductors In_2O_3 and SnO_2 have been employed in TFTs, however poor control over the carrier concentration in these materials has hindered their incorporation Wang *et al.* (2006) Presley *et al.* (2004). A number of ternary TCOs have also been incorporated into transparent TFT devices and integrated with transparent OLEDs Görrn *et al.* (2006), such as ZTO, $ZnSnO_3$. ZIO, $Zn_2In_2O_5$, IGO, $InGaO_3$, and IGZO, $InGaO_3(ZnO)_5$ have also been used for the semiconducting channel in transparent TFTs Dehuff *et al.* (2005) Presley *et al.* (2006) Yabuta *et al.* (2006).

The realisation of several functioning transparent p-n hetero- and homo-junctions, utilising the bipolar nature of these oxide semiconductors, suggests the potential to fabricate a fully electrically active bipolar junction transistor with transparent properties. This device concept may have been overlooked by researchers, as evidenced by the distinct absence of reports of its fabrication and investigation, due to the low mobilities observed in the current p-type TCO materials, however it has been the final goal of this research endeavour.

6.2 p-n Junction

A semiconductor device of fundamental importance to the field of electronics is formed at the junction of p and n-type semiconductor regions. This device is important in its own right for rectifying and switching applications, moreover, it forms a critical component of a number of more sophisticated electronic devices such as the bipolar transistor and MOSFETs (metal-oxide-semiconductor field-effect transistors), and even photonic devices such as solar cells and LEDs. A p-n junction is typically formed between distinct p and n regions of the same semiconductor material, in which case it is referred to as a homojunction, however, two dissimilar semiconductor materials can also be employed in a heterojunction. This device, which has some of its own distinct attributes, will be explored later in this section.

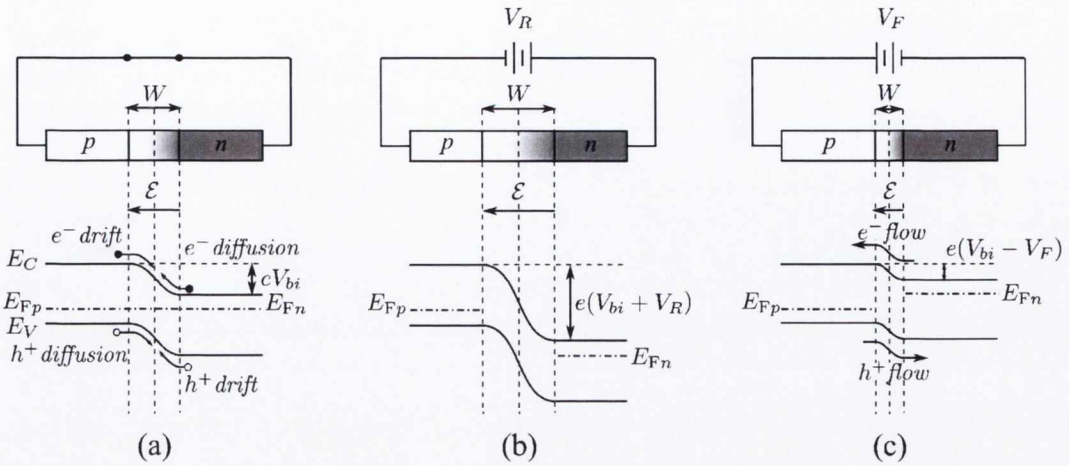

Figure 6.1: Energy band diagrams of a p-n junction under (a) zero bias, (b) reverse bias and (c) forward bias.

The most utilitarian feature exhibited by the p-n junction is rectification, or the capacity to allow easy current flow in one direction but not in the counter-direction. This is achieved by applying a bias to the junction. If the junction is biased in the forward direction, or "forward biased", as illustrated in fig. 6.1 (c), the current will increase swiftly with increasing voltage. Applying a voltage in a forward direction translates to applying a positive voltage to the p region, or a negative voltage to the n region. Conversely, if the junction is biased in the reverse direction, or "reverse biased", as shown in fig. 6.1 (b), almost no current will flow until a very high critical voltage is exceeded. Once this critical point is surpassed the current increases suddenly, this effect is called junction breakdown. The theoretical treatise of the physics involved in a diode can be found in classical textbook Sze (1985).

6.3 Transparent p-n Homojunction

A bilayer structure composed of 5 % Ca-doped $CuInO_2$ and 1 % Sn-doped $CuInO_2$ thin film layers was fabricated by pulsed laser deposition under the optimised growth conditions determined in chapter 4. A ceramic shadow mask, which covered one half of the sample surface, was used for deposition of the top layer of the structure. The optical properties of this structure have been examined by UV-visible range optical spectrometry measurements, which are presented in fig. 6.2. This bilayer structure has a transparency of between 45 and 80 % in the visible range of the spectrum, and exhibits a similar spectral shape to that of the Sn-doped $CuInO_2$ thin films observed in chapter 4.

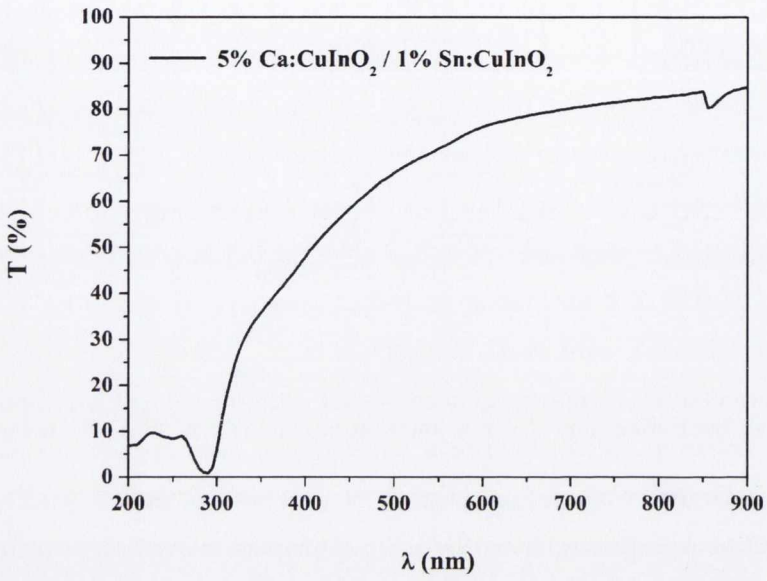

Figure 6.2: Optical transmission of a 5 % $Ca{:}CuInO_2$ / 1 % $Sn{:}CuInO_2$ homojunction as a function of wavelength.

The I-V characteristics of the structure have been measured on a high impedance measurement system, between 35 and 300 K with Dr. P. Stamenov. This data is presented in fig. 6.3. All of the I-V curves exhibit a linear dependence and no rectification was observed across the junction.

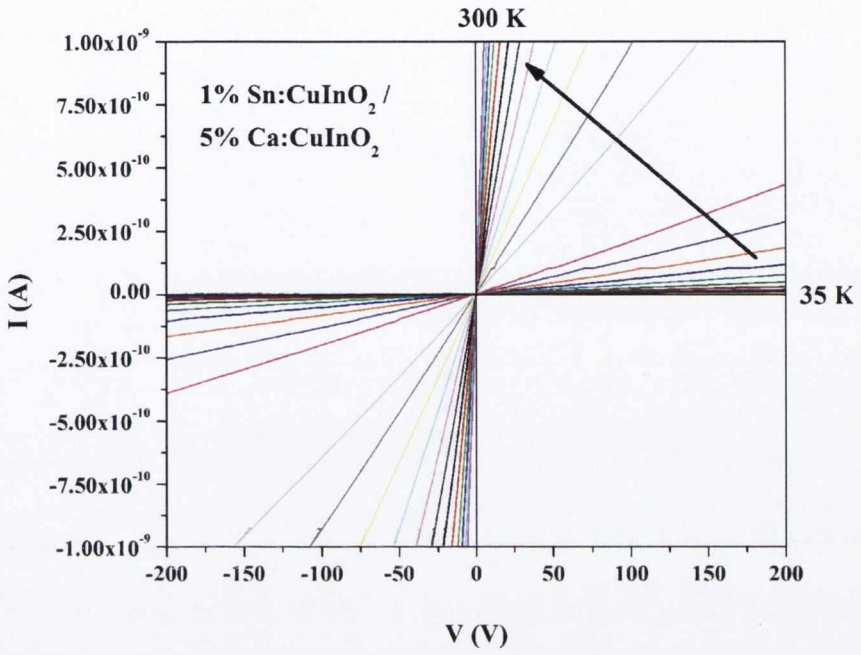

Figure 6.3: *I-V* characteristics of a 5 % Ca:$CuInO_2$ / 1 % Sn:$CuInO_2$ homojunction.

6.4 Transparent Transistor

Although semiconductor research had been largely considered futile around the time of WWI, only a few decades later huge strides had been taken in this field of research. A number of important discoveries, including that of surface states Tamm (1932) Bardeen (1947), the importance of carrier injection Haynes & Shockley (1949) and the minority carriers Shive (1949), advanced the understanding of semiconductor circuit elements. By 1945, semiconductors had many applications in electronic devices such as diodes, varistors and thermistors. Researchers were working towards an amplifying device based on semiconductors. To this end, the most prominent ideas were the insertion of a grid in the space charge layer at the contact, in order to control the flow of electrons across it, and the application of a transverse electric field to control the conductance of a semiconducting thin film.

After decades of further advancement, the list of transistors can be divided into three basic types, the bipolar transistor, the metal-oxide-semiconductor field-effect transistor (MOSFET), and the junction field-effect transistor (JFET). Unlike the switching p-n junction diode, described in earlier passages, the transistor is a device that is capable of performing a number of useful functions

in electronics, such as current gain, voltage gain and signal-power gain, therefore it is considered to be an active rather than a passive device. The device described in this thesis belongs to the bipolar category and it is a junction transistor, hence it is a bipolar junction transistor (BJT).

6.4.1 Transistor Action

The bipolar junction transistor (BJT), shown schematically in fig. 6.4, consists of three semiconducting layers in contact, the emitter, the base and the collector, that are doped to form *n-p-n* or *p-n-p* structures. Operation of the bipolar transistor involves contributions from both holes and electrons, hence its name. The base layer, which is designed to be narrow compared with the diffusion length of its minority carriers, is straddled on either side by two *p-n* junctions that effectively interact with each other due to their close proximity. In general, the emitter is the most heavily doped region in the device. The *n-p-n* BJT is the complementary structure of the *p-n-p* device, and although the following discussion will concern the latter structure, it can equally be used to describe the former upon reversal of the current flow and voltages, and exchange of n for p and p for n in the device.

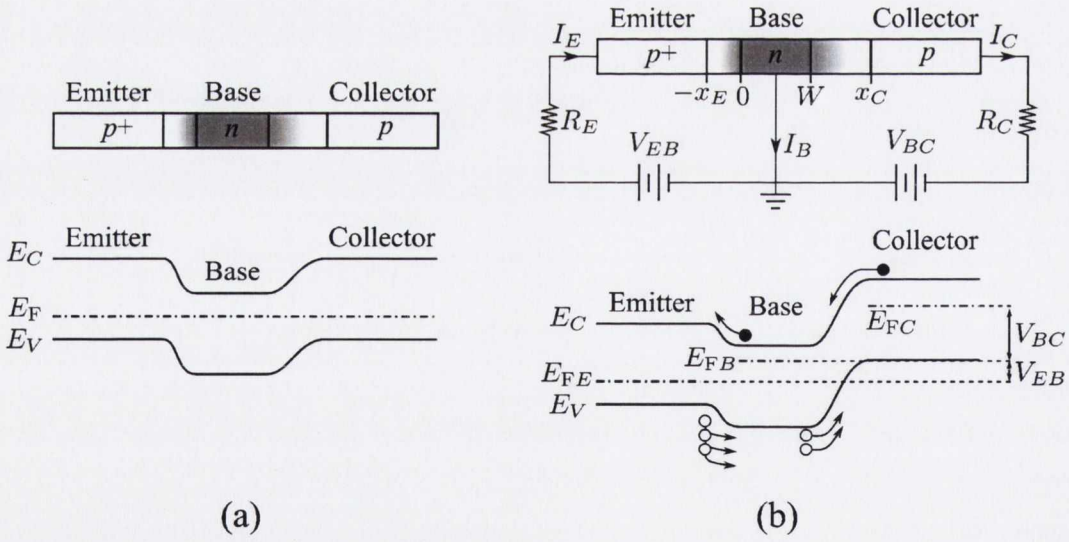

Figure 6.4: Schematic and energy band diagrams of a *p-n-p* Transistor (a) at zero bias, (b) in forward active mode. Adapted from Sze (1985).

Forward Active Mode For a *p-n-p* transistor in normal operation, or forward active mode which is illustrated in fig. 6.4 (b), a positive potential is applied to the emitter-base (E-B) *p-n* junction,

J_E, making it forward biased, while a strong negative voltage is applied to the collector-base (C-B) p-n junction, J_C, making it strongly reverse biased and inducing a state of high resistance at the junction. If the carrier concentration in the emitter is greater than that in the base, an appreciable emitter current, I_{Ep}, consisting primarily of holes, is induced to flow across the forward biased junction into the base. At the same time electrons are injected from the base back into the emitter which are taken account of in the I_{En}. Under the ideal-diode condition, there is no generation-recombination current in the depletion region, therefore total emitter current, I_E, consists solely of these two components. The injection of holes into the base creates an excess concentration of minority carriers in the base, and since the junction J_C is reverse biased, the concentration of these minority carrier holes in the base at the edge of the depletion zone of J_C is ideally zero. A large hole concentration gradient arises across the base region, thus the holes injected across J_E diffuse across the base with minimal recombination as far as the J_C space charge region where the electric field will then sweep the holes into the collector. The base width is ideally smaller than the minority carrier diffusion length to limit the recombination of the minority carrier holes with the majority carrier electrons in the base. If most of the carriers injected from the emitter can reach the collector without recombining in the base, the collector hole current, I_{Cp} will be close to the emitter hole current I_{Ep}. In this way, carriers injected from a nearby emitter junction can give rise to a large current flow in a reverse biased collector junction, this is the transistor action. If the two junctions, J_E and J_C, are too far apart to interact, all the injected holes will recombine with majority carrier electrons in the base and the transistor is effectively reduced to two diodes connected back to back.

Modes of Operation There are four possible modes of operation for a bipolar transistor. The active mode, which has already been discussed. The saturation mode, the cutoff mode, and the inverted mode. The saturation mode refers to a configuration where a forward bias is applied to both junctions in the device. In this configuration the transistor is conducting, it requires a small biasing voltage to deliver a large output current, and acts as a closed (or on) switch. The cutoff mode requires both junctions to be reverse biased, a high-voltage and low-current state results, in which case it can operate as a closed (off) switch. The final mode is the inverted mode, wherein the emitter-base junction is reverse biased, while the collector-base junction receives a forward bias. It is the opposite configuration to that of the active mode of operation, and as such behaves in reverse. The current gain achieved in this mode is lower than that for the forward active mode since the collector doping is less than the base doping resulting in inefficient carrier emission.

Common base configurations The transistor can be employed with three different input and output parameter combinations. The first, referred to as the common-base arrangement, which is illustrated in fig. 6.5, has the base connection common to both circuits, it inputs the voltage V_{EB} and current I_E, and outputs the voltage V_{BC} and current I_C. This set-up results in a collector current that is almost equal to the emitter current, such that the current gain

$$\alpha_0 = \frac{I_C}{I_E} \lesssim 1 \tag{6.1}$$

and practically independent of V_{BC}. There is little variation in the minority carrier gradient in the base upon reducing V_{BC} to zero, therefore I_C remains virtually unchanged over the complete active mode of operation. In fact, in order to reduce I_C to zero, it is necessary to apply a small forward bias to the base-collector junction, so the system is no longer active but is in the saturation mode, until the hole density across the base is constant.

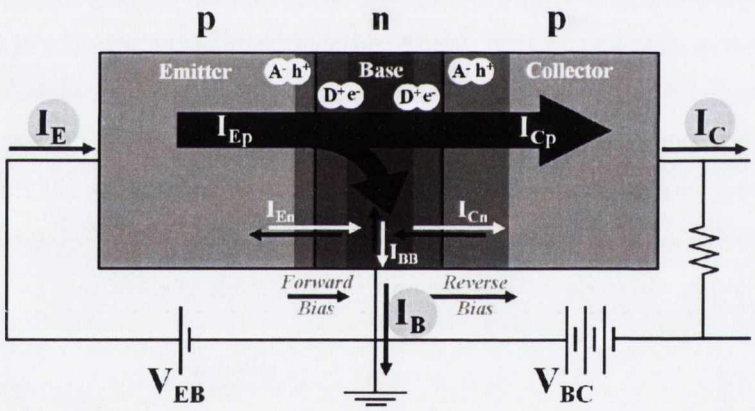

Figure 6.5: Bipolar junction transistor in common base configuration. Adapted from Sze (1985).

Common emitter configurations The second arrangement, termed the common-emitter configuration, has the emitter connection common to the two circuits, it applies the voltage V_{EB} and current I_B and outputs V_{EC} and I_C. This configuration is more frequently used in applications since it provides good voltage, current, and power gain. Under this scheme, a minor change in I_B can have a very large effect on I_C, and the current gain is defined as :

$$\beta_0 = \frac{I_B}{I_C} \gg 1 \tag{6.2}$$

A schematic of the common-emitter arrangement is presented in fig. 6.6.

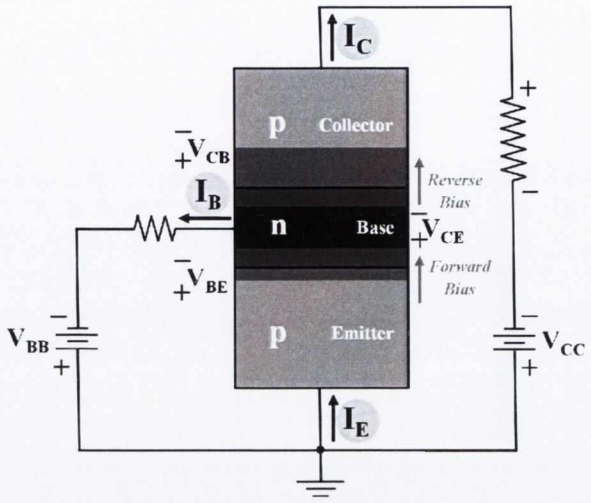

Figure 6.6: Bipolar junction transistor in common emitter configuration. Adapted from Sze (1985).

Common collector configurations The last arrangement, termed the common-collector configuration, has the collector connection common to the two circuits, it applies the voltage V_{CE} and current I_E and outputs V_{BC} and I_B. It is used mostly for impedance matching. It is also used as a current driver, because of its substantial current gain. It is particularly useful in switching circuitry, since it has the ability to pass signals in either direction (bilateral operation). The common collector current gain is defined as :

$$\gamma = \frac{I_E}{I_B} \tag{6.3}$$

Since a transistor can be connected in any of the three basic configurations, there is a relationship between the three gain parameters :

$$\alpha = \frac{\beta}{1+\beta}, \beta = \frac{\alpha}{1-\alpha} \tag{6.4}$$

The Heterojunction Bipolar Transistor One limitation of the homojunction bipolar transistor is its weak performance at high frequency. To obtain high power efficiency at high frequency heterojunction bipolar transistors are used. Furthermore, in devices with emitter and base of different band gaps, the gain and the carrier concentration in the base is increased. More detail can be found in Sze (1985). In this work, the building of a heterojunction structure is not motivated by these improvements on the classical BJT, but by the lack of oxide materials exhibiting ampibolar conduction. Another hindrance to consider in the design of a HJBT from ZnO and $CuCrO_2$, is the lack of information on the relative band alignment at the junctions. Moreover, considering

the growth method employed, the diffusion of species from one layer to the other at the interfaces cannot be excluded.

On the theoretical performance of a $CuCrO_2/ZnO/CuCrO_2$ transistor For an ideal BJT, it is possible to calculate the current gain from a set of parameters. If we consider a *p-n-p* homojunction with emitter and base thicknesses that are much smaller than the minority carrier diffusion length, the thin layer approximation for the minority carrier distribution can be used, and the current gain can be expressed as:

$$\beta = \frac{1}{\frac{D_{nE}N_{dB}x_{Beff}}{D_{pB}N_{aE}x_{Eeff}} + \frac{1}{2}\left(\frac{x_{Beff}}{L_{pB}}\right)^2} \tag{6.5}$$

where $D_{nE,pB}$ are the diffusivity of the minority carrier in the emitter and collector, $x_{B,Ceff}$ the effective base and collector thicknesses (the metallurgical thickness corrected for the depletion region), $N_{aE,dB}$ the carrier concentrations in the emitter and the base, and L_{pB} the minority carrier diffusion length in the base. The diffusivity can be obtained using the Einstein relation:

$$D = \frac{kT}{q}\mu \tag{6.6}$$

where μ is the drift mobility which can be approximated to the Hall mobility for small bias. The carrier diffusion length is defined as:

$$L = \sqrt{D\tau} \tag{6.7}$$

where τ is the carrier lifetime which is strongly dependent on the purity of the material. In the case of Si devices $L_{pB} \approx 10\mu$m, considering a carrier life time of 10^{-6} s and a mobility of 100 cm^2/Vs at room temperature, and it can be assumed that the minority carrier diffusion length in the base is much smaller than the thickness of the base. In the case of a hypothetical $CuCrO_2/ZnO/CuCrO_2$ structure, assuming that the mobility of the minority carrier is 10^{-3} cm^2/Vs, the minority carrier diffusion length in the base is 50 nm, the base thickness should be much smaller than that in order for the transistor to work. This is an optimistic estimate for the mobility of the minority carrier in the material, since we have no information apart from the Hall data collected on a single layer which only gives information on the majority carrier mobility. Another obstacle to the operation of this device is that the carrier concentration obtained by Hall effect measurement in the single layers 10^{22} cm^{-3} and 10^{18} cm^{-3} for $CuCrO_2$ and ZnO respectively would create a depletion layer of around 30 nm which would be predominantly in the ZnO region, since this has a lower carrier concentration. If the ZnO layer is less than 100 nm, the depletion region on both sides of the base

will overlap. Even if the depletion regions do not overlap and the effective base thickness is greater than zero, the gain will only just exceed unity due to the poor mobility in these materials.

6.4.2 Fabrication and Structure of Device

A *p-n-p* structure has been fabricated by PLD, using *p*-type Mg-doped $CuCrO_2$ and *n*-type Al-doped ZnO, employing the source materials and conditions that have been optimised for each of the constituent materials as discussed in chapters 3 and 5. The proposed structure was a vertical trilayer, as illustrated in fig. 6.7. The individual device layers would be contacted from above, therefore it was necessary to devise a masking technique to use during the deposition of the middle and top layers. For this two separate shadow masks were required, since the initial (bottom) layer did not require masking. Bespoke shadow masks, ordered from and fabricated by Crystal GMBH, were specifically designed for use in depositing this device structure. The shadow masks were engineered with a number of requirements in mind, they had to

- be compatible with the sample mount of the PLD system,
- be made of a ceramic material in order to withstand high temperatures and to avoid reaction with the sample layers by diffusion,
- have sharp edges to be in close contact with the substrate or previous layer in order to achieve distinct, well defined layers with minimal spreading of the film during ablation,
- be precision cut to exact specifications in order to be reproducible in their positioning relative to the sample and to each other
- be made from a material that would avoid significant back-sputtering contamination

The shadow masks were produced from 10 × 10 × 1 mm^3 single crystal sapphire wafers. A 0.6 mm deep groove was cut into the wafer to allow the substrate to sit snugly into it allowing 0.1 mm for the silver paint used to mount the substrate. The groove measured 5.4 × 5 mm^2 in the plane of the wafer allowing a 0.4 mm tolerance on either side of the 5 × 5 × 0.5 mm^2 sample substrate. The shadow mask was secured onto the sample holder, encapsulating the sample, with a small amount of silver paint and positioned with one edge aligned with that of the sample, the remaining three edges surrounded by the mask. This allowed the removal of the shadow mask, using a delicate chiselling technique, without interfering with the sample in any way. Two shadow masks were necessary to realise the structure presented in fig. 6.7. The first mask had a 4 mm

diameter circular window for the second layer to be deposited through, this circular opening was positioned acentrically relative to the groove for the sample substrate leaving enough surface area unexposed to accommodate an electrical contact on the bottom layer. The second mask had a 2 mm diameter opening for deposition of the third and final layer of the device structure, this aperture was positioned off-centre relative both to the larger opening of the previous mask and the sample substrate, however a sufficient border was left between the two windows to ensure that the top and bottom layers would never be in contact.

Unfortunately, the employment of the masking technique precluded deposition of the complete stack without breaking vacuum, since it was necessary to mount or change the shadow masks between depositions. This should not cause dramatic composition or structural quality changes in the layers since they are oxides and should be stable in air. The damage that could occur at the surface of the layer such as carbonate or hydroxide formation and water adsorption should be removed upon deposition of the subsequent layer which is done at relatively high temperature (for these impurity compounds) and under high vacuum. The high temperature deposition could cause other unwanted phenomena such as interdiffusion between the two layers. XRR measurements were carried out to assess the layer thicknesses and XRD measurements to characterise the structural quality of the sample after the growth of each successive layer.

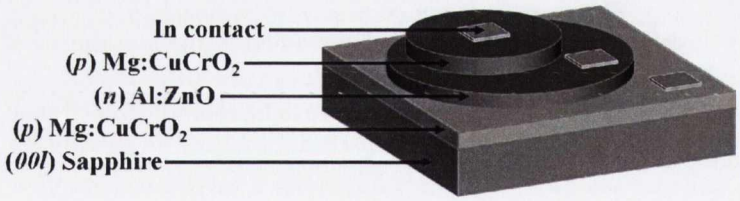

Figure 6.7: Structure of *p-n-p* bipolar junction transistor consisting of $Mg{:}CuCrO_2$ *p*-layers and $Al{:}ZnO$ *n*-layers deposited on a *c*-cut sapphire substrate, with contacts on each component layer.

Each step in the device fabrication process is demonstrated by the flow chart in fig. 6.8. Growth of the device structure began with the deposition of a nominal 10 % Mg-doped $CuCrO_2$ thin film, as normal, in the conditions reported in chapter 3. The practised growth temperature of 923 K and oxygen partial pressure condition of 20 μbar were appropriate for the deposition of the *p*-type layer, and afterwards the sample was cooled in the growth oxygen pressure. The high doping concentration was chosen to maximise the density of carriers in the *p*-type layer. The *p*-type emitter and collector layers were required to be thicker than the *n*-type base layer and were therefore deposited for longer.

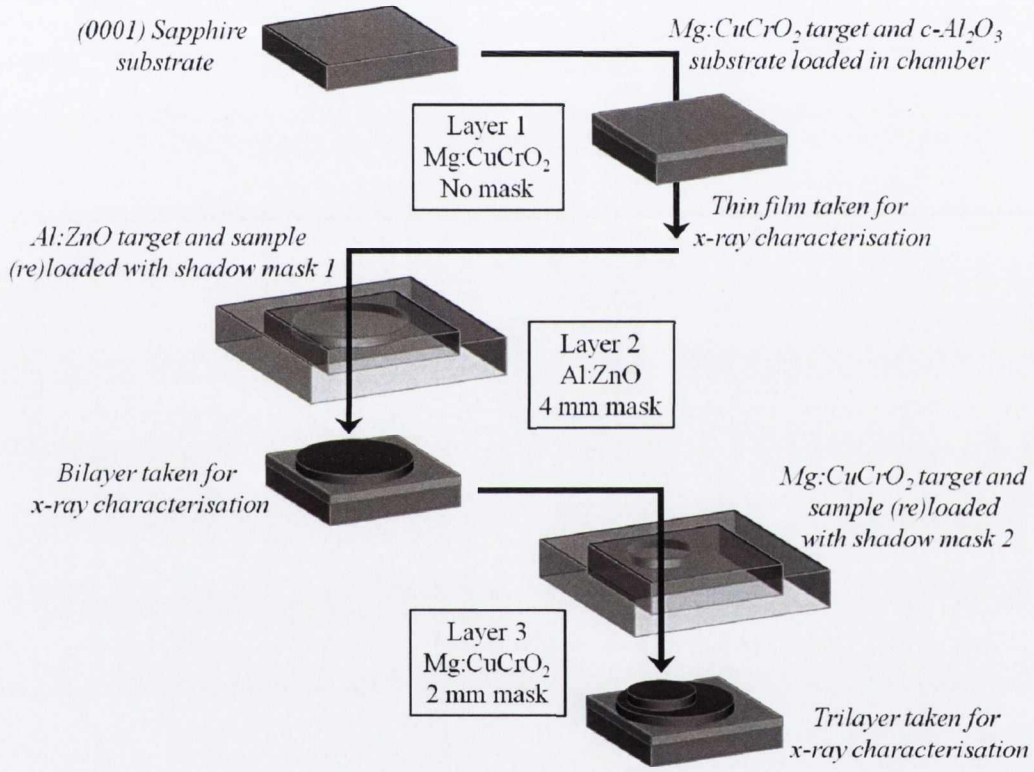

Figure 6.8: Flow chart of heterojunction bipolar transistor fabrication process.

Following analysis of the initial layer, the sample, together with the nominal 0.1 % *Al*-doped *ZnO* target, was reloaded into the PLD chamber masked by the first shadow mask. The sapphire single crystal shadow mask was mounted over the sample such that a 4 mm diameter circular region of the sample was exposed. The sample was heated to deposition temperature in the growth oxygen pressure that was optimal for the initial *p*-type layer, and the oxygen pressure was increased just prior to deposition. The rationale of this was to avoid the introduction of excess oxygen and potentially interstitial oxygen into the lattice of the initial $CuCrO_2$ layer by heating to high temperature in oxidising conditions. The *n*-type second layer of the device structure was grown at 1023 K under 100 μbar oxygen partial pressure. This layer grew at a much faster rate than the previous layer, and since the middle base layer was required to be very thin, of the order of 20 nm thick, the deposition lasted a very short duration. After the deposition the sample was cooled to room temperature in 100 μbar of oxygen. The sample was removed from the chamber and the first shadow mask was removed by chiselling before the sample was analysed by x-ray reflectivity and x-ray diffraction. The 0.1 % *Al*-doped *ZnO* layer was deposited at slightly lower than the optimal temperature, determined in chapter 5, in an effort to reduce interactions with the $CuCrO_2$ layer beneath and to prevent the decomposition of the *p*-type layer which is grown at a lower temperature. The post-deposition cooling of the bilayer was carried out in higher oxygen pressure than that used for the optimum growth of the initial *p*-type layer, however this condition was necessary to avoid the possible introduction of oxygen vacancy defects into the *n*-type *Al*-doped *ZnO* layer.

For the final layer, a relatively thick *p*-type 10 % *Mg*-doped $CuCrO_2$ film was again deposited at the optimum conditions mentioned above. The target was loaded into the chamber with the sample this time shielded by the second mask, which afforded a 2 mm circular aperture through which the top layer was deposited. The bilayer structure was heated to 923 K in 100 μbar oxygen, to ensure maximal oxygen stoichiometry in the base layer, and the pressure was reduced to 20 μbar oxygen just prior to deposition. After deposition of the thick final layer, the trilayer structure was cooled in the same gas pressure as during the deposition. During the heating and cooling processes compromises had to be made to promote certain properties in some of the constituent layers while sacrificing others.

6.4.3 Structural Characterisation

The growth of a trilayer structure was studied *in situ* by RHEED, the diffraction patterns of the substrate and each successive layer of the structure are presented in fig. 6.9. This sample was

unmasked, and monitored without breaking vacuum, in order to obtain diffraction patterns for each layer. The RHEED pattern of the first $CuCrO_2$ layer becomes spotty after approximately 20 mins of deposition, the pattern corresponding to this film after 30 mins of deposition is shown in fig. 6.9 (b). As discussed in previous chapter 3, the 30^o rotation with respect to the substrate is also evident in the device structure. The growth of ZnO on top of $CuCrO_2$ has been observed to be 3-dimensional, and fig. 6.9 (c) reveals that no rotation of the ZnO relative to the underlying delafossite layer takes place. The diffraction pattern of the final $CuCrO_2$ layer is shown in fig. 6.9 (d), this indicates that the $CuCrO_2$ layer starts to degrade to a more polycrystalline form with the appearance of spots along a ring pattern in the diffraction.

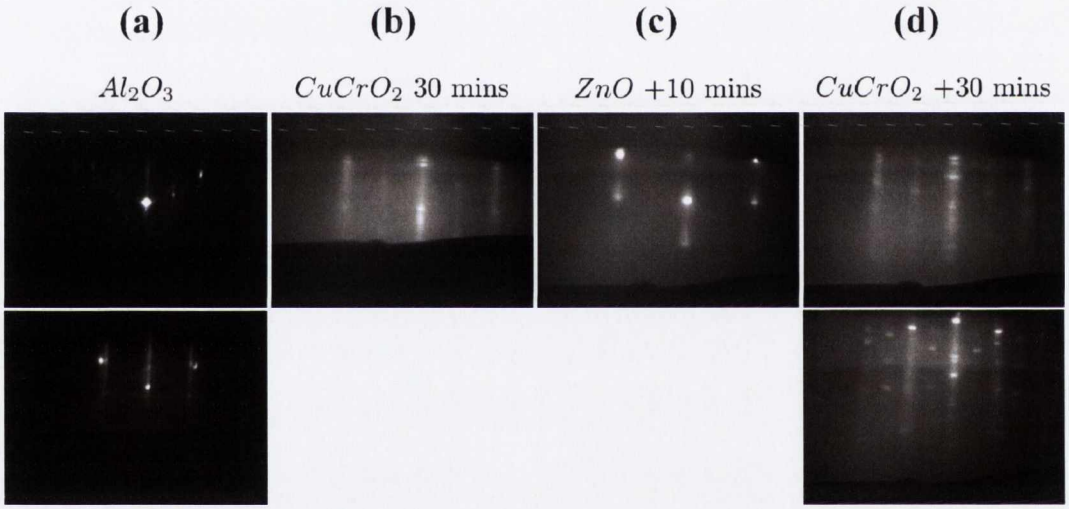

Figure 6.9: RHEED patterns of along the (a) [$\bar{1}$10] direction (top) and [$\bar{1}$00] direction of Al_2O_3 substrate (bottom), showing (b) the initial $CuCrO_2$ layer with respect to the Al_2O_3 [$\bar{1}$10] direction after 30 mins of deposition, (c) the middle ZnO layer with respect to the Al_2O_3 [$\bar{1}$10] direction after 10 mins of deposition, and (d) the final $CuCrO_2$ layer with respect to the Al_2O_3 [$\bar{1}$10] direction (top) and with respect to the Al_2O_3 [$\bar{1}$00] direction (bottom) after 30 mins of deposition of a p-Mg:$CuCrO_2$/n-Al:ZnO/p-Mg:$CuCrO_2$ device structure.

Each step in the device process was monitored post-deposition by x-ray scattering analysis, as previously mentioned. In this way it was possible to analyse the structure of each new layer in addition to the evolution of the underlying layers. Normalised x-ray reflectivity measurements after each step in the device fabrication process of one trilayer structure are presented in fig. 6.10. The thickness of the initial $CuCrO_2$ layer was found to be 72 nm. Although the period of oscillation in the x-ray reflectivity after the deposition of the ZnO and top $CuCrO_2$ layers changes, the

determination of each layer thickness is difficult since the beam footprint on the sample exceeds the diameter of the patterned films.

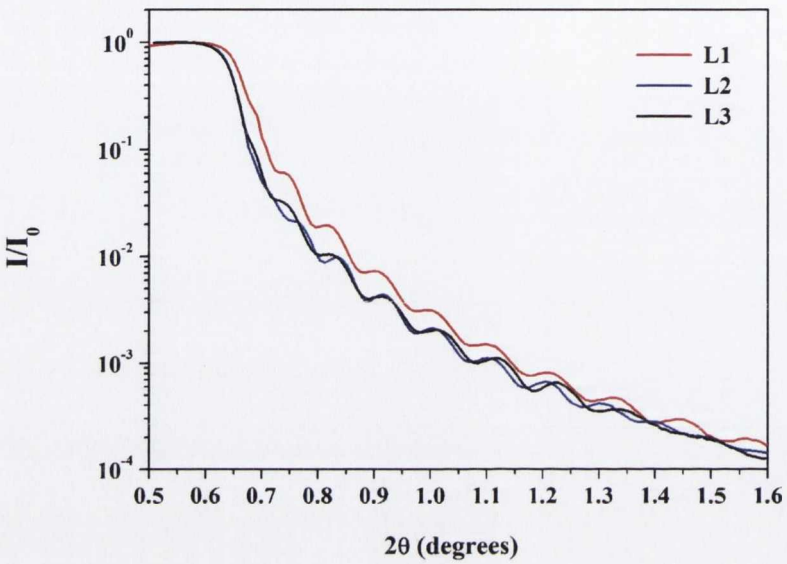

Figure 6.10: Normalised x-ray reflectivity of the device structure after each step of the fabrication process.

2θ-ω scans of the three layers of one of the devices are shown in fig. 6.11. The initial $CuCrO_2$ layer (L1) is observed to be well crystallised with a high intensity c-axis oriented (006) peak. The minor impurity phases and secondary orientation of the $CuCrO_2$ phase, as previously observed, are evident in this layer. The addition of a highly oriented ZnO film after the deposition of layer 2 (L2) is confirmed by the observation of the (002) reflection. The final step in the process involved the deposition of a second $CuCrO_2$ layer (L3). Although some impurity phases are clearly present, no significant changes are observed in the diffraction pattern after the deposition of L3, suggesting the growth of a second c-axis oriented $CuCrO_2$ layer.

The identification and indexing of the minor impurity phases observed between the primary Bragg peaks of the two component materials is presented in figure 6.12. Small additional peaks corresponding to the CuO and Cu_2O phases together with another orientation of the $CuCrO_2$ film have been labelled in the figure. A possible $CuCr_2O_4$ phase may be present with a Bragg peak shifted with respect to the PDF. The presence of parasitic x-ray wavelengths complicates the identification of these impurity phases.

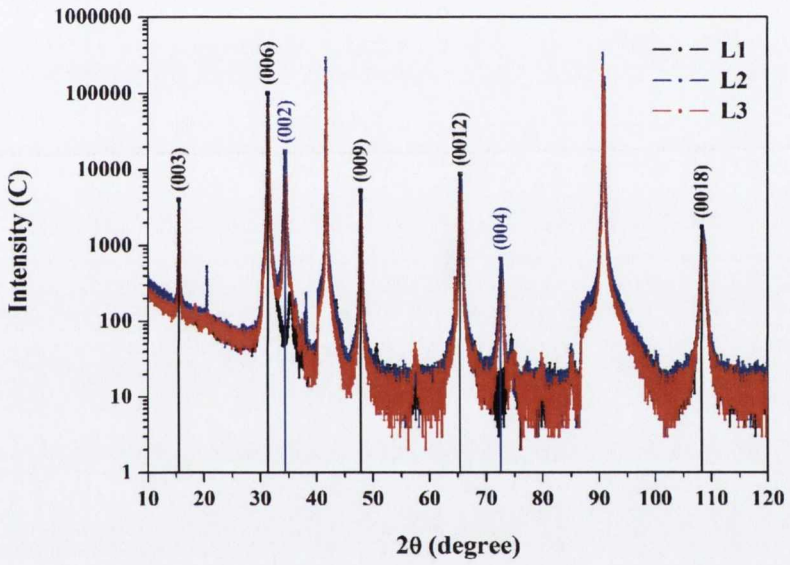

Figure 6.11: $2\theta - \omega$ scans of each successive layer of the $p\text{-}Mg{:}CuCrO_2/n\text{-}Al{:}ZnO/p\text{-}Mg{:}CuCrO_2$ transistor device structure. The scan of the sample after deposition of layer 1 (L1) is shown in black, the scan after deposition of layer 2 (L2) is shown in blue, and the scan of the complete structure after deposition of layer 3 (L3) is in red.

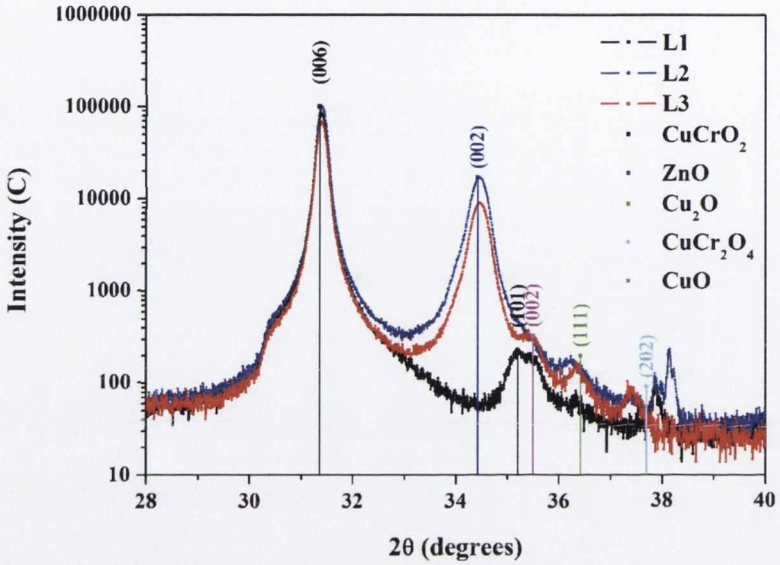

Figure 6.12: Zoom on the primary $CuCrO_2$ and ZnO peaks of the $2\theta - \omega$ x-ray diffraction pattern of the device structure. The unidentified impurity peak around 38.2^o in L2 has been attributed to a $CuO_{1-\delta}$ phase, the Bragg peak around 37.5^o corresponding to the W L_α wavelength.

The crystal quality of each layer has been assessed by rocking curve XRD analysis. The evolution of the rocking curves of the $CuCrO_2$ (006) and ZnO (002) reflections have been measured throughout the device fabrication process, as shown in fig. 6.13. The familiar double peak rocking curve has again been observed in the initial $CuCrO_2$ layer, and no change has been observed in the normalised rocking curve intensities of the (006) $CuCrO_2$ peaks from L1 to L2. The top layer, however, influences the rocking curve of this peak by increasing the FWHM ω of the broad, lower-intensity contribution. The FWHM ω of the rocking curve of the (002) ZnO peak is not affected by the addition of the final layer of the device structure.

The quality of the $CuCrO_2$ and ZnO thin film layers, in the direction normal to the sample surface (out-of-plane), is evidenced by the alignment and similar mosaicity of the (006) and (002) reflections of the respective films as shown in fig. 6.14.

6.4.3.1 Transmission Electron Microscopy

Since the characterisation used previously gives only an information on the average structural quality over a wide zone of the samples, transmission electron microscopy was used to have more

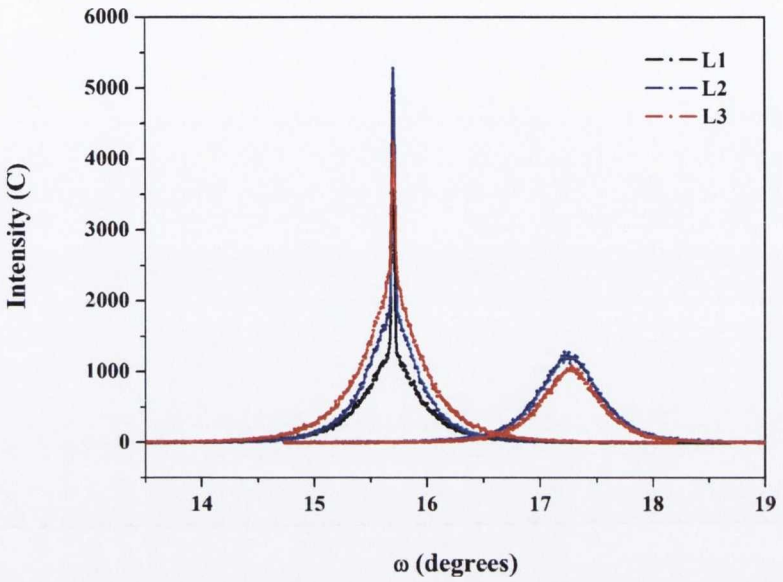

Figure 6.13: Rocking curves of the primary $CuCrO_2$ and ZnO peaks of the constituent layers of device structure.

local information. In order to examine the interfaces of the constituent layers and the crystal of the layers of the device structure a cross-sectional TEM study was carried out with Dr. S. Colis and Dr. C. Ulhaq-Bouillet. The sample preparation for cross-sectional TEM analysis together with the specifications of the electron microscope is described in appendix A.

Fig. 6.15 is a TEM image of an unmasked trilayer device structure. Four distinct regions are visible in the image, and are identified as the Al_2O_3 substrate, the Mg:$CuCrO_2$ first layer, the Al:ZnO central layer and the Mg:$CuCrO_2$ top layer. The thicknesses of each of the layers are indicated on the figure[1]. A smooth interfacial quality is evident throughout the device structure, excluding one disoriented crystallite which was observed within the ZnO layer. The appearance of this crystallite confirms the RHEED observation that the ZnO layer has a 3D growth mode. The crystallographic coherence of the growth is established by the presence of atomic planes. Fourier transforms of selected regions in each of the layers, indicated by the coloured squares, are shown on the right hand side of the image. The interatomic distances calculated from the Fourier transform correspond to the $(00l)$ direction for each layer, confirming the c-axis growth orientation observed by XRD. It is clear from this picture that some irregularities are present along the layers,

[1]The layer thicknesses within this film were chosen for the structural characterisation. For electrical operation, both of the $CuCrO_2$ layers were designed to be significantly thicker than the ZnO base layer.

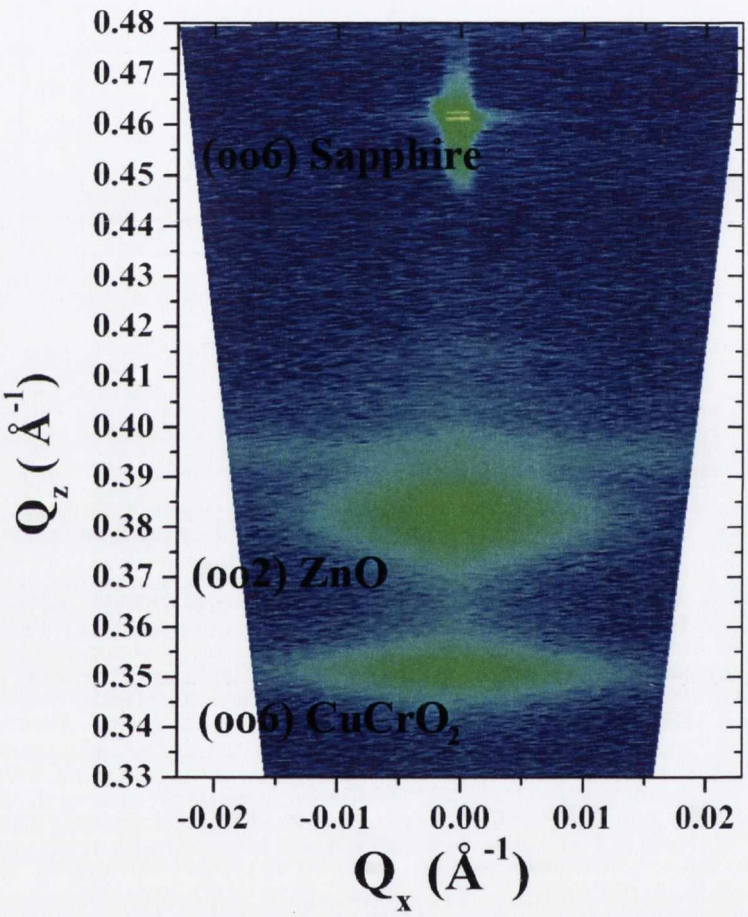

Figure 6.14: Reciprocal space map of the (006) reflection of the $CuCrO_2$ layer, the (002) reflection of the ZnO layer, and together with the (006) Bragg peak of the Al_2O_3 substrate of a device structure.

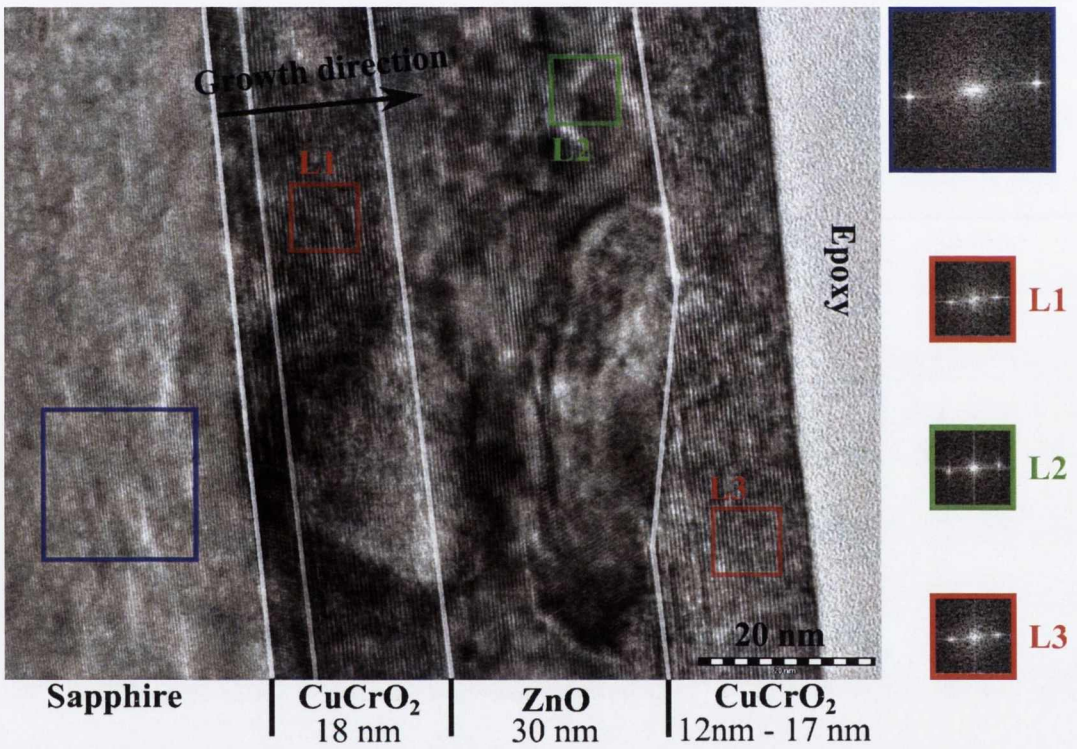

Figure 6.15: TEM image of a $Mg{:}CuCrO_2/Al{:}ZnO/Mg{:}CuCrO_2$ *p-n-p* device structure. Selected windows in each layer with their respective Fourier transform are indicated.

but although it is hard to estimate how many of these defects are present, in each of the zones examined, the ZnO layer was continuous. This is not enough to confirm that no discontinuity exists throughout the three layers however, since TEM probes on a very local level.

A selected area diffraction pattern (SAED) of the same sample is presented in fig. 6.16. The pattern exhibits spots characteristic of single crystal diffraction. The aligned nature of the diffraction spots indicates that the electron beam is perpendicular to a high symmetry axis (zone axis) in the crystals. The intensity profile along the red line is shown in fig. 6.16 (b). The peaks are indexed with respect to the d-values from the powder diffraction files of Al_2O_3, $CuCrO_2$ and ZnO. The most intense peak corresponds to the $(00l)$ family of planes of Al_2O_3. The smaller peaks are all identified with $CuCrO_2$ $(00l)$ and ZnO $(00l)$ planes confirming the coherent growth direction throughout the entire device. Two forbidden peaks are observed for Al_2O_3 and ZnO respectively, both corresponding to double diffraction, a dynamical effect which is often observed in electron diffraction by single crystal materials.

A similar line profile analysis has been performed in the perpendicular direction, as indicated by the blue line in fig. 6.16 (a). The intensity profile, shown in fig. 6.16 (c), is indexed with Al_2O_3 (110) and ZnO (100) planes. The determination of these two perpendicular directions allows the calculation of the zone axis along which the diffraction is taken. A simulated pattern of the three components and their respective zone axes is presented in fig. 6.16 (d). The simulated pattern perfectly reproduces the observed electron diffraction pattern, confirming the epitaxial relationship between Al_2O_3, $CuCrO_2$ and ZnO discussed in chapters 3 and 5.

6.4.4 Morphological Characterisation

The surface morphology of each of the components of the trilayer structure has a critical role in the performance of the device. Disorder at the layer interfaces can affect the electrical carrier transport, for this reason, the morphological character of each of the layer surfaces has been examined by Dr. S. Colis using AFM. The image in fig. 6.17 (a) corresponds to the initial Mg-doped $CuCrO_2$ layer, a similar morphology to that in the thinnest $CuCrO_2$ film, shown in chapter 3, is presented with the presence of droplets of approximately 100 nm diameter. The r.m.s. roughness over a 15 μm^2 area is 3 nm and the maximum peak to peak height is 10 nm. The image shown in fig. 6.17 (b) corresponds to the second Al-doped ZnO base layer. Particles of 200 nm size have been observed on the surface, the r.m.s. roughness and the maximum peak to peak height have been determined to be 10 nm and 50 nm respectively. The final image in fig. 6.17 (c) corresponds to the top Mg-doped $CuCrO_2$ layer. This layer appears to have a degraded morphology in comparison

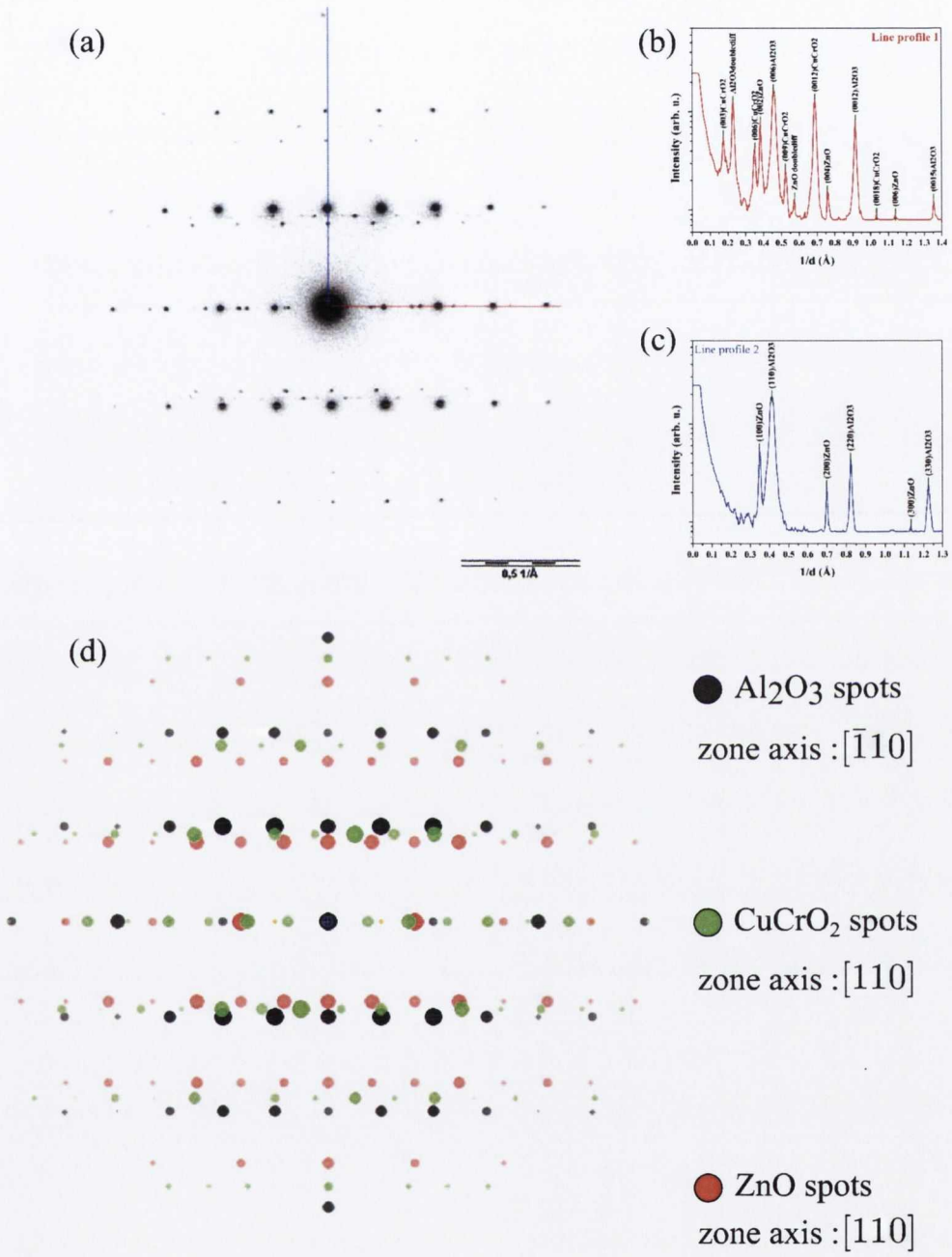

Figure 6.16: (a) Selected area electron diffraction (SAED) pattern of a $Mg{:}CuCrO_2/Al{:}ZnO/Mg{:}CuCrO_2$ *p-n-p* device structure. (b) and (c) are line intensity profiles along the highlighted directions in (a). (d) Simulated SAED pattern of the trilayer structure with the respective zone axes of the layers.

to the bottom layer with a r.m.s. roughness of 20 nm and a vertical peak to peak maximum value of 80 nm. It is clear from these images that morphology of the successive layers suffers a degradation due to growth on the previous thin film rather than the single crystal substrate. This is further evidenced by the appearance of some impurity phases in the x-ray diffraction patterns of the layered structure.

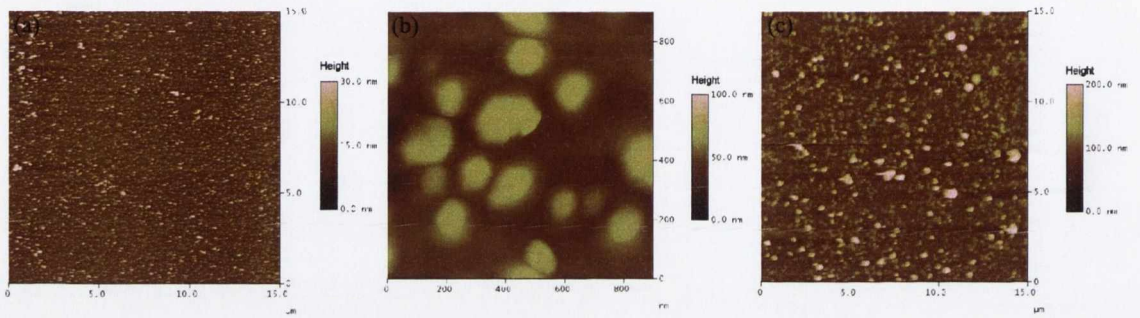

Figure 6.17: AFM images of each of the layers of a $Mg{:}CuCrO_2$ / $Al{:}ZnO$ / $Mg{:}CuCrO_2$ thin film structure. The image (a) corresponds to the initial $Mg{:}CuCrO_2$ layer, (b) corresponds to the $Al{:}ZnO$ base layer, and (c) corresponds to the top $Mg{:}CuCrO_2$ layer.

6.4.5 Optical Characterisation

The optical transmission spectra of two of the *p-n-p* device structures, one thicker, one thinner, were measured in order to determine the transparency of such a device in the visible range. The measured spectra are shown in fig. 6.18. The absorption of the thicker film, identified by the black curve, is increased in the visible range relative to that the thinner structure, which corresponds to the red curve. This effect has also been observed for $CuCrO_2$ thin films, as described in chapter 3. The transparency of the thick structure is between 30 and 70 % in the visible range, while the thinner structure has an optical transparency of between 40 and 70 %, these figures and the spectral shapes of the structure compare with values reported for a $Mg{:}CuCrO_2/ZnO$ *p-n* junction Tonooka & Kikuchi (2006).

6.4.6 Electrical and Magneto-transport Measurements

Electrical characterisation of the structure was carried out in a custom-built cryogenic high-impedance probe used within the Quantum Design PPMS with Dr. P. Stamenov. The structure was connected in a common base configuration and a schematic of the electrical circuit is presented in fig. 6.19. Since the dopant in both the collector and emitter should be similar, the measurement

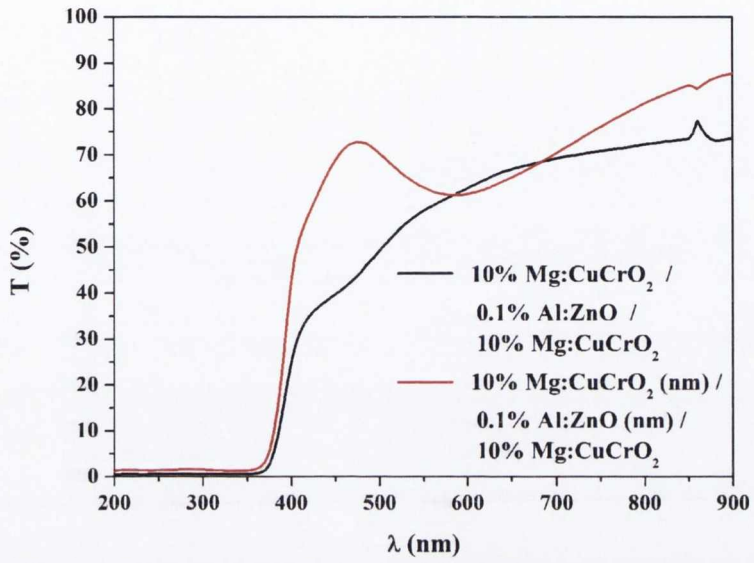

Figure 6.18: UV-Visible spectrometry of a $Mg{:}CuCrO_2/Al{:}ZnO/Mg{:}CuCrO_2$ *p-n-p* device structure showing optical transmission as a function of wavelength.

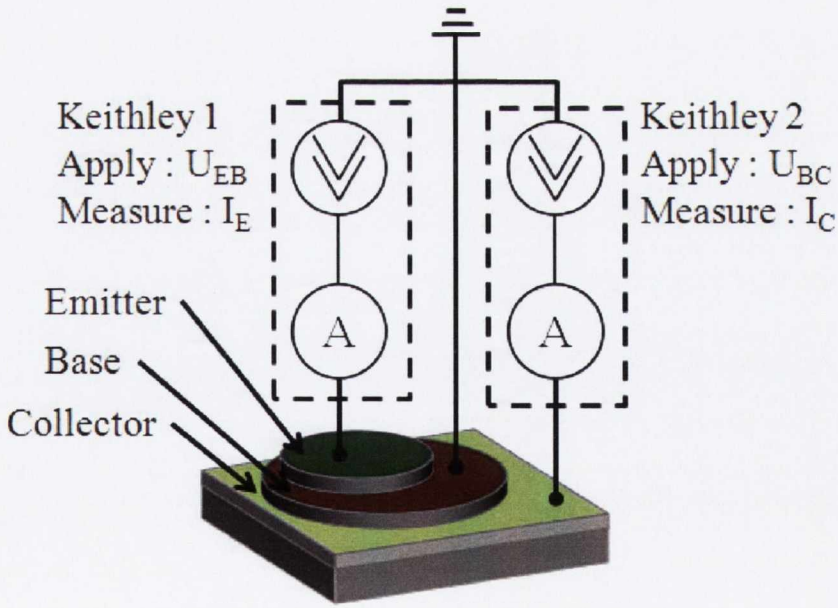

Figure 6.19: Schematic of the electrical circuit used to measure the electrical properties of the $CuCrO_2/ZnO/CuCrO_2$ structure.

strategy was to measure both polarities in both circuits using voltage sourcing and current sensing. The majority of the characterisation was performed at fixed points in temperature and magnetic field whilst scanning at V_{EB} and V_{BC} and measuring I_E and I_C. Examples of such datasets are shown in fig. 6.20 for a 20 nm thick ZnO layer and fig. 6.21 for a 50 nm thick ZnO layer.

At room temperature, all devices measured (6 stacks with varying base thickness) displayed linear I-V characteristics for both EB and BC junctions. This can be attributed to the fact that the $CuCrO_2$ layers are effectively n-type degenerate semiconductors for temperatures above 150 K. At temperatures below 100 K, the individual I-V characteristics become nonlinear with evidence for both rectifying and tunnelling behaviour. At no temperature is any saturating behaviour observed for either transconductance characteristic and no attempt of extracting a current gain is attempted.

The reproducibility of both single-circuit and transconductance characteristics between devices produced under similar conditions is poor, this could be due to the necessity for exposure of the individual deposited layers for shadow masking.

Signal-to-noise ratios (due to high single-circuit impedance and low transconductance) do not permit the analysis of the partial rectifying behaviour in any detail. Quite the contrary, the obvious tunnelling-dominated conductance through both the emitter-base and base-collector circuits (as shown on fig. 6.20) could be readily analysed by fitting individual emitter-base I-V characteristics at fixed base-collector voltage to a simple exponential voltage activation of the transmission model Simmons (1963).

$$I \propto I_{off} + \text{signum}(U) \cdot A \cdot \exp\left(-\frac{|U - U_{off}|}{\phi}\right) \tag{6.8}$$

where I_{off} and U_{off} are accounting for experimental bias offsets of the current and voltage preamplifiers, respectively; A gives the magnitude of the total current; and ϕ is an effective coefficient proportional to the barrier power (i.e. the product of the barrier height and barrier width). Examples of these processes are given in fig. 6.22. Extracted voltage activation scales ϕ vary in the region $13 - 35$ V for the first structure and $25 - 40$ V for the second. I-V characteristics above about 30 K were essentially linear and did not permit the extraction of ϕ. If a simple rectangular barrier profile is assumed, corresponding to the entire thickness of the basal region, the effective barrier height should therefore be of the order of 0.5 eV, corresponding roughly to the bandgap difference between ZnO and $CuCrO_2$, suggesting light tunnelling of quasi-electrons close to the CB of ZnO. The extracted activation ϕ is not a measure of any fundamental parameters of the material, and the temperature dependance of ϕ could be due do different phenomena such as a change in carrier concentration as a function of temperature on both side of the base, resulting in a change in the thickness of the depletion layer or the superposition of a tunnelling and thermionic emission

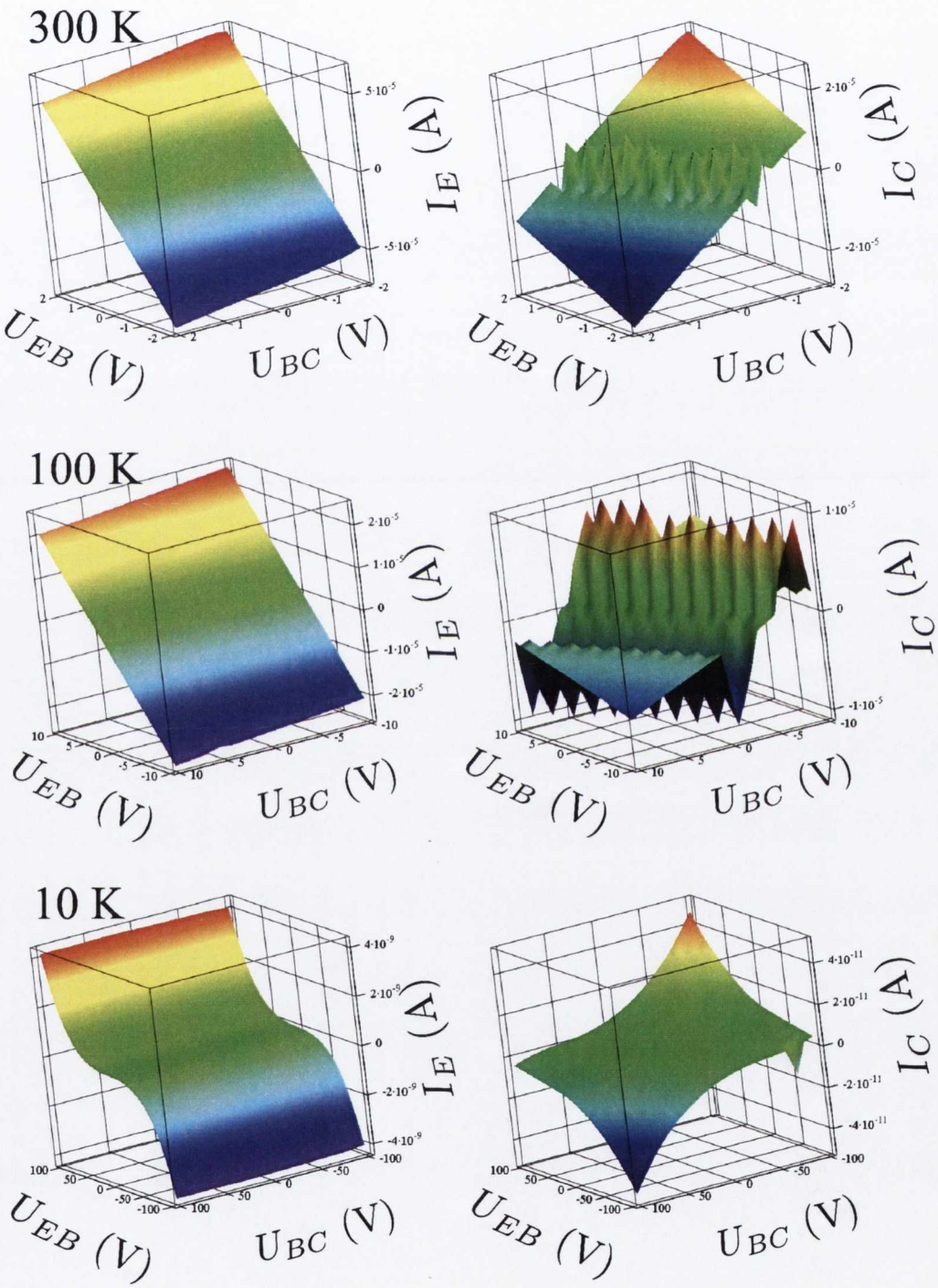

Figure 6.20: 3-dimensional *I-V* characteristics of a 10 % $Mg{:}CuCrO_2$ / 0.1 % $Al{:}ZnO$ / 10 % $Mg{:}CuCrO_2$ structure measured at 300 K, 100 K and 10 K, plotted for I_C (right hand side) and I_E (left hand side). The 300 and 100 K I_B data must be flattened. The ZnO layer for this structure is 20 nm

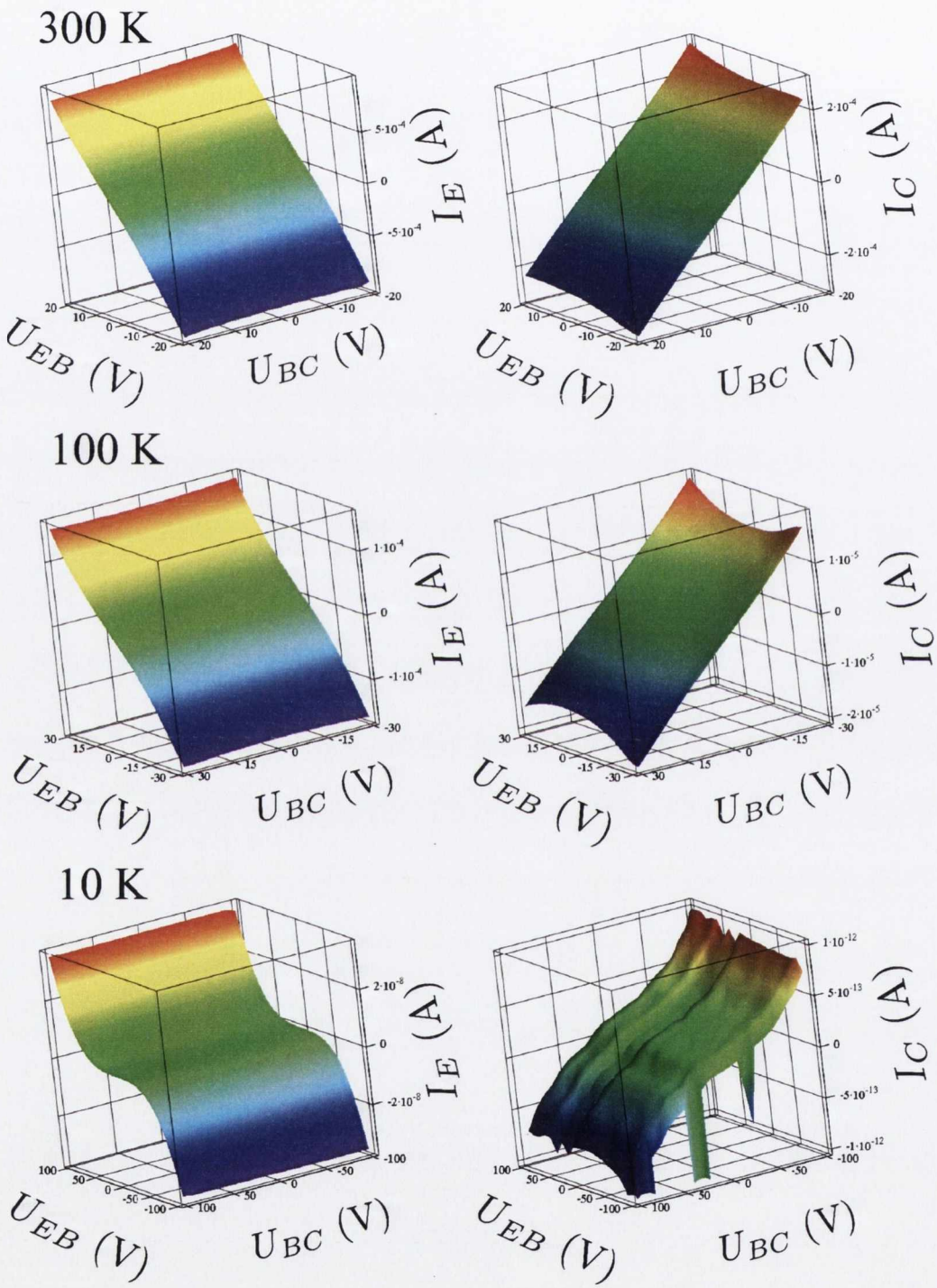

Figure 6.21: 3-dimensional *I-V* characteristics of a 10 % Mg:$CuCrO_2$ / 0.1 % Al:ZnO / 10 % Mg:$CuCrO_2$ structure device measured at 300 K, 100 K and 10 K, plotted for I_C (right hand side) and I_E (left hand side). The ZnO layer for this structure is 50 nm

contribution. The good fit of the data at low temperature shows that it is a good assumption to consider tunneling as the dominant limiting current mechanism.

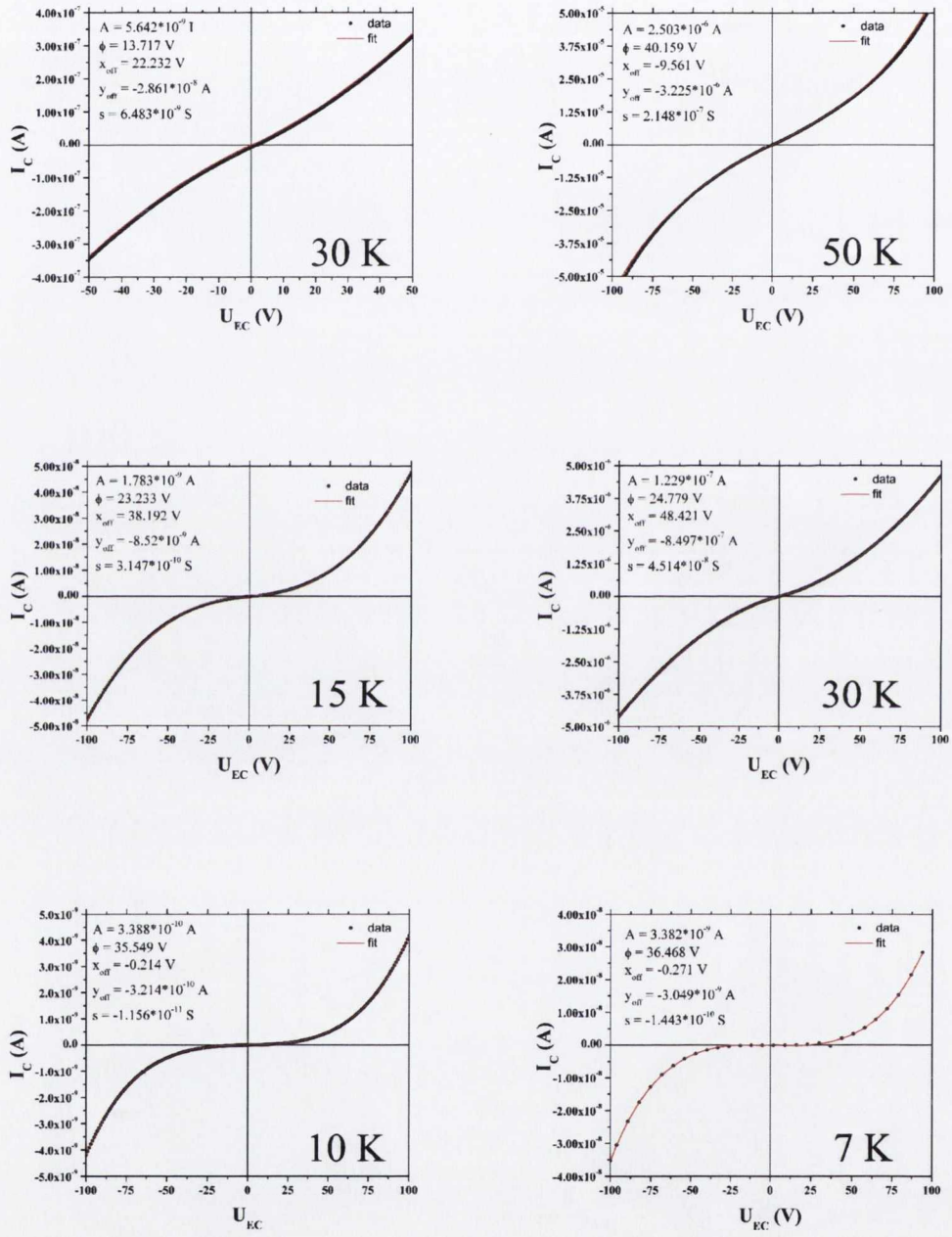

Figure 6.22: Low temperature *I-V* characteristics of two 10 % $Mg{:}CuCrO_2$ / 0.1 % $Al{:}ZnO$ / 10 % $Mg{:}CuCrO_2$ bipolar heterojunction devices, one on the left and one on the right, measured at different temperatures with a base-collector bias of 50 V in each graph.

6.5 Conclusions

Shadow masking has been used to produce trilayer structures by PLD in the advancement towards all-oxide devices. In order to avoid backsputtering from classical shadow masks, sapphire masks were designed to withstand high temperatures and to achieve non-reactivity with the grown layer. Good growth coherence has been observed throughout the structure between the $CuCrO_2$ and ZnO layers by TEM and XRD. Close epitaxial relationship between the layers has been observed by SAED showing ZnO [001] || $CuCrO_2$ [001] and ZnO [100] || $CuCrO_2$ [100]. A moderate transparency on the order of 60 % has been achieved throughout the structure. Although one of the objectives of this work was to produce an all-oxide bipolar transistor, a simple analysis and comparison with a typical silicon-based device reveals the inherent weakness of the design. The materials involved in this study are restricted by a very low mobility, a property which would inhibit the performance of a typical silicon device. A number of devices, on the order of 20, have been fabricated, of which a total of 6 have been characterised electrically in a common base configuration down to low temperatures and in high magnetic fields. In all of the measured devices the junctions at both interfaces have exhibited linear characteristics above 50 K. At low temperature, however, some of the devices have demonstrated nonlinear behaviour, which could be explained by a tunnelling-dominated conduction. It is clear that none of these devices behave as a typical bipolar junction transistor, this is expected in view of the low mobilities of the materials involved. It should be noted that the observed low mobility in the *p*-type oxides is not due to poor quality layers, but is intrinsic to the material. Realisation of an all-oxide bipolar junction transistor based on this combination of materials is not possible, and new component materials must be explored.

Chapter 7

Conclusions and Outlook

The broad focus of this research project has been the development of two members of the rare class of transparent conducting oxide materials, possessing the delafossite crystal structure, and manifesting p-type and bipolar conductivity, $CuCrO_2$, and sister material, $CuInO_2$, respectively. The advancement of these materials has been motivated by the potential to demonstrate a functioning active transparent electronic device based on the bipolar semiconducting characters of the components. The materials synthesis and thin film fabrication and optimisation processes have been a major focus of this work, and as a consequence of this attention to sample quality the progression from inceptive materials to device development has been achieved.

As a precursor to the successful growth and characterisation of thin film p-type conductive delafossite TCOs, a set of powder specimens have been prepared and analysed. Two different synthesis routes have been explored, one is diffusion-based solid state reaction, and the second is a kinetically controlled liquid phase sol-gel method. The resulting powders have been structurally characterised by means of x-ray diffraction and the amount of impurity phases present (such as CuO, $CuCr_2O_4$, and $MgCr_2O_4$) minimised. The antiferromagnetic transition temperature has been established to be just below 25 K for an arbitrary Mg doping concentration up to 3.5 %. Significant discrepancy has been observed between the asymptotic Curie temperature and the actual transition in accordance with expectations for severe local frustration arising from the triangular antiferromagnetic ordering.

Consequently, thin films with significantly higher Mg-doping concentrations up to 15 % have been successfully grown (by means of pulsed laser deposition) on c-cut sapphire substrates and a non-equilibrium solid state solubility limit has been established at around 10 %. Detailed x-ray study has established the epitaxial relation to the substrate and the high degree of orientation

of the resulting films. Careful three-axis x-ray diffraction has revealed evidence of partial long-range order of the Mg impurities coherent with the matrix. Surface morphology has been studied by means of atomic force microscopy and it has been established that, should film thickness be kept below 30 nm, short-range surface roughness can be as low as 5 nm r.m.s. and peak to peak roughness of 50 nm, while much thicker films exhibit heterogeneous growth and precipitation of micron-sized single crystals on the top surface. The direct bandgap has been estimated by means of optical transmission to be $\sim$ 3.2 eV. Mg-dopant incorporation has been confirmed by x-ray photoemission spectroscopy. Clear evidence for conduction-electron-to-localised-spin scattering has been established in electrical measurements via thermal scans at fixed external magnetic fields, and by magnetoconductance studies at various temperatures. Very high, linear magnetoconductance has been observed for the highest Mg-doping concentration (10 %). For the first time, Hall effective mobilities and carrier concentrations were determined in this system. The highest mobility has been measured to be 0.007 cm^2/Vs at 200 K with a corresponding carrier concentration of $\sim 2{\cdot}10^{22}$ cm^{-3}.

A potential candidate system for a bipolar transparent semiconductor - $CuInO_2$, has been studied in its Sn and Ca-doped forms. Highly oriented thin films have successfully been produced with dopant concentrations as high as 8 %. Only small amounts of impurity phases such as CuO and In_2O_3 have been identified by x-ray diffraction, and surface morphology has been verified to be acceptable for device application (short scale surface roughness of $\sim$ 4 nm r.m.s and a peak to peak roughness of 30 nm). The optimised films are highly optically transparent, up to 80 % at the red end of the visible electromagnetic spectrum, and the direct bandgap has been confirmed to be approximately 4.1 eV. Despite the fact that the films exhibit very high sheet resistances, on the order of 10^{19} Ω/m, it was possible to resolve two distinct activation energies, just below room temperature, for the n and p-doped variations, 0.34 and 0.37 eV, respectively. These relatively high activation energy scales combined with the low carrier mobilities have prohibited the construction of the two demonstration devices envisaged: diffused p-n homojunction rectifying diode and bipolar homojunction transparent transistor.

Because of the unavailability of a suitable bipolar transparent (and magnetic) semiconductor, research efforts were redirected towards the construction of a low-temperature prototype device - a magnetic bipolar heterojunction transistor. Based on previous experience, n-type Al-doped ZnO was chosen as a potential candidate for sizeable mobility basal region of a p-n-p bipolar transistor. Growth of undoped ZnO films has been successfully optimised before introducing Al-doping into the system. High quality, oriented and epitaxial Al-doped ZnO films have been

successfully deposited by pulsed laser deposition on *c*-cut sapphire substrates, with reproducible structure and carrier concentrations. The direct bandgap has been confirmed to be 3.3 eV, and the mobility was evaluated at 40 cm^2/Vs at carrier concentrations as high as $5 \cdot 10^{18}$ cm^{-3}. At this point the films were considered to be of acceptable quality to be included as basal regions within the pursued magnetic bipolar heterojunction transistors.

Comparison of the theoretical performance of a transistor based on $CuCrO_2$ and ZnO with a classical Si-based transistor, using the information accumulated on the properties of these two materials, indicates that the device would barely function. The growth of well-oriented heteroepitaxial trilayers of 10 % Mg-doped $CuCrO_2$ / 0.1 % Al-doped ZnO / 10 % Mg-doped $CuCrO_2$ was, nevertheless, optimised by varying the deposition substrate temperatures and deposition times. Lateral structuring of the sought-after transistors was achieved by contact shadow-masking (using purpose-designed single crystalline sapphire masks). Structural and interfacial quality has been carefully examined by means of x-ray diffraction and transmission electron microscopy. The resulting devices exhibit optical transmittance in excess of 65 % in the red end of the visible spectrum. Finally, a number of devices have been characterised electrically down to temperatures of $\sim$ 10 K, in magnetic fields of up to 14 T. None of the measured devices present a classical transistor characteristic down to low temperatures, but rather they exhibit tunnelling-dominated conduction. Since the low mobility of these materials is an intrinsic property, the realisation of an all-oxide bipolar junction transistor would require the development of new materials with improved mobilities.

Appendix A

Sample preparation

A.1 Powders

A.1.1 Solid state reaction

$CuCrO_2$ The $CuCrO_2$ powder was prepared according to the following equation:

$$\frac{1}{2}Cu_2O + \frac{1}{2}(1-x)Cr_2O_3 + xMgCO_3 \longrightarrow CuCr_{1-x}Mg_xO_2 + CO_2 + O_2$$

Powders of Cu_2O (99.99 % pure), Cr_2O_3 (99.995 % pure) and $MgCO_3$ (99.5 % pure) were weighed and mixed in appropriate amounts, then ground thoroughly. An investigation of the optimum sintering temperature for $CuCrO_2$ was undertaken in this work as illustrated by Fig.A.1. The mixture was calcined in air in an alumina crucible for 24 hours at temperatures ranging from 873 K to 1273 K at 50 K intervals. The furnace heating was at a rate of 5 K/min while the cooling rate was 1 K/min. Once the optimum temperature was identified, the resultant powder was reground, pressed into a pellet of 20 mm diameter, and sintered again in air at that temperature for 24 hours to make the final target.

$CuInO_2$ The $Cu_2In_2O_5$ powder was prepared by solid state reaction. Stoichiometric amounts of CuO (99.99+ % pure), In_2O_3 (99.99 % pure) and SnO_2 (99.995 % pure) or CaO (99.99 %) powders were weighed, mixed and ground. The mixtures were heated to 1223 K for 24 hours. The powder was ground once again, pressed into a pellet and sintered at the same temperature for 24 hours. Finally, the phase of both sets of targets were examined by x-ray diffraction prior to laser ablation.

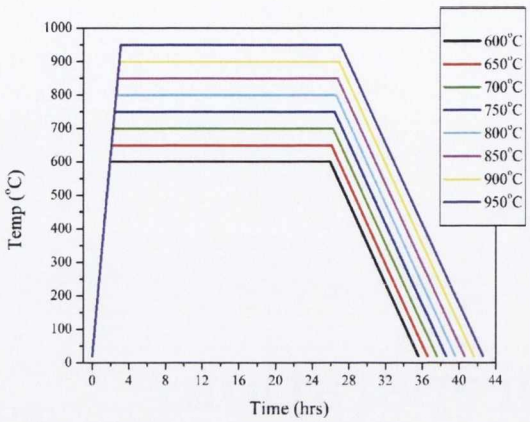

Figure A.1: Powder preparation temperature profile

A.1.2 Soft chemistry

A.1.2.1 Sol gel

A study of $CuCrO_2$ powder synthesised by the method of sol-gel was carried out. In general, powders prepared by this method have an extremely small grain size, of the order of hundreds of nanometres, which ensures atomic mixing of the reagents. Copper acetate and chromium nitrate salts in the correct stoichiometric proportions were used for this method Li *et al.* (2007), with citric acid employed as the gelling agent. A solution of the above salts and gelling agent in 100 mL deionised water was prepared in a beaker. The solution was heated to 373 K and simultaneously stirred until all of the salts were completely dissolved. Continued heating evaporated off the water from the solution leaving a dry gel residue. This dried powder was subsequently fired at various temperatures in the range 873 K to 1273 K again according to Fig. A.1. The resultant powders were finally characterised by x-ray diffraction, as shown in fig. A.2 to determine the optimum preparation conditions.

A.1.2.2 Coprecipitation

Among wet chemistry synthesis techniques, coprecipitation is known to be quite a simple and convenient way of achieving high quality oxide powders. In general, coprecipitation is carried out by preparing aqueous solutions of the constituent metals (in the form of nitrates, acetates and chlorides) and of a titrant such as hydroxide and oxalate, the metallic solutions and titrant are

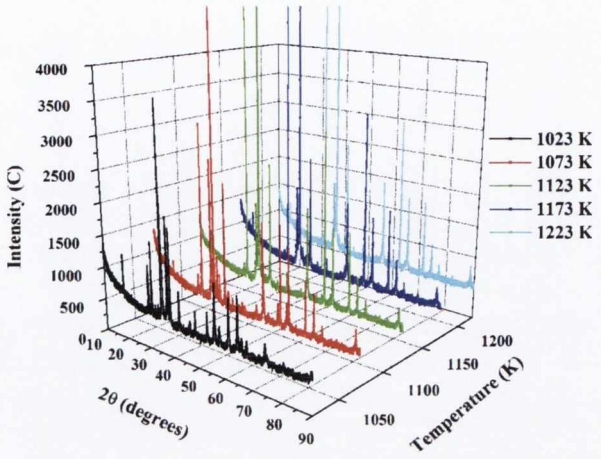

Figure A.2: Reaction temperature scan of $CuCrO_2$ powder prepared by the sol-gel method

then mixed together, coprecipitated, filtered, washed and finally calcined.

Zn acetate and aluminium chloride have been dissolved in deionised water in the desired stoichiometric proportion to prepare the source solution with the total metal ion concentration of 0.2 mol/L. A solution of oxalic acid with a concentration of 0.2 mol/L was prepared in a separate beaker. This solution was then slowly added to the metal ions solution while stirring. The oxalic acid solution was added in excess to make sure that the precipitation is complete. The white precipitate obatined was then filtered and washed. The obtained powder was dried overnight and fired at 1073 K for 15 mins.

A.2 Thin Films

A.2.1 Pulsed laser deposition

A.2.1.1 Target and Substrate Preparation

Solid state reaction is typically used to prepare targets. This method typically involves weighing stoichiometric amounts of the cation-containing starter materials, mixing and grinding them together with a pestle and mortar until homogeneously distributed and then annealing this powder mixture, at the appropriate temperature, under air or some desired gas flow, such as O_2 or Ar. The sintered powder is then grinded again before being compressed in a pellet press and die and lastly sintered again.

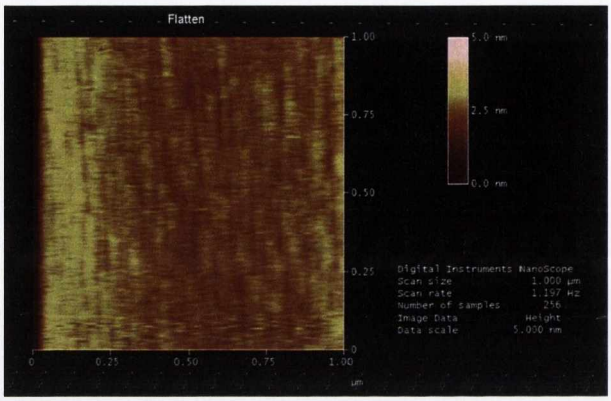

Figure A.3: AFM image showing step-and-terrace surface of STO substrates after HF etching and subsequent high temperature annealing

In order to obtain highly crystalline samples to analyse, STO substrates were chosen to achieve 2-dimensional layer-by-layer epitaxial growth. Various substrate preparation techniques are commonly employed to obtain atomically flat, step-and-terrace surfaces for epitaxial growth. To prepare the STO wafers, a buffered-HF etching procedure was carried out, followed by a high temperature, high vacuum annealing step. The substrates were sonicated in acetone for 20 mins, to achieve a strontium hydroxide termination at the surface, they were subsequently dipped in NH_4OH-buffered HF acid for 10 mins, to remove the hydroxide layer, before loading into the vacuum chamber to undergo a 1 hr anneal at 1073 K in a flow of O_2 gas. AFM analysis of the resultant surface revealed a step-and-terrace surface, as shown in fig. A.3. Pre-deposition treatment for Al_2O_3 substrates, to achieve atomically flat step-structured surface Kimura & Takahashi (2000), involved chemical etching with a H_3PO_4:H_2SO_4 (1:3) solution at 383 K for 30 mins.

A.2.1.2 Laser Ablation

The thin film growth technique has a very significant effect on the properties of the films. Different deposition techniques generate films with diverse structural, optical and electrical properties. Even for the same deposition technique, a slight variation in the deposition parameters produces films with different properties. Pulsed laser deposition (PLD), a plasma deposition process carried out in a vacuum system, was chosen as the growth method. PLD offers potentially stoichiometric transfer of material from the target rendering this non-equilibrium process very attractive for complex material film growth. This deposition process, shown schematically in Fig. A.4, can be broken down into a number of steps

- Photon – solid interaction: A pulsed laser beam is focused onto a target of the source material to be deposited. This results in a locally very high energy density, or fluence, on the target surface. The electromagnetic energy is converted into thermal energy via electronic processes and, for sufficiently high laser energy density (above the ablation threshold), this results in evaporation and subsequent ablation of a small amount of the source material.

- Plasma formation and expansion: The ablated material forms a plasma which expands due to the pressure gradient close to the target surface in a direction perpendicular to the surface in the vacuum chamber. These highly energetic ablated particles interact with the background gas in the chamber and recombine emitting photons in the process resulting in the characteristic luminous plasma plume (Fig. A.5 (a)). This ablation plume provides the material flux for film growth.

- Condensation on the substrate: The transported material that has reacted with the background gas arrives at the substrate and condenses. When thermal equilibrium is reached, the rate of condensation on the substrate exceeds the flux of high energy ions arriving at the surface, and a nucleation centre emerges.

- Nucleation and growth: A crystal seed starts to grow from the nucleation centre in a particular range of substrate temperatures and gas pressures. These deposition conditions determine the size of the nucleation centre which determines the growth mode. Two-dimensional layer-by-layer growth is generally observed at high temperatures, for materials that are lattice matched to the substrate, at a low rate of growth. Step-flow growth is an extremely high temperature growth mode. Three-dimensional growth is observed for higher deposition rates and results in reduced crystallinity of the thin films.

For multicomponent inorganics, PLD has proven remarkably effective at yielding epitaxial films. In this case, ablation conditions are chosen such that the ablation plume consists primarily of atomic, diatomic, and other low-mass species. This is typically achieved by selecting an ultraviolet (UV) laser wavelength and nanosecond pulse width that is strongly absorbed by a small volume of the target material. For low laser fluence and/or low absorption at the laser wavelength, the laser pulse would simply heat the target, with ejected flux due to thermal evaporation of target species. As the laser fluence is increased, an ablation threshold is reached, where laser energy absorption is higher than that needed for evaporation. The ablation threshold is dependent on the absorption coefficient of the material and is thus wavelength dependent. At still higher fluences, absorption

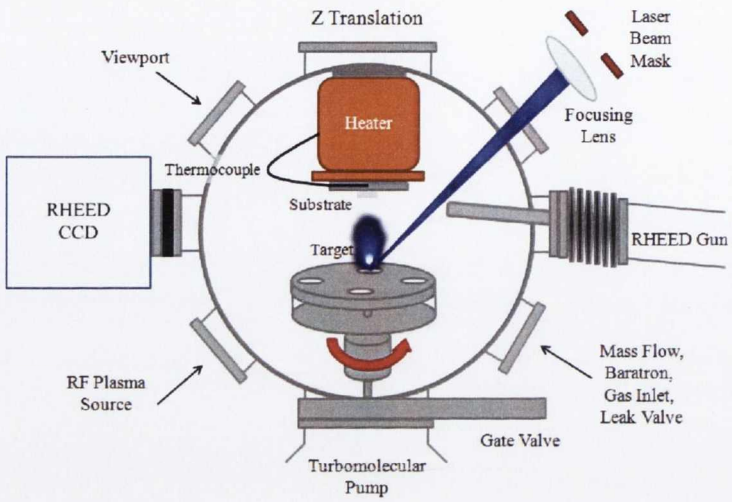

Figure A.4: PLD Schematic

by the ablated species occurs, resulting in the formation of a plasma at the target surface. With appropriate choice of ablation wavelength and absorbing target material, high-energy densities are absorbed by a small volume of material, resulting in vaporisation that is not dependent on the vapour pressures of the constituent cations.

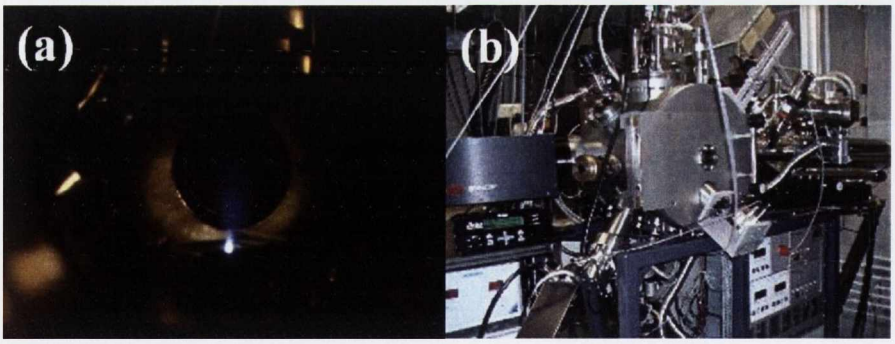

Figure A.5: (a) ZnO plasma plume, (b) Surface PLD chamber

In pulsed-laser deposition, a background gas is often introduced that serves two purposes. Firstly, the formation of multi-cation thin-film materials often requires a reactive species (e.g. molecular oxygen for oxides) as a component of the flux. In addition, the surrounding gas pressure can influence the mean free path of the ablated species and can determine their deceleration. Control of this background gas pressure allows the kinetic energy of the ablated species to be

tuned from high values ($\sim$ 100 eV) in vacuum to low energies ($\sim$ 0.1 eV) at high background pressures.

A.2.1.3 Deposition chamber

The high vacuum PLD system consists of a Surface vacuum chamber (Fig. A.5 (b)), which can be pumped (via a 250 L/s turbo molecular pump) to a base pressure of 2×10^{-7} mbar. A mass flow controller and MKS baratron pressure sensor allows regulation of background gas pressure in the chamber, in this case oxygen, in the range 0.3 - 150 μbar with an accuracy of 0.1 μbar. A 248 nm wavelength KrF excimer laser with a pulse duration of approximately 25 ns is used for ablation. The laser can fire with repetition rates from 1 Hz to 20 Hz. A rectangular mask shapes the beam selecting only the homogeneous part. A lens makes an image of the mask on the target resulting in a well defined illuminated area. The target holder is designed to hold four targets. Switching between targets is computer controlled, and when ablating the targets are rotating and rastering slightly to prevent the creation of holes. The laser beam is incident on the rotating target at an angle of 45^o to the plane of the target resulting in a vertical plume. The target to substrate distance is 7 cm and the substrate is offset from the plume by approximately 2^o. A thermocouple and temperature controller are used to maintain the substrate temperature during deposition.

The substrate is suspended on a stainless steel sample holder with colloidal silver paste (purchased from Agar scientific) which is heated by radiation from the Pt heater. The heater is designed to work under vacuum or mild oxidising atmosphere from room temperature up to 1173 K. The temperature is controlled with a thermocouple inserted in the middle of the sample holder. A inconvenient of this sample mounting method is the possible contamination of the substrate with material from the substrate holder. The high temperature baking of the silver paste and the contact of the stainless steel and the substrate seems to give rise to substantial diffusion of a unidentified red materials as shown in fig. A.6. This can impede proper measurement of the optical properties by transmission (fig.B.10) and magnetic characterisation.

The system is equipped with a high pressure RHEED allowing real-time monitoring of 2-dimensional layer-by-layer growth of highly crystalline thin films. This permits extremely accurate thickness measurement and is an indication of the growth orientation and crystallinity of the films.

Target and substrate selection and preparation have a profound impact on film growth. The source targets used were made from powder prepared by solid state reaction as described earlier. In general, only the correct cation stoichiometry is needed in the target, as the anion content can be influenced by the background gas in the chamber (in this case oxygen). During deposition the

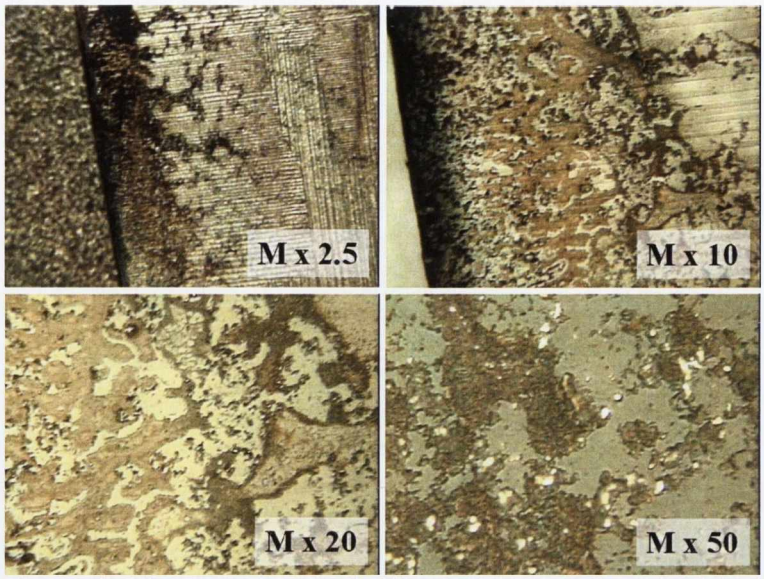

Figure A.6: Optical microscope images of $SrTiO_3$ substrates that have been annealed at 1073 K in thin film deposition conditions, where the substrate is mounted on the stainless steel substrate holder via Ag paint.

substrate temperature, oxygen background pressure, laser fluence and repetition rate and number of laser shots were used to promote certain properties in the films. After the deposition, the films were cooled to room temperature in the deposition O_2 partial pressure and then removed for characterisation.

A.3 TEM Sample Preparation

The preparation of samples for cross-sectional analysis by TEM can be performed according to two different procedures. The first method involves the use of a focused ion beam (FIB) to mill the sample in order to obtain a zone that is sufficiently thin to allow the electron beam to be transmitted through the material. This technique is effective on soft materials, where the rate of ion milling is efficient. In the case of oxides, and Al_2O_3 in particular, this method cannot be used since the ion beam renders the thin film amorphous. The heavy doping of the thin film, which results from the ion milling, and which could potentially alter the structure and composition of the sample, is a further disadvantage of this preparation method.

An alternative method, which was employed for the preparation of the trilayer device structures

encountered in chapter 6 of this thesis, consists of a combination of mechanical and ionic abrasion of the sample. In this case the ion milling is done with Ar ions, which are much lighter than the Ga ions used in the previous method. The procedure can be divided into a number of steps which are illustrated on fig.A.7, and described as follows:

1. The first step involves cutting the sample into two symmetric pieces with a diamond coated wire saw.

2. The second step consists of glueing together the two separate pieces, with the film surfaces positioned face-to-face, using an epoxy mixture. It is necessary to apply pressure to the sample during the curing process to obtain a thin epoxy layer. The quality of the interface is examined by optical microscopy to ensure a uniform thickness of the glue layer throughout the sample, in order to avoid the separation of the two pieces during the subsequent mechanical polishing step.

3. The penultimate step involves the mechanical thinning of the sample on either side, to achieve a cross sectional thickness of less than ~ 40 μm, however the sample must maintain a sufficiently robust structure to survive the final manipulation steps. Each cross-sectional face is mirror polished until no scratches can be observed across the interface.

4. The final step consists of opening an aperture in the centre of the specimen between the two contacted surfaces by ion milling. The sample is glued onto a copper ring which is loaded into a precision ion polisher system (Gatan PIPS). Ar ion milling with a dual beam is performed at 5 keV until a small hole is just observed in the specimen. The sample is ion milled for a further 3 keV for 2 minutes in order to remove any possible redeposition and amorphous layers.

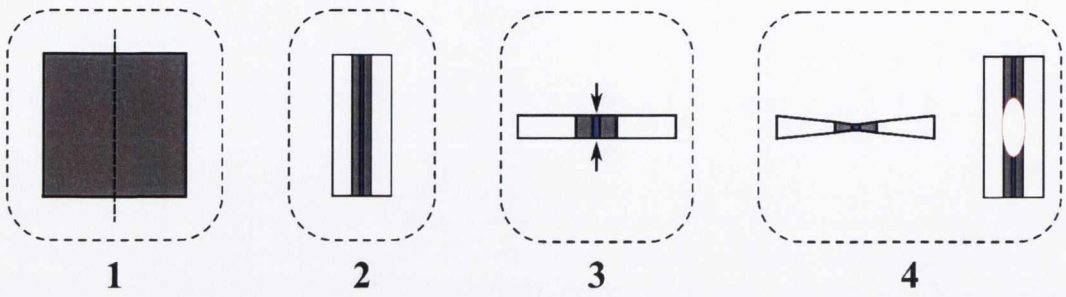

Figure A.7: Schematic of the procedure for the preparation of a thin film sample for cross-sectional TEM analysis.

A.4 Electrical Contacts

For most of the low temperature electrical measurements high purity In contacts were soldered to the surface of the thin film samples to create electrical contact, and high purity Au wires were then soldered to the contacts to provide the connections. Some room temperature electrical measurements were also performed on the samples, for which Ag paint was used to make the contacts. Some of the electrical contacts were made using evaporated Al/Au layers by shadow masking in a BOC Edwards AUTO 306 thermal evaporator.

Appendix B

Characterisation methods

B.1 *Insitu* Analysis

B.1.1 RHEED

The high pressure RHEED system consists of a kSA-400 acquisition system (phosphorus screen and camera) and a 35 kV Oxford electron gun pumped differentially to allow operation with background gas pressure from high vacuum up to 400 μbar.

Reflection High Energy Electron Diffraction allows real time monitoring of the pulsed laser deposition thin film growth process. The grazing incidence geometry of this electron diffraction technique allows probing of the surface monolayers of the thin film as it grows. This technique provides information on the growth mode and evolving crystal structure of the surface of the thin film, and allows thickness monitoring of layer-by-layer growth.

Characteristic growth modes that can be discerned from RHEED patterns

- An initially blurry diffraction pattern, with a diffuse background, indicates the formation of an amorphous interface.
- Observation of rings in the diffraction pattern, is indicative of a polycrystalline surface.
- Narrow elongated stripes are characteristic of two-dimensional growth, known as the Franc-Van der Merwe mode.
- Elongated dots are observed for tri-dimensional growth, known as the Volmer-Weber growth mode.

- A diffraction pattern that initially exhibits a stripey diffraction pattern and then changes to a spotty pattern after a critical thickness, indicates that the growth mode has transitioned from two-dimensional to three-dimensional, and this is known as the Stranski-Krastanov mode.

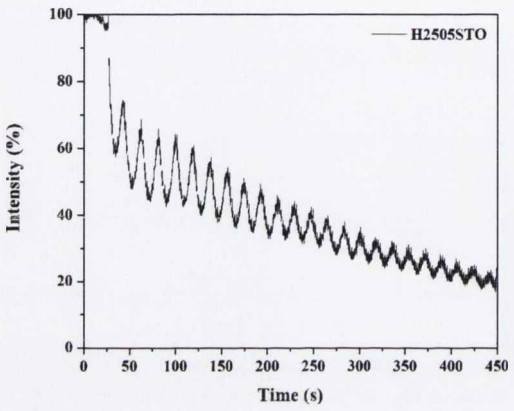

Figure B.1: In situ RHEED analysis of epitaxial layer-by-layer growth, indicated by the oscillations, of an $SrTiO_3$ thin film on an STO substrate during deposition by PLD

B.1.2 Langmuir Probe

Most *in situ* characterisation tools are focused on the properties of the deposited material. The PLD system used in this study was equipped with a Langmuir probe allowing analysis of the plasma of ablated material. The Langmuir probe consists of a conductor with a collecting area introduced into the plasma and biased with respect to a defined ground. The acquisition of the signal from the ions in the plasma is measured with respect to the triggered laser pulse. In general, analysis of Langmuir probe data is complex, however since the measured current is proportional to the density of ions in the plasma, it can be used to monitor the flux of material. Typical curve obtained for a $CuCrO_2$ target are presented on fig. B.3 for various O_2 background pressure.

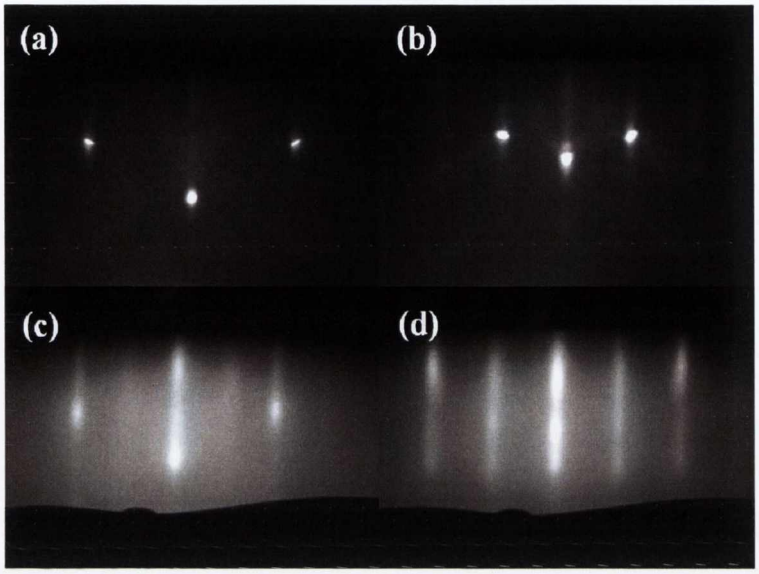

Figure B.2: In situ RHEED diffraction patterns of (a) the (100) reflection of the STO substrate before deposition, (b) the (110) direction of the STO substrate before deposition, (c) the (100) reflection of the $SrTiO_2$ thin film after deposition, and (d) the (110) reflection of the $SrTiO_2$ film after deposition

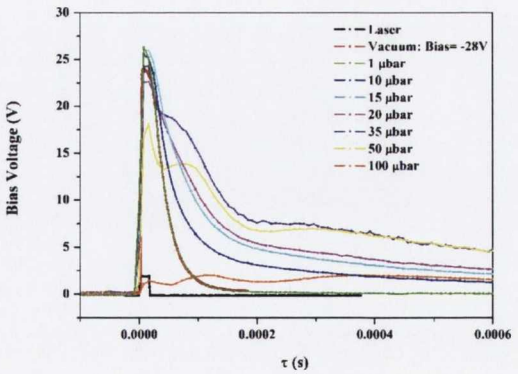

Figure B.3: Langmuir probe signals of ablated species used for optimisation of oxygen partial pressure conditions for $CuCrO_2$ thin film growth.

B.2 X-Ray Scattering

B.2.1 X-Ray Diffraction

A technique for examining the structure of a solid must be capable of probing to the levels of interatomic distances in the solid which are typically of the order of an angstrom. For an electromagnetic probe, it is necessary to operate at wavelengths, λ, of this order or less. The required energy scales are thus computed,

$$\hbar\omega = \frac{hc}{\lambda} = \frac{hc}{10^{-10}} \approx 12.3 \times 10^3 eV$$

Energies of the order of keVs are characteristic of x-rays. X-Ray diffraction is therefore a suitable, versatile and widely used technique for structure analysis in solids.

A Panalytical X'Pert Pro MPD (Multiple Purpose Diffractometer) was used for all of the x-ray reflectivity and diffraction analysis in this study. This system is configured in the Bragg-Brentano para-focussing $\theta - \theta$ geometry for a flat sample. The x-ray source is a conventional sealed tube with a Cu anode ($Cu\ k_\alpha\ \lambda = 1.54056$ Å), in line focus. The sample stage was capable of x, y and z adjustment, ψ tilt and ϕ rotation. A schematic representing the different angles involved in the measurement is presented on fig. B.4.

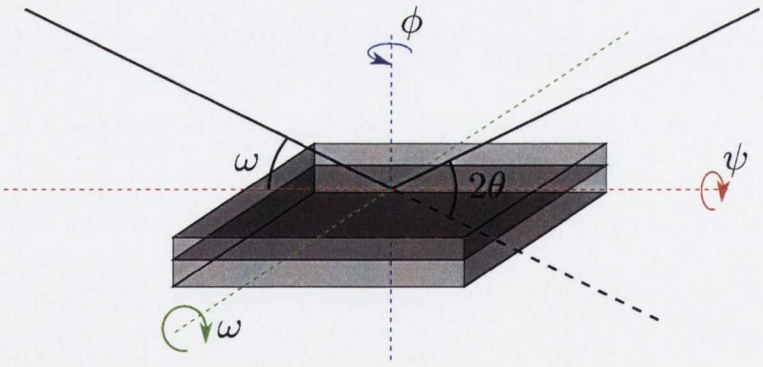

Figure B.4: Schematic showing the different azimuthal angles for an Eulerian cradle XRD sample stage.

The X'Celerator, a multistrip detector, was used for improved statistics on phase analysis scans, while the PRS/PASS detector, a gas detector, with increased instrumental resolution but slower acquisition was used for x-ray reflectivity, rocking curves, reciprocal space maps and pole figures.

B.2.2 Powder x-ray diffraction

Powders were sprinkled on a glass slide and placed in the centre of the sample stage. The height was adjusted to the required position and a suitable size beam mask was selected to expose only the sample to the x-ray beam. The data were collected using the X'Celerator detector.

B.2.3 Thin films x-ray analysis

The structural characterisation of thin films was performed on the same x-ray diffractometer described above. Although, for powder diffraction, the sample presents random crystallite orientations, the thin films, when prepared in optimal conditions, can present a strong orientation in a particular direction. It is therefore important to align the sample in the flat configuration. Depending on the information required on the sample, several types of measurement can be performed. The phase analysis is performed with a measurement similar to that used for powder measurement ($\theta - 2\theta$ scan) with the X'Celerator detector. In this measurement the intensity of the substrate peaks are intense, and the $Cu\ K_\beta$ (and the $W\ L_\alpha$ with ageing of the tube) wavelength contributes significantly to the diagram, therefore a Ni filter is introduced between the x-ray source and the sample. This produce a sharp cut-off at the absorption edge of the Ni as presented on fig.B.5.

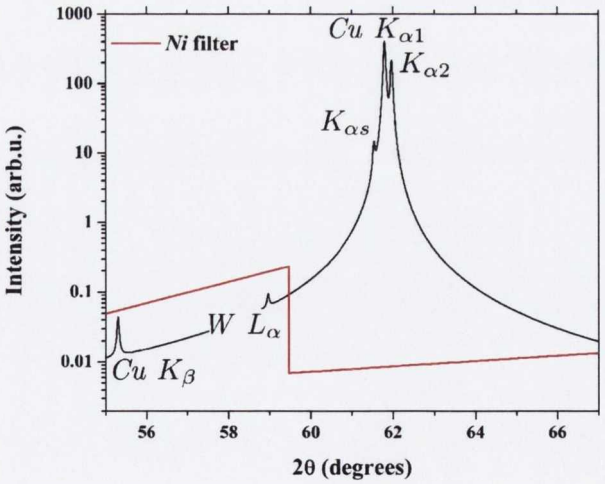

Figure B.5: Illustration of the effect of a Ni filter on the shape of the x-ray data.

It was already shown in the case of a symmetric $\theta - 2\theta$ scan that the scattering vector $\boldsymbol{Q}$ has

only a nonzero component in the direction of the substrate normal (that may be denoted by Q_z in the sample reference frame). During a rocking curve scan, however, there is also a nonvanishing in-plane component Q_x for all angular positions ω except for the one point where $\omega = 2\theta/2$ holds. We can visualise the different scanning techniques in the plane of momentum transfer by the in-plane component Q_x and the out-of-plane component Q_z of the scattering vector. We are interested in such a representation because the Von Laue equation that determines the condition for a diffraction peak to occur can be visualised in $\boldsymbol{Q}$ space in a simple and instructive form. The relation between the instrumental coordinates ω and 2θ and the more convenient Q_x and Q_z are:

$$Q_x = \frac{2}{\lambda}(\cos(\theta - \omega) - \cos(\theta + \omega)) \tag{B.1}$$

$$Q_y = \frac{2}{\lambda}(\sin(\theta - \omega) - \sin(\theta + \omega)) \tag{B.2}$$

When the film shows a good degree of orientation, other crystallographic directions can be studied by performing asymmetric scans ($\omega \neq 2\theta$) or in-plane measurement where the sample is tilted by an angle ψ from the flat position. In this case an Eulerian cradle sample stage is used. The texture of the sample can also be studied in this geometry by performing ϕ scans where the sample is rotated around the axis normal to the sample. The advantage of the $\boldsymbol{Q}$ representation is fully realised when this plot is combined with a reciprocal space map of the sample.

B.2.3.1 Reciprocal space mapping

The combined representation of the different scanning techniques and the $\boldsymbol{Q}$ representation of the lattice are shown on fig. B.6

Reciprocal space mapping is performed such that the Bragg reflection under investigation is fully mapped in a confined area in bmQ space. This means that the reflection is not only monitored by one rocking curve crossing it, but the whole area in the vicinity of the reflection is included in the measurement.

B.2.3.2 Pole figure

Another experiment giving information on the orientational nature of the samples is a pole figure. The diffractometer is set to the Bragg peak position $\theta/2\theta$ under consideration. The measurement begins at the center (ψ, ϕ) = (0, 0) of the stereographic projection and subsequently changes to increasing tilt angles ψ_i, for each of which the azimuth is varied (phi_i,ψ_i) and the peak intensity is measured. The course of the measurement of a pole figure as seen from the sample reference frame is shown schematically in fig.B.7.

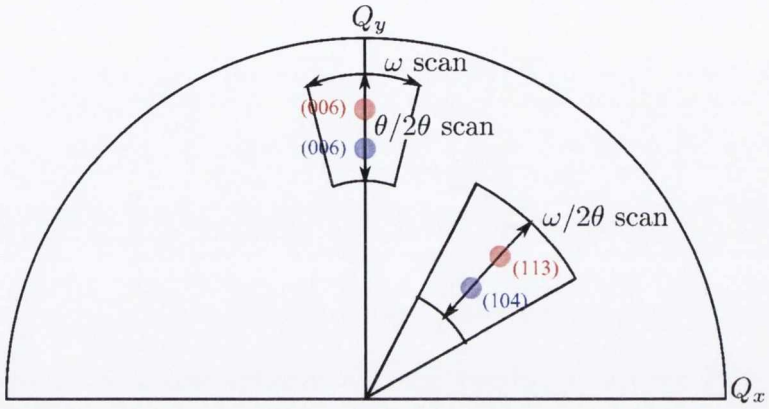

Figure B.6: Combined plot of (Qx, Qz) plane and net of position of Bragg peaks for a $CuCrO_2$ film on a c-cut sapphire.

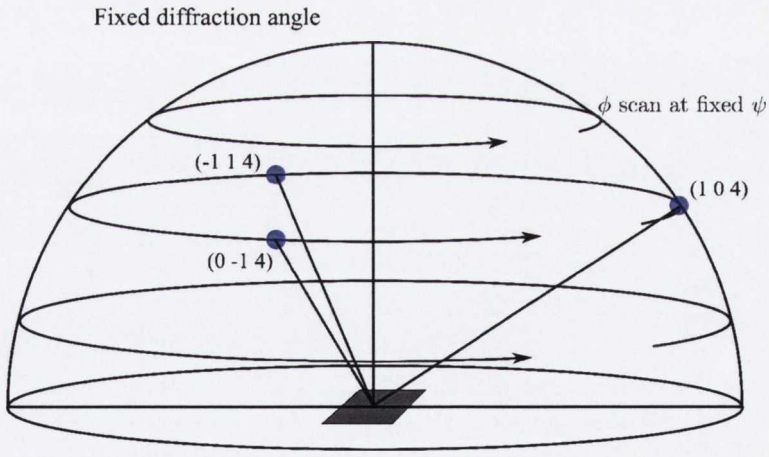

Figure B.7: Schematic of a the scattering vector course during a pole figure. The blue point are the node of the <104> for $CuCrO_2$.

B.2.3.3 x-ray reflectivity

X-Ray reflection from the surface of either a crystalline or an amorphous material occurs when the x-ray beam is incident on the sample surface at a glancing angle. The real part of the complex refractive index, n, is marginally less than one for typical x-ray wavelengths,

$$n = 1 - \delta - i\beta$$

where δ is the decrement in the refractive index due to scattering, and β is the absorption index, and this gives rise to total external reflection at the sample surface when the angle of incidence is close to the critical angle $\theta_c \approx cos^{-1}(1-\delta)$ Gibaud & Hazra (2000). This effect is widely employed in studying the structure of thin films and multilayers. In particular, grazing incidence x-ray specular reflectivity can divulge the film thickness to a high degree of accuracy, while also providing information on the average surface and interface roughness.

An x-ray beam travelling through a thin film is diffracted in such a way that the intensity of the diffracted x-ray beam in a certain direction is proportional to the square of the structure factor, $F_g(k)$. The structure factor is then proportional to the Fourier coefficient of the electron density ρ, where

$$\rho(\mathbf{r}) = \sum_g \rho_g exp(-i\mathbf{g}\cdot\mathbf{r})$$

and $\mathbf{g}$ is the reciprocal space vector. In x-ray reflectivity $\mathbf{g} = 0$, and the intensity of the reflected x-rays is therefore related to the average electron density.

Interfacial specular reflectivity An x-ray beam incident on the interface between two materials, the initial medium identified as 1 and the latter medium identified as 2, with corresponding refractive indices n_1 and n_2 will be partially reflected. The intensity, I, of the reflected x-ray beam can be expressed as follows

$$I = I_0 exp\left(-\frac{4\pi\mu d}{k_{z,1}\lambda}\right)\left|rexp\left(-2k_{z,1}^2\sigma^2\right)\right|^2 \tag{B.3}$$

where the first exponential term describes the absorption of x-rays, of wavelength λ in vacuum, travelling a distance d through the initial medium, with a linear absorption coefficient μ before hitting the interface, and the second exponential term describes the declining reflectivity due to interfacial roughness, σ [1]. The component of the wave vector perpendicular to the interface is $k_{z,j}$ where j identifies the medium, and

$$k_{z,j} = \frac{2\pi}{\lambda} n_j sin\theta_j \tag{B.4}$$

[1] σ is the r.m.s. interfacial roughness

The Fresnel reflection coefficient, r, describes the reflectivity of a smooth interface in terms of the incident angle, θ_i, and the transmitted angle, θ_t,

$$r = \frac{n_1 sin\theta_i - n_2 sin\theta_t}{n_1 sin\theta_i + n_2 sin\theta_t} = \frac{k_{z,1} - k_{z,2}}{k_{z,1} + k_{z,2}} \tag{B.5}$$

The angle of incidence of the x-ray beam is related to the angle of transmission via Snell's law,

$$n_1 cos\theta_i = n_2 cos\theta_t \tag{B.6}$$

Thin film specular reflectivity X-Ray reflectivity measurements are performed using 2θ-ω scans, where the total specular reflectivity intensity is recorded as a function of the angle of incidence of the x-ray beam ($\omega \approx \theta$). When the angle at grazing incidence exceeds the critical angle of the material, the intensity decreases rapidly with increasing angle. For angles of incidence lower than the critical angle, $\theta_c \approx cos^{-1} n_2$, however, the x-rays are totally reflected.

With the addition of a thin film, a second interface is introduced, and the intensity of the reflected x-rays can be described by the coherent superposition of the x-ray beams reflected from the individual interfaces. The resultant fringes observed in the reflected x-ray intensity are characteristic of the interference of these reflected x-rays.

A matrix method can be used to calculate the reflectivity of planar multilayers, allowing for multiple x-ray reflections in the layered material. The transfer matrix can relate the magnitude and phase of the electric field [1] in air with that in the medium, j, as follows

$$\begin{bmatrix} U(+k_{z,0}, z=0) \\ U(-k_{z,0}, z=0) \end{bmatrix} = \begin{bmatrix} M_{11} & M_{12} \\ M_{21} & M_{22} \end{bmatrix} \cdot \begin{bmatrix} U(+k_{z,j}, z=D_j) \\ U(-k_{z,j}, z=D_j) \end{bmatrix} \tag{B.7}$$

where $z = 0$ corresponds to the surface (air/thin film) interface, and $z = D_j$ corresponds to the interlayer (thin film/substrate) interface at a depth D_j.

$$U(+k_{z,j}, z=D_j) = A_j^+ exp[+ik_{z,j}] \tag{B.8}$$

$$U(-k_{z,j}, z=D_j) = A_j^- exp[-ik_{z,j}] \tag{B.9}$$

where A_j^+ and A_j^- are the amplitudes of the waves travelling through layer j.

The reflection coefficient, r, at the surface of a material is the ratio of the reflected and incident electric fields, and can be obtained from the transfer matrix

$$r = \frac{M_{12}}{M_{22}} \tag{B.10}$$

[1] The + sign refers to the electric field component travelling in the upward direction through the media, while the − sign corresponds to a downward electric field

Similarly, the transmission coefficient is the ratio of the transmitted and incident electric fields and can be obtained as follows

$$t = \frac{1}{M_{22}} \tag{B.11}$$

A single thin film layer grown on a substrate presents two interfaces, and the transfer matrix, in such a case, can be determined from the refraction, R, and transmission, T, matrices in accordance with the relation

$$M = R_{air-film} T_{film} R_{film-substrate} \tag{B.12}$$

where

$$R_{j,j+1} = \frac{1}{t^*_{j,j+1}} \begin{bmatrix} 1 & r^*_{j,j+1} \\ r^*_{j,j+1} & 1 \end{bmatrix} \tag{B.13}$$

and

$$T_j = \begin{bmatrix} f_j^- & 0 \\ 0 & f_j^+ \end{bmatrix} \tag{B.14}$$

The Fresnel reflection and transmission coefficients at the interface, between media j and $j+1$, are corrected for interfacial roughness with an exponential factor as follows

$$r^*_{j,j+1} = r_{j,j+1} exp\left(-2k_{z,j}k_{z,j+1}\sigma^2_{j+1}\right) \tag{B.15}$$

$$t^*_{j,j+1} = t_{j,j+1} exp\left(\frac{(k_{z,j} - k_{z,j+1})^2 \sigma^2_{j+1}}{2}\right) \tag{B.16}$$

and the Fresnel transmission coefficient can be expressed

$$t_{j,j+1} = \frac{2n_j sin\theta_j}{n_j sin\theta_j + n_{j+1} sin\theta_{j+1}} = \frac{2k_{z,j}}{k_{z,j} + k_{z,j+1}} \tag{B.17}$$

The terms of the transmission matrix, $f_j^{\pm}$, are composed of the product of two exponential factors

$$f_j^{\pm} = exp\left(-\frac{\pi\mu_j}{k_{z,j}\lambda} d_j\right) exp\left(\pm i k_{z,j} d_j\right) \tag{B.18}$$

where the first factor is due to x-ray absorption in layer j, with thickness d_j and linear absorption coefficient μ_j, and the second exponential term is a phase factor of the reflected x-rays at the interface between layers $j-1$ and j.

A multilayered structure can equally be described by the transfer matrix, superimposing the contributions from each interface as follows

$$M = R_{air,layer1} T_{layer1} R_{layer1,layer2} T_{layer2} ... R_{layerN,substrate} \tag{B.19}$$

Numerical calculations are necessary to account for the multiple x-ray reflections that occur at the interfaces of a multilayered thin film. Neglecting these multiple reflections, however, the

reflected wave can be approximated by the superposition of x-rays reflected only once at each interface of the layered structure.

$$\begin{aligned} r = r^*_{0,1} + t^*_{0,1} exp\left(-\tfrac{2\pi\mu_1}{k_{z,1}\lambda} d_1\right) \left(r^*_{1,2} exp\left(i2k_{z,1}d_1\right)\right) \\ + \prod_{k=1}^{j} t^*_{k-1,k} exp\left(-\frac{2\pi\mu_k}{k_{z,k}\lambda} d_k\right) \left(r^*_{j,j+1} exp\left(i\sum_{k=1}^{j} 2k_{z,k}d_k\right)\right) + ... \end{aligned} \tag{B.20}$$

Assuming that the x-ray absorption in extremely thin layers is negligible, this expression can be further simplified to

$$r = r^*_{0,1} + r^*_{1,2} exp\left(iQ_{z,1}d_1\right) + ... + r^*_{j,j+1} exp\left(i\sum_{k=1}^{j} Q_{z,k}d_k\right) + ... \tag{B.21}$$

The wave vector transfer, $Q_{z,j} = 2k_{z,j}$, in medium j can be related to the wave vector transfer in vacuum,

$$Q_z = 2k_{z,layer1} = \frac{4\pi}{\lambda} sin\theta_i \tag{B.22}$$

and the critical angle, $\theta_{c,j}$, as follows

$$Q_{z,j} = \sqrt{Q_z^2 - Q_{c,j}^2} \tag{B.23}$$

where

$$Q_{c,j} = \frac{4\pi}{\lambda} sin\theta_{c,j} \tag{B.24}$$

In a further approximation, the refraction can also be neglected in the exponential absorption and phase terms, assuming $Q_{z,j} \approx Q_z$, and the reflectivity reduces to

$$r = \sum_{j=0}^{N} r^*_{j,j+1} exp\left(iq_z D_j\right) \tag{B.25}$$

This relation reproduces the measured interference fringes tolerably well with a slight shift with respect to the experimental data. The deviation is most noticeable in the region just after the critical angle.

The reflection coefficient, r, can be approximated as the Fourier transform of the corrected Fresnel coefficient, $r^*(D)$, which depends upon the interface depth, D. This allows the intensity of the reflected x-rays to be expressed as

$$I(Q_z) \approx I_0 \left|\tilde{r}^*(D)\right|^2 \tag{B.26}$$

Under the same approximation as above, $Q_{z,j} \approx q_z$, the corrected Fresnel reflection coefficient can be written

$$r^*(D) \approx \Phi(Q_z)\rho'(D) \tag{B.27}$$

where $\Phi(Q_z)$ is a continuous function of Q_z, and $\rho'(D)$ is the derivative of the electron density [1].

The intensity can thus be written

$$\frac{I(Q_z)}{I_0\Psi(Q_z)} \approx \left|\tilde{\rho}'(D)\right|^2 \tag{B.28}$$

where $Psi(Q_z)$ is a continuous function of Q_z. The reflectivity fringes are therefore related to the amplitude of the Fourier transform of the derivative of the electron density, $\tilde{\rho}'(D)$. In this way, Fourier transform methods can be used to determine the thickness of the layers from x-ray reflectivity measurements as a function of grazing incidence angle.

B.2.3.4 Useful crystallographic relations

Rhombohedral to hexagonal setting Although the primitive cell of the $3R$ $CuCrO_2$ is rhombohedral, an hexagonal setting was used throughout the main text of this thesis since it convenient to describe the crystal structure in this way. The relation between the rhombohedral and the hexagonal cells is presented on fig.B.8.

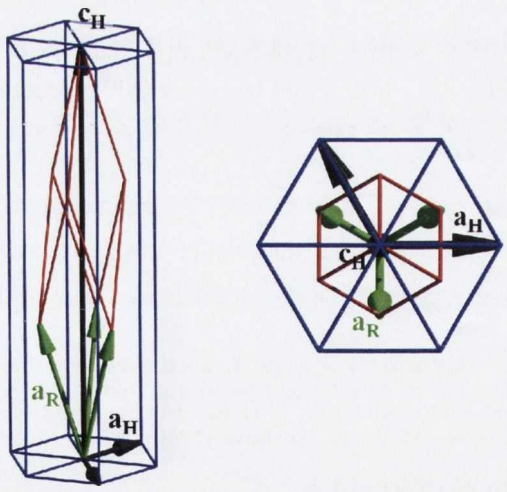

Figure B.8: Schematic of the rhombohedral and hexagonal unit cell in delafossite ABO_2 for the $3R$ polytype, $R\bar{3}m$ space group symmetry.

[1] ρ' is zero between the interfaces, but has a peak at each interface

Miller to Miller-Bravais indices The indexing of the planes and directions for an hexagonal system can be done using two conventions: the classical notation for cubic system using the three Miller indices or the four Miller-Bravais indices. The advantage of the latter being to represent more clearly the hexagonal symmetry in the basal plane and ascribe similar indices to similar planes. It is possible to convert from one notation to the other using the following relations:

$$(hkil) = (hkl) \tag{B.29}$$

$$(hkl) = (hk(-h-k)l) \tag{B.30}$$

$$= [(u-t)(v-t)w] \tag{B.31}$$

$$= [(2u-v)(2v-u)(-u-v)3w] \tag{B.32}$$

Interplanar angles between two planes The angle ψ between the plane $(h_1k_1l_1)$, of spacing d_1, and the plane $(h_2k_2l_2)$ of spacing d_2, can be calculated from the following equations. V is the volume of the unit cell.

$$\frac{1}{d^2} = \frac{1}{V^2}(S_{11}h^2 + S_{22}k^2 + S_{33}l^2 + 2S_{12}hk + 2S_{23}kl + 2S_{13}hl) \tag{B.33}$$

$$S_{11} = b^2c^2\sin^2(\alpha) \tag{B.34}$$

$$S_{22} = a^2c^2\sin^2(\beta) \tag{B.35}$$

$$S_{33} = a^2b^2\sin^2(\gamma) \tag{B.36}$$

$$S_{12} = abc^2(\cos(\alpha)\cos(\beta) - \cos(\gamma)) \tag{B.37}$$

$$S_{23} = a^2bc(\cos(\beta)\cos(\gamma) - \cos(\alpha)) \tag{B.38}$$

$$S_{13} = ab^2c(\cos(\gamma)\cos(\alpha) - \cos(\beta)) \tag{B.39}$$

$$V = abc\sqrt{1 - \cos^2(\alpha) - \cos^2(\beta) - \cos^2(\gamma) + 2\cos(\alpha)\cos(\beta)\cos(\gamma)} \tag{B.40}$$

$$\cos(\psi) = \frac{d_1d_2}{V^2}[S_{11}h_1h_2 + S_{22}k_1k_2 + S_{33}l_1l_2 + S_{23}(k_1l_2 + k_2l_1) + S_{13}(l_1h_2 + l_2h_1) + S_{12}(h_1k_2 + h_2k_1)] \tag{B.41}$$

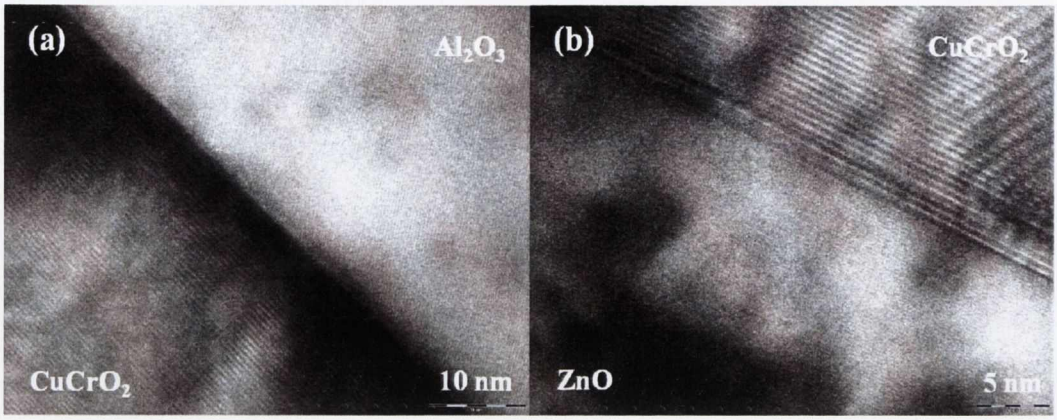

Figure B.9: TEM images of (a) $Mg{:}CuCrO_2$ thin film and c-cut Al_2O_3 substrate and (b) $Al{:}ZnO$ thin film and $Mg{:}CuCrO_2$ thin film layers in a device structure.

B.3 TEM

TEM was measured on several unmasked trilayer structure in the IPCMS together with Dr. S. Colis and Dr. C. Ulahq-Bouillet. The images were collected on a Topcon 002B operating at 200 kV with a point to point resolution of 1.8 Å.

Data analysis was done using the freeware ImageJ, and the simulated SAED were generated using the software JEMS.

B.4 AFM

AFM measurements were carried out in the IPCMS by Dr. S. Colis on a AFM Nanoscope Dimension 3100 in tapping mode.

B.5 Optical spectrometry

The optical transmission through the samples were measured using a UV-visible spectrophotemeter Perkin Elmer Lambda 950. The data were collected relative to a blank sapphire substrate baseline, in the wavelength range 1100 to 200 nm, however, data recorded above 900 nm were discounted since the data became to noisy to measure this far into the infrared energy range using this equipment. A bump appears in the data at approximately 355 and 855 nm wavelength, this is due to the switching over to the UV lamp for higher energy measurement.

The back of the films were polished prior to measurement due to the contamination from the stainless steel sample holder as mentioned previously. The data before and after polishing are presented on fig.B.10. This could introduce differences in the absolute value of the transmittance from film to film.

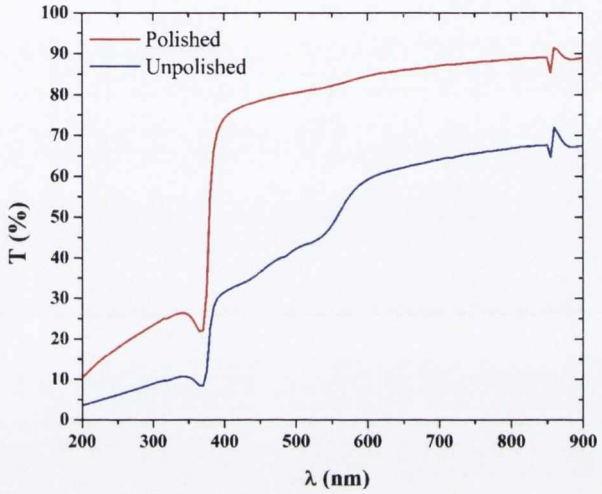

Figure B.10: UV-visible transmission of a ZnO thin films before (blue curve) and after polishing (red curve) of the backside of the sample.

B.6 Spectroscopy

XPS spectra were collected on an Omicron system, the samples were cleaned *in situ* by Ar cleaning for 30 mins. During the collection of the data a charge neutraliser was used to avoid charging effects.

B.7 Magnetometry

Magnetic measurements were performed by applying a DC magnetic field using SQUID magnetometer (Quantum Design Magnetic Measurement System MPMS XL). The measurement of the polycrystalline samples have been carried out with Dr. M. Venkatesan. A known quantity of powder was packed into a gelatine capsule which was inserted into a plastic straw. This mounting

method introduces a diagmagnetic background, however this only becomes relevant for measurement of magnetic moments of less than 10^{-6} Am^2.

The magnetic susceptibility measurements were carried out in an applied DC magnetic field of 0.5 T or 0.1 T, as indicated in the text. The temperature was varied between 1.8 and 300 K. The signal was measured with an RSO option and auto-tracking mode was enabled to avoid inaccurate measurement due to thermal displacement.

B.8 Electrical and magneto-transport measurements

All of the electrical property measurements were realised in a Quantum Design Physical Properties Measurement System (PPMS) equipped with a 14 T superconducting solenoid. The system is capable of accessing temperatures in the range 2 – 300 K.

High Impedance Set-up A cryogenic probe is equipped with two low loss stainless steel flexible triaxial lines, a guarded sample mount allows for rotation of the field axis at angles up to 30^o. The electrical measurements were performed using a set of two sub-femtoampére source meters (Keithley 6430) with remote preamplifiers sitting on top of the cryogenic head. The total length of triaxial line (per circuit) was of the order of 1.5 m. Leakage currents of the complete assembly, at biases up to 210 V, do not exceed 5 pA. A schematic of this high-impedance set-up configuration is shown on fig. B.11

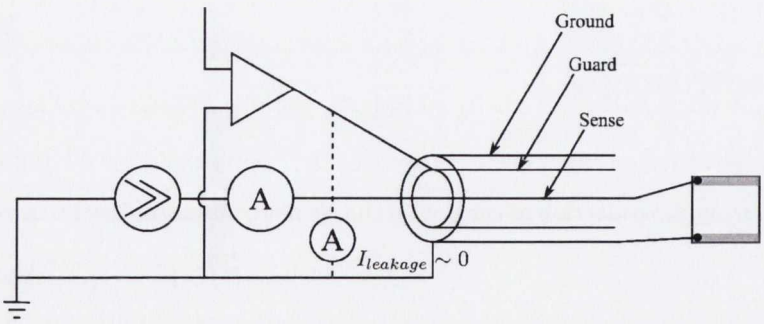

Figure B.11: High-impedance set-up configuration showing the low-loss stainless steel triaxial line and the principle of operation of the sub-femtoampére Keithley 6430 source meter.

Van der Pauw configuration The simplest way to measure the resistivity and Hall effect of a certain material is to cut a bar-shaped sample, and to make separate current contacts on the short edges and voltage contacts on the surface. The use of four terminals ensures that the measured voltage does not include the voltage drop due to the current contacts. The downfalls of this method are the difficulty of cutting samples in a bar shaped and the strong dependence of the resistance depending on the crystallographic direction of the current flow. To overcome this difficulty Van der Pauw proposed a method to measured resistivity and Hall effect on samples with arbitrary shape van der Pauw (1958). He stipulated several requirement for the measurement to be correct :

- The contacts are on the edge of the sample. Actually, if the thickness of the sample is not negligible, the contacts should have the shape of very thin vertical lines across the whole thickness. This requirement is due to the fact that, in the original paper as well as in all the later developments, the thickness d is a merely multiplicative factor and the equipotential surfaces in the sample are taken to be cylindrical (while, if the contacts are point-like and the thickness is not negligible, they rather assume a spherical shape).
- The contacts are sufficiently small. In principle, they should be point-like (in a very thin sample) or have a negligible section (in thicker samples).
- The sample is homogeneous in thickness. Again, this is necessary to ensure that the 3d geometry can be reduced to a flat geometry by simply dividing by the thickness d - that is, equipotential surfaces are cylindrical.
- The surface of the sample is simply connected, i.e., the sample does not have isolated holes.

Some of these requirements, which are needed to carry out calculations, are difficult to fulfill experimentally. Therefore, the effects on the measured resistivity of the finite size of the contacts and of their erroneous placement (away from the samples edge) were calculated in the case of samples with different shape Koon (1989). A detailed procedure to measure resistivity and Hall effect in thin films can be found Thurber (2008).

Appendix C

Magnetic Exchange Interactions in Ionic Compounds

C.1 Exchange interactions in ionic compounds

Long range magnetic order in materials is governed by the interatomic exchange interactions that take place between local magnetic moments on the atoms. Correlations between two electrons localised on two distinct neighbouring atoms are affected by their relative spin configurations. An energy difference arises between the parallel and antiparallel alignment of the neighbouring spins on sites i and j, this energy difference is represented by the effective exchange constant J_{ij}. Magnetic insulators, where localised moments are responsible for the magnetic interactions, subject to an external field, B, can be described by the following Hamiltonian

$$\mathcal{H} = -2\sum_{i>j} J_{ij}(aS_i^z S_j^z + b(S_i^x S_j^x + S_i^y S_j^y)) - g\mu_B H \cdot \sum_i S_i$$

which is generalised to include exchange interactions between all neighbouring atoms, i and j. When J is positive, the antiparallel alignment of the electronic spins dominates the ground state spin structure. Conversely, when J is negative, the parallel spin configuration is sustained.

Two electrons localised on the same atom will tend to have a positive exchange constant since separation between the electrons is encouraged by the Coulomb repulsion, and an antisymmetric spatial wavefunction with a symmetric spin state, also known as the triplet state, serves to minimise the Coulomb energy. When two electrons are localised on neighbouring atoms, however, it

is possible for the system to minimise its kinetic energy by bonding to minimise the kinetic energy of the system, since the electrons will no longer be constrained to just one atomic orbital, but can circulate about in molecular orbitals. The molecular orbitals are split into bonding and antibonding orbitals, where the bonding orbitals are spatially symmetric and cost less energy, while the antibonding orbitals are spatially antisymmetric, and require higher energy. Thus, the symmetric spatial wavefunction with an antisymmetric spin state is energetically favoured and it is characterised by a negative exchange constant. This situation arises with the superexchange interaction which will be dealt with more thoroughly later in this section. In general, the exchange in a system depends upon the competing kinetic and Coulomb energies between the electrons located on the neighbouring ions.

There are typically three exchange interaction mechanisms encountered by ionic or semi-covalent compounds, the magnetic cation–cation direct exchange, and the cation-anion-cation superexchange and double exchange regimes. These exchange mechanisms and their relevance to magnetic oxides will be discussed in subsequent passages. The above spin Hamiltonian can be used to represent three distinct magnetic models. The Ising model is obtained when $a = 1$ and $b = 0$, the XY-model emerges when $a = 0$ and $b = 1$, and the isotropic Heisenberg model appears when $a = b$. Under the Ising model, the spin structure is restricted to collinear orientations, the XY-model is limited to coplanar spin alignment, and the Heisenberg model can be used to describe configurations with out-of-plane spin orientations.

C.1.1 Direct Exchange

Electrons localised on two neighbouring magnetic cations, where there is direct overlap of the wave functions, can engage in direct exchange. This cation-cation interaction can be considered in terms of combining the symmetric and antisymmetric spatial states of the electronic orbitals, $|\phi_i\rangle$ and $|\phi_j\rangle$, on each ion with the antisymmetric and symmetric spin states, χ_S and χ_T, to form an overall antisymmetric joint wave function $|\psi\rangle$ in accord with the Pauli exclusion principle

$$\psi(\mathbf{r}_1, \mathbf{r}_2) = \frac{1}{\sqrt{2}} \left[\phi_i(\mathbf{r}_1)\phi_j(\mathbf{r}_2) \pm \phi_i(\mathbf{r}_2)\phi_j(\mathbf{r}_1)\right] \chi_{S,T}$$

such that

$$\psi(\mathbf{r}_1, \mathbf{r}_2) = -\psi(\mathbf{r}_2, \mathbf{r}_1)$$

The direct exchange interaction depends upon the Coulomb repulsion between the neighbouring electrons

$$\frac{e^2}{4\pi\epsilon_0|\mathbf{r}_1 - \mathbf{r}_2|}$$

where J represents the exchange integral between the orbitals of the two electrons. Electrons on neighbouring magnetic atoms that interact through such an exchange interaction, without requiring an intermediate ion, demonstrate the direct exchange mechanism. This scheme, however, requires sufficient direct overlap of the magnetic orbitals which is rarely the case. In an ionic crystal, in order for the electrons to be localised on the magnetic cations, the latter must be separated by a nonmagnetic anion. The direct exchange becomes essentially zero since the exchange constant varies as an inverse function of $|\mathbf{r}_1 - \mathbf{r}_2|$. Indirect exchange interactions arise more frequently in magnetic materials, and will be discussed in relation to magnetic oxide compounds in the following passages.

C.1.2 Superexchange

Antiferromagnetic and ferrimagnetic ordering are common in transition metal oxides, and the exchange interactions they engage in are generally the superexchange and double exchange (ferromagnetic) mechanisms. Kramers was the first to recognise that the exchange interactions in these ionic systems are indirect interactions between local magnetic moments, where there is no direct overlap of the magnetic $3d$ orbitals since their separation is too great, but where the nonmagnetic anion between the magnetic ions mediates the interaction Kramers (1934). In oxides the two outermost $2p$ electron orbitals of the O^{2-} anion overlap with the d wave functions of the magnetic cations, a virtual hopping process can create an intermediate pair state with one site empty and the other site doubly occupied, the Pauli principle allows this if the spins are antiparallel and the effective hybridising of these wave functions acts to create virtual excited states, equivalent to conduction electrons, so that the p and d electrons are effectively delocalised over the molecule. The interatomic hopping depends critically on the relative spin orientations of the two d electrons, and antiferromagnetic ordering of the spins reduces the kinetic energy of the system, by allowing the electrons to become delocalised over the entire structure. In this way, the hopping can be seen to favour antiferromagnetic exchange. According to second-order perturbation theory Anderson (1959), the superexchange interaction is given by

$$J \propto -\frac{t^2}{U}$$

where t is the hopping integral for the virtual transition, which is proportional to the CB bandwidth under a tight-binding model, and U is the Coulomb energy. The degree of overlap of the orbitals, and therefore the strength of the superexchange interaction, is sensitive to the cation-anion-cation $(M_1 - O - M_2)$ bond angle according to the Goodenough-Kanamori rules Goodenough (1963)

Kanamori (1959), varying as $cos^2\theta_{12}$. In general, the rules state that the exchange will be antiferromagnetic unless the orbital overlap cancels due to symmetry, as in fig. C.1 (a), in which case a direct exchange interaction will give rise to ferromagnetic ordering.

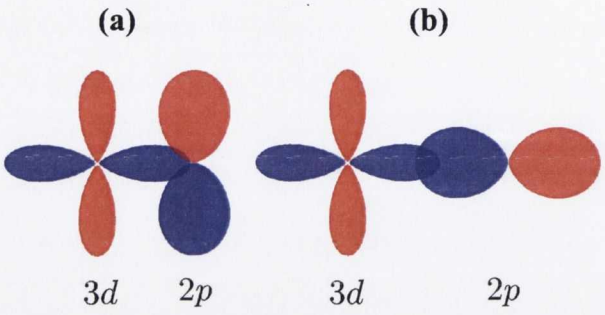

Figure C.1: Goodenough-Kanamori rules of superexchange

The types of d orbitals (e_g or t_{2g}) and the number of participating d electrons also strongly influence the superexchange interaction. Since this exchange mechanism involves overlap between orbitals centred on neighbouring ions, the interaction operates over short distances only.

C.1.3 Dzyaloshinsky-Moriya Exchange

Another similar exchange interaction of interest that participates in magnetic exchange in insulators is the antisymmetric Dzyaloshinsky-Moriya exchange interaction Sergienko & Dagotto (2006). For this interaction no mediating anion is required, spin-orbit coupling on the d electrons of one of the magnetic ions provides the necessary excited state, before an exchange interaction takes place between the excited state and the ground state of the neighbouring magnetic ion. This anisotropic Dzyaloshinsky-Moriya exchange interaction between the spins $\mathbf{S}_1$ and $\mathbf{S}_2$ can be represented in the Hamiltonian by the term

$$\mathcal{H}_{DM} = \mathbf{D} \cdot \mathbf{S}_1 \times \mathbf{S}_2$$

The vector $\mathbf{D}$ becomes zero for spins on equivalent sites. When $\mathbf{D}$ is nonzero, it lies either parallel or perpendicular to a line joining the two spins, depending on the inversion symmetry of the crystal field. This mechanism encourages the spins $\mathbf{S}_1$ and $\mathbf{S}_2$ to be mutually orthogonal and to lie in a plane perpendicular to $\mathbf{D}$ such that a negative exchange energy is achieved. This interaction favours antiferromagnetic exchange, however it often results in slight canting of the spins, which can give rise to a weak ferromagnetic contribution in a direction normal to the spin-axis of the antiferromagnet.

C.1.4 Magnetic Anisotropy

The layered magnetic triangular lattice can be described in terms of the following Hamiltonian

$$\mathcal{H} = J \sum_{i,j}^{chains} \mathbf{S}_i \mathbf{S}_j + J' \sum_{k,l}^{planes} \mathbf{S}_k \mathbf{S}_l + D \sum_i (\mathbf{S}_i^z)^2 - g\mu_B \mathbf{H} \sum_i \mathbf{S}_i$$

where $\mathbf{S}$ is a spin of the magnetic ion, J is the exchange integral along the crystal c axis, J' is the perpendicular exchange integral, and D is the anisotropy constant, whose sign determines the relative orientation of the spin plane with respect to the crystal axes Collins & Petrenko (1997). The first term describes the exchange energy along the chain of the crystal, the second term accounts for the exchange energy in the basal plane, and the third and fourth terms represent the single-ion anisotropy energy and the Zeeman energy of the spins in an external magnetic field $\mathbf{H}$, respectively. The Hamiltonian describes a pure Heisenberg system when the anisotropy constant, $D = 0$. In reality, this is never the case and all triangular magnetic materials exhibit nonzero D. If, however, $|D|$ is minor in comparison to both $|J|$ and $|J'|$ the magnetic properties will behave similarly to those of a Heisenberg system, only deviating at very low temperatures, $T < DS^2$, or close to the critical point. For cases when $D > 0$, in the absence of an applied field, the ground state spins will be confined to the xy plane. Conversely, when $D < 0$, the anisotropy energy will be minimised for spins aligned perpendicular to the xy plane. This term will compete with the antiferromagnetic J' exchange term and lead to additional frustration.

C.1.5 Geometric Magnetic Frustration

When the geometry of the crystal lattice prevents the simultaneous minimisation of all the magnetic exchange interactions within the system, it is deemed magnetically frustrated. Such frustrated systems typically have extremely low magnetic ordering temperatures, far below the scale of their exchange interaction energies. A purely frustrated magnetic system will remain in a disordered state right down to very low temperatures rather than adopting a unique magnetic ground state, since the ground state where all the interactions are satisfied at once cannot be achieved with the given crystal geometry. This renders the lowest-energy state degenerate, with a multitude of possible equal energy spin configurations. The magnetic frustration degeneracy can be partially lifted, for example, by the weak interaction effects of single-ion or exchange anisotropy, next-nearest neighbour interactions, lattice distortion, or a magnetic field, which can promote certain spin structures.

C. MAGNETIC EXCHANGE

Typical lattice configurations that are susceptible to geometric frustration are the equilateral triangular lattice antiferromagnet (TLA), the kagome and pyrochlore ($A_2B_2O_7$, A = rare earth, B = transition metal) lattices. In these systems, the antiferromagnetically interacting spins are situated on the vertices of the triangular or tetrahedral networks of magnetic ions that they are comprised of.

A constraint function, F_c, was proposesd to measure the degree of magnetic frustration in a system Lacorre (1987). The function compares the total energy per spin to the base energy per spin in a system as follows

$$F_c = -\frac{E}{E_b} = -\frac{\sum_{k=1}^{n} J_k S_{k1} \cdot S_{k2}}{\sum_{k=1}^{n} |J_k||S_{k1}||S_{k2}|}$$

where the base energy is the sum of the contributions from all the other exchange energies present neglecting the frustration, while the total energy is sum of all the exchange energies of the system including the energy increase due to the frustration. The sum is carried out over all n exchange constants J_k. The extrema are F_c = 1, which corresponds to a fully frustrated scenario, and F_c = -1, which relates to a non-frustrated system. For an equilateral triangular spin lattice with a constant exchange integral, F_c = - 0.5. For a planar triangular system, a constraint angle, θ_c, related to the constraint function, can describe the deviation of the spins from collinearity as follows

$$\theta_c = cos^{-1}(F_c)$$

Considering a triangular spin lattice, with exchange constants J' and J, where J' appears for only one spin site, and J is the exchange constant for the other two spin sites, and both exchange constants are negative since the material is antiferromagnetic. The constraint function $F_c(X)$ where $X = J'/J$ can be used to compute the angle $\alpha = 2\theta_c$ between the magnetic moments coupled by J'. For parallel spin alignment $\alpha = 0^o$, and for antiparallel alignment $\alpha = 180^o$, and all possible spin orientations in between these limiting angles are accessible. The 120^o TLA spin structure occurs when $X = 1$ (or $J' = J$).

References

Agura, H., Suzuki, A., Matsushita, T., Aoki, T. & Okuda, M. (2003). Low resistivity transparent conducting Al-doped ZnO films prepared by pulsed laser deposition. *Thin Solid Films*, **445**, 263. 3, 150

Anderson, P.W. (1959). New approach to the theory of superexchange interactions. *Phys. Rev.*, **115**, 2. 243

Aoki, T., Hatanaka, Y. & Look, D.C. (2000). Zno diode fabricated by excimer-laser doping. *Appl. Phys. Lett.*, **76**, 3257. 177

Arima, T. (2007). Ferroelectricity induced by proper-screw type magnetic order. *J. Phys. Soc. Jpn.*, **76**, 073702. 69

Arnold, T., Payne, D.J., Bourlange, A., Hu, J.P., Egdell, R.G., Piper, L.F.J., Colakerol, L., DeMasi, A., Glans, P.A., Learmonth, T., Smith, K.E., Guo, J., Scanlon, D.O., Walsh, A., Morgan, B.J. & Watson, G.W. (2009). X-ray spectroscopic study of the electronic structure of $CuCrO_2$. *Phys. Rev. B*, **79**, 075102. 40, 55, 60, 110, 111

Ashcroft, N.W. & Mermin, N.D. (1976). *Solid State Physics*. Harcourt College Publishers. 29, 34, 35

Ashmore, N.A. & Cann, D.P. (2005). Electrical and structural characteristics of non-stoichiometric Cu-based delafossites. *J. Mater. Sci.*, **40**, 3891. 72

Ataev, B.M., Bagamadova, A.M., Djabrailov, A.M., Mamedov, V.V. & Rabadanov, R.A. (1995). Highly conductive and transparent Ga-doped epitaxial ZnO films on sapphire by CVD. *Thin Solid Films*, **260**, 19. 154

Attili, R.N., Uhrmacher, M., Lieb, K.P., Ziegeler, L., Mekata, M. & Schwarzmann, E. (1996). Electric-field gradients at ^{111}Cd in delafossite oxides ABO_2 (A = Ag, Cu; B = Al, Cr, Fe, In, Nd, Y). *Phys. Rev. B*, **53**, 600. 54

Baedekar, K. (1907). Uber die elektrische Leitfähigkeit und die thermoelektrische Kraft einiger Schwermetall-Verbindungen. *Ann. Phys., Lpz.*, **22**, 749. 2, 13

Bailar, J.C., Emelus, H.J., Ronald, N. & Trotman-Dickenson, A.F. (1973). *Comprehensive Inorganic Chemistry*. Pergamon, New York. 41

Banerjee, A.N. & Chattopadhyay, K.K. (2005). Recent developments in the emerging field of crystalline *p*-type transparent conducting oxide thin films. *Prog. Cryst. Growth Charact. Mater.*, **50**, 52. 1, 49, 61, 72, 149

Banerjee, A.N., Maity, R., Ghosh, P.K. & Chattopadhyay, K.K. (2005). Thermoelectric properties and electrical characteristics of sputter-deposited *p*-$CuAlO_2$ thin films. *Thin Solid Films*, **474**, 261. 73

Bardeen, J. (1947). Surface states and rectification at a metal semi-conductor contact. *Phys. Rev.*, **71**, 717. 181

Bellingham, J.R., Phillips, W.A. & Adkins, C.J. (1992). Intrinsic performance limits in transparent conducting oxides. *J. Mater. Sci. Lett.*, **11**, 263. 3, 38

Benko, F.A. & Koffyberg, F.P. (1984). Opto-electronic properties of $CuAlO_2$. *J. Phys. Chem. Solids*, **45**, 57. 46, 55, 61, 73, 76

Benko, F.A. & Koffyberg, F.P. (1986). Preparation and opto-electronic properties of semiconducting $CuCrO_2$. *Mat. Res. Bull.*, **21**, 753. 73, 76

Benko, F.A. & Koffyberg, F.P. (1987). Opto-electronic properties of *p*- and *n*-type delafossite, $CuFeO_2$. *J. Phys. Chem. Solids*, **48**, 431. 54, 74, 76

Bian, J.M., Li, X.M., Zhang, C.Y., Chen, L.D. & Yao, Q. (2004). Synthesis and characterization of two-layer-structured ZnO *p*-*n* homojunctions by ultrasonic spray pyrolysis. *Appl. Phys. Lett.*, **84**, 3783. 154

Bloch, F. (1928). Ueber die Quantenmechanik der Elektronen in Kristallgittern. *Z. Phys.*, **52**, 555. 9

Bosman, A.J. & van Daal, H.J. (1970). Small-polaron versus band conduction in some transition-metal oxides. *Adv. Phys.*, **19**, 1. 77, 78

Brooks, H. (1955). *Advances in electronics and electron physics*. Academic Press, New York. 38

Buljan, A., Alemany, P. & Ruiz, E. (1999). Electronic structure and bonding in $CuMO_2$ (M = Al, Ga, Y) delafossite-type oxides: An ab initio study. *J. Phys. Chem. B*, **103**, 8060. 55

Busch, G. (1989). Early history of the physics and chemistry of semiconductors - from doubts to fact in a hundred years. *Eur. J. Phys.*, **10**, 254. 13

Castaneda, L., Morales-Saavedra, O.G., Acosta, D.R., Maldonado, A. & de la Olvera, M. (2006). Structural, morphological, optical, and nonlinear optical properties of fluorine-doped zinc oxide thin films deposited on glass substrates by the chemical spray technique. *Phys. Stat. Sol. (a)*, **203**, 1971. 153

Cava, R.J., Zandbergen, H.W., Ramirez, A.P., Takagi, H., Chen, C.T., Krajewski, J.J., Jr., W.F.P., Waszczak, J.V., Meigs, G., Roth, R.S. & Schneemeyer, L.F. (1993). $LaCuO_{2.5+x}$ and $YCuO_{2.5+x}$ delafossites: Materials with triangular $Cu^{2+\delta}$ planes. *J. Solid State Chem.*, **104**, 437. 49, 75

Cava, R.J., Jr., W.F.P., Krajewski, J.J., Cheong, S.W. & Hwang, H.Y. (1994). Electrochemical and high pressure superoxygenation of $YCuO_{2+x}$ and $LaCuO_{2+x}$ delafossites. *J. Mater. Res.*, **9**, 314. 49

Chen, M., Pei, Z.L., Wang, X., Yu, Y.H., Liu, X.H., Sun, C. & Wen, L.S. (2000). Intrinsic limit of electrical properties of transparent conductive oxide films. *J. Phys. D: Appl. Phys.*, **33**, 2538. 3, 38

Chen, Y., Bagnall, D.M., Koh, H.J., Park, K.T., Hiraga, K., Zhu, Z.Q. & Yao, T. (1998). Plasma assisted molecular beam epitaxy of ZnO on *c*-plane sapphire: Growth and characterization. *J. Appl. Phys.*, **84**, 3912. 162

Cheng, H.C., Chen, C.F. & Lee, C.C. (2005). Thin-film transistors with active layers of zinc oxide (ZnO) fabricated by low-temperature chemical bath method. *Thin Solid Films*, **498**, 142. 178

Chiang, C.K., Druy, M.A., Gau, S.C., Heeger, A.J., Louis, E.J., MacDiarmid, A.G., Park, Y.W. & Shirakawa, H. (1978). Synthesis of highly conducting films of derivatives of polyacetylene, (CH_x). *J. Am. Chem. Soc.*, **100**, 1013. 1

Chiu, T.W., Tonooka, K. & Kikuchi, N. (2009). Fabrication of transparent $CuCrO_2$:Mg / ZnO *pn* junctions prepared by pulsed laser deposition on glass substrates. *Vacuum*, **83**, 614. 177

Choi, Y.S., Lee, C.G. & Cho, S.M. (1996). Transparent conducting $Zn_xCd_{1-x}O$ thin films prepared by the sol-gel process. *Thin Solid Films*, **289**, 153. 153

Chopra, K.L., Major, S. & Pandya, D.K. (1983). Transparent conductors - A status review. *Thin Solid Films*, **102**, 1. 1, 33, 149

Christopher, J. & Swamy, C.S. (1992). Catalytic activity and XPS investigation of delafossite oxides, $CuMO_2$ (M = Al, Cr or Fe). *J. Mater. Sci.*, **27**, 1353. 111

Coey, J.M.D. (2006). Dilute magnetic oxides. *Current Opinion in Solid State and Materials Science*, **10**, 83. 151

Collins, M.F. & Petrenko, O.A. (1997). Triangular antiferromagnets. *Can. J. Phys.*, **75**, 605. 245

Contreras, M.A., Barnes, T., van de Lagemaat, J., Rumbles, G., Coutts, T.J., Weeks, C., Glatkowski, P., Levitsky, I., Peltola, J. & Britz, D.A. (2007). Replacement of transparent conductive oxides by single-wall carbon nanotubes in $Cu(In,Ga)Se_2$ -based solar cells. *J. Phys. Chem. C*, **111**, 14045. 2

Coutts, T.J., Li, X., Barnes, T.M., Keyes, B.M., Craig, L.P., Asher, S.E., Zhang, S.B. & Wei, S.H. (2006). *Zinc Oxide Bulk, Thin Films, and Nanostructures*. Elsevier, New York. 153

Crottaz, O., Kubel, F. & Schmid, H. (1996). Preparation of trigonal and hexagonal cuprous chromite and phase transition study based on single crystal structure data. *J. Solid State Chem.*, **122**, 247. 75

Dannhauser, W. & Vaughan, P.A. (1955). The crystal structure of cuprous chromite. *J. Am. Chem. Soc.*, **77**, 896. 44

DEHUFF, N.L., KETTENRING, E.S., HONG, D., CHIANG, H.Q., WAGER, J.F., HOFFMAN, R.L., PARK, C.H. & KESZLER, D.A. (2005). Transparent thin-film transistors with zinc indium oxide channel layer. *J. Appl. Phys.*, **97**, 064505. 178

DEKKERS, J.M. (2007). *Transparent conducting oxides on polymeric substrates by pulsed laser deposition*. Ph.D. thesis, University of Twente. 39

DENG, Z., FANG, X., LI, D., ZHOU, S., TAO, R., DONG, W., WANG, T., MENG, G. & ZHU, X. (2009). Room temperature ozone sensing properties of *p*-type transparent oxide $CuCrO_2$. *J. Alloys Compd.*, **484**, 619. 53, 76

DEVAULT, D. (1944). A method of teaching the electronic structure of the atom - I. Elementary presentation. *J. Chem. Educ.*, **21**, 526. 41

DINGLE, R.B. (1955). Scattering of electrons and holes by charged donors and acceptors in semiconductors. *Phil. Mag.*, **46**, 831. 38

DODSON, E.M. & SAVAGE, J.A. (1968). Vapour growth of single-crystal zinc oxide. *J. Mater. Sci.*, **3**, 19. 153

DORDOR, P., CHAMINADE, J.P., WICHAINCHAI, A., MARQUESTAUT, M., DOUMERC, J.P., POUCHARD, M., HAGENMULLER, P. & AMMAR, A. (1988). Crystal growth and electrical properties of $CuFeO_2$ single crystals. *J. Solid State Chem.*, **75**, 105. 54, 74

DOUMERC, J., AMMAR, A., WICHAINCHAI, A., POUCHARD, M. & HAGENMULLER, P. (1987). Sur quelques nouveaux composes de structure de type delafossite. *J. Phys. Chem. Solids*, **48**, 37. 132

DOUMERC, J.P., WICHAINCHAI, A., AMMAR, A., POUCHARD, M. & HAGENMULLER, P. (1986). On magnetic properties of some oxides with delafossite-type structure. *Mat. Res. Bull.*, **21**, 745. 66, 67, 75, 90

DRUDE, P. (1900a). Zur elektronentheorie der metalle, I. Teil, II. Teil, und Berichtigung. *Ann. Phys., Lpz.*, **1**, 566. 9, 11, 34

DRUDE, P. (1900b). Zur elektronentheorie der metalle, I. Teil, II. Teil, und Berichtigung. *Ann. Phys., Lpz.*, **3**, 369. 9, 11, 34

DUAN, N., SLEIGHT, A.W., JAYARAJ, M.K. & TATE, J. (2000). Transparent p-type conducting $CuScO_{2+x}$ films. *Appl. Phys. Lett.*, **77**, 1325. 46, 48, 49, 59, 73, 75, 77

EDWARDS, P.P., PORCH, A., JONES, M.O., MORGAN, D.V. & PERKS, R.M. (2004). Basic materials physics of transparent conducting oxides. *Dalton Trans.*, **19**, 2995. 1, 3, 33, 34

EXARHOS, G.J. & ZHOU, X.D. (2007). Discovery-based design of transparent conducting oxide films. *Thin Solid Films*, **515**, 7025. 33, 40

FALABRETTI, B. & ROBERTSON, J. (2007). Electronic structures and doping of SnO_2, $CuAlO_2$, and $CuInO_2$. *J. Appl. Phys.*, **102**, 123703. 128

FAN, J.C.C. & GOODENOUGH, J.B. (1977). X-ray photoemission spectroscopy studies of Sn-doped indium-oxide films. *J. Appl. Phys.*, **48**, 3524. 33

FIGGIS, B.N. (1966). *Introduction to Ligand Fields*. John Wiley & Sons. 63

FONS, P., IWATA, K., NIKI, S., YAMADA, A. & MATSUBARA, K. (1999). Growth of high-quality epitaxial ZnO films on α-Al_2O_3. *J. Cryst. Growth*, **201**, 627. 162

FONS, P., TAMPO, H., KOLOBOV, A.V., OHKUBO, M., NIKI, S., TOMINAGA, J., CARBONI, R., BOSCHERINI, F. & FRIEDRICH, S. (2006). Direct observation of nitrogen location in molecular beam epitaxy grown nitrogen-doped ZnO. *Phys. Rev. Lett.*, **96**, 045504. 155

FRAGA, S., KARWOWSKI, S. & SAXENA, K. (1976). *Handbook of Atomic Data*. Elsevier, Amsterdam. 40

FREEMAN, A.J., POEPPELMEIER, K.R., MASON, T.O., CHANG, R.P.H. & MARKS, T.J. (2000). Chemical and thin-film strategies for new transparent conducting oxides. *Mater. Res. Bull.*, **25**, 45. 3, 150

FRIEDEL, M.C. (1873). Sur une combinaison naturelle des oxydes de fer et de cuivre, et sur la reproduction de l'atacamite. *C. R. Hebd. Acad. Sci.*, **77**, 211. 43

GADALLA, A.M.M. & WHITE, J. (1964). The system Cu_2O-CuO-Cr_2O_3 and its bearing on the performance of basic refractories in copper melting furnaces. *Trans. Brit. Ceram. Soc.*, **63**, 535. 81

GESSNER, W. (1970). *Silikattechnik*, **21**, 45. 132

GIBAUD, A. & HAZRA, S. (2000). X-ray reflectivity and diffuse scattering. *Curr. Sci.*, **78**, 1467. 230

GINLEY, D., ROY, B., ODE, A., WARMSINGH, C., YOSHIDA, Y., PARILLA, P., TEPLIN, C., KAYDANOVA, T., MIEDANER, A., CURTIS, C., MARTINSON, A., COUTTS, T., READEY, D., HOSONO, H. & PERKINS, J. (2003). Non-vacuum and PLD growth of next generation TCO materials. *Thin Solid Films*, **445**, 193. 128, 129, 130

GINLEY, D.S. & BRIGHT, C. (2000). Transparent conducting oxides. *Mater. Res. Soc. Bull.*, **25**, 15. 2, 7, 8, 37, 149, 150

GOODENOUGH, J.B. (1960). Direct cation-cation interactions in several oxides. *Phys. Rev.*, **117**, 1442. 69

GOODENOUGH, J.B. (1963). *Magnetism and the chemical bond*. John Wiley & Sons. 243

GORDON, R.G. (2000). Criteria for choosing transparent conductors. *Mater. Res. Bull.*, **25**, 52. 1, 2, 7, 40

GÖRRN, P., SANDER, M., MEYER, J., KRÖGER, M., BECKER, E., JOHANNES, H.H. & RIEDL, W.K.T. (2006). Towards see-through displays: Fully transparent thin-film transistors driving transparent organic light-emitting diodes. *Adv. Mater.*, **18**, 738. 178

GÖTZENDÖRFER, S., BYWALEZ, R. & LÖBMANN, P. (2009). Preparation of *p*-type conducting transparent $CuCrO_2$ and $CuAl_{0.5}Cr_{0.5}O_2$. *J. Sol-Gel Sci Technol.*, **52**, 113. 54

GU, Z.H. & FAHIDY, T.Z. (1999). Electrochemical deposition of ZnO thin films on tin-coated glasses. *J. Electrochem. Soc.*, **146**, 156. 153

GUDDEN, B. (1930). Ueber die Elektrizitätsleitung in Halbleitern. *Sitzungsber. Phys. - Med. Soz. Erlangen*, **62**, 289. 13

GUO, X.L., TABATA, H. & KAWAI, T. (2001). Pulsed laser reactive deposition of *p*-type ZnO film enhanced by an electron cyclotron resonance source. *J. Cryst. Growth*, **223**, 135. 4, 154

HAHN, H. & LORENT, C. (1955). Untersuchungen ber ternre chalkogenide. VII. Versuche zur darstellung ternrer oxyde des aluminiums, galliums und indiums mit einwertigem kupfer und silber. *Z. Anorg. Allg. Chem.*, **279**, 281. 46

HALL, E.H. (1879). On a new action of the magnet on electric currents. *Phil. Mag.*, **9**, 225. 13, 28

HAMADA, I. & KATAYAMA-YOSHIDA, H. (2006). Energetics of native defects in $CuAlO_2$. *Physica B*, **376**, 808. 75

HAMBERG, I. & GRANQVIST, C.G. (1985). Transparent and infrared-reflecting indium-tin-oxide films: quantitative modeling of the optical properties. *Appl. Opt.*, **24**, 1815. 38

HAMILTON, E.M. (1972). Variable range hopping in a non-uniform density of states. *Phil. Mag.*, **26**, 1043. 78

HARRISON, S.E. (1954). Conductivity and Hall effect of ZnO at low temperatures. *Phys. Rev.*, **93**, 52. 154

HARTNAGEL, H.L., DAWAR, A.L., JAIN, A.K. & JAGADISH, C. (1995). *Semiconducting Transparent Thin Films*. IOP Publishing Ltd. 1

HAYNES, J.R. & SHOCKLEY, W. (1949). Investigation of hole injection in transistor action. *Phys. Rev.*, **75**, 691. 181

HAYNES, J.R. & SHOCKLEY, W. (1951). The mobility and life of injected holes and electrons in Germanium. *Phys. Rev.*, **81**, 835. 24

HEIKES, R.R. & JOHNSTON, W.D. (1957). Mechanism of conduction in Li-substituted transition metal oxides. *J. Chem. Phys.*, **26**, 582. 77

HEINKE, H., KIRCHNER, V., SELKE, H., CHIERCHIA, R., EBEL, R., EINFELDT, S. & HOMMEL, D. (2001). X-ray scattering from GaN epitaxial layers - an example of highly anisotropic coherence. *J. Phys. D: Appl. Phys.*, **34**, A25. 99

HEINZE, S., KRTSCHIL, A., BLASING, J., HEMPEL, T., VEIT, P., DADGAR, A., CHRISTEN, J. & KROST, A. (2007). Homoepitaxial growth of ZnO by metalorganic vapor phase epitaxy in two-dimensional growth mode. *J. Cryst. Growth*, **308**, 170. 153

HEISENBERG, W. (1931). Zum Paulischen Ausschliessungsprinzip. *Ann. Phys., Lpz.*, **10**, 888. 14

HIRAMATSU, H., UEDA, K., OHTA, H., ORITA, M., HIRANO, M. & HOSONO, H. (2002). Preparation of transparent p-type ($La_{1-x}Sr_xO$) CuS thin films by r.f. sputtering technique. *Thin Solid Films*, **411**, 125. 2

HIRAMATSU, H., UEDA, K., OHTA, H., HIRANO, M. & HOSONO, H. (2005). Excitonic blue luminescence from p-LaCuOSe / n-$InGaZn_5O_8$ light emitting diode at room temperature. *Appl. Phys. Lett.*, **87**, 21107. 177

Hirao, T., Furuta, M., Furuta, H., Matsuda, T., Hiramatsu, T., Hokari, H. & Yoshida, M. (2006). High mobility top-gate zinc oxide thin-film transistors (ZnO-TFTs) for active-matrix liquid crystal displays. *SID Digest*, **37**, 18. 178

Hirsch, J.E. (1995). *Polarons and Bipolarons in High-T_c Superconductors and Related Materials*, chap. Electron-hole asymmetric polarons, 234 – 257. Cambridge Univ. Press, Cambridge. 78

Hittorf, J.W. (1851). Ueber das elektrische Leitungsvermögen des Schwefelsilbers und des Halbschwefelkupfers. *Ann. Phys., Lpz.*, **84**, 1. 13

Hoffman, R., Norris, B. & Wager, J. (2003). ZnO-based transparent thin-film transistors. *Appl. Phys. Lett.*, **82**, 733. 178

Hoffman, R.L., Wager, J.F., Jayaraj, M.K. & Tate, J. (2001). Electrical characterisation of transparent *p-i-n* heterojunction diodes. *J. Appl. Phys.*, **90**, 5763. 177

Hosono, H., Ohta, H., Orita, M., Ueda, K. & Hirano, M. (2002). Frontier of transparent conductive oxide thin films. *Vacuum*, **66**, 419. 130

Hu, J. & Gordon, R.G. (1991). Textured fluorine-doped zinc oxide films by atmospheric pressure chemical vapour deposition and their use in amorphous silicon solar cells. *Solar Cells*, **30**, 437. 154

Hu, J. & Gordon, R.G. (1992). Textured aluminum-doped zinc oxide thin films from atmospheric pressure chemical-vapor deposition. *J. Appl. Phys.*, **71**, 880. 154

Hu, J. & Gordon, R.G. (1993). Electrical and optical properties of indium doped zinc oxide films prepared by atmospheric pressure chemical vapor deposition. *Mater. Res. Soc. Symp. Proc.*, **283**, 891. 154

Hutson, A.R. (1957). Hall effect studies of doped zinc oxide single crystals. *Phys. Rev.*, **108**, 222. 154

Hwang, D.K., Bang, K.H., Jeong, M.C. & Myoung, J.M. (2003). Effects of rf power variation on properties of ZnO thin films and electrical properties of *p-n* homojunction. *J. Cryst. Growth*, **254**, 449. 154

Ingram, B.J., Mason, T.O., Asahi, R., Park, K.T. & Freeman, A.J. (2001). Electronic structure and small polaron hole transport of copper aluminate. *Phys. Rev. B*, **64**, 155114. 46, 55, 61, 76

INGRAM, B.J., GONZALEZ, G.B., MASON, T.O., SHAHRIARI, D.Y., BARNABE, A., KO, D. & POEPPELMEIER, K.R. (2004a). Transport and defect mechanisms in cuprous delafossites. 1. Comparison of hydrothermal and standard solid-state synthesis in $CuAlO_2$. *Chem. Mater.*, **16**, 5616. 49, 55, 72, 73, 75

INGRAM, B.J., HARDER, B.J., HRABE, N.W., MASON, T.O. & POEPPELMEIER, K.R. (2004b). Transport and defect mechanisms in cuprous delafossites. 2. $CuScO_2$ and $CuYO_2$. *Chem. Mater.*, **16**, 5623. 49, 61, 72, 73, 74

INGRAM, B.J., BERTONI, M.I., POEPPELMEIER, K.R. & MASON, T.O. (2005). Point defects and transport mechanisms in transparent conducting oxides of intermediate conductivity. *Thin Solid Films*, **486**, 86. 61, 72, 75, 76

ISAWA, K., YAEGASHI, Y., KOMATSU, M., NAGANO, M., SUDO, S., KARPPINEN, M. & YAMAUCHI, H. (1997). Synthesis of delafossite-derived phases, $RCuO_{2+\delta}$ with R = Y, La, Pr, Nd, Sm, and Eu, and observation of spin-gap-like behaviour. *Phys. Rev. B*, **56**, 3457. 72, 74, 75, 76

ISAWA, K., YAEGASHI, Y., OGOTA, S., NAGANO, M., SUDO, S., YAMADA, K. & YAMAUCHI, H. (1998). Thermoelectric power of delafossite-derived compounds, $RCuO_{2+\delta}$ (R = Y, La, Pr, Nd, Sm and Eu). *Phys. Rev. B*, **57**, 7950. 76

ISHIGURO, T., KITAZAWA, A., MIZUTANI, N. & KATO, M. (1981). Single-crystal growth and crystal structure refinement of $CuAlO_2$. *J. Solid State Chem.*, **40**, 170. 46

ISHIGURO, T., ISHIZAWA, N., MIZUTANI, N. & KATO, M. (1982). High temperature structural investigation of the delafossite type compound $CuAlO_2$. *J. Solid State Chem.*, **41**, 132. 46

ISHIGURO, T., ISHIZAWA, N., MIZUTANI, N. & KATO, M. (1983). Charge-density distribution in crystals of $CuAlO_2$ with d-s hybridization. *Acta. Crystallogr.*, **B39**, 564. 42, 43, 46

JACOB, K.T., KALE, G.M. & IYENGAR, G.N.K. (1986). Oxygen portentials, Gibbs' energies and phase relations in the Cu-Cr-O system. *J. Mater. Sci.*, **21**, 2753. 81

JANOTTI, A. & DE WALLE, C.G.V. (2005). Oxygen vacancies in ZnO. *Appl. Phys. Lett.*, **87**, 122102. 154

JANOTTI, A. & DE WALLE, C.G.V. (2007a). Hydrogen multicenter bonds. *Nature Mater.*, **6**, 44. 154

JANOTTI, A. & DE WALLE, C.G.V. (2007b). Native point defects in ZnO. *Phys. Rev. B*, **75**, 165202. 154

JAYARAJ, M.K., DRAESEKE, A.D., TATE, J., HOFFMAN, R.L. & WAGER, J.F. (2000). Transparent p-n heterojunction thin film diodes. *Proceedings of the MRS workshop on Transparent Conductive Oxides, Denver, CO*. 49

JAYARAJ, M.K., DRAESEKE, A.D., TATE, J. & SLEIGHT, A.W. (2001). p-Type transparent thin films of $CuY_{1-x}Ca_xO_2$. *Thin Solid Films*, **397**, 244. 46, 48, 49, 59, 60, 73, 74

JOHNSON, M.A.L., FUJITA, S., ROWLAND, W.H., HUGHES, W.C., COOK, J.W. & SCHETZINA, J.F. (1996). MBE growth and properties of ZnO on sapphire and SiC substrates. *J. Electron. Mater.*, **25**, 855. 153

JOSEPH, M., TABATA, H. & KAWAI, T. (1999). p-Type electrical conduction in ZnO thin films by Ga and N codoping. *Jpn. J. Appl. Phys.*, **38**, L1205. 4, 155

KADOWAKI, H., KIKUCHI, H. & AJIRO, Y. (1990). Neutron powder diffraction study of the two-dimensional triangular lattice antiferromagnet $CuCrO_2$. *J. Phys.: Condens. Matter*, **2**, 4485. 54, 62, 65, 67, 68, 69, 76, 90

KAKEHI, Y., NAKAO, S., SATOH, K. & YOTSUYA, T. (2003). Properties of copper-scandium oxide thin films prepared by pulsed laser deposition. *Thin Solid Films*, **445**, 294. 73

KANAMORI, J. (1959). Superexchange interaction and symmetry properties of electron orbitals. *J. Phys. Chem. Solids*, **10**, 87. 244

KAWAZOE, H., YASUKAWA, M., HYODO, H., KURITA, M., YANAGI, H. & HOSONO, H. (1997). p-Type electricial conduction in transparent thin films of $CuAlO_2$. *Nature*, **389**, 939. 4, 40, 42, 46, 55, 60, 73, 75, 76, 127

KAWAZOE, H., YANAGI, H., UEDA, K. & HOSONO, H. (2000). Transparent p-type conducting oxides: Design and fabrication of p-n heterojunctions. *Mater. Res. Bull.*, **25**, 28. 2, 4, 32, 41, 42, 46, 55, 72

KHAN, M.A., KUZNIA, J.N., OLSON, D.T., HOVE, J.M.V., BLASINGAME, M. & REITZ, L.F. (1992). High-responsivity photoconductive ultraviolet sensors based on insulating single-crystal GaN epilayers. *Appl. Phys. Lett.*, **60**, 2917. 1

KIM, H.S., LEE, B.S., JI, S.H., KIM, H., KIM, D., IHM, Y.E. & CHOO, W.K. (2004). Transport and magnetic properties of delafossite $CuAl_{1-x}Mn_xO_2$ ceramics. *Phys. Stat. Sol. B*, **241**, 1545. 73

KIM, S., KIM, S., PARKS, J., JU, S. & MOHAMMADI, S. (2010). Fully transparent pixel circuits driven by random network carbon nanotube transistor circuitry. *ACS Nano*, **4**, 2994. 2

KIMURA, K., NAKAMURA, H., OHGUSHI, K. & KIMURA, T. (2008). Magnetoelectric control of spin-chiral ferroelectric domains in a triangular lattice antiferromagnet. *Phys. Rev. B*, **78**, 140401(R). 54, 66, 67, 68, 75

KIMURA, R. & TAKAHASHI, K. (2000). High quality epitaxial growth of hexagonal GaN on Al_2O_3 (0001) and cubic GaN on GaAs (100) by MBE. *Phys. Stat. Sol. (a)*, **180**, 235. 216

KIMURA, T., LASHLEY, J.C. & RAMIREZ, A.P. (2006). Inversion-symmetry breaking in the noncollinear magnetic phase of the triangular-lattice antiferromagnet $CuFeO_2$. *Phys. Rev. B*, **73**, 220401. 65

KLEINMAN, L. & MEDNICK, K. (1980). Self-consistent energy bands of Cu_2O. *Phys. Rev. B*, **21**, 1549. 42

KLINGSHIRN, C. (2007). ZnO: From basics towards applications. *Phys. Stat. Sol. (b)*, **244**, 3027. 154

KOENIGSBERGER, J. (1914). Das elektrische Verhalten der variablen Leiter und deren Beziehung zur Elektronentheorie. *Jahrb. Radioakt. Elektron.*, **11**, 84. 13

KOENIGSBERGER, J. & WEISS, J. (1911). Ueber die thermoelektrischen Effekte (Thermokräfte, Thomsonwärme) und die Wärmeleitung in einigen Elementen und über die experimentelle Prüfung der Elektronentheorien. *Ann. Phys., Lpz.*, **35**, 1. 13

KOHLER, B.V. & JANSEN, M. (1986). Darstellung und strukturdaten von delafossiten $CuMO_2$ (M = Al, Ga, Sc, Y). *Z. Anorg. Allg. Chem.*, **543**, 73. 46

KOON, D.W. (1989). Effect of contact size and placement, and of resistive inhomogeneities on van der pauw measurements. *Rev. Sci. Instrum.*, **60**, 271. 239

KRAMERS, H. (1934). L'interaction entre les atomes magnétogènes dans un cristal paramagnétique. *Physica*, **1**, 182. 243

KUDO, A., YANAGI, H., HOSONO, H. & KAWAZOE, H. (1998). $SrCu_2O_2$: A *p*-type conductive oxide with wide band gap. *Appl. Phys. Lett.*, **73**, 220. 4, 40, 127

KUDO, A., YANAGI, H., YANO, Y., UEDA, K., HOSONO, H. & KAWAZOE, H. (1999). Fabrication of transparent p/n heterojunction thin film diodes based entirely on oxide semiconductors. *Appl. Phys. Lett.*, **75**, 2851. 177

KURTZ, S.R. & GORDON, R.G. (1986). Chemical vapor deposition of titanium nitride at low temperatures. *Thin Solid Films*, **139**, 277. 1

KWON, Y., LI, Y., HEO, Y.W., JONES, M., HOLLOWAY, P.H., NORTON, D.P., PARK, Z.V. & LI, S. (2004). Enhancement-mode thin-film field-effect transistor using phosphorus-doped (Zn, Mg)O channel. *Appl. Phys. Lett.*, **84**, 2685. 178

KYKYNESHI, R., NIELSEN, B.C., TATE, J., LI, J. & SLEIGHT, A.W. (2004). Structural and transport properties of $CuSc_{1-x}Mg_xO_{2+y}$ delafossites. *J. Appl. Phys.*, **96**, 6188. 73

LACORRE, P. (1987). The constraint functions: an attempt to evaluate the constraint rate inside structures that undergo ordered magnetic frustration. *J. Phys. C: Solid State Phys.*, **20**, L775. 246

LANDER, J.J. (1960). Reactions of lithium as a donor and an acceptor in ZnO. *J. Phys. Chem. Solids*, **15**, 324. 154

LAVROV, E.V., HERKLOTZ, F. & WEBER, J. (2009). Identification of two hydrogen donors in ZnO. *Phys. Rev. B*, **79**, 165210. 154

LEE, E.C., KIM, Y.S., JIN, Y.G. & CHANG, K.J. (2001). Compensation mechanism for N acceptors in ZnO. *Phys. Rev. B*, **64**, 085120. 155

LEE, J.H., LIN, P., HO, J.C. & LEE, C.C. (2006). Chemical solution deposition of $Zn_{1-x}Zr_xO$ thin films as active channel layers of thin-film transistors. *Electrochem. Solid State Lett.*, **9**, G117. 178

LEWIS, B.G. & PAINE, D.C. (2000). Applications and processing of transparent conducting oxides. *Mater. Res. Bull.*, **25**, 22. 2, 7, 32, 149

LI, D., FANG, X., DENG, Z., ZHOU, S., TAO, R., DONG, W., WANG, T., ZHAO, Y., MENG, G. & ZHU, X. (2007). Electrical, optical and structural properties of $CuCrO_2$ films prepared by pulsed laser deposition. *J. Phys. D: Appl. Phys.*, **40**, 4910. 54, 75, 81, 214

LI, D., FANG, X., DENG, Z., DONG, W., TAO, R., ZHOU, S., WANG, J., WANG, T., ZHAO, Y. & ZHU, X. (2009a). Characteristics of $CuCr_{1-x}Mg_xO_2$ films prepared by pulsed laser deposition. *J. Alloys Compd.*, **486**, 462. 73

LI, D., FANG, X., DONG, W., DENG, Z., TAO, R., ZHOU, S., WANG, J., WANG, T., ZHAO, Y. & ZHU, X. (2009b). Magnetic and electrical properties of p-type Mn-doped $CuCrO_2$ semiconductors. *J. Phys. D: Appl. Phys.*, **42**, 055009. 53, 66, 67, 90, 111

LIU, L., BAI, K., GONG, H. & WU, P. (2005a). First-principles study of bipolar dopability in the $CuInO_2$ transparent semiconductor. *Chem. Mater.*, **17**, 5529. 127, 129, 134, 142

LIU, L., BAI, K., GONG, H. & WU, P. (2005b). First-principles study of Sn and Ca doping in $CuInO_2$. *Phys. Rev. B*, **72**, 125204. 129, 131

LOOK, D.C., REYNOLDS, D.C., LITTON, C.W., JONES, R.L., EASON, D.B. & CANTWELL, G. (2002). Characterization of homoepitaxial p-type ZnO grown by molecular beam epitaxy. *Appl. Phys. Lett.*, **81**, 1830. 154, 155

LORENTZ, M., HOCHMUTH, H., LENZNER, J., NOBIS, T., ZIMMERMANN, G., DIACONU, M., SCHMIDT, H., VON WENCKSTERN, H. & GRUNDMANN, M. (2005). Room-temperature luminescence of n-type ZnO thin films grown by pulsed laser deposition in N_2, N_2O, and O_2. *Thin Solid Films*, **486**, 205. 153

MAHAPATRA, S. & SHIVASHANKAR, S.A. (2003). Low-pressure metal-organic chemical vapor deposition of transparent and p-type conducting $CuCrO_2$ thin films with high conductivity. *Chem. Vap. Deposition*, **9**, 238. 53, 54, 72, 73, 75, 77

MAIGNAN, A., MARTIN, C., FRÉSARD, R., EYERT, V., GUILMEAU, E., HÉBERT, S., POIENAR, M. & PELLOQUIN, D. (2009). On the strong impact of doping in the triangular antiferromagnet $CuCrO_2$. *Solid State Commun.*, **149**, 962. 54, 55, 62, 66, 67, 71, 76, 78, 79, 81, 84, 86, 119

MAKHOVA, L., WETT, D., LORENZ, M. & KONOVALOV, I. (2006). X-ray spectroscopic investigation of forbidden direct transitions in $CuGaO_2$ and $CuInO_2$. *Phys. Stat. Sol. (a)*, **203**, 2861. 128

MARQUARDT, M.A., ASHMORE, N.A. & CANN, D.P. (2006). Crystal chemistry and electrical properties of the delafossite structure. *Thin Solid Films*, **496**, 146. 54, 61, 75

MASUDA, S., KITAMURA, K., OKUMURA, Y., MIYATAKE, S., TABATA, H. & KAWAI, T. (2003). Transparent thin film transistors using ZnO as an active channel layer and their electrical properties. *J. Appl. Phys.*, **93**, 1624. 178

MCLACHLAN, D.S., BLASZKIEWICZ, M. & NEWNHAM, R.E. (1990). Electrical resistivity of composites. *J. Am. Ceram. Soc.*, **73**, 2187. 75

MINAMI, T. (2000). New *n*-type transparent conducting oxides. *Mater. Res. Bull.*, **25**, 38. 2, 7, 150

MINAMI, T. (2005). Transparent conducting oxide semiconductors for transparent electrodes. *Semicond. Sci. Technol.*, **20**, S35. 3, 4, 150

MINEGISHI, K., KOIWAI, Y., KIKUCHI, Y., YANO, K., KASUGA, M. & SHIMIZU, A. (1997). Growth of *p*-type zinc oxide films by chemical vapor deposition. *Jpn. J. Appl. Phys.*, **36**, L1453. 155

MISRA, S.K. & CHAKLADER, A.C.D. (1963). System Copper Oxide-Alumina. *J. Amer. Ceram. Soc.*, **46**, 1963. 81

MONROY, E., CALLE, F., MUNOZ, E. & OMNES, F. (1999). AlGaN metal-semiconductor-metal photodiodes. *Appl. Phys. Lett.*, **74**, 3401. 1

MORIN, F.J. (1954). Electrical properties of NiO. *Phys. Rev.*, **93**, 1199. 77

MOTT, N.F. (1968). Conduction in glasses containing transition metal ions. *J. Non-Cryst. Solids*, **1**, 1. 78

MOTT, N.F. (1990). *Metal-Insulator Transition*. Taylor and Francis, London. 34

MÜLLER, G. (1976). Optical and electrical spectroscopy of zinc oxide crystals simultaneously doped with copper and donors. *Phys. Stat. Sol. (b)*, **76**, 525. 154

MYONG, S.Y., BAIK, S.J., LEE, C.H., CHO, W.Y. & LIMPIJUMNONG, K.S. (1997). Extremely transparent and conductive ZnO:Al thin films prepared by photo-assisted metalorganic chemical vapor deposition (photo-MOCVD) using $AlCl_3(6H_2O)$ as new doping material. *Jpn. J. Appl. Phys.*, **36**, L1078. 154

NAGARAJAN, R., DRAESEKE, A.D., SLEIGHT, A.W. & TATE, J. (2001a). *p*-Type conductivity in $CuCr_{1-x}Mg_xO_2$ films and powders. *J. Appl. Phys.*, **89**, 8022. 46, 48, 49, 53, 61, 62, 73, 75

NAGARAJAN, R., DUAN, N., JAYARAJ, M.K., LI, J., VANAJA, K.A., YOKOCHI, A., DRAESEKE, A., TATE, J. & SLEIGHT, A.W. (2001b). *p*-Type conductivity in the delafossite structure. *Int. J. Inorg. Mater.*, **3**, 265. 48, 49, 54, 60, 61, 74, 75

NAGARAJAN, R., UMA, S., JAYARAJ, M.K., TATE, J. & SLEIGHT, A.W. (2002). New $CuM_{2/3}Sb_{1/3}O_2$ and $AgM_{2/3}Sb_{1/3}O_2$ compounds with the delafossite structure. *Solid State Sci.*, **4**, 787. 50

NAKAMURA, S., MUKAI, T. & SENOH, M. (1994). Candela-class high-brightness InGaN / AlGaN double-heterostructure blue-light-emitting diodes. *Appl. Phys. Lett.*, **64**, 1687. 1

NAUSE, J. & NEMETH, B. (2005). Pressurized melt growth of ZnO boules. *Semicond. Sci. Technol.*, **20**, S45. 153

NIE, X., WEI, S.H. & ZHANG, S.B. (2002). Bipolar doping and band-gap anomalies in delafossite transparent conductive oxides. *Phys. Rev. Lett.*, **88**, 066405. 56, 57, 128, 129, 130, 142

NIKITINE, S., GRUN, J.B. & SIESKIND, M. (1961). Etude spectrophotometrique de la serie jaune de Cu_2O aux basses temperatures. *J. Phys. Chem. Solids*, **17**, 292. 42

NOMURA, K., OHTA, H., UEDA, K., KAMIYA, T., HIRANO, M. & HOSONO, H. (2003). Thin-film transistor fabricated in single-crystalline transparent oxide semiconductor. *Science*, **300**, 1269. 177

NOZIK, A.J. (1972). Optical and electrical properties of Cd_2SnO_4: A defect semiconductor. *Phys. Rev. B*, **6**, 453. 3, 150

OHSHIMA, E., OGINO, H., NIIKURA, I., MAEDA, K., SATO, M., ITO, M. & FUKUDA, T. (2004). Growth of the 2-in-size bulk ZnO single crystals by the hydrothermal method. *J. Cryst. Growth*, **260**, 166. 153

OHTA, H., KAWAMURA, K., ORITA, M., HIRANO, M., SARUKURA, N. & HOSONO, H. (2000a). Current injection emission from a transparent *pn* junction composed of *p*-$SrCu_2O_2$ / *n*-ZnO. *Appl. Phys. Lett.*, **77**, 475. 177

OHTA, H., KAWAMURA, K., ORITA, M., SARUKURA, N., HIRANO, M. & HOSONO, H. (2000b). A UV-emitting diode composed of transparent oxide semiconductors: *p*-$SrCu_2O_2$ / *n*-ZnO. *Electron. Lett.*, **36**, 984. 177

OHTA, H., ORITA, M. & HIRANO, M. (2001). Fabrication and characterization of ultraviolet-emitting diodes composed of transparent *p*-*n* heterojunction, *p*-$SrCu_2O_2$ and *n*-ZnO. *J. Appl. Phys.*, **89**, 5720. 177

OHTA, H., HIRANO, M., NAKAHARA, K., MARUTA, H., TANABE, T., KAMIYA, M., KAMIY, T. & HOSONO, H. (2003a). Fabrication and photoresponse of a *pn*-heterojunction diode composed of transparent oxide semiconductors, *p*-NiO and *n*-ZnO. *Appl. Phys. Lett.*, **83**, 1029. 177

OHTA, H., MIZOGUCHI, H., HIRANO, M., NARUSHIMA, S., KAMIYA, T. & HOSONO, H. (2003b). Fabrication and characterisation of heteroepitaxial *p*-*n* junction diode composed of wide-gap oxide semiconductors *p*-$ZnRh_2O_4$ / *n*-ZnO. *Appl. Phys. Lett.*, **82**, 823. 177

OHTA, H., NOMURA, K., HIRAMATSU, H., UEDA, K., KAMIYA, T., HIRANO, M. & HOSONO, H. (2003c). Frontier of transparent oxide semiconductors. *Solid State Elec.*, **47**, 2261. 130

OHTOMO, A., TAKAGI, S., TAMURA, K., MAKINO, T., SEGAWA, Y., KOINUMA, H. & KAWASAKI, M. (2006). Photo-irresponsive thin-film transistor with $Mg_xZn_{1-x}O$ channel. *Japan. J. Appl. Phys.*, **45**, L694. 178

OK, H.N., BAEK, K.S. & CHOI, E.J. (1989). Mössbauer study of $CuFe_{0.7}Cr_{1.3}O_4$. *Phys. Rev. B*, **40**, 84. 87

OKUDA, T., JUFUKU, N., HIDAKA, S. & TERADA, N. (2005). Magnetic, transport, and thermoelectric properties of the delafossite oxides $CuCr_{1-x}Mg_xO_2$ ($0 \leq x \leq 0.04$). *Phys. Rev. B*, **72**, 144403. 54, 57, 66, 67, 75, 76, 79, 81, 84, 85, 119, 120

OKUDA, T., ONOE, T., BEPPU, Y., TERADA, N., DOI, T., MIYASAKA, S. & TOKURA, Y. (2007). Magnetic and transparent properties of delafossite oxides $CuCr_{1-x}(Mg, Ca)_xO_2$. *J. Magn. Magn. Mater.*, **310**, 890. 54, 66, 67, 71, 79, 119

OKUDA, T., BEPPU, Y., FUJII, Y., ONOC, T., TERADA, N. & MIYASAKA, S. (2008). Specific heat of delafossite oxide $CuCr_{1-x}Mg_xO_2$ ($0 \leq x \leq 0.03$). *Phys. Rev. B*, **77**, 134423. 54, 65, 66, 67, 71, 84

ONO, Y., SATOH, K., NOZAKI, T. & KAJITANI, T. (2007). Structural, magnetic and thermoelectric properties of delafossite-type oxide, $CuCr_{1-x}Mg_xO_2$ ($0 \leq x \leq 0.05$). *Japan. J. Appl. Phys.*, **46**, 1071. 65, 66, 67, 90

ORGEL, L.E. (1958). Stereochemistry of metals of the B sub-groups. Part I. Ions with filled *d*-electron shells. *J. Chem. Soc.*, **843**, 4186. 42

ORGEL, L.E. (1966). *An Introduction to Transition-Metal Chemistry: Ligand-Field Theory.* Methuen, London. 42, 55

OZGUR, U., ALIVOV, Y.I., LIU, C., TEKE, A., RESHCHIKOV, M.A., DOGAN, S., AVRUTIN, V., CHO, S.J. & MORKOC, H. (2005). A comprehensive review of ZnO materials and devices. *J. Appl. Phys.*, **98**, 041301. 162

PABST, A. (1946). Notes on the structure of delafossite. *Am. Mineral.*, **31**, 539. 44

PALMER, G.B., POEPPELMEIER, K.R. & MASON, T.O. (1997). $Zn_{2-x}Sn_{1-x}In_{2x}O_{4-\delta}$: An indium-substituted spinel with transparent conducting properties. *J. Solid State Chem.*, **134**, 192. 3

PAN, C.A. & MA, T.P. (1981). Highly transparent conductive films of thermally evaporated In_2O_3. *J. Electron. Mater.*, **10**, 43. 3

PARK, S. & KESZLER, D.A. (2003). Synthesis of 3R-$CuMO_{2+\delta}$ (M = Ga, Sc, In). *J. Solid State Chem.*, **173**, 355. 134

PARK, S.H.K., HWANG, C.S., LEE, J., CHUNG, S.M., YANG, Y.S., DO, L.M. & CHU, H.Y. (2006). Transparent ZnO thin film transistor array for the application of transparent AM-OLED display. *SID Digest*, **37**, 25. 178

PELLICER-PORRES, J., SEGURA, A., GILLILAND, A.S., MUNOZ, A., RODRIGUEZ-HERNANDEZ, P., KIM, D., LEE, M.S. & KIM, T.Y. (2006). On the band gap of $CuAlO_2$ delafossite. *Appl. Phys. Lett.*, **88**, 181904. 128

PETRITZ, R.L. (1956). Theory of photoconductivity in semiconductor films. *Phys. Rev.*, **104**, 1508. 39

POIENAR, M., DAMAY, F., MARTIN, C., HARDY, V., MAIGNAN, A. & ANDRÉ, G. (2009). Structural and magnetic properties of $CuCr_{1-x}Mg_xO_2$ by neutron powder diffraction. *Phys. Rev. B*, **79**, 014412. 66, 67, 68, 69, 71, 76, 83, 85, 120

POIENAR, M., DAMAY, F., MARTIN, C., ROBERT, J. & PETIT, S. (2010). Spin dynamics in the geometrically frustrated multiferroic $CuCrO_2$. *Phys. Rev. B*, **81**, 104411. 69

PRESLEY, R.E., MUNSEE, C.L., PARK, C.H., HONG, D., WAGER, J.F. & KESZLER, D.A. (2004). Tin oxide transparent thin-film transistors. *J. Phys. D: Appl. Phys.*, **37**, 2810. 178

PRESLEY, R.E., HONG, D., CHIANG, H.Q., HUNG, C.M., HOFFMAN, R.L. & WAGER, J.F. (2006). Transparent ring oscillator based on indium gallium oxide thin-film transistors. *Solid St. Electron.*, **50**, 500. 178

PREWITT, C.T., SHANNON, R.D. & ROGERS, D.B. (1971). Chemistry of noble metal oxides. II. Crystal structures of platinum cobalt dioxide, palladium cobalt dioxide, copper iron dioxide, and silver iron dioxide. *Inorg. Chem.*, **10**, 719. 44, 46

RAMIREZ, A.P., ESPINOSA, G.P. & COOPER, A.S. (1992). Elementary excitations in a diluted antiferromagnetic kagomé lattice. *Phys. Rev. B*, **45**, 2505. 65

RAMIREZ, A.P., HAYASHI, A., CAVA, R.J., SIDDHARTHAN, R. & SHASTRY, B.S. (1999). Zero-point entropy in 'spin ice'. *Nature*, **399**, 333. 65

RASTOGI, A.C., LIM, S.H. & DESU, S.B. (2008). Structure and optoelectronic properties of spray deposited Mg doped p-$CuCrO_2$ semiconductor oxide thin films. *J. Appl. Phys.*, **104**, 023712. 73, 75, 76, 110

ROBERTSON, J., PEACOCK, P.W., TOWLER, M.D. & NEEDS, R. (2002). Electronic structure of p-type conducting transparent oxides. *Thin Solid Films*, **411**, 96. 42, 46, 55, 56, 57, 72, 129

ROGERS, A.F. (1913). Delafossite, a cuprous metaferrite from Bisbee, Arizona. *Am. J. Sci.*, **35**, 290. 43

ROGERS, A.F. (1922). Delafossite from Kimberly, Nevada. *Am. Mineral.*, **7**, 102. 43

ROGERS, D.B., SHANNON, R.D., PREWITT, C.T. & GILLSON, J.L. (1971). Chemistry of noble metal oxides. III. Electrical transport properties and crystal chemistry of ABO_2 compounds with the delafossite structure. *Inorg. Chem.*, **10**, 723. 43, 44, 45, 61, 74

ROWLAND, H.A. (1880). Preliminary notes on Mr. Hall's recent discovery. *Phil. Mag.*, **9**, 432. 13

RYU, Y.R., ZHU, S., LOOK, D.C., WROBEL, J.M., YEONG, H.M. & WHITE, H.W. (2000). Synthesis of p-type ZnO films. *J. Cryst. Growth*, **216**, 330. 154, 155

SADIK, P.W., IVILL, M., CRACIUN, V. & NORTON, D.P. (2009). Electrical transport and structural study of $CuCr_{1-x}Mg_xO_2$ delafossite thin films grown by pulsed laser deposition. *Thin Solid Films*, **517**, 3211. 53, 54, 73, 75

SASAKI, M. & SHIMODE, M. (2003). Fabrication of bipolar $CuInO_2$ with delafossite structure. *J. Phys. Chem. Solids*, **64**, 1675. 74, 129, 130

SATO, H., MINAMI, T., TAKATA, S. & YAMADA, T. (1993). Transparent conducting *p*-type NiO thin films prepared by magnetron sputtering. *Thin Solid Films*, **236**, 27. 40

SCANLON, D.O., WALSH, A., MORGAN, B.J., WATSON, G.W., PAYNE, D.J. & EGDELL, R.G. (2009a). Effect of Cr substitution on the electronic structure of $CuAl_{1-x}Cr_xO_2$. *Phys. Rev. B*, **79**, 035101. 54, 55, 56, 58, 59, 60, 77

SCANLON, D.O., WALSH, A. & WATSON, G.W. (2009b). Understanding the *p*-type conduction properties of the transparent conducting oxide $CuBO_2$: A density functional theory analysis. *Chem. Mater.*, **21**, 4568. 77

SCANLON, D.O., GODHINHO, K.G., MORGAN, B.J. & WATSON, G.W. (2010). Understanding conductivity anomalies in Cu(I)-based delafossite transparent conducting oxides: Theoretical insights. *J. Chem. Phys.*, **132**, 024707. 55, 59, 62, 77

SCHILLER, S., BEISTER, G., BUEDKE, E., BECKER, H.J. & SCHICHT, H. (1982). Properties of cadmium stannate thin films produced by reactive high rate d.c. magnetron-plasmatron sputtering. *Thin Solid Films*, **96**, 113. 3

SEKI, S., ONOSE, Y. & TOKURA, Y. (2008). Spin-driven ferroelectricity in triangular lattice antiferromagnets $ACrO_2$ (A = Cu, Ag, Li, or Na). *Phys. Rev. Lett.*, **101**, 067204. 54, 66, 67, 68

SERGIENKO, I.A. & DAGOTTO, E. (2006). Role of the Dzyaloshinskii-Moriya interaction in multiferroic perovskites. *Phys. Rev. B*, **73**, 094434. 244

SHAHRIARI, D.Y., BARNABE, A., MASON, T.O. & POEPPELMEIER, K.R. (2001). A high-yield hydrothermal preparation of $CuAlO_2$. *Inorg. Chem.*, **40**, 5734. 49

SHAKED, H., HASTINGS, J.M. & CORLISS, L.M. (1970). Magnetic structure of magnesium chromite. *Phys. Rev. B*, **1**, 3116. 87

SHANNON, R.D. (1976). Revised effective ionic radii and systematic studies of interatomic distances in halides and chalcogenides. *Acta. Cryst.*, **A32**, 751. 45

Shannon, R.D., Rogers, D.B. & Prewitt, C.T. (1971). Chemistry of noble metal oxides. I. Syntheses and properties of ABO_2 delafossite compounds. *Inorg. Chem.*, **10**, 713. 44

Shanthi, E., Banerjee, A., Dutta, V. & Chopra, K.L. (1982). Electrical and optical properties of tin oxide films doped with F and (Sb+F). *J. Appl. Phys.*, **53**, 1615. 3

Sheng, S., Fang, G., Li, C., Xu, S. & Zhao, S. (2006). *p*-Type transparent conducting oxides. *Phys. Stat. Sol. (a)*, **203**, 1891. 42, 127

Shi, L.J., Fang, Z.J. & Li, J. (2008). First-principles study of *p*-type transparent conductive oxides $CuXO_2$ (X = Y, Sc, and Al). *J. Appl. Phys.*, **104**, 073527. 77

Shimode, M., Sasaki, M. & Mukaida, K. (2000). Synthesis of the delafossite-type $CuInO_2$. *J. Solid State Chem.*, **151**, 16. 46, 127, 128, 131, 132

Shive, J.N. (1949). The double-surface transistor. *Phys. Rev.*, **75**, 689. 181

Simmons, J.G. (1963). Generalized formula for the electric tunnel effect between similar electrodes separated by a thin insulating film. *J. Appl. Phys.*, **34**, 1793. 202

Sindzingre, P., Misguich, G., Lhuillier, C., Bernu, B., Pierre, L., Waldtmann, C. & Everts, H.U. (2000). Magnetothermodynamics of the spin-1/2 kagomé antiferromagnet. *Phys. Rev. Lett.*, **84**, 2953. 65

Snure, M. & Tiwari, A. (2007). $CuBO_2$: A *p*-type transparent oxide. *Appl. Phys. Lett.*, **91**, 092123. 74

Soda, M., Kimura, K., Kimura, T., Matsuura, M. & Hirota, K. (2009). Electric control of spin helicity in multiferroic triangular lattice antiferromagnet $CuCrO_2$ with proper-screw order. *J. Phys. Soc. Jpn.*, **78**, 124703. 68

Soller, W. & Thompson, A.J. (1935). The crystal structure of cuprous ferrite. *Phys. Rev.*, **47**, 644. 43

Stamenov, P. (2007). *Metals, Semimetals and Semiconductors for Spinelectronics*. Ph.D. thesis, Trinity College Dublin. 32

Stauber, R.E., Perkins, J.D., Parilla, P. & Ginley, D.S. (1999). Thin film growth of transparent *p*-type $CuAlO_2$. *Electrochem. Solid-State Lett.*, **2**, 654. 101

STAUBER, R.E., PARILLA, P.A., PERKINS, J.D. & GINLEY, D.S. (2000). Growth and chemical substitution of transparent p-type $CuAlO_2$. *Mater. Res. Soc. Symp. Proc.*, **623**, 265. 73

STIFTER, D. & SITTER, H. (1995). Growth of C_{60} thin films on mica by hot wall epitaxy. *J. Cryst. Growth*, **156**, 79. 99

SUZUKI, A., MATSUSHITA, T., AOKI, T., MORI, A. & OKUDA, M. (2002). Highly conducting transparent indium tin oxide films prepared by pulsed laser deposition. *Thin Solid Films*, **411**, 23. 3, 150

SZE, S.M. (1985). *Semiconductor Devices Physics and Technology*. John Wiley & Sons, Inc. 20, 179, 182, 184, 185

TAKAHASHI, Y., MATSUSHITA, H. & KATSUI, A. (2007). Synthesis and characterisation of delafossite $CuLaO_2$ for thermoelectric application. *Mater. Sci. Forum*, **534**, 1081. 74

TAKAHATA, S., SAIKI, K., IMAO, T., NAKANISHI, H. & SUGIYAMA, M. (2009). Fabrication of a n-type ZnO / p-type Cu-Al-O heterojunction diode by sputtering deposition methods. *Phys. Status Solidi C*, **6**, 1105. 177

TAMM, I. (1932). *Phys. Z. Sowjet.*, **1**, 733. 181

TATE, J., JAYARAJ, M.K., DRAESEKE, A.D., ULBRICH, T., SLEIGHT, A.W., VANAJA, K.A., NAGARAJAN, R., WAGER, J.F. & HOFFMAN, R.L. (2002). p-Type oxides for use in transparent diodes. *Thin Solid Films*, **411**, 119. 46, 48, 49, 50, 53, 72, 73, 74, 75

TAUC, J., GRIGOROVICI, R. & VANCU, A. (1966). *Phys. Stat. Sol.*, **15**, 627. 108

TEPLIN, C.W., KAYDANOVA, T., YOUNG, D.L., PERKINS, J.D. & GINLEY, D.S. (2004). A simple method for the preparation of transparent p-type Ca-doped $CuInO_2$ films: Pulsed-laser deposition from air-sintered Ca-doped $Cu_2In_2O_5$ targets. *Appl. Phys. Lett.*, **85**, 3789. 74, 128, 129, 130, 131, 142

THOMAS, G. (1997). Invisible circuits. *Nature*, **389**, 907. 4, 6, 49

THOMSON, W. (1857). On the electro-dynamic qualities of metals: Effects of magnetization on the electric conductivity of Nickel and of Iron. *Proc. R. Soc. Lond.*, **8**, 546. 30

THURBER, W.R. (2008). Hall effect measurements. 169, 239

TONOOKA, K. & KIKUCHI, N. (2006). Preparation of transparent $CuCrO_2$:Mg / ZnO *p-n* junctions by pulsed laser deposition. *Thin Solid Films*, **515**, 2415. 177, 200

TONOOKA, K., BANDO, H. & AIURA, Y. (2003). Photovoltaic effect observed in transparent *p-n* heterojunctions based on oxide semiconductors. *Thin Solid Films*, **445**, 327. 177

TSUKAZAKI, A., OHTOMO, A., YOSHIDA, S., KAWASAKI, M., CHIA, C.H., MAKINO, T., SEGAWA, Y., KOIDA, T., CHICHIBU, S.F. & KOINUMA, H. (2003). Layer-by-layer growth of high-optical-quality ZnO film on atomically smooth and lattice relaxed ZnO buffer layer. *Appl. Phys. Lett.*, **83**, 2784. 153

UEDA, K. & HOSONO, H. (2002). Crystal structure of $LaCuOS_{1-x}Se_x$ oxychalcogenides. *Thin Solid Films*, **411**, 115. 2

UEDA, K., HASE, T., YANAGI, H., KAWAZOE, H., HOSONO, H., OHTA, H., ORITA, M. & HIRANO, M. (2001). Epitaxial growth of transparent *p*-type conducting $CuGaO_2$ thin films on sapphire (001) substrates by pulsed laser deposition. *J. Appl. Phys.*, **89**, 1790. 46, 48, 73, 101

VAN DER PAUW, L.J. (1958). A method of measuring the resistivity and hall coefficient on lamellae of arbitrary shape. *Philips Technical Review*, **20**, 220. 239

VLASENKO, L.S. & WATKINS, G.D. (2005). Optical detection of electron paramagnetic resonance for intrinsic defects produced in ZnO by 2.5-MeV electron irradiation in situ at 4.2 K. *Phys. Rev. B*, **72**, 035203. 154

WAGNER, C. & SCHOTTKY, W. (1931). Theorie der geordneten Mischphasen. *Z. Phys. Chem.*, **11**, 163. 13

WANG, L., YOON, M.H., LU, G., YANG, Y., FACCHETTI, A. & MARKS, T.J. (2006). High performance transparent inorganicorganic hybrid thin-film-type transistors. *Nat. Mater.*, **5**, 893. 178

WANG, X., ZHI, L. & MÜLLEN, K. (2008). Transparent, conductive graphene electrodes for dye-sensitized solar cells. *Nano Lett.*, **8**, 323. 2

WILSON, A.H. (1931a). The theory of electronic semi-conductors I. *Proc. R. Soc. Lond.*, **A133**, 458. 8, 14

WILSON, A.H. (1931b). The theory of electronic semi-conductors II. *Proc. R. Soc. Lond.*, **A134**, 277. 8, 14

Xiu, F.X., Yang, Z., Mandalapu, L.J., Zhao, D.T. & Liu, J.L. (2005). High-mobility Sb-doped *p*-type ZnO by molecular-beam epitaxy. *Appl. Phys. Lett.*, **87**, 152101. 155

Yabuta, H., Sano, M., Abe, K., Aiba, T., Den, T., Kumomi, H., Nomura, K., Kamiya, T. & Hosono, H. (2006). High-mobility thin-film transistor with amorphous $InGaZnO_4$ channel fabricated by room temperature rf-magnetron sputtering. *Appl. Phys. Lett.*, **89**, 112123. 178

Yaicle, C., Blacklocks, A., Chadwick, A.V., Perriere, J. & Rougier, A. (2007). Relationship between structure and deposition conditions for $CuInO_2$ thin films. *Appl. Surf. Sci.*, **254**, 1343. 134

Yan, M., Lane, M., Kannewurf, C.R. & Chang, R.P.H. (2001). Highly conductive epitaxial CdO thin films prepared by pulsed laser deposition. *Appl. Phys. Lett.*, **78**, 2342. 2

Yanagi, H., Inoue, S., Ueda, K., Kawazoe, H., Hosono, H. & Hamada, N. (2000a). Electronic structure and optoelectronic properties of transparent *p*-type conducting $CuAlO_2$. *J. Appl. Phys.*, **88**, 4159. 4, 46, 48, 55, 57, 73, 77

Yanagi, H., Kawazoe, H., Kudo, A., Yasukawa, M. & Hosono, H. (2000b). Chemical design and thin film preparation of *p*-type conductive transparent oxides. *J. Electroceram.*, **4**, 427. 73

Yanagi, H., Kawazoe, H., Kudo, A., Yasukawa, M. & Hosono, H. (2000c). Chemical design of transparent *p*-type conducting oxides. *J. Electroceram.*, **4**, 407. 40, 128

Yanagi, H., Hase, T., Ibuki, S., Ueda, K. & Hosono, H. (2001a). Bipolarity in electrical conduction of transparent oxide semiconductor $CuInO_2$ with delafossite structure. *Appl. Phys. Lett.*, **78**, 1583. 40, 46, 48, 49, 74, 127, 128, 130

Yanagi, H., Ueda, K., Ohta, H., Orita, M., Hirano, M. & Hosono, H. (2001b). Fabrication of all oxide transparent *p*-*n* homojunction using bipolar $CuInO_2$ semiconducting oxide with delafossite structure. *Solid State Commun.*, **121**, 15. 46, 49, 127, 130, 177

Yanagi, H., Park, S., Draeseke, A.D., Keszler, D.A. & Tate, J. (2003a). *p*-Type conductivity in transparent oxides and sulfide fluorides. *J. Solid State Chem.*, **175**, 34. 48

Yanagi, H., Tate, J., Park, S., Park, C.H. & Keszler, D.A. (2003b). *p*-Type conductivity in wide-band-gap BaCuQF (Q = S, Se). *Appl. Phys. Lett.*, **82**, 2814. 2

Zeng, Y.J., Ye, Z.Z., Lu, J.G., Xu, W.Z., Zhu, L.P., Zhao, B.H. & Limpijumnong, S. (2006). Identification of acceptor states in Li-doped p-type ZnO thin films. *Appl. Phys. Lett.*, **89**, 042106. 154

Zhang, S.B., Wei, S.H. & Zunger, A. (1998). A phenomenological model for systematization and prediction of doping limits in II-VI and I-III-VI_2 compounds. *J. Appl. Phys.*, **83**, 3192. 77

Zhang, S.B., Wei, S.H. & Zunger, A. (2000). Microscopic origin of the phenomenological equilibrium "Doping Limit Rule" in n-type III-V semiconductors. *Phys. Rev. Lett.*, **84**, 1232. 77

Zhao, J.L., Li, X.M., Krtschil, A., Krost, A., Yu, W.D., Zhang, Y.W., Gu, Y.F. & Gao, X.D. (2007). Study on anomalous high p-type conductivity in ZnO films on silicon substrate prepared by ultrasonic spray pyrolysis. *Appl. Phys. Lett.*, **90**, 062118. 154

Zheng, S.Y., Jiang, G.S., Su, J.R. & Zhu, C.F. (2006). The structural and electrical property of $CuCr_{1-x}Ni_xO_2$ delafossite compounds. *Mat. Lett.*, **60**, 3871. 73

Zhou, S., Fang, X., Deng, Z., Li, D., Dong, W., Tao, R., Meng, G., Wang, T. & Zhu, X. (2008). Hydrothermal synthesis and characterization of $CuCrO_2$ laminar nanocrystals. *J. Cryst. Growth*, **310**, 5375. 54, 76

Zhou, S., Fang, X., Deng, Z., Li, D., Dong, W., Tao, R., Meng, G. & Wang, T. (2009). Room temperature ozone sensing properties of p-type $CuCrO_2$ nanocrystals. *Sensor Actuat. B Chem.*, **143**, 119. 53